DESIGN, SYNTHESIS AND STUDIES ON NEW MOLECULAR PROBES FOR DIAGNOSIS AND TREATMENT OF CANCER

Thesis Submitted to AcSIR for the Award of the Degree of
DOCTOR OF PHILOSOPHY
in Chemical Sciences

By

SARANYA GIRIDHARAN

Registration No: 10CC15A39005

Under the guidance of

Dr. A. AJAYAGHOSH and Dr. KAUSTABH KUMAR MAITI

CSIR-NATIONAL INSTITUTE FOR INTERDISCIPLINARY
SCIENCE AND TECHNOLOGY (CSIR-NIIST)
THIRUVANANTHAPURAM-695 019, KERALA, INDIA

May, 2020

Dedicated to

My Family & My Teachers

DECLARATION

I hereby declare that the matter embodied in the thesis entitled: "**Design, Synthesis and Studies on New Molecular Probes for Diagnosis and Treatment of Cancer**" is the result of the investigations carried out by me at the Chemical Sciences and Technology Division, CSIR-National Institute for Interdisciplinary Science and Technology (CSIR-NIIST), Thiruvananthapuram, under the supervision of Prof. A. Ajayaghosh and Dr. Kaustabh Kumar Maiti and the same has not been submitted elsewhere for the award of any other degree or diploma.

In keeping with the general practice of reporting scientific observations, due acknowledgement has been made wherever the work described is based on the findings of other investigators.

Saranya Giridharan

National Institute for Interdisciplinary Science and Technology (NIIST)
(Formerly Regional Research Laboratory)
Council of Scientific & Industrial Research (CSIR)
Industrial Estate P.O., Trivandrum - 695 019
Kerala, INDIA

May 27, 2020

CERTIFICATE

This is to certify that the work described in this Ph. D. thesis entitled ***"Design, Synthesis and Studies on New Molecular Probes for Diagnosis and Treatment of Cancer"*** *submitted by* ***Ms. Saranya Giridharan*** *to the Academy of Scientific and Innovative Research (AcSIR) in fulfilment of the requirements for the award of the* ***Degree of Doctor of Philosophy in Chemical Sciences*** *embodies original research work carried out by her under our supervision. We further certify that this work has not been submitted to any other University or Institution in part or full for the award of any degree or diploma. Research materials obtained from other sources have been duly acknowledged in the thesis. Any text, illustration, table etc., used in the thesis from other sources, have been duly cited and acknowledged.*

Saranya Giridharan

A. Ajayaghosh
(Supervisor)

Kaustabh Kumar Maiti
(Supervisor)

Acknowledgements

It is with great pleasure that I extend my deep sense of gratitude to Prof. A. Ajayaghosh and Dr. Kaustabh Kumar Maiti, my thesis supervisors, for suggesting the research problem, for their valuable guidance, support, encouragement and scientific freedom, leading to the successful completion of this work. I also want to thank them for the expression of faith in my abilities.

I would like to express my gratitude to Late Prof. M. V. George for being an inspiration.

I would like to acknowledge Dr. G. Vijay Nair for his constant motivation and support.

My sincere thanks are also due to:

- *Dr. Mangalam S. Nair and Dr. R. Luxmi Varma and Dr. C. H. Suresh, former and present AcSIR coordinators.*
- *Dr. K. R. Gopidas and Dr. P. Sujatha Devi, former and present Heads, Chemical Sciences and Technology Division for their valuable suggestions*
- *Dr. K. V. Radhakrishnan, Dr. K. G. Raghu and Dr. Joshy Joseph, the Doctoral Advisory Committee (DAC) members and the whole AcSIR faculty for the successful completion of course work.*
- *Dr. T. T. Sreelekha (Regional Cancer Centre, Thiruvananthapuram), Dr. K. Sujathan (Regional Cancer Centre, Thiruvananthapuram) and Dr. R. S. Jayasree (Sree Chitra Tirunal Institute for Medical Sciences and Technology, Thiruvananthapuram) and their group members for the collaborative support.*
- *Dr. K. N. Narayanan Unni, Dr. J. D. Sudha, Dr. Joshy Joseph, Dr. K. Yoosaf, Dr. C. Vijayakumar, Dr. Biswapriya Deb, Dr. V. Karunakaran, Dr. V. K. Praveen, Dr. Suraj Soman, Dr. Sreejith Shankar, Dr. Manas Panda, Dr. Animesh Samanta, Dr. Ishita Neogi, present and former scientists of the Photosciences and Photonics Section, Chemical Sciences and Technology Division (CSTD), for their help and support.*
- *Dr. Kumaran, Dr. L. Ravishankar, Dr. B. S. Sasidhar, Dr. Sunil Varughese, Dr Jubi John and Dr. Sridevi, scientists of the Organic Chemistry Section, Chemical Sciences and Technology Division (CSTD), for their help and support.*

- *Sincere thanks to Dr. Manu M. Joseph, Ms. Varsha Karunakaran and Dr. Vishnupriya Murali for teaching and helping biological experiments.*
- *Dr. P. Anees, Dr. Thirumalai, Dr. Sandeep, A., Dr. Sandeep C., Dr. Rahul Dev Mukhopadhyay, Dr. Divya Susan Philips, Dr. Samrat Ghosh, Dr. Vishnu, Dr. B. Vedhanarayanan, Dr. K. V. Sudheesh, Dr. Arindam Mal, Dr. Hifsudheen, Dr. Nisha N., Dr. Santhi Maniganda, the former group members for their help, guidance and support.*
- *Sincere thanks to my group members Dr. Jyothi B. Nair, Dr. Satyajit Das, Ms. Ramya A.N., Mr. Sujai P.T., Ms. Arya J.S., Mr. Sandip Chakraborthy, Mr Gourab Das, Mr. Vijayakumar, Mr. Syamjith S., Ms. Deepika S., Mr. Madhukrishnan M., Ms. Vidyalekshmi, Ms. Anjitha Ajith, Mr. Shihas Ahamed, Mr. Dipak Patra, Ms. Drishya, Ms. Shamna and Ms. Anusree for their love, friendship and support.*
- *All former and present members of CSTD for their cooperation and help.*
- *Mr. Janardhan and Ms. Thushara, Masters and summer project students for their generous support.*
- *Special thanks to Dr. Dhanya S. R., Dr. Sajin Francis, Dr. Vineeth Vijayan, and Dr. Susan Alex for their timely help and support.*
- *Mr. Robert Philip, Mr. Kiran J. S. and Vishnu Gurjar for their general help and support.*
- *Mr. Kiran Mohan for TEM analysis, Mr. Aswin Maheshwar, Mr. Vishnu M., and Mr. Vibhu Darshan for AFM analysis.*
- *Dr. Chandrakanth and Mr. Hareesh for SEM analysis.*
- *Mrs. M. Saumini, Mr. P. Saran and Mr. R. Gokul for NMR and Mrs. S. Viji, Ms. Athira for mass spectral analyses.*
- *A special word of thanks to my chemistry teacher, Mrs. Ambili P. Nair, for being an inspiration to love chemistry.*
- *All my beloved teachers at every stages of my academic career.*
- *All my friends at NIIST.*
- *University Grants Commission (UGC), Government of India, for financial assistance.*

I am deeply and forever indebted to my family for their love, blessings, guidance and support. Finally, I would like to thank all my dear friends and teachers from my school and college and each and every person who has made my life bright and cheerful.

Above all, I bow to Almighty for bestowing his blessings upon me.

Saranya Giridharan

CONTENTS

List of Schemes

List of Figures

Page

List of Tables

List of Abbreviations

A549	Adenocarcinomic human alveolar basal epithelial cells
AA	Amino acid
AcOH	Acetic acid
AFM	Atomic force microscopy
Ag	Silver
AIE	Aggregation induced emission
Ala	Alanine
Arg	Arginine
ATP	Adenosine triphosphate
AuNP	Gold nanoparticle
AuNR	Gold nanorod
Bel 7702	Benign human liver cell line
BODIPY	4,4-Difluoro-4-bora-3a,4a-diaza-*s*-indacene
BSA	Bovine serum albumin
ca.	Approximately
CathB	Cathepsin B
CCD	Charge-coupled device
$CDCl_3$	Deuterated chloroform
$CHCl_3$	Chloroform
CH_3COOH	Acetic acid
CH_3CN	Acetonitrile
CHO	Chinese Hamster Ovary cell line
CK	Cytokeratin
cm	Centimeter
CO	Carbon monoxide
CO_2	Carbon dioxide
$COCl_2$	Cobalt chloride
CPCSEA	Committee for the Purpose of Control and Supervision of Experiments

	on Animals
Cys	Cysteine
D-A-D	Donor-acceptor-donor
DCM	Dichloromethane
DCF	2’, 7’-dichlorofluorescein
DCFDA	2’, 7’-dichlorofluorescein diacetate
DIC	N, N’-diisopropylcarbodiimide
DIPEA	Diisopropyl ethylamine
DLA	Dalton’s lymphoma ascites
DLS	Dynamic light scattering
DMEM	Dulbecco's modified eagle’s medium
DMF	Dimethyl formamide
DMSO	Dimethyl sulphoxide
DNA	Deoxyribonucleic acid
DOX	Doxorubicin
DPBF	1,3-diphenylisobenzofuran
DTT	Dithiothreitol
eq.	equivalent
EDC	N-(3-(dimethylamino)-propyl)-N’-ethylcarbodiimide
EDTA	Ethylenediamine tetraacetic acid
EGFR	Epidermal growth factor receptor
EPO	Endoperoxide
ESIPT	Excited state intramolecular proton transfer
ESR	Electron spin resonance
et al.	*Et allii/alia*
EtOH	Ethanol
FA	Folic acid
FAB	Fast atom bombardment
FBS	Fetal bovine serum
FITC	Fluorescein isothiocyanate
FKC	Phenylalanine-Lysine-Cysteine

FR	Folate receptor
FRET	Fluorescence resonance energy transfer
g	gram
Glu	Glutamic acid
Gly	Glycine
GM	Goppert Mayer
GSH	Glutathione
GSSG	Glutathione-disulfide
h	Hour
$h\upsilon_{ex}$	Excitation energy
$h\upsilon_{em}$	Emission energy
H69AR	Multidrug resistant lung cancer cell line
H9C2	Murine myoblast cell line
H-bonding	Hydrogen bonding
HBTU	(2-1H-benzotriazo-1-yl)-1,1,3,3-tetramethyluronium hexafluorophosphate
HCl	Hydrochloric acid
Hcy	Homocysteine
HeLa	Human cervical cancer cell line
HEPES	4-(2-hydroxyethyl)-1-piperazineethanesulfonic acid
HepG2	Human liver hepatocellular carcinoma cell line
HL-7702	Hepatic immortal cell line
H_2O	Water
H_2O_2	Hydrogen peroxide
HOBt	Hydroxybenzotriazole
Hp	Hematoporphyrin
HRMS	High resolution mass spectrometry
HRP	Horseradish peroxidase
HSA	Human serum albumin
H_2S	Hydrogen sulphide
H_2SO_4	Sulphuric acid

Hz	Hertz
IAEC	Institutional Animal Ethics Committee
ICPMS	Inductively coupled plasma mass spectrometry
ICT	Intramolecular charge transfer
lle	Isoleucine
ip	Intra-peritoneal
Ir	Iridium
IR	Infrared
J	Coupling constant
K_2CO_3	Potassium carbonate
KI	Potassium iodide
$KMnO_4$	Potassium permanganate
k_{obs}	Observed rate constant
L	Litre
Leu	Leucine
LNCaP	Human prostate adenocarcinoma cells
LOD	Limit of detection
LPA	α-lipoic acid
M	Molar
M^+	Molecular ion peak
MCF7	Human breast cancer cells
MDA-MB231	Epithelial human breast cancer cells
MDM2	Mouse double minute protein
MES	2-(N-morpholino)ethanesulfonic acid
MeOH	Methanol
MES	2-(*N*-morpholino)ethanesulfonic acid
MLCT	Metal to ligand charge transfer
MMP	Matrix metalloproteinase
MnO_2	Manganese oxide
MST	Mean survival time
MTT	3-(4,5-dimethylthiozolyl-2)-2,5-diphenyltetrazolium bromide

min	Minutes
mL	Millilitre
mm	Millimeter
mM	Millimolar
mmol	Millimoles
mol	Mole
mp	Melting point
Na_2CO_3	Sodium carbonate
NaD(P)H	Nicotinamide adenine dinucleotide phosphate hydrogen
NaH	Sodium hydride
Nap	Napsin
Na_2SO_4	Sodium sulfate
NEM	*N*-ethyl maleimide
NHS	N-hydroxysuccinimide
NH_4PF_6	Ammonium hexafluorophosphate
NIR	Near-infrared
nm	Nanometer
nM	Nanomolar
Nm^{-1}	Newton per meter
NMM	*N*-methylmaleimide
NMR	Nuclear magnetic resonance
NPs	Nanoparticles
ONOO	Peroxynitrite
O_2	Molecular oxygen
$^1O_2$	Singlet oxygen
PBS	Phosphate buffered saline
PDT	Photodynamic therapy
PEG	Polyethylene glycol
PET	Photoinduced electron transfer
PET	Positron emission tomography
PFC	Perfluorocarbon

pH	Hydrogen ion concentration at logarithmic scale
Phe	Phenyl alanine
pKa	Acid dissociation constant at logarithmic scale
pmol	Picomolar
ppm	Parts per million
Pro	Proline
PS	Photosensitizer
PSA	Prostate specific antigen
Pt	Platinum
PTT	Photothermal therapy
RhB	Rhodamine B
Rh110	Rhodamine 110
ROS	Reactive oxygen species
rpm	Revolutions per minute
rt	Room temperature
Ru	Ruthenium
S^{2-}	Sulphide anion
S_0	Ground electronic state
S_1	Lower electronic excited state
S_1*	Higher electronic excited state
s	Seconds
SDS	Sodium dodecyl sulphate
sec	Seconds
SERS	Surface enhanced Raman scattering
SiO_2	Silica
SOSG	Singlet oxygen sensor green
SPECT	Single photon emission computed tomography
str.	Stretching
T	Temperature
TEM	Transmission electron microscopy
TFA	Trifluoroacetic acid

THF	Tetrahydrofuran
TICT	Twisted intramolecular charge transfer
TIS	Triisopropyl silane
TME	Tumor microenvironment
TMS	Tetramethylsilane
Tyr	Tyrosine
US	Ultrasound
UV	Ultraviolet
v	Volume
Vis	Visible
WI38	Normal human diploid fibroblasts
Zn^{+2}	Zinc (II)
δ	Chemical shift
°C	Degree Celsius
Φ_F	Fluorescence quantum yield
v_{em}	Frequency of emission
v_{ex}	Frequency of excitation
µg	Microgram
µm	Micrometer
µM	Micromolar
ε	Molar extinction coefficient
λ_{abs}	Wavelength of absorption
λ_{ex}	Wavelength of excitation
λ_{em}	Wavelength of emission

PREFACE

The development of novel bioanalytical tools for the detection and monitoring of biologically relevant target materials and associated cellular events *in vitro* and *in vivo* poses a great challenge in clinical diagnostics and chemical biology. Among the various detection techniques, optical assays based on fluorescence and surface enhanced Raman scattering (SERS) facilitate a comprehensive and in-depth understanding of the complex biological systems and processes with high accuracy and sensitivity. In this regard, design and fabrication of materials with improved detection capability has become a hot topic of interest among the researchers. In addition to effective diagnosis, precise treatment and proper follow-up of therapeutic responses are essential for the efficient management of diseases. In order to meet these requirements, design of multifunctional materials with both sensing and therapeutic potential has emerged as a promising strategy. **Chapter 1** of the thesis gives an overview of the recent developments in the construction of optical probes that work on fluorescence and SERS and their potential in the diagnostic and theranostic applications for efficient clinical outcome. In addition, specific objectives of the present thesis are briefly described at the end of this chapter.

In **Chapter 2**, we have designed a ratiometric squaraine based fluorescent probe (**Sq**) for the detection and imaging of endogenous thiols under *in vitro* conditions. The probe afforded a ratiometric detection of thiols by switching its emission from NIR (690 nm) to visible region (560 nm). Further, the probe was utilized for the quantification of intracellular GSH concentrations in live cells and cell extracts, owing to its favorable attributes of high biocompatibility, excellent membrane permeability, and fast detection response in the intracellular conditions. The dye molecule also facilitated the accurate discrimination of cancer cells from normal cells via the investigation of cellular redox status. The promising potential of **Sq** was further explored for quantifying the GSH imbalance during various stages of apoptosis. These observations opened before us a new non-invasive pathway for diagnosing apoptosis which helps in understanding the fate of therapeutic responses in living systems.[1]

The design and fabrication of smart programmable nanostructures for the multiplexed detection of most prevalent panel of disease biomarkers present in lung cancer is described in **Chapter 3**. The multiplex nanoprobes comprised of dual responsive Raman active fluorophores attached to the surface of gold nanospheres through a strategically positioned peptide (Phe-Lys-Cys; FKC) sequence which is recognized as a specific substrate for cathepsin B (cathB), a key protease involved in cancer invasion and progression. The tripeptide linker was engineered to get cleaved upon homing into the cancer cells, which results in the release of the initially dormant fluorophores through a break in the conjugation which increases the distance of the dyes from the gold nanoparticle surface thereby causing the arresting of SERS activity, thereby realizing an on−off switching between the two imaging modalities. The anticipated mode of action of fluorescence-SERS encoded nanoparticle probes (**FSENP**s) was utilized for the detection of defined protein targets after decorating with specific monoclonal antibody recognition units. Moreover, as a major step towards the clinical applicability of the probe, we have performed the profiling of the disease biomarkers in patient specimens which offers new avenues for the development of a clinical screening tag for point-of-care diagnosis and personalized treatment applications.[2]

Hypoxia, as featured by low oxygen concentrations severely attenuates the treatment outcome of photodynamic therapy (PDT), which puts it beyond the reach of a successful therapeutic procedure in clinical scenario. In the final chapter, **Chapter 4**, we have demonstrated a new strategy for cutting off the intracellular oxygen consumption by developing a redox activatable singlet oxygen ($^1O_2$) self-enriched photoreactor (**Ir-Pyr-EPO@MnO$_2$-FA**) to meet the requirements of intracellular oxygen independent PDT. Upon target specific accumulation into the cancer cells followed by near infrared light irradiation, the photothermal effect generated by MnO_2 nanosheets facilitated the thermal cycloreversion of **Ir-Pyr-EPO** to release cytotoxic $^1O_2$, thereby paving way for the first phase of photodynamic therapy. Additionally, the redox responsive nature (high H_2O_2 and low pH) of tumor environment caused an activation of the luminescence properties of **Ir-Pyr** by the reduction of MnO_2, thereby enabling it for self-guided therapeutic applications. Furthermore, by taking advantage of the reduction properties of MnO_2, the as-produced molecular oxygen which got slowly released into the tumor region was utilized for the second phase of PDT by photosensitization using a 532 nm laser. The probe displayed excellent therapeutic efficacy *in vitro* and *in vivo* which facilitated the accurate diagnosis and positioned treatment of hypoxic tumors via oxygen irrelevant PDT/PTT under the guidance of luminescence imaging, thereby offering opportunities for the development of next generation cancer phototherapeutics.[3]

References

1. A Ratiometric Near-Infrared Fluorogen for the Real Time Visualization of Intracellular Redox Status during Apoptosis. **Saranya, G.**; Anees, P.; Joseph, M. M.; Maiti, K. K.; Ajayaghosh, A. *Chem. Eur. J.* **2017**, *23*, 7191−7195.

2. Enzyme-Driven Switchable Fluorescence-SERS Diagnostic Nanococktail for the Multiplex Detection of Lung Cancer Biomarkers. **Saranya, G.**; Joseph, M. M.; Karunakaran, V.; Nair, J. B.; Saritha, V. N.; Veena, V. S.; Sujathan, K.; Ajayaghosh, A.; Maiti, K. K. *ACS Appl. Mater. Interfaces* **2018**, *10*, 38807−38818.

3. A Rechargeable Singlet Oxygen Photogenerator with Tumor Niche Responsive Luminescence Imaging Capability for Intracellular Oxygen Independent Multiphase Photodynamic Therapy. **Saranya, G.**; Joseph, M. M.; Sujai, P. T.; Jibin, K.; Jayasree, R. S.; Ajayaghosh, A.; Maiti, K. K. (Manuscript under preparation).

Chapter 1

Optical Probes for Sensing, Imaging and Therapeutic Applications in Biomedicine: Recent Developments

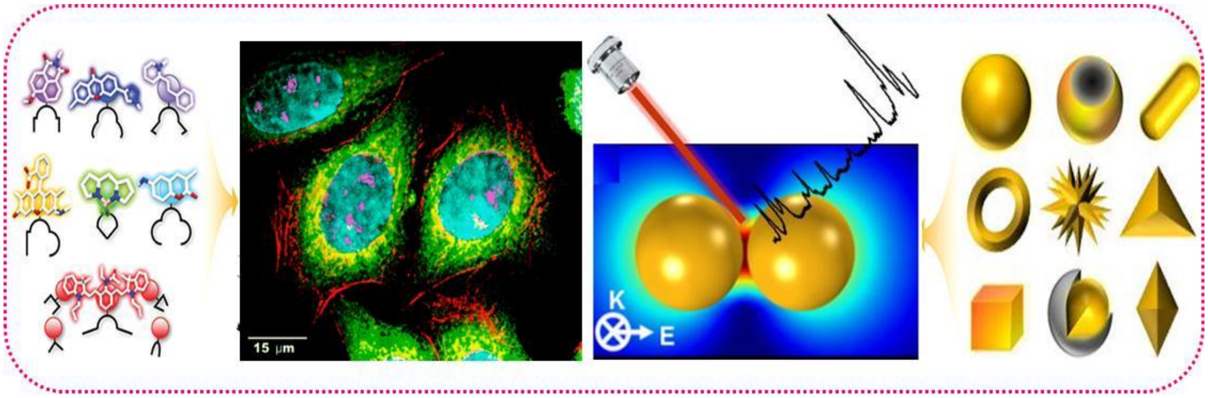

1.1. Abstract

Development of bioanalytical tools for the detection and monitoring of various biological targets and their associated events in vitro and in vivo remains a great challenge in biomedicine. Among the various detection techniques, optical assays based on fluorescence and surface enhanced Raman scattering (SERS) facilitate a comprehensive and in-depth understanding of the complex biological systems with high accuracy and sensitivity. In this regard, design and fabrication of materials with improved detection capability has become a topic of interest among the researchers. In addition to effective diagnosis, precise treatment and proper follow-up of therapeutic responses are essential for the efficient management of diseases. In order to meet these requirements, design of multifunctional materials with both sensing and therapeutic potential has emerged as a promising strategy. This introductory chapter

provides an overview of the recent developments in the construction of optical probes that work on fluorescence and SERS and their potential in the diagnostic and theranostic applications for efficient clinical outcome. Finally, the aim and the outline of the thesis are presented.

1.2. Introduction

Biosensing and bioimaging constitute the key tools to understand and visualize the function and regulation of many cellular processes and also in the profiling of heterogeneous disease conditions. A biosensor functions as an integrated device to convert a molecular recognition event to a detectable physicochemical signal. Thus, a biosensor primarily consists of a recognition motif to provide a specific binding with the target and a detector component for signaling the binding phenomenon. However, bioimaging is a relatively recent development that has created an outbreak in the medical field by making use of digital technology. Being non-invasive, bioimaging facilitates precise monitoring of biomarkers that can be used as targets for disease identification, therapy and follow-up of treatment responses. Among the various imaging techniques, fluorescence based probes are one of the most extensively used tools for optical imaging owing to its ability to analyze complex biological processes with high spatial and temporal resolution. The development of novel fluorescent imaging agents has brought significant advances in the field of disease diagnostics and personalized medicine.[1-4]

In addition to fluorescence based assays, surface enhanced Raman scattering (SERS) has transpired as a frontline biosensing tool, offering broad range analyte detection with high specificity and sensitivity.[5,6] In SERS, the inherently weak Raman vibrations of the molecule/analyte are subjected to amplification by several orders of magnitude via their interaction with nanoroughened metal substrates such as gold or silver. Design and fabrication of SERS active metal substrates and novel Raman reporter molecules facilitated the massive utilization of this technique in biomedical applications.[7] In recent years, significant efforts have been put towards the development of novel biosensors for diagnostic purposes using these two non-invasive imaging techniques.[8,9]

Following a successful diagnostic procedure, the next key step involved in the disease management is the therapy. Among the various currently available treatment modalities, phototherapies namely photodynamic therapy (PDT) and photothermal therapy (PTT) deserve special attention owing to their minimally invasive nature and excellent therapeutic efficiency.[10,11] Combination of diagnostic tools with therapeutic agents has given birth to a new paradigm in biomedicine known as theranostics. Theranostic agents not only offer targeted therapy but also elucidate the underlying disease mechanisms and facilitate pre- and post-treatment assessment.[12-14] These favorable attributes endow the multifunctional theranostic systems with immense potential in both translational and clinical research.

1.3. Bioimaging

Comprehensive profiling of cellular level interactions in biological systems in their native habitat poses a great challenge, particularly in the field of disease diagnostics and therapy. Over the past century, most of our understanding about the molecular level processes occurring in cells was from the traditional biochemical analysis that were carried out in test tubes which employed biomolecules in their isolated or pure form. Although this approach could provide valuable insights, it has limited scope that the actual cellular environment is fundamentally different from the solution state reaction conditions. In order to gain an in-depth understanding of the chemistry behind the living cells, it is important to consider the cell itself as the test tube and visualize the whole process. This kind of visualization will give a clear picture of the functioning of the cells and also the presence of any abnormalities, which will subsequently aid in diagnosing various diseases. The observation of the cellular and subcellular functions demands the need of highly sensitive instrumentation along with the use of some potential reporters or contrast agents. Contrast agents make the process visible and measurable which a simple light microscope cannot perform. Development in imaging techniques and contrast agents now enable imaging across a wide window ranging from 1-2 nm scale to whole organism phenotyping. Depending on the source employed, bioimaging has given birth to various imaging techniques such as fluorescence imaging, photoacoustic imaging, magnetic resonance imaging (MRI), SERS imaging, computed tomography (CT), positron emission tomography (PET) etc. Among these modalities, fluorescence imaging and SERS imaging stands as two promising techniques that enable real-time visualization of molecular events in the cellular environment with high sensitivity and resolution.

1.3.1. Fluorescence Imaging

Fluorescence is a form of luminescence that involves the dissipation of light energy from electronically excited states of a molecule or material that has absorbed suitable energy. In the fluorescence process, a photon of energy, $h\upsilon_{ex}$ will be given to the molecules, which will absorb and gets excited to a higher electronic level (S_1*). The molecule then relaxes to a lower electronic state S_1 by vibrational relaxation which occurs in picosecond timescale. Finally, the molecule will return to the ground electronic state S_0 by the emission of a lower energy photon ($h\upsilon_{em}$), which takes place in a relatively longer timeframe of nanoseconds. Although the entire process occurs in less than millionth of a second, this phenomenon of light matter interaction marks the basis of fluorescence imaging (**Figure 1.1a**). Owing to excellent sensitivity, high resolution and non-invasive nature, fluorescence technique has become an indispensable imaging tool in chemical biology.

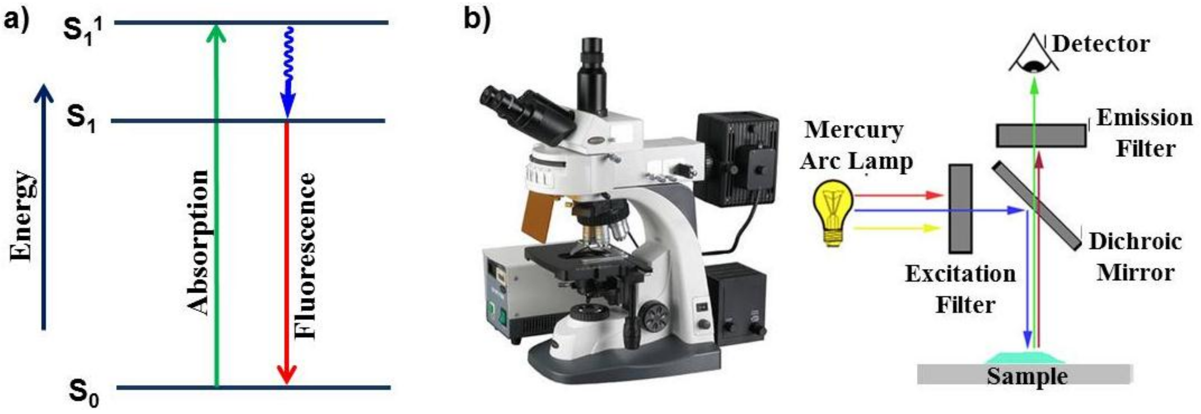

Figure 1.1. a) Simplified Jablonski diagram of the main processes involved in fluorescence and b) the working principle of a fluorescence microscope.

The basic principle involved in the working of a fluorescence microscope is shown in **Figure 1.1 b**. Light of the excitation wavelength produced from the source after passing through an excitation filter gets reflected through the objective to the sample using a dichroic mirror. The fluorescence emitted by the sample after passing through the emission filter is directed to the detector by the objective lens. Most of the fluorescence microscopes used is of the epifluorescence design, wherein both the excitation of the fluorophore as well as the detection of fluorescence occurs through the same light path (i.e. through the objective). Although, the imaging of various endogenous systems[15-17] such as NAD(P)H, tryptophans and flavins provided a general understanding of the various processes inside the cell, the emergence of different fluorescent molecules, genetically modified fluorescent proteins and fluorescent nanomaterials opened up a new dimension to make cellular processes more visible which enabled the precise tracking and real-time monitoring of the complex biomolecular reactions, their dynamics, transport characteristics and interaction with various cellular components.

1.3.2. Fluorescence Probes for Sensing and Imaging

Fluorescent probes are systems which undergo a change in their emission properties upon interaction with a specific analyte, thereby giving a measurable fluorescence signal. The development of fluorogenic probes has a significant role in the current advances in disease diagnostics and cell biology owing to their high sensitivity and excellent spatial and temporal resolution.[18] In the past few decades, a large number of new fluorogenic materials have been developed based on small organic molecules, quantum dots, fluorescent proteins, polymers, carbon dots etc.[19-24] However, the most popular candidates among this category are the small molecule based probes because of their favourable features in terms of small size, effective intracellular permeability, good biocompatibility etc. Several rationales can be adopted in the design of fluorescent probes such as intramolecular charge transfer (ICT), twisted intramolecular charge transfer (TICT), photoinduced electron transfer (PET), Forster resonance energy transfer (FRET), excimer/exciplex formation, excited state intramolecular proton transfer (ESIPT), aggregation induced emission (AIE) and lot more.[25-27] Depending on the mode of emission change occurring during the signaling process, fluorescent probes can be classified into three main categories: (i) turn-off (ii) turn-on and (iii) ratiometric probes.

1.3.2.1. Turn-off Fluorescent Probes

Probes which produce a decline in the fluorescence intensity upon recognition with the target analyte are referred to as turn-off fluorescent probes. Up to now, a large number of turn-off fluorescent sensors have been designed and developed for the sensing and imaging of biologically and/or clinically relevant targets.

Ramamurthy *et al.,* reported a number of amidothiourea linked acridinedione based chemosensors for the detection of Hg^{2+}.[28] The dyes showed a strong emission in the 440 nm region via the ICT process from ring nitrogen to carbonyl centre of the acridinedione moiety. On addition of Hg^{+2}, the fluorescence signal revealed a quenching in the emission intensity which can be attributed to the intramolecular PET process from the aniline unit to the acridinedione fluorophore. Furthermore, the molecule **1e** has been successfully applied for the two-photon imaging of Hg^{+2} *in vitro* (**Figure 1.2**). Breuer and co-workers demonstrated the potential of calcein and its acetoxymethylester (AM) derivative for the detection of iron. The probes consisted of iminodiacetate units as the metal ion receptor and fluorescein core as the fluorophore. The emission signal showed a 46% decline in its intensity upon binding of iron with the receptor unit. However the probe failed to discriminate between Fe^{+2} and Fe^{+3} since Fe^{+2} gets oxidized to Fe^{+3} upon calcein

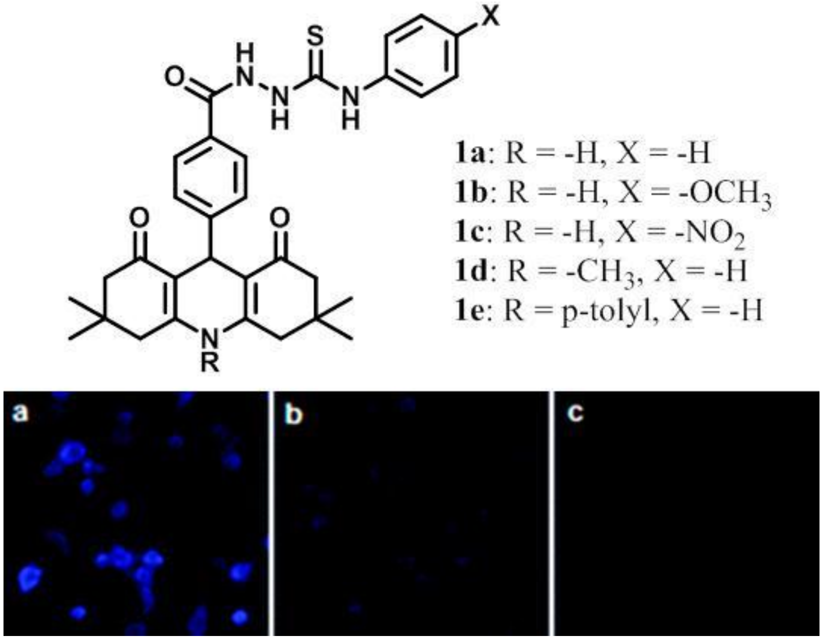

Figure 1.2. Molecular structures of probes for Hg^{+2} detection and two photon fluorescence microscopic images of H9C2 cells administered with **1e** upon addition of increasing concentrations of Hg^{+2}.

binding. The authors succeeded in monitoring the intracellular iron flux in K562 cells using their probe.[29,30] Now, calcein and calcein-AM are commercially available probes which are widely used to track labile iron pool in biological systems.

Protons play a key role in regulating several cellular processes and hence identified as an important target for the early diagnosis of many serious diseases including cancer. Li and colleagues developed a pyridine appended Troger's base **2** (**Figure 1.3a**) that exhibited a pH dependent fluorescence response in the

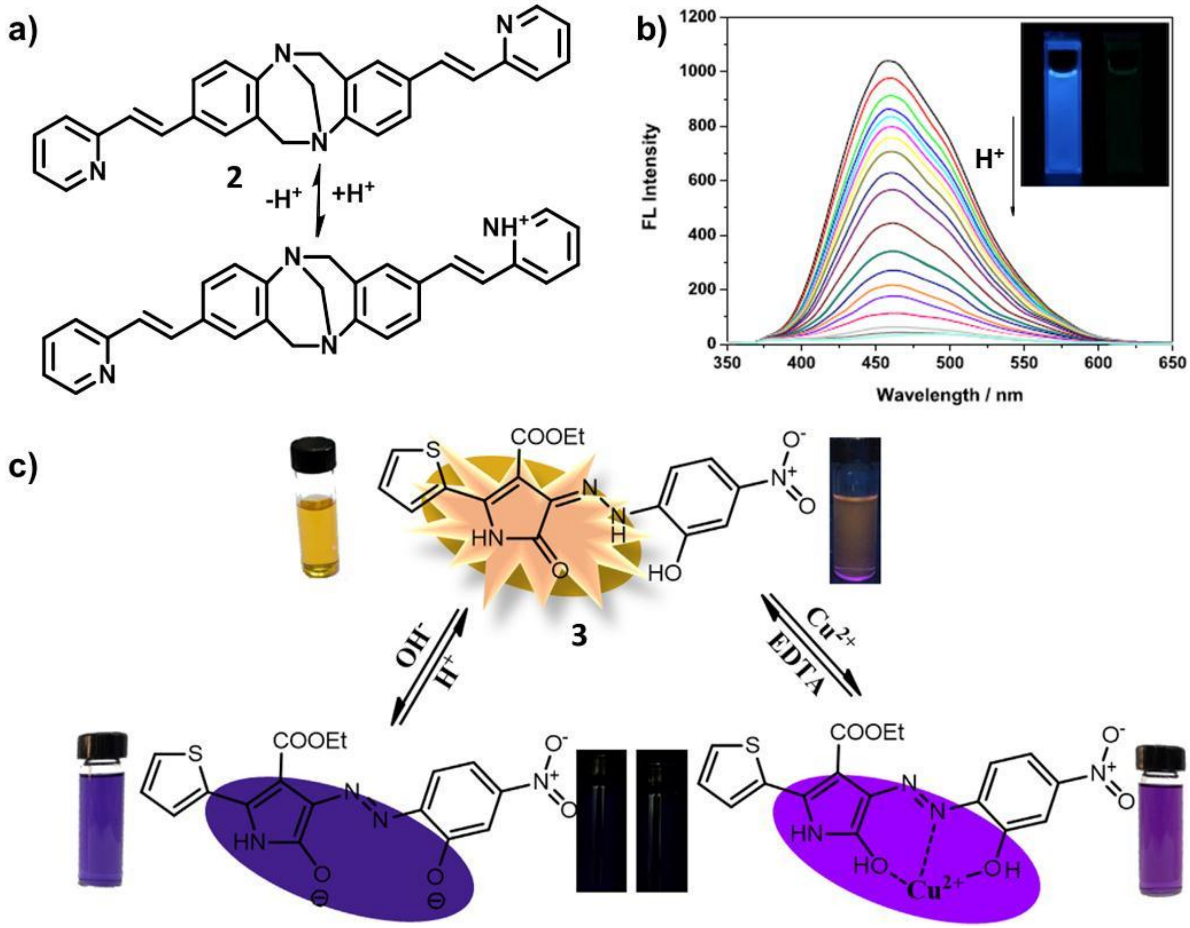

Figure 1.3. a) Sensing action of **2** for pH detection, b) emission spectral analysis of **2** with increasing H^+ concentration and c) the proposed mechanism of Cu^{+2} and H^+ detection by **3**.

acidic window.[31] The molecule displayed strong blue emission which got gradually decreased with increasing concentrations of H^+ (**Figure 1.3b**). Owing to the high sensitivity, excellent selectivity, large Stokes shift and short response time, **2** proved to be an efficient fluorescent probe for pH detection under acidic conditions. A dual functional fluorescent probe **3** built on pyrrolidine ester hydrazone dye was designed for the detection of Cu^{+2} and pH. The probe **3** exhibited a turn-off response towards Cu^{+2} with high sensitivity with a detection limit as low as 0.63 µM. Moreover, the dye also showed excellent fluorescence response in the basic pH window with pKa around 8.5. Thus, the dye worked as a multifunctional sensor platform for the simultaneous detection of Cu^{+2} ions and pH (**Figure 1.3c**).[32]

A report by Martinez-Manez *et al.,* demonstrated squaraine based chemodosimeters (**4** and **5**) for the detection of thiols via a nucleophilic addition reaction (**Figure 1.4a**).[33] The dye molecules exhibited intense absorption bands in the near infrared (NIR) region together with strong fluorescence in the aqueous conditions. In acetonitrile/MES buffer (pH 6; 2:8 v/v), the molecules showed a remarkable bleaching in presence of cysteine. This decrease in absorption was concomitantly followed by a quenching in the emission signals which enabled the authors to determine the level of cysteine and cysteine derivatives in human plasma. In a recent study, Ajayaghosh and coworkers developed a CO_2 detection probe (**6**) based on phenylenevinylene core (**Figure 1.4b**) which displayed an on-off response towards carbon dioxide among other neutral gases. In aqueous medium, the molecule exhibited an intense emission at 550 nm which can be attributed to the aggregation induced emission (AIE) property of the dye. However, in the presence of CO_2, the molecular aggregates of **6** underwent a protonation which induced a hydrophobic to hydrophilic transformation. These changes were indicated by a reduction in the AIE property which was reflected in the emission spectral analysis which showed a

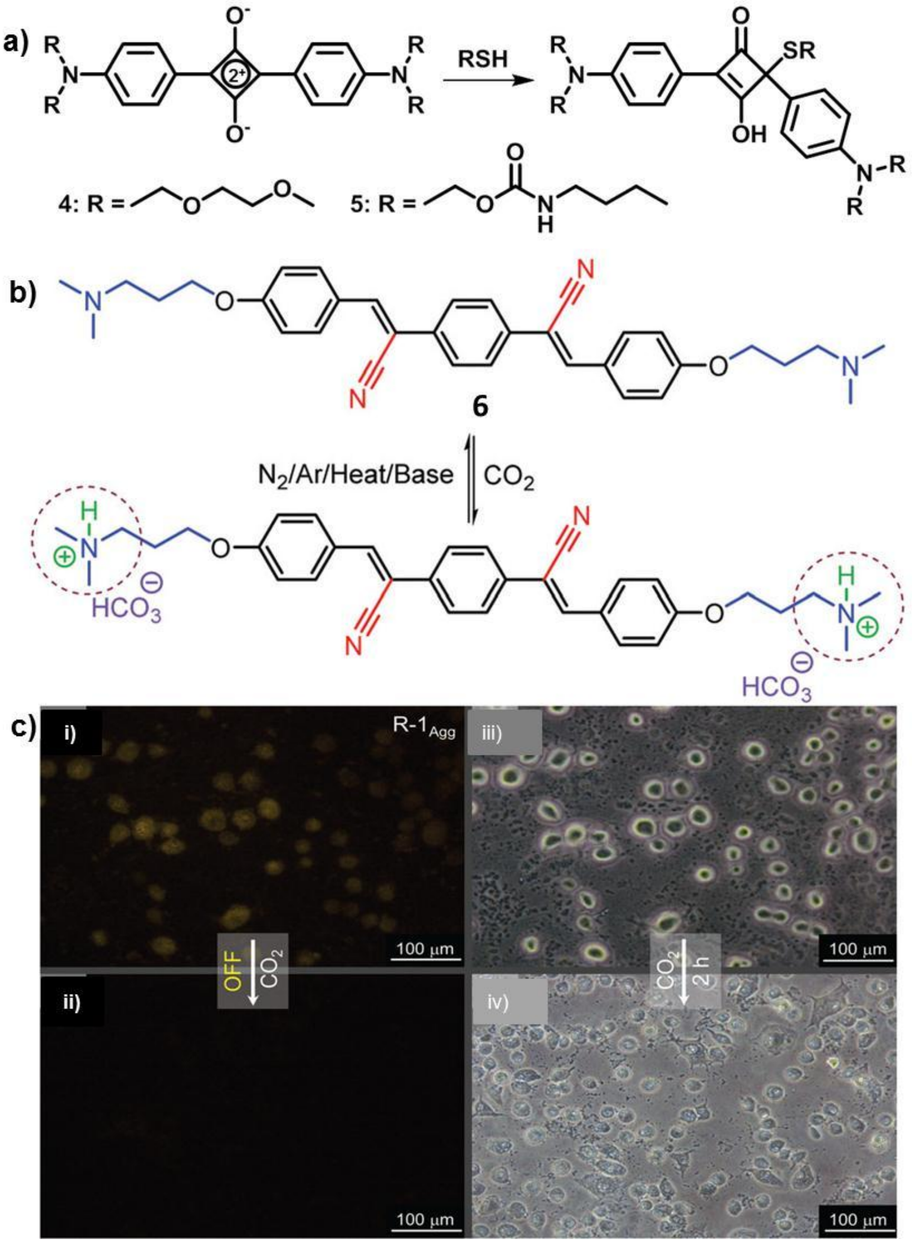

Figure 1.4. a) Sensing mechanism of squaraine dyes **4** and **5** with thiols. b) Molecular structure of *p*-phenylenevinylene dye **6** and its interaction with CO_2. c) Fluorescence microscopic analysis of CO_2 sensing *in vitro*. i) Fluorescence and iii) bright field images of A549 cells incubated with **6**. ii) and iv) represent the corresponding fluorescence and bright field images of cells pretreated with **6** and further exposed to 5% CO_2.

quenching of the emission intensity at 550 nm. Furthermore, the authors demonstrated the utility of **6** as a probe for evaluating CO_2 levels in biological samples. Human lung adenocarcinoma cells (A549) incubated with **6** showed a strong yellow fluorescence suggesting the internalization of the molecular aggregates in the cells. Upon incubation with 5% CO_2, the yellow emission got dramatically decreased while the control cells kept in the absence of CO_2 retained the same emission, thereby revealing the potential of **6** to monitor CO_2 variations in cell specimens (**Figure 1.4c**).[34]

1.3.2.2. Turn-on Fluorescent Probes

Although there have been many studies on the development of turn-off fluorescent sensors, their application is limited in the biological fields which greatly demand good

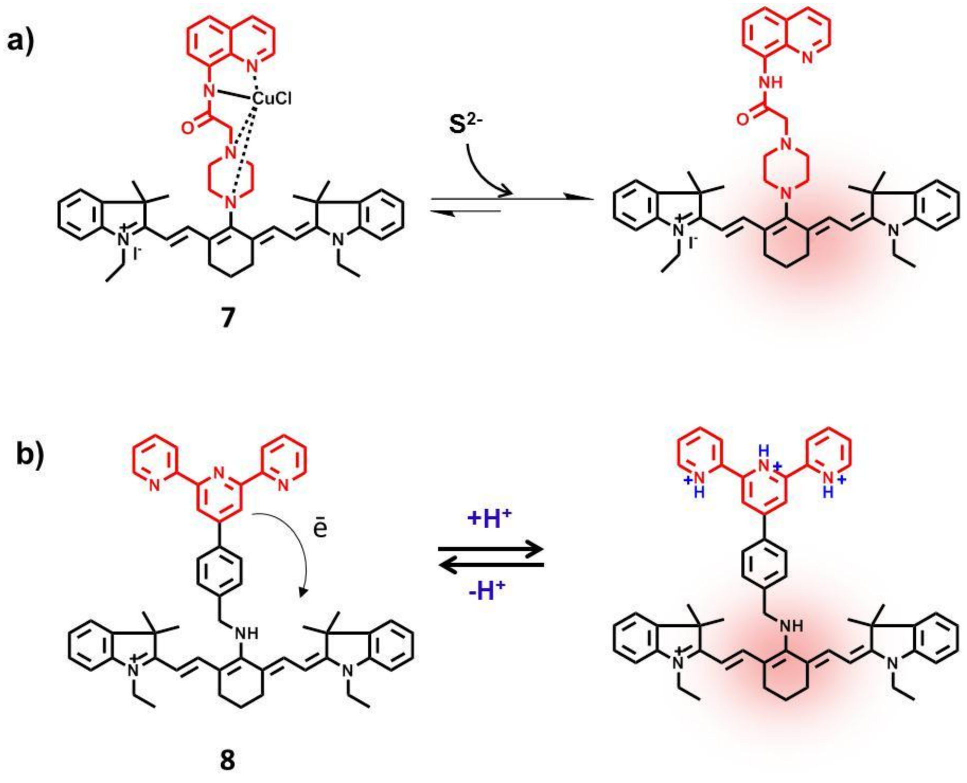

Figure 1.5. a) Sensing action of NIR fluorescent probe **7** for sulfide ion. b) Proposed mechanism of fluorescence response of **8** towards pH variations.

imaging potential by the working probe. However, fluorescent sensors with a turn-on response offer several advantages like excellent sensitivity, high signal to noise ratio, and good imaging capability. Therefore, the development of turn-on fluorescent probes flourished through various design strategies with different applications in a wide variety of disciplines.

Cao *et al.*, developed an NIR fluorescent probe (**7**) for the detection of sulfide anions (**Figure 1.5a**).[35] The probe being a Cu^{+2} complex, is initially non-fluorescent, which upon addition of sulfide anions, cause the decomplexation of Cu^{2+}

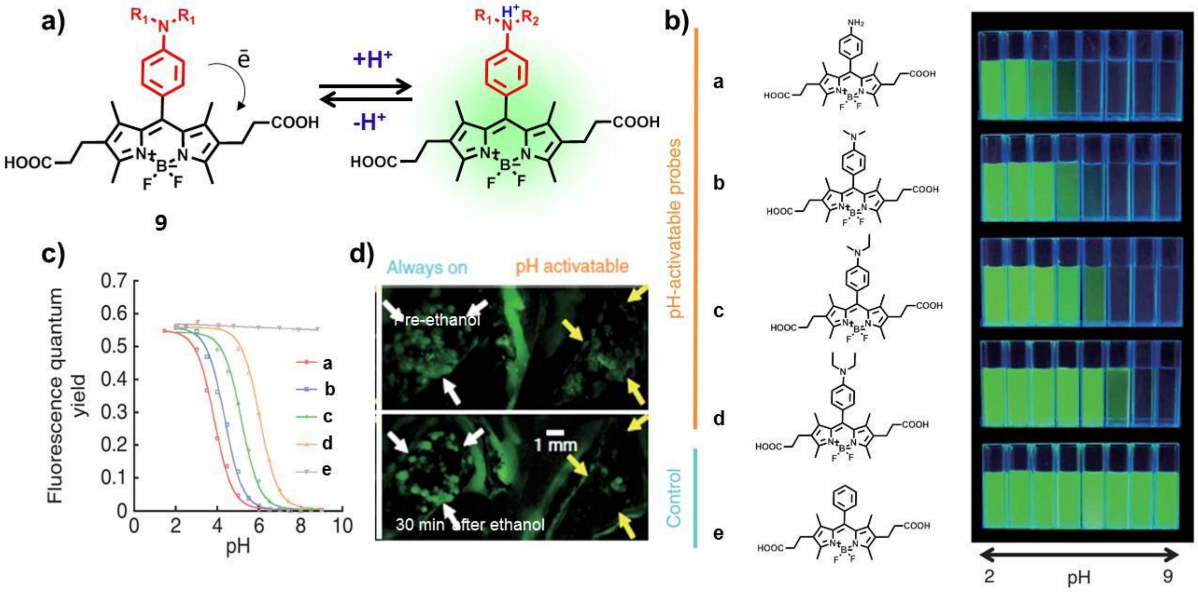

Figure 1.6. (a) Molecular structures of **9** in its deprotonated and protonated form. b) pH dependent emission profiles of **9a-d** with **9e** as a control always turn-on probe. c) pH-Dependent fluorescence intensity changes of pH responsive BODIPY dyes. d) Spectrally unmixed and composite fluorescence images of lungs of a mouse one day post intravenous injection with the always-on control probe (left, white arrows) and activatable ones (right, yellow arrows) before treatment (upper panel) or 30 min after dipping the lungs in 100% ethanol (lower panel).

with the simultaneous release of tricarbocyanine fluorophore, thereby providing a large enhancement in the NIR fluorescence. The probe was highly selective towards S^{2-} since it remained silent towards all other anions. Tang and coworkers developed a pH sensitive NIR fluorescent probe **8** by appending a proton sensitive terpyridine moiety to the tricarbocyanine core (**Figure 1.5b**). The probe responded to minor pH variations in the range 6.7 to 7.9 with a pKa of 7.1. The water soluble probe **8** was further explored for the real time monitoring of cellular pH in HL-7702 and HepG2

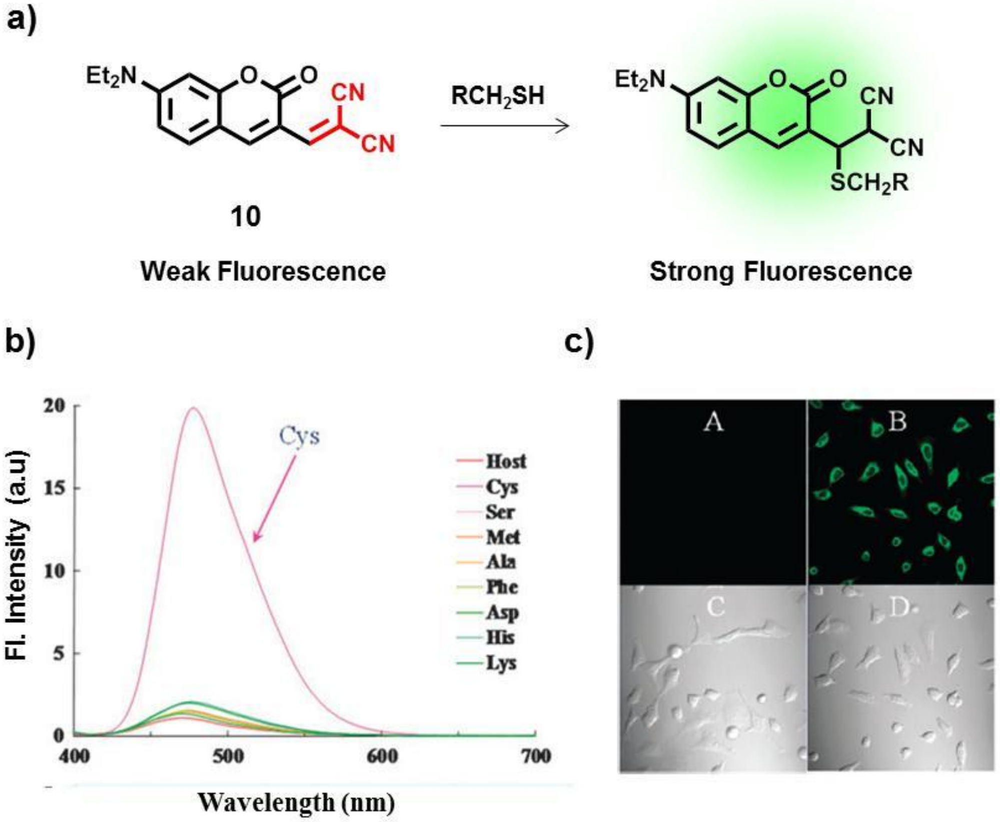

Figure 1.7. a) Molecular structures of **10** and its thiol conjugate. b) Fluorescence response of **10** (20 mM in 33% DMSO/HEPES buffer, pH 7.4) in presence of various amino acids. c) Fluorescence microscopic images of HeLa cells before (A) and after (B) treatment with **10** (10 μM) and their corresponding bright field images are represented by C and D respectively.

cells.[36] Later, Urano *et al.*, constructed a few pH activatable fluorescent probes for imaging acidic organelles in cancer cells (**Figure 1.6**). The molecules are initially non-fluorescent in the deprotonated form which becomes highly fluorescent upon protonation which occurs at the aniline nitrogen. Furthermore, the authors checked the clinical applicability of their probe for imaging endosomes in cancer cells by tagging it with cancer targeting monoclonal antibody, trastuzumab which causes its accumulation in the endosomal compartment with a light-up of the fluorescence signal.[37]

A study by Kim *et al.*, developed a Michael reaction based, coumarin-malononitrile derivative **10** for the selective detection of thiols (**Figure 1.7a**).[38] The coumarin group in the probe acts as the sensor moiety while the α, β-unsaturated malononitrile moiety served as the Michael acceptor, which is susceptible to attack by nucleophilic thiols. Addition of thiol to the double bond between the fluorophore and the malononitrile, caused an enhancement in the emission intensity at 475 nm. The probe displayed high selectivity towards biothiols (GSH, Cys, Hcy) when compared to other natural amino acids and was applied for investigating the cellular expression and detection of biothiols in HeLa cells (**Figure 1.7b**). Later, Han and colleagues have synthesized a NIR fluorescent probe (**11**) containing an organoselenium

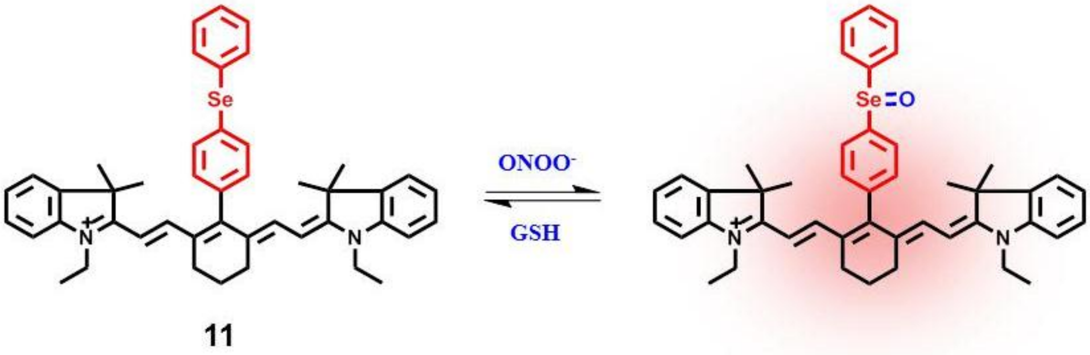

Figure 1.8. Sensing strategy of **11** towards peroxynitrite to afford its oxidized product.

functional group that responds to oxidation and reduction events under physiological conditions.[39] The probe consisted of a cyanine dye as the fluorophore and 4-(phenylselenyl)aniline, as the receptor unit for the redox reaction. The probe is non-fluorescent as a result of PET between the fluorophore and the receptor, but the addition of peroxynitrite (ONOO) causes the oxidation of Se which prevents the PET, causing the fluorescence emission to be “turned on” (**Figure 1.8**). On the other hand, this reaction can be reversed in presence of reducing agents like GSH, thereby allowing it to serve as an efficient sensor for monitoring redox processes.

1.3.2.3. Ratiometric Fluorescent Probes

Fluorescence measurements based on the detection of single emission signal (turn-on or turn-off) tend to be influenced by certain factors such as dye concentration, excitation intensity, probe environment etc. These problems can be addressed by means of a ratiometric approach, which allows the measurement of emission

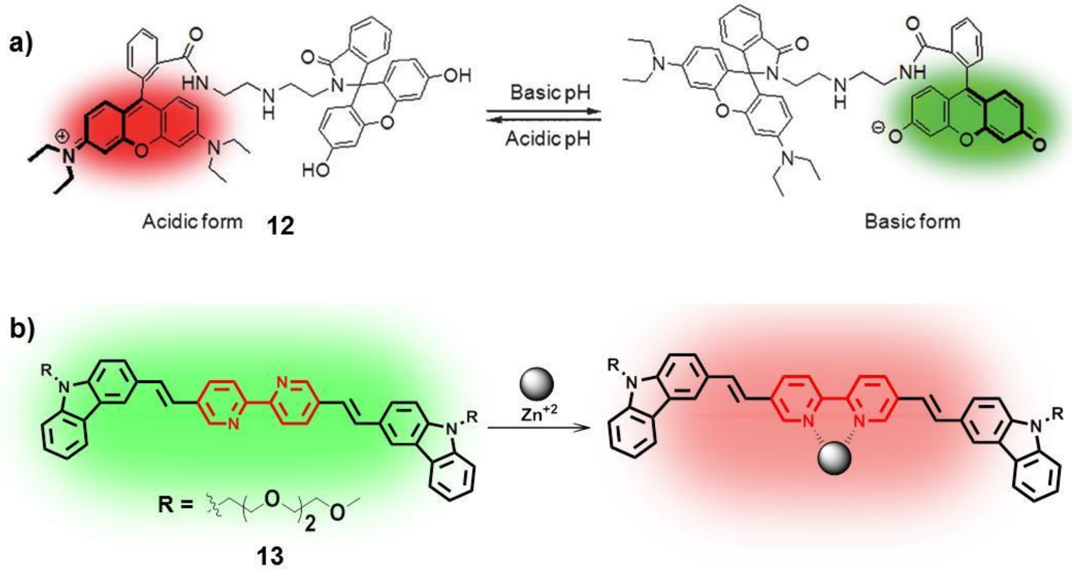

Figure 1.9. a) Mechanism of action of probe **12** towards changes in pH. b) Proposed mechanism for the two photon fluorescence changes of **13** upon addition of Zn^{+2}.

intensities at two wavelengths, such that the ratio of two peaks will be independent of the various environmental factors.[40] Moreover, ratiometric probes nullify the variations resulting from factors such as non-homogeneous distribution or uneven loading of fluorophores inside the cells. Different kinds of sensing mechanisms have been used for the construction of ratiometric fluorescent probes such as ICT, FRET, excimer/exciplex formation, chemodosimetry, PET etc.

A first example of a broad range pH sensor (**12**) constructed from a single molecular system was developed by Kim *et al.*, by combining two fluorophores having different pKa values (**Figure 1.9a**).[41] In this system, a fluorescein moiety that provides pH sensitivity under neutral to basic pH region is conjugated to a rhodamine dye that shows sensitivity in the acidic pH window. On increasing the pH from acidic to basic (3-10) regions, the probe **12** showed a ratiometric fluorescence response from red to green. This sharp ratiometric response over a wide pH window was utilized to visualize the various intracellular organelles with different pH values. Ajayaghosh and coworkers developed a donor-acceptor-donor (D-π-A-π-D) type ratiometric fluorescent probe (**13**) with a high two-photon absorption activity for the sensing of Zn^{2+} (**Figure 1.9b**).[42] Two photon excitation at 820 nm displayed a noticeable red shift in the emission maximum from 520 nm to 630 nm upon addition of Zn^{2+}. Authors also demonstrated the suitability of the probe in monitoring free zinc ions in live cells and tissues. Hamachi's group reported a FRET-based ratiometric probe for the detection of polyphosphate based on binding-induced modulation of FRET between coumarin and xanthene skeleton (**Figure 1.10a**). Upon binding with polyphosphates, the probe **14** underwent a decomplexation of Zn^{2+}, which displayed a clear dual-emission signal change at 454/525 nm, while no apparent change was observed with monophosphates and phosphodiester species as well as various other anions. The probe was also utilized for real-time fluorescence monitoring of enzyme reactions and ratiometric visualization of ATP in live cells.[43]

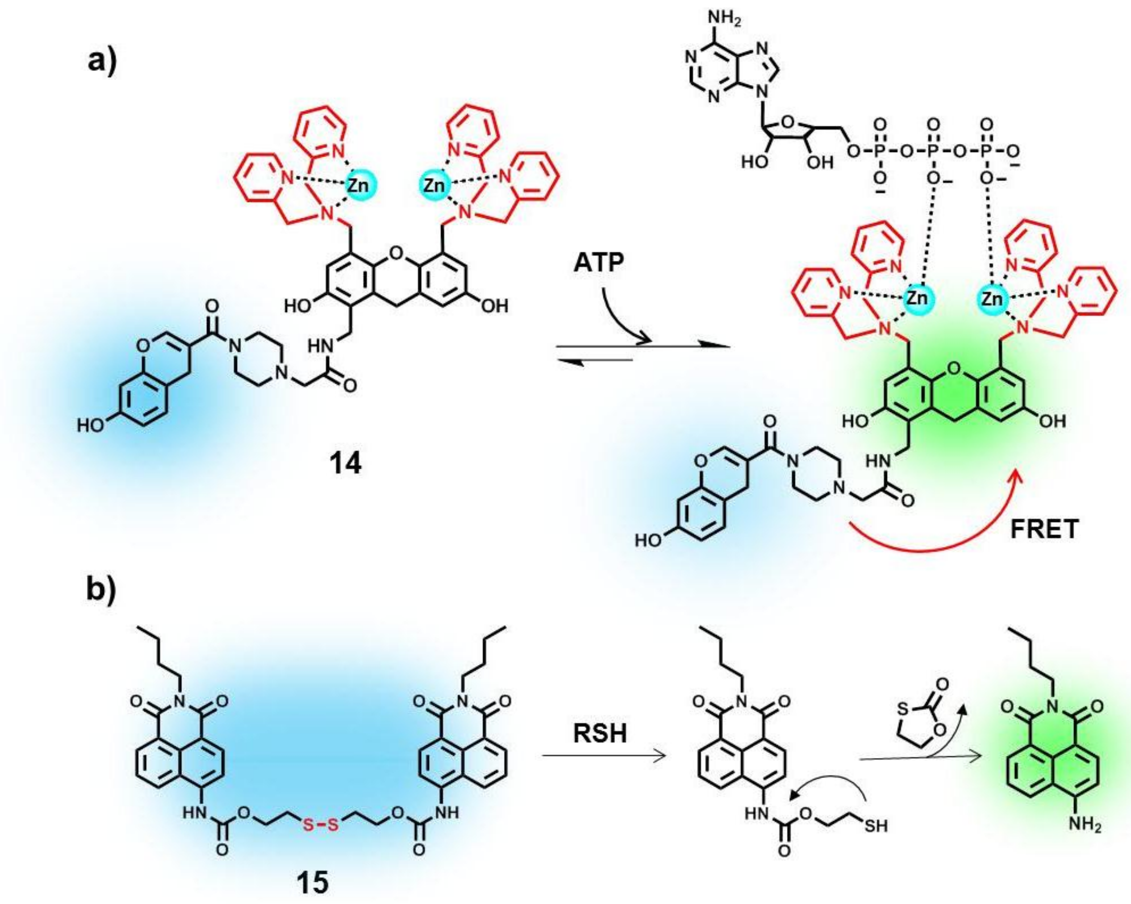

Figure 1.10. a) Scheme representing the dual-emission sensing of ATP based on a decomplexation mechanism. b) Reaction mechanism of the naphthalimide probe **15** for the sensing of thiols.

Zhu *et al.*, constructed a naphthalimide derivative **15** for the ratiometric detection of thiols under physiological conditions (**Figure 1.10b**).[44] The reaction of **15** with thiol, triggers the cleavage of the disulfide-based carbamate protecting group present in the probe, resulting in a red-shift of 48 nm due to significant changes in internal charge transfer. Moreover, the probe was successfully applied for the bioimaging of thiols in living HeLa cells. In another study, Cho and colleagues reported a two-photon fluorescent chemodosimeter, **16** for the ratiometric sensing of

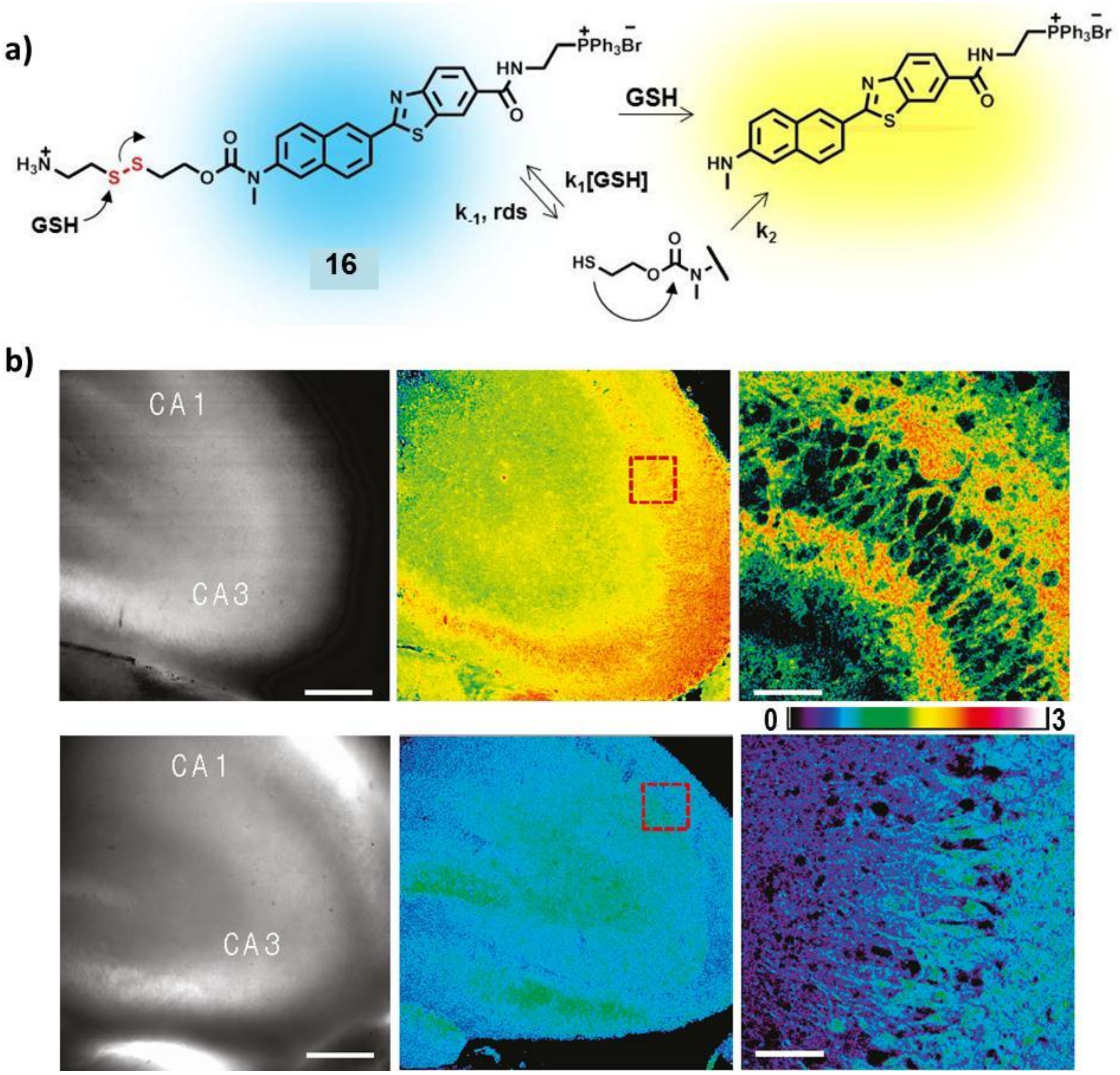

Figure 1.11. a) Detection strategy of probe **16** for the two photon fluorescence sensing of thiols. b) Ratiometric two photon microscopic images of rat hippocampal slices treated with **16** in the absence (top panel) and presence (bottom panel) of *N*-ethylmaleimide.

mitochondrial thiols (**Figure 1.11a**).[45] The probe comprised of 6-(benzo[d]thiazol-2-yl)-2-(*N*,*N*-dimethylamino)naphthalene as the two photon active fluorophore, a disulfide group as the thiol-cleavage site, and a triphenyl phosphonium salt as the mitochondrial targeting group. The reaction of **16** with thiols caused the cleavage of the disulphide bond, resulting in a ratiometric fluorescence response from blue to yellow emission, which can be attributed to the pronounced ICT effect. Considering the large two photon cross sectional area, the authors employed **16** for the successful visualization of mitochondrial thiol levels in live cells as well as in living tissues at depths of 90−190 μm (**Figure 1.11b**).

1.3.3. SERS Imaging

Surface enhanced Raman scattering, a promising spectroscopic technique has emerged as a complementary tool to fluorescence modality in bioimaging and therapeutics. This technique based on Raman effect accounts for the inelastic scattering of photons by the sample under excitation. The probability of such scattering is nearly 14 orders weaker than that of fluorescence, which limits its applications in the field of biology and medicine. However, when the molecules are in close proximity with nanoroughened metal surfaces, the Raman vibrational modes could be amplified by several orders of magnitude which forms the basis of SERS. The enhancement of Raman signals occurs primarily from the enhanced electric fields produced by the conducting electrons present on the metal surface which gives rise to collective oscillations referred to as surface plasmons. Besides this, signal enhancement also results from chemical means which involve charge transfer interactions between the metal and the reporter molecule. Because of the huge enhancements (10^6-10^{10}) offered by both these mechanisms, SERS allows detection of biomolecules down to single molecule level with high specificity and low background noise.

SERS measurements can be performed either by directly acquiring the signals characteristic of the analyte under examination (label free detection) or through indirect method (label based detection) which uses spectral fingerprints of a reporter molecule for analysis.[46] Label free SERS employs metallic nanoparticles of different shapes and sizes which will provide maximum enhancements so as to afford a highly sensitive detection. This technique is of importance in the identification of analytes with molecular structures rich in heteroatoms, conjugated double bonds, aromatic rings and other functionalities. However, the complex biochemical environment of the target analytes poses great difficulty in the interpretation of SERS spectra which makes the direct detection of a particular biomarker of interest, a challenging task.

On the other hand, label based detection using SERS nanotags offers sensitive detection even in complex chemical and biological environments. The SERS tags comprises of a) metal nanoparticle as the Raman substrate, b) a reporter molecule as the SERS label, c) a stabilizing material as the biocompatible surface coating and d) a targeting unit for target specific binding. Nanoparticles (NPs) of gold and silver are regarded as the classic SERS substrates owing to their inert nature, low toxicity, strong plasmonic absorption, ease in surface modification etc. Nowadays, a wide variety of metal substrates are being used for obtaining maximum enhancement efficiency which includes gold and silver spherical NPs, nanostars, nanoshells, hybrid NPs, nanorods, nanopyramids, nanoflowers, nanocubes, nanocages, nanorings and so on (**Figure 1.12**).[47] Another key component required in the construction of SERS tags constitutes the Raman reporter which are mainly molecules containing nitrogen or sulphur functionalities that facilitates strong binding with the metal substrate. When the excitation wavelength matches with the optical absorption of the reporter molecule, additional enhancements occur by a phenomenon known as surface enhanced resonance Raman scattering which amplifies the signal by another 10^2 to 10^3 folds. In order to provide strong adherence of Raman label to metal nanoparticles and to prevent leakage of the molecules, they will be subjected to surface coating with some polymeric agents such as bovine serum albumin (BSA), polyethylene glycol (PEG), silica etc. The final step involved in the construction of SERS tags involves

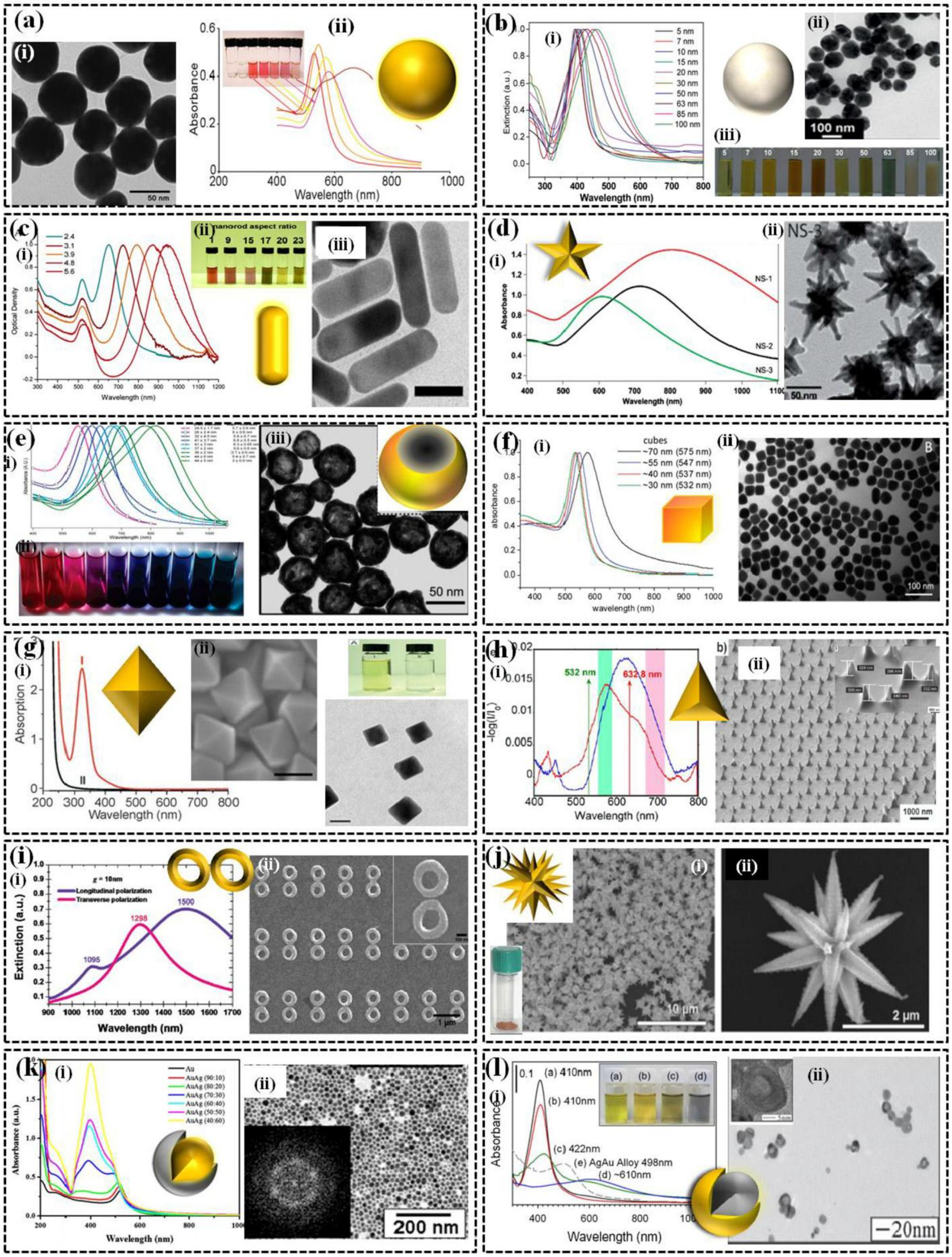

Figure 1.12. Representative images of various nanostructures used for SERS analysis.

attachment with a targeting ligand such as peptides, small molecule ligands, aptamers or antibodies which provide specific recognition of the desired target. The as-developed SERS tags offer broad avenues for analyzing biomolecules, proteins, viruses, bacteria, toxins, disease biomarkers, cells and many more. SERS based nanoplatforms are being increasingly employed in cell studies as they meet the desirable requirements of live cell imaging namely the use of low power lasers and high penetration capabilities which facilitates real time probing of biological events with high spatio-temporal resolution.[47]

1.3.4. SERS Probes for Sensing and Imaging

SERS has been utilized as a promising tool for the sensing of various biomolecules such as DNA, proteins and other small molecules which allow an in-depth understanding of various processes and its abnormalities occurring in a living organism. Moreover, the high specificity and sensitivity associated with this technique offers specific recognition of target cells, multiplexed detection of disease biomarkers and real time monitoring of therapeutic responses which strengthens its applicability in both clinical and translational research.

In 2012, Robson and colleagues formulated an SERS based assay platform for the detection of mouse double minute (MDM2) protein, which has been found to play a major role in many cancers. In this study, authors used a peptide mimic of the tumor suppressing protein p53 which has been conjugated chemically on to the surface of silver nanoparticles. In the presence of MDM2 protein, the p53 conjugated nanoparticles formed an assembly which caused an enhancement in the SERS intensity of the Raman reporter present on the nanoparticle surface.[48] In another report by Wang *et al.*, a SERS based immunoassay was developed for the detection of mucin protein, MUC4 in cancer patients.[49] The results revealed a higher SERS signal response from the sera of pancreatic cancer patients compared to that collected from healthy donors and those from patients with benign tumors. This assay has been proved to be successful in the identification of other cancer biomarkers as well.

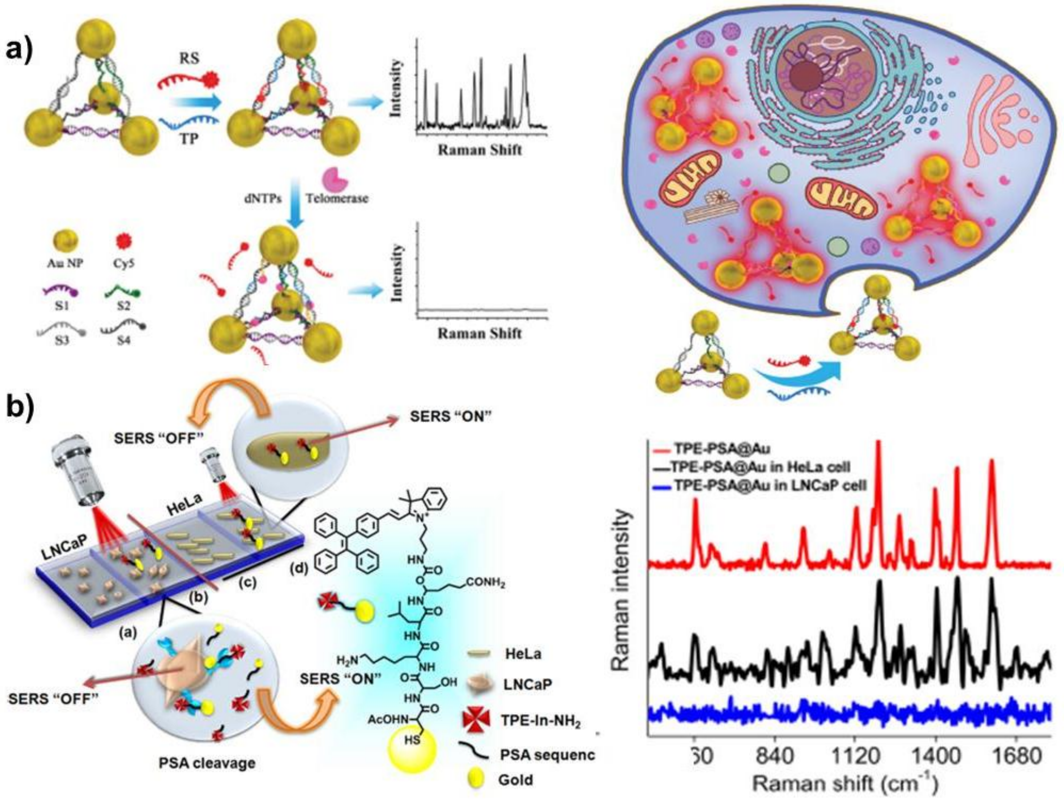

Figure 1.13. a) Scheme representing the design of gold nanopyramid based SERS probe for the monitoring of intracellular telomerase activity. b) Schematic illustration of tetraphenylethylene reporter labeled SERS tag for the detection of PSA *in vitro*.

More recently, Xu *et al.*, fabricated an SERS probe built on gold nanoparticles (AuNPs) that undergoes a DNA driven self-assembly to form Au nanopyramid, which has been utilized for the detection of intracellular telomerase activity.[50] In the presence of the DNA and telomerase, the telomerase primer tethered with a Raman reporter gets extended, with the subsequent replacement of the inner DNA chain, thereby resulting in a decline in the SERS signal intensity (**Figure**

1.13a). The sensor showed a linear response in the concentration range of 1×10^{-14} to 5×10^{-11} IU with a detection limit down to 6.2×10^{-15} IU. Maiti and co-workers have developed a SERS nanoconstruct built on tetraphenylethylene based Raman label for the specific detection of prostate cancer.[51] In the presence of PSA enzyme, the SERS tag equipped with a target specific PSA peptide sequence underwent a cleavage which was indicated by a turn-off Raman signal. Authors also demonstrated the specificity of their probe towards PSA in LNCaP cells against HeLa cells which showed relatively low expression of the enzyme (**Figure 1.13b**).

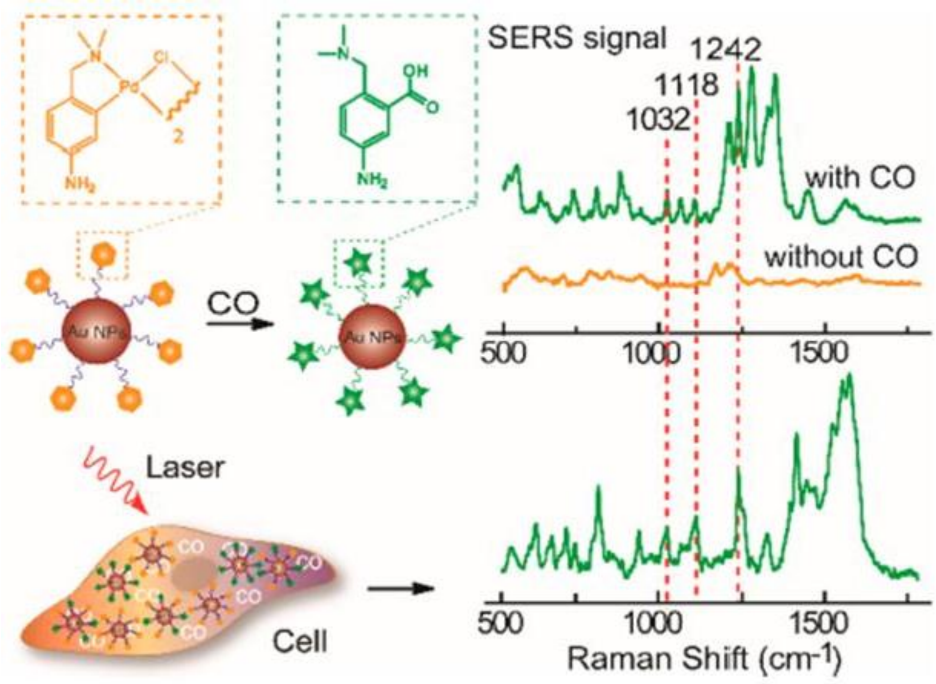

Figure 1.14. SERS based sensing mechanism of palladacycle carbonylation for CO detection *in vitro*.

Cao *et al.*, reported a palladacycle based SERS probe for the intracellular monitoring of carbon monoxide.[52] The sensing mechanism relies on the carbonylation of AuNP bound palladacycle reporters which results in the depalladation of the molecule thereby producing a carboxylic acid group with distinct

SERS peaks. This approach has been successfully tested for the detection of carbon monoxide releasing molecules *in vitro* (**Figure 1.14**).

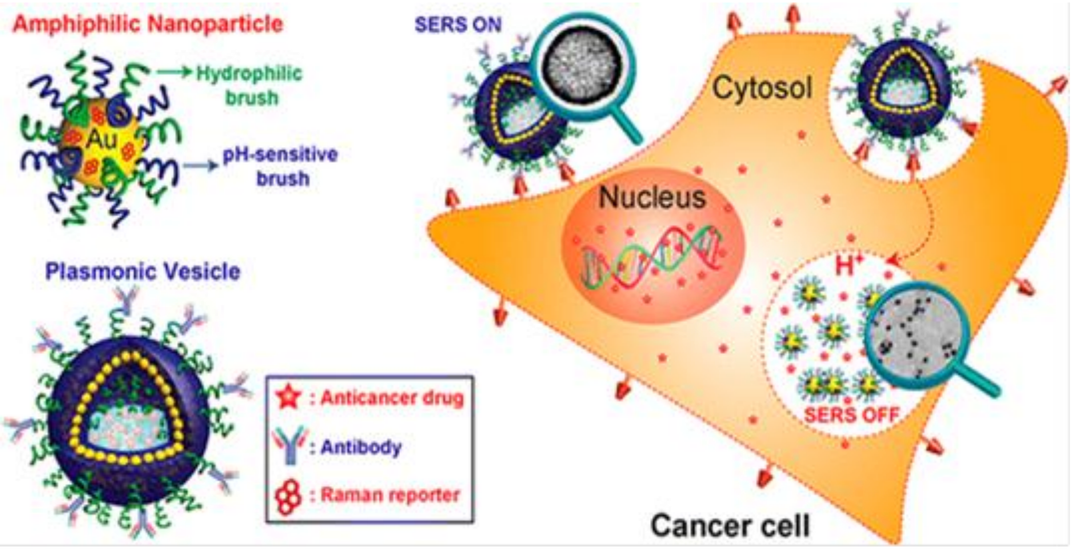

Figure 1.15. Schematic illustration of bioconjugated plasmonic vesicles for SERS guided intracellular drug delivery.

The unique advantages of SERS has also been utilized in the understanding of molecular level and cellular level changes occuring as a result of cell death phenomena in response to various therapeutic approaches. Song and co-workers demonstrated the design and construction of bioconjugated plasmonic vesicles assembled from SERS-labeled amphiphilic AuNPs for drug delivery applications.[53] The plasmonic vesicles in-built with a hollow cavity facilitated efficient loading and release of anticancer drugs along with the SERS guided "ON/OFF" sensing to monitor the drug delivery event (**Figure 1.15**). The as-developed SERS guided plasmonic nanoprobe stood as a potential platform for targeted therapy by combining the synergy of chemotherapy with PTT. In another report, Seo and co-workers fabricated a silica coated gold nanorod for single laser triggered PTT and PDT. The methylene blue molecules loaded in the nanoprobe served the role of a photosensitizer while the nanorod was used for photothermal heating.[54] An SERS assisted multifunctional theranostic platform was developed by Maiti *et al.*, for synergistic photothermal chemotherapeutic action on matrix metalloproteinase (MMP) expressing cancer cells.[55] Moreover, the probe afforded accurate monitoring of various biochemical and molecular level changes during different stages of therapy which highlighted the potential of SERS in the effective management of diseases (**Figure 1.16**).

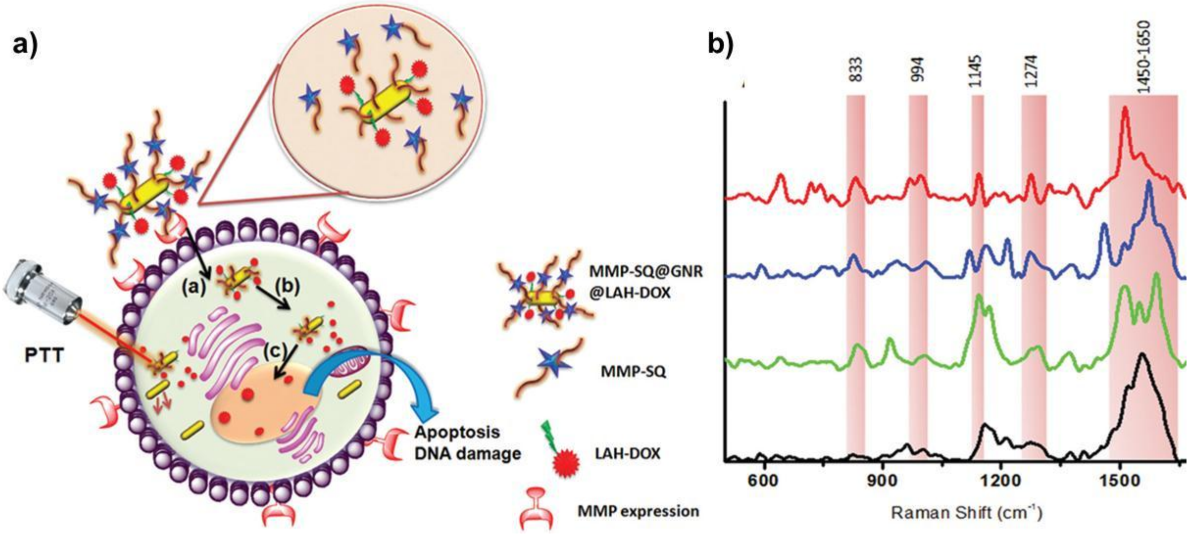

Figure 1.16. a) Schematic representation of the theranostic nanoprobe for SERS assisted photothermal chemotherapy and b) SERS spectral evaluation of cellular changes occurring during the course of treatment induced by the nanoconstruct.

1.4. Therapeutic Approaches in Biomedicine

Accurate diagnosis of a disease condition followed by a precise and effective therapeutic procedure is highly demanded for the proper management of diseases. There exists an assortment of different therapeutic strategies that have emerged to meet the increasing needs in the medical field to improve the quality of life of patients suffering from serious diseases such as cancer. Among the various therapeutic modalities, PDT deserves special attention as it has become a good alternative to the conventional cancer treatment options due to its high specificity in imparting toxicity to the tumor cells against the normal healthy ones. In this section, various aspects of PDT and its importance in biomedical applications has been discussed.

1.4.1. Photodynamic Therapy

A therapeutic procedure which involves the generation of highly cytotoxic reactive oxygen species (ROS) upon light induced excitation of a photosensitizing agent is known as photodynamic therapy. PDT mainly comprises of four stages: the first stage involves the administration of photosensitizer (PS) into the body. In the second stage, the PS gets distributed in different sites which gets finally accumulated around the target tissues when allowed for a suitable period of incubation. The third stage involves the irradiation of PS at the target site using a light source which causes the generation of ROS. The as-formed reactive species react with various bio-analytes such as amino acids, proteins, lipids, nucleic acids etc. which in turn disrupts the normal cell functioning and induces cell death in stage 4 (**Figure 1.17**). PDT

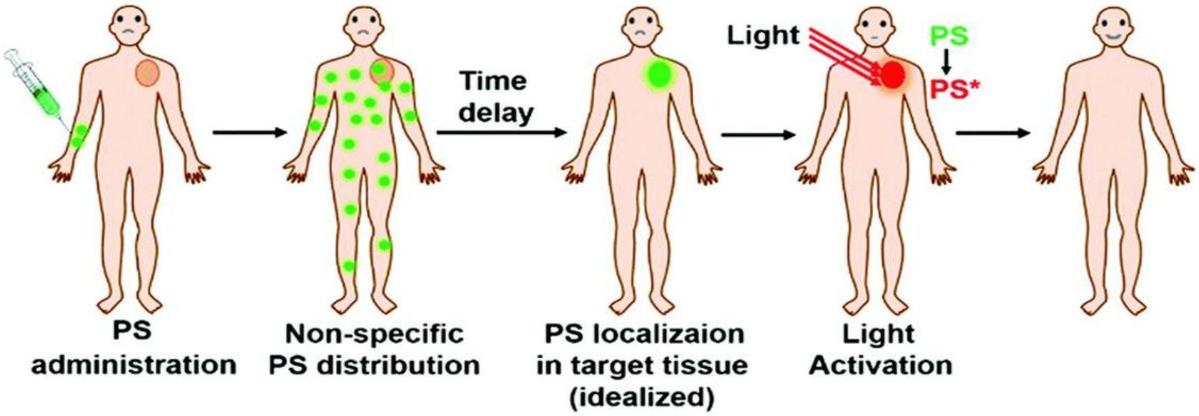

Figure 1.17. Schematic illustration of the PDT process involving the administration, distribution, localization and light activation of PS for relieving tumor.

possesses several advantages over traditional cancer therapies in terms of its minimally invasive nature, high target specificity, ability to cure patients with repeated dosages without imparting any resistance, fast healing properties, minimal side effects etc. Based on the type of photochemical reaction occurring during the therapeutic process, PDT can be classified into two types: Type I and Type II PDT. In the first pathway, called the type I mechanism, radical species are generated through either hydrogen abstraction or redox processes that occurs between a sensitizer in the excited state and the biomolecule. On the other hand, the type II mechanism involves the generation of singlet oxygen ($^1O_2$) via an energy transfer process from the sensitizer in the triplet excited state to oxygen molecule in the ground electronic state (**Figure 1.18**).[56,57]

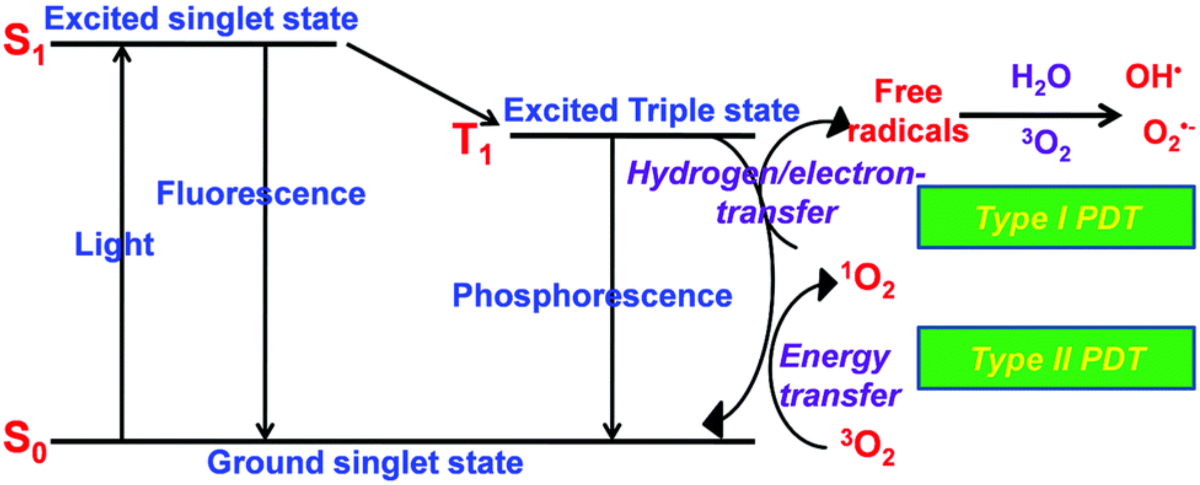

Figure 1.18. Schematic representation of the photochemical reaction pathways for type I and type II photodynamic therapy.

1.4.1.1. Photosensitizers Used in Photodynamic Therapy

By definition, photosensitizers are compounds that are capable of absorbing light of suitable wavelength and converting it into cytotoxic reactive species such as singlet oxygen ($^1O_2$), hydroxyl radicals ($OH^{\cdot}$), superoxide anion radical ($O_2^{\cdot-}$), hydrogen peroxide (H_2O_2) etc. For a PS to be used in biological treatment applications, it should possess good photochemical reactivity, strong optical absorption, minimal dark toxicity, superior light toxicity, excellent cell permeability etc. The commonly used molecular PSs include organic dyes, porphyrins, phthalocyanines and transition metal

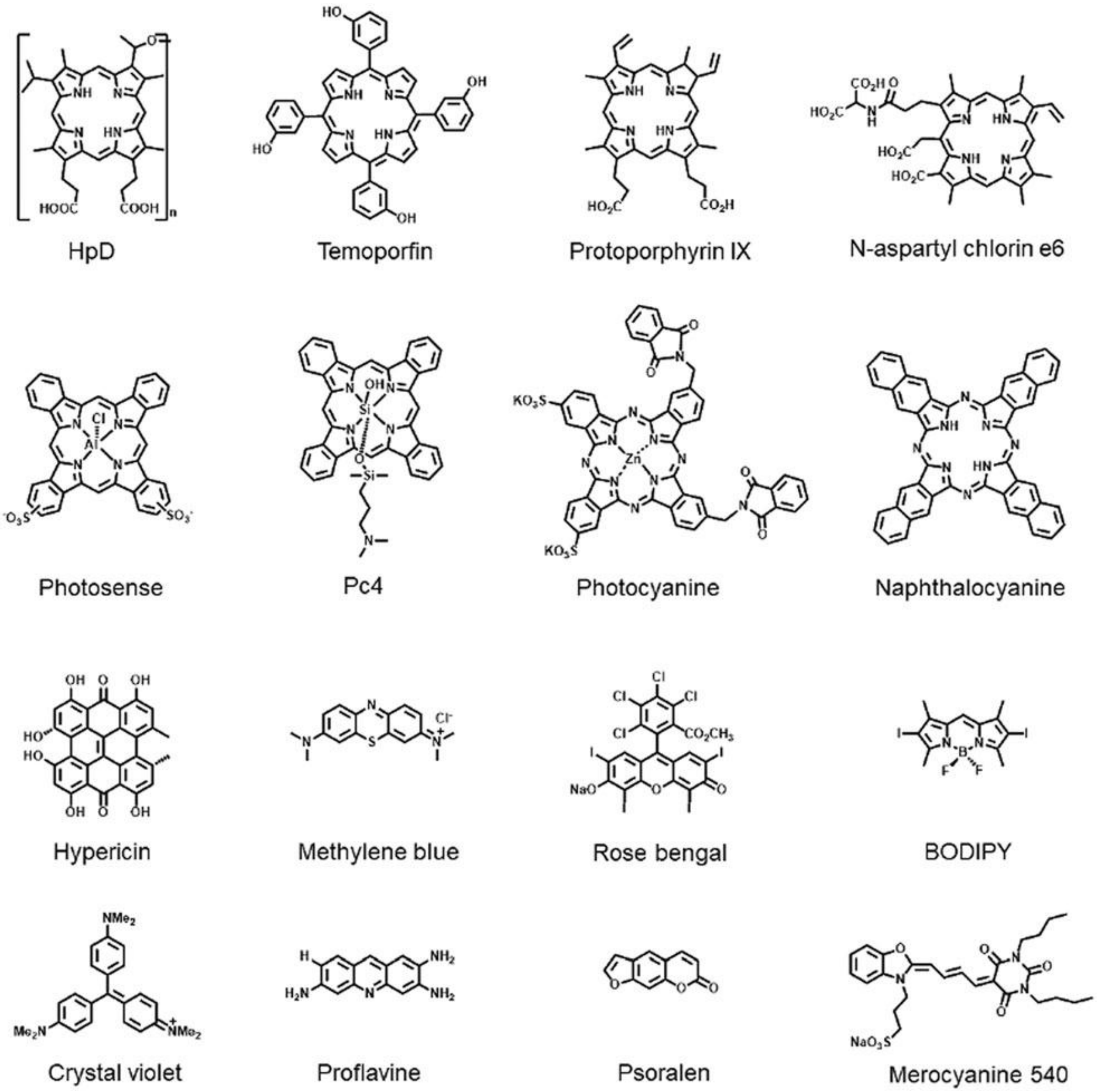

Figure 1.19. Structures of some common photosensitizers.

complexes. Porphyrins represent an active member of photosensitizers since they satisfy most of the criteria required for an ideal PS. Hematoporphyrin (Hp)[58] was the first porphyrin compound to be used as a PDT agent. Indeed, the chemical functionalization of Hp led to the discovery of a more potent PS which is being currently marketed as a PDT drug under the trade name Photofrin II® for the treatment of oesophageal cancer, cervical dysplasia, lung cancer and bladder cancer. Following the chemical modification on these first generation PSs, the biomedical field witnessed the development of a series of new porphyrinoid and non-porphyrinoid PSs including protoporphyrins, metalloporphyrins, purpurins, porphycenes, hypericin, phthalocyanines, cyanines, phenothiazines, dipyromethenes, xanthenes and lot more (**Figure 1.19**).[59-61]

Most of the research in PDT used organic molecules as photosensitizers but there are also few inorganic metal complexes that have shown great promise in efficient ROS generation. Atoms with higher atomic mass can facilitate intersystem crossing (ISC), which in turn enhance the photosensitizing efficiency. Therefore design of PSs with heavy atom substitution can give rise to efficient PDT agents. Due to the heavy atom effect of transition metals such as Ir, Ru, Pt etc., the complexes formed by these metals act as good PSs. Among these, Ir (III) complexes offer several

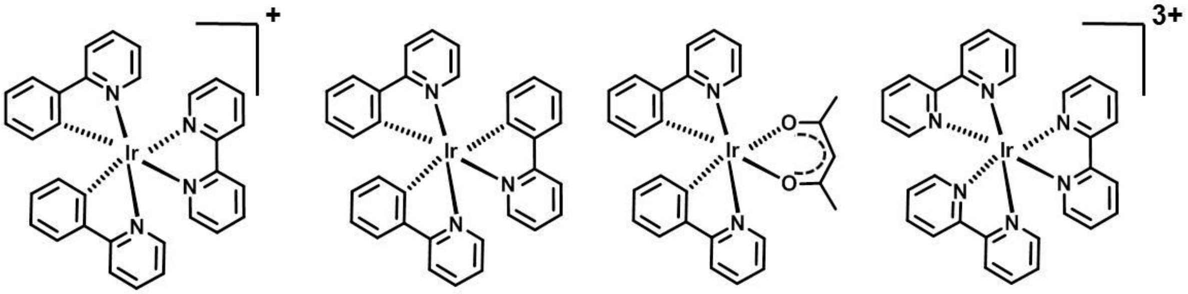

Figure 1.20. Representative examples of some common classes of Ir (III) metal complexes used for PDT and imaging applications.

benefits when compared against the poor membrane permeability of Ru complexes and labile nature of Pt complexes. Moreover, the favourable features of high ROS generation efficacy, long lifetime, good photostability, high phosphorescence quantum yield, easy color tunability and large Stokes shift enable them as potential candidates in cancer diagnosis and therapy.[62] Some of the common classes of Ir (III) complexes tested for imaging and PDT applications are given in **Figure 1.20**.

1.4.2. Luminescent Photosensitizers for Imaging and Therapy

In recent years, PDT assisted cancer treatment has gained significant attention owing to its improved therapeutic outcome with minimal side effects. Most of the PSs tend to be emissive which owes them with the additional advantage of luminescent imaging along with targeted therapy.[63,64] Theranostics refers to an attractive combination of clubbing diagnosis and therapy into a single platform thereby realising maximum treatment cure with accurate diagnostic guidance. The optical signals from the PS molecule can be used as optical biopsy, which can discriminate tumor cells from normal ones, thereby avoiding sophisticated histological examination. Furthermore, the probe also enables the evaluation of treatment responses and also the fate of therapy, which may serve as useful dosimetric guide for real-time modification during therapy.[64]

Yang *et al.,* demonstrated the design and synthesis of a phosphorescent PS built on an Ir (III) metal complex (**17**) consisting of bipyridine and 2-phenylpyridine as the ligands. The complex **17** exhibited a strong absorption band around 450 nm with a high molar absorption coefficient of the order of 2.4 x 10^4 $M^{-1}cm^{-1}$. The molecule also showed an orange-red phosphorescence at 620 nm with a quantum yield of ~3% in phosphate buffer. The singlet oxygen generation capability of **17** was evaluated through 1,3-diphenylisobenzofuran (DPBF) scavenging assay and electron spin resonance (ESR) spectroscopy. Further, the photodynamic therapeutic effect of the complex was demonstrated *in vivo* using a 730 nm continuous wave laser (**Figure 1.21**).[65] Draper and co-workers developed a Bodipy linked binuclear Ir (III) complex that exhibited high photosensitizing efficacy due to the presence of two metal centers.[66] The singlet oxygen quantum yield of the molecule turned out to be 74.9% with a high upconversion quantum efficiency of 25.5%. The PDT activity of the complex was investigated in HeLa cells that showed superior light toxicity and minimal dark toxicity. The cytotoxicity exerted by the complex caused the localized production of ROS which executed cell death in the apoptotic pathway. In a similar

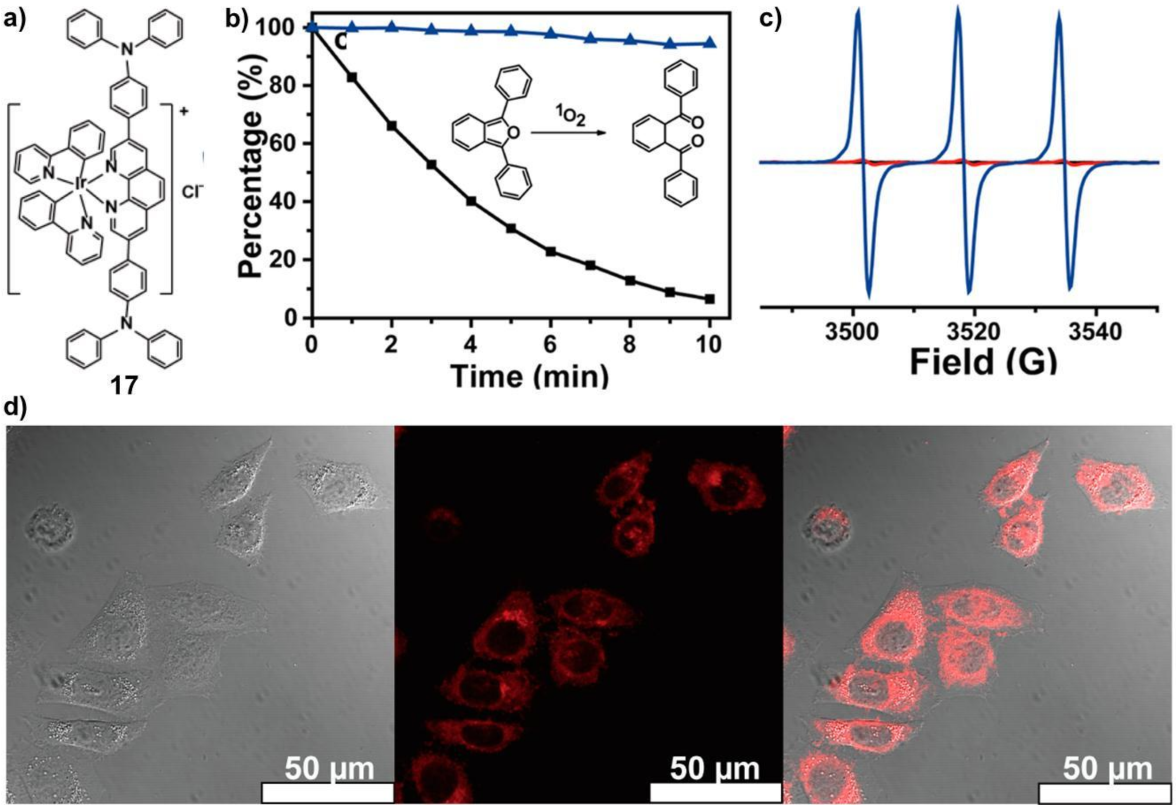

Figure 1.21. a) Molecular structure of compound **17**. b) and c) represent the evaluation of singlet oxygen generation ability of **17** through DPBF scavenging assay and ESR spectroscopy respectively. d) Confocal luminescence images of HeLa cells treated with **17** for 2 h.

report, Palao *et al.*, demonstrated biscyclometalated Ir (III) complexes with Bodipy as the ancillary ligand that have been linked to the metal complexes via its meso position. The molecules exhibited higher molar absorptivity with a moderate emission in the visible region. The molecules also served as effective photosensitizers upon irradiation using a visible light source. The *in vitro* therapeutic potential of the complexes investigated in HeLa cells highlighted their superior photo-toxicity along with poor dark toxicity, thereby enabling them as promising therapeutic candidates for cancer treatment applications.[67]

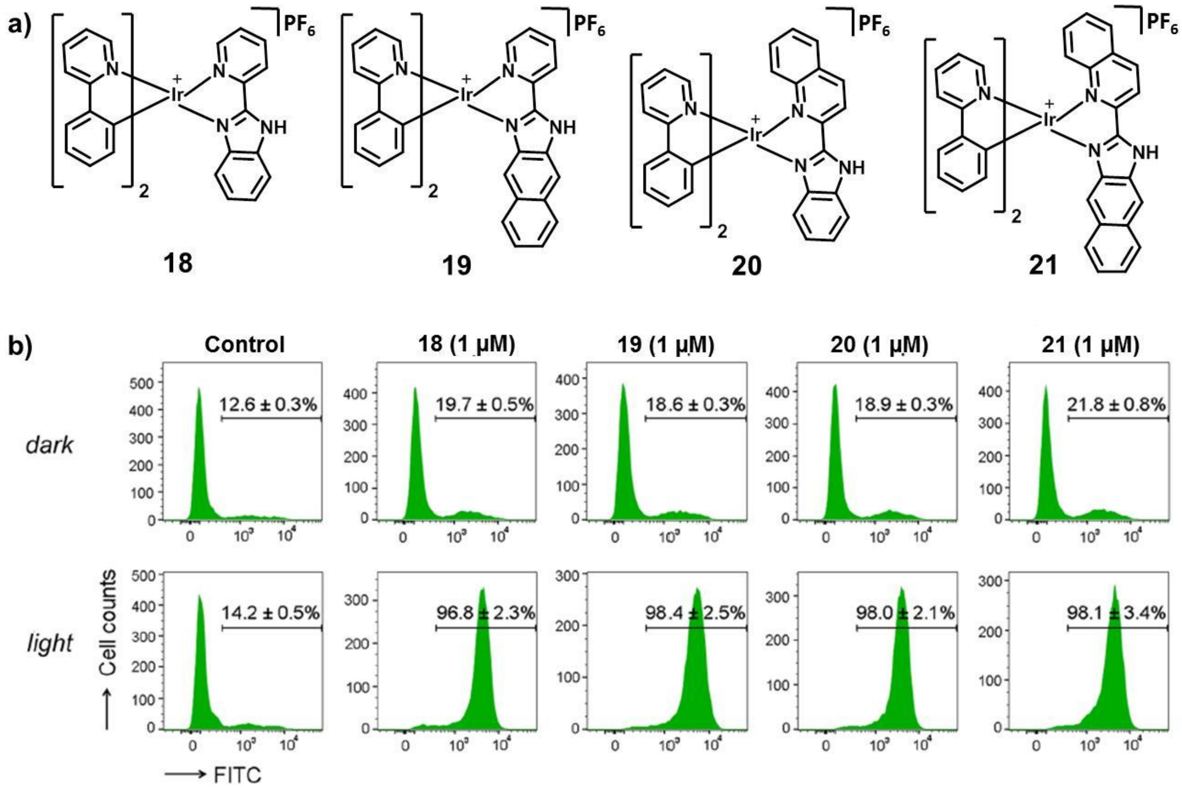

Figure 1.22. a) Molecular structures of compounds **18-21**. b) *In vitro* evaluation of therapeutic efficiency of complexes **18-21** (1 µM) through Annexin V-FITC flow cytometric analysis.

Mao *et al.*, reported the design and synthesis of four cyclometalated phosphorescent iridium (III) metal complexes (**18-21**) appended with benzimidazole unit for lysosome targeted photodynamic therapy (**Figure 1.22**).[68] The complexes displayed pH dependent phosphorescence emission with significant localization in the lysosomal compartments of the cells. Among the four complexes, **21** showed maximum therapeutic efficacy which induced apoptosis through ROS generation, lysosomal damage and caspase activation.

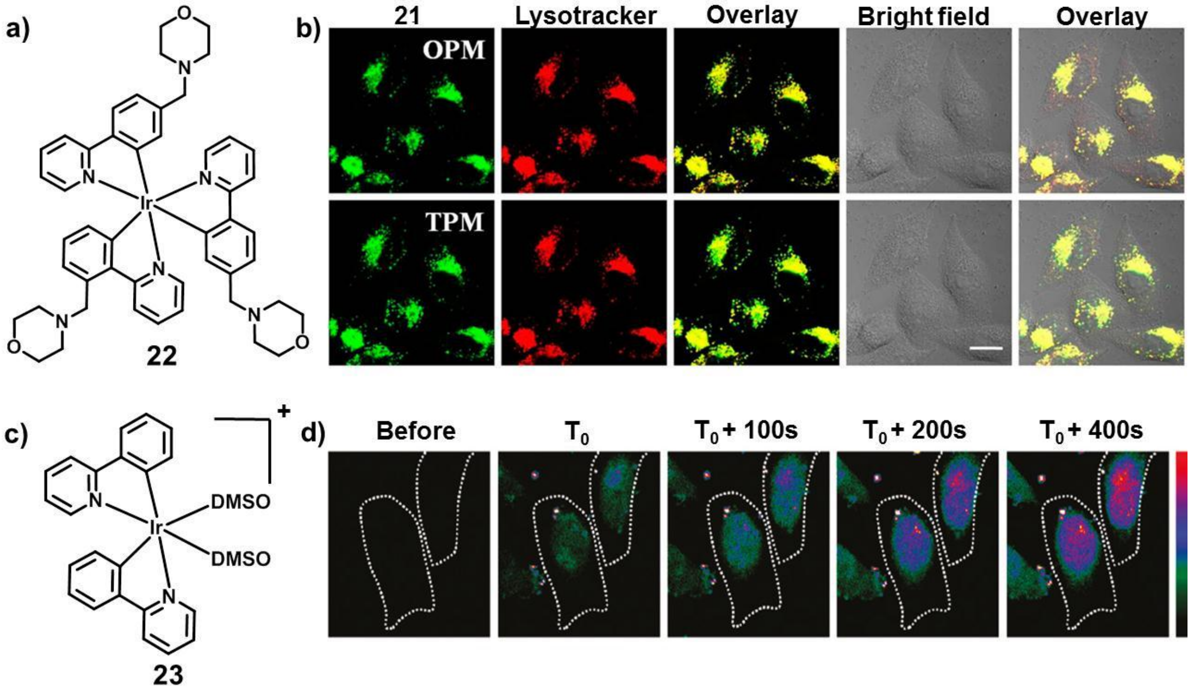

Figure 1.23. a) Molecular structure of compound **22**. b) One photon and two photon microscopic imaging of HeLa cells administered with **22** and co-stained with lysotracker red. c) Represents the molecular structure of nucleus targeting probe **23** and d) real time visualization of nuclear staining ability of **23** upon administration with HeLa cells. T_0 represents a short time interval (<30s) for the cells to enter the focal plane soon after the addition of **23**.

A water soluble two photon luminescent Ir (III) complex (**22**) was reported by Chao *et al.*, for phosphorescence imaging assisted PDT. The probe showed excellent localization in the lysosomes due to the presence of morpholine moieties present in the bipyridine ligands. The favourable attributes of large Stokes shift, excellent two-photon activities and high photostability allowed **22** to track lysosomes during the apoptotic process (**Figure 1.23a** and **1.23b**).[69] Li and colleagues developed a cyclometalated Ir (III) metal complex (**23**) that showed a turn-on phosphorescence response for imaging nucleus of live cells (**Figure 1.23c** and **1.23d**).[70] The complex upon internalization into the cell, gets specifically localized in the nuclear regions and then reacts with histidine/histidine containing proteins to produce a green emission. Moreover, the very low dark toxicity and rapid internalization kinetics promise the practical utility of **23** in biomedical applications.

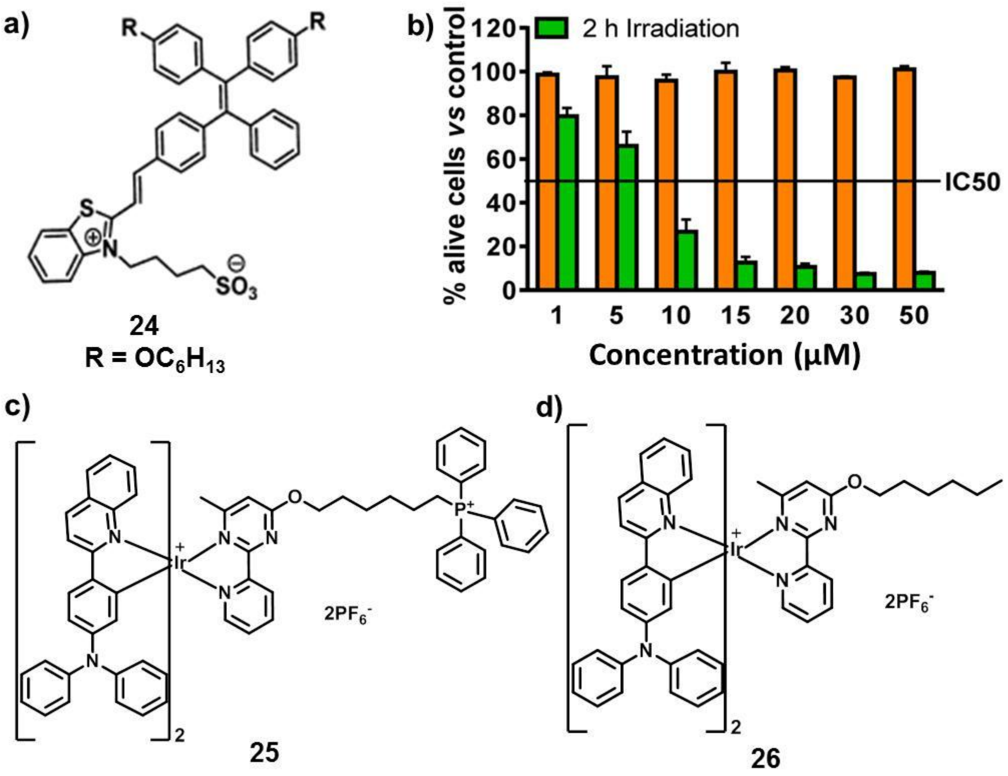

Figure 1.24. a) Molecular structure of compound **24** and b) dose dependent cytotoxicity evaluation of **24** in PC3 cells under dark and light conditions. c) and d) Molecular structures of mitochondria targeting probe, **25** and lysosome targeting probe, **26** respectively.

Ramaiah and co-workers synthesized a novel donor-acceptor type tetraphenylethylene dye, **24** for fluorescence imaging guided PDT applications (**Figure 1.24a** and **1.24b**). The aggregation induced emission property of **24** allowed to probe the intracellular distribution of the molecule which was mainly confined in the cytoplasmic regions of the cell. Moreover, the singlet oxygen generation capability of **24** was utilized to kill the cancer cells specifically by shining laser at the target site. The therapeutic efficacy of the molecule was further evaluated *in vivo* which demonstrated the potential of **24** in cancer theranostic applications.[71] Huang *et al.,* demonstrated the design of two iridium (III) complexes, **25** and **26** for mitochondria and lysosome targeted PDT (**Figure 1.24c** and **1.24d**). Both the complexes displayed good phosphorescence quantum yield together with moderate singlet oxygen generation efficiency. The photocytotoxicity experiments carried out on HeLa cells showed that the mitochondria targeting complex, **25** exhibited a slower respiration rate, resulting in a higher ROS generation under hypoxia. This study

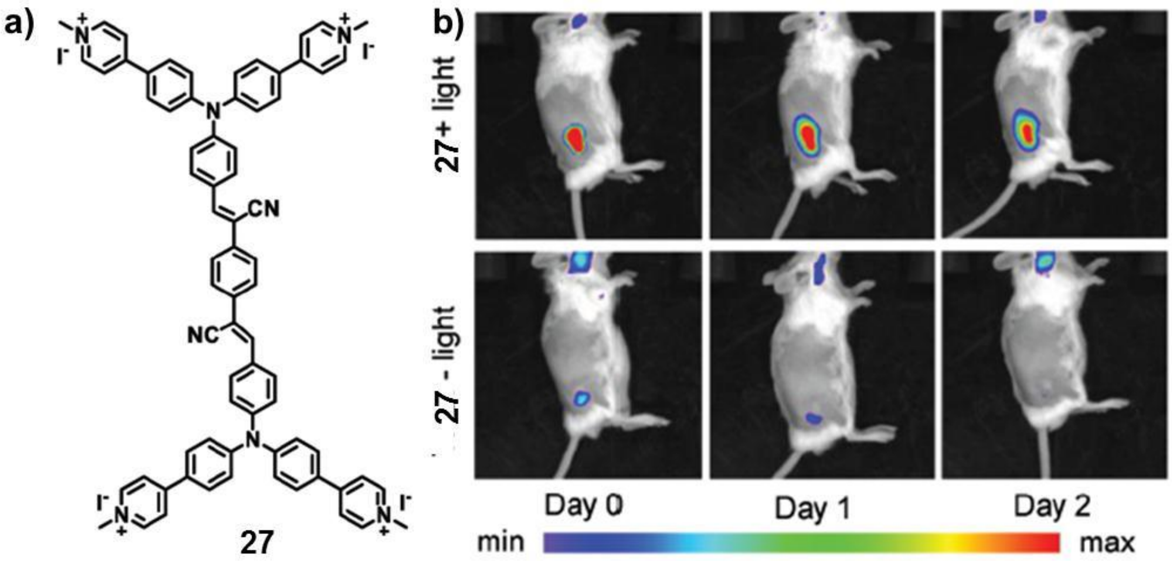

Figure 1.25. a) Chemical structure of photosensitizer molecule, **27**. b) *In vivo* fluorescence imaging of tumor bearing mice by **27** before and after light irradiation during the first three days after PDT.

revealed the potential of mitochondria targeting photosensitizers for hypoxic cancer treatments.[72]

Recently, Tang *et al.*, reported the design and development of a dual functional PS (**27**) that can act as a PDT agent as well as a self-reporter for tracking the therapeutic events in real time (**Figure 1.25**).[73] The molecule exhibited an exceptionally high singlet oxygen quantum yield of 98.6% in water which was equally reflected in the *in vitro* and *in vivo* conditions as well. Moreover, the molecule enabled the real time visualization of the treatment responses via the activation of its fluorescence signals upon binding with chromatin due to its strong affinity towards DNA. The molecule served as an excellent example for single molecule based theranostic approaches which open further avenues for the development of therapeutic agents with self-reporting characteristics.

1.5. Objectives and Methodologies of the Present Investigation

Inspired by the recent advancements in the design and development of synthetic molecular probes for sensing, imaging and therapeutic applications, the possibility of utilizing a few optically active (either luminescent or Raman active) molecules for diagnostic and therapeutic applications has been explored in the present thesis. The utility of small molecule based probes for cancer detection and treatment has been well studied and has been a topic of great interest in the present decade owing to the increased incidence of cancer related deaths worldwide. Therefore, we aimed to develop a few organic molecules for sensing and imaging of cancer specific biomarkers together with the development of a photosensitizer for optical imaging guided PDT applications.

In the present work, the first objective was to develop a NIR squaraine dye which could sense thiols in the intracellular environmental conditions. With this aim, an unsymmetrical squaraine dye, **Sq** was synthesized which was appended with alkylated aniline on one side and pyrrole styryl pyridine chromophore on the other side of the squaraine ring. From the literature background, it was envisaged that the presence of aniline unit would improve the overall reactivity of the molecule while the styryl unit will serve as a thiol activatable chromophore which may help in developing a ratiometric fluorescent probe for thiols. A systematic investigation of the various photophysical aspects was performed and subsequently the sensing ability of **Sq** was evaluated which showed that the molecule is capable of detecting thiols with very high sensitivity and selectivity. These observations enabled **Sq** for the quantitative sensing of intracellular thiols and also established the diagnostic potential of the probe in cancer detection and apoptotic evaluation.

The next objective was to design a few molecular probes for simultaneous detection of multiple biomarkers in a single platform which could enable more accurate and precise diagnosis of the disease condition. For this purpose, three molecular probes (Coum-cathB, Rh110-cathB, RhB-cathB) with different emission and Raman spectral profile were synthesized that have been conjugated to a cathepsin B (cath B) specific peptide sequence for realising an “on-off” switching between fluorescence and SERS modalities. The bimodal probes containing gold nanoparticle tethered peptide dye conjugates were further functionalized with monoclonal antibody units to afford multiplexed detection of epidermal growth factor receptor (EGFR), cytokeratin-19 and napsin-A, the key biomarkers involved in the invasion and progression of lung cancer. The probes were further utilized for evaluation of the biomarker status in clinical patient specimens using fluorescence and SERS analyses. In addition to effective diagnosis, precise treatment and proper follow-up of therapeutic responses are essential for the efficient management of diseases. With this objective in mind, a photosensitizer molecule, **Ir-Pyr** built on an iridium complex containing 2-hydroxypyridine appended bipyridine ligand was designed to meet the requirements of oxygen independent photodynamic therapy. The design strategy was such that the presence of 2-hydroxypyridine ligand will trap and release singlet oxygen by heat triggered cycloreversion of endoperoxides to afford a multifunctional photosensitizer for hypoxic tumors. A hybrid complex of **Ir-Pyr** with MnO_2 nanosheets was prepared in order to realise a photothermally triggered release of the singlet oxygen payload for programmed cell death applications. Moreover, the tumor microenvironment responsiveness of MnO_2 was utilized in a favourable manner to increase the local oxygen concentration via its degradation in presence of H_2O_2 to provide room for the second phase of photodynamic therapy. The detailed investigations performed *in vitro* and *in vivo* showed superior therapeutic performance of the probe anchored with promising imaging capabilities. Taken together, the present thesis deals with a systematic study on the design, synthesis and assessment of a few rationally designed small molecule based optical probes for diagnostic and therapeutic applications in cancer.

1.6. References

[1] Yao, J.; Yang, M.; Duan, Y. *Chem. Rev.* **2014**, *114*, 6130.

[2] Ghasemi M.; Nabipour I.; Omrani, A.; Alipour Z.; Assadi, M. *Am. J. Nucl. Med. Mol. Imaging* **2016**, *6*, 310.

[3] Kobayashi, H.; Ogawa, M.; Alford, R.; Choyke, P. L.; Urano, Y. *Chem. Rev.* **2010**, *110*, 2620.

[4] Garland M.; Yim, J. J.; Bogyo, M. *Cell Chem. Biol.* **2016**, *23*, 122.

[5] Xie, W.; Qiu, P.; Mao, C. *J. Mater. Chem.* **2011**, *21*, 5190.

[6] Xie, W.; Schlucker, S. *Phys. Chem. Chem. Phys.* **2013**, *15*, 5329.

[7] Lane, L. A.; Qian, X.; Nie, S. *Chem. Rev.* **2015**, 11*5*, 10489.

[8] Wang, Z.; Zong, S.; Wu, L. *Chem. Rev.* **2017**, *117*, 7910.

[9] Gao, M.; Yu, F.; Lv, C.; Choo, J.; Chen, L. *Chem. Soc. Rev.* **2017**, *46*, 2237.

[10] Lucky, S. S.; Soo, K. C.; Zhang, Y. *Chem. Rev.* **2015**, *115*, 1990.

[11] Hu, J. J.; Cheng, Y. J.; Zhang, X. Z. *Nanoscale* **2018**, *10*, 22657.

[12] Kumar, R.; Shin, W. S.; Sunwoo, K.; Kim, W. Y.; Koo, S.; Bhuniya, S.; Kim, J. S. *Chem. Soc. Rev.* **2015**, *44*, 6670.

[13] Lee, D. E.; Koo, H.; Sun, I. C.; Ryu, J. H.; Kim, K.; Kwon, I. C. *Chem. Soc. Rev.* **2012**, *41*, 2656.

[14] Torchilin, V. P. *Nat. Rev. Drug Discov.* **2014**, *13*, 813.

[15] Brookner, C. K.; Follen, M.; Boiko, I.; Galvan, J.; Thomsen, S.; Malpica, A.; Suzuki, S.; Lotan, R.; Richards-Kortum, R. *Photochem. Photobiol.* **2000**, *71*, 730.

[16] Reinert K. C.; Dunbar R. L.; Gao, W.; Chen, G.; Ebner T. J. *J Neurophysiol.* **2004**, *92*, 199.

[17] Skala, M.C.; Riching, K.M.; Gendron-Fitzpatrick, A.; Eickhoff, J.; Eliceiri, K. W.; White, J. G.; Ramanujam, M. *Proc. Natl. Acad. Sci. USA* **2007**, *104*, 10494.

[18] Ueno, T.; Nagano, T. *Nat. Methods* **2011**, *8*, 642.

[19] Li, X.; Gao, X.; Shi, W.; Ma, H. *Chem. Rev.* **2014**, *114*, 590.

[20] Newman, R. H.; Fosbrink, M. D.; Zhang, J. *Chem. Rev.* **2011**, *111*, 3614.

[21] Kim, H. N.; Guo, Z.; Zhu, W.; Yoon, J.; Tian. H. *Chem. Soc. Rev.* **2011**, *40*, 79.

[22] Yao, J.; Yang, M.; Duan, Y. *Chem. Rev.* **2014**, *114*, 6130.

[23] Biju, V. *Chem. Soc. Rev*. **2014**, *43*, 744.

[24] Atabaev, T. S. *Nanomaterials* **2018**, *8,* 342.

[25] de Silva, A. P.; Gunaratne, H. Q. N.; Gunnlaugsson, T.; Huxley, A, J, M.; McCoy, C. P.; Rademacher, J. T.; Rice, T. E. *Chem. Rev.* **1997**, *97*, 1515.

[26] Wu, J.; Liu, W.; Ge, J.; Zhang, H.; Wang, P. *Chem. Soc. Rev.* **2011**, *40*, 3483.

[27] Yuan, L.; Lin, W.; Zheng, K.; Zhu, S. *Acc. Chem. Res.* **2013**, *46*, 1462.

[28] Koteeswari, R.; Ashokkumar, P.; Malar, E. J. P.; Ramakrishnan, V. T.; Ramamurthy, P. *Chem. Commun.* **2011**, *47*, 7695.

[29] Breuer W.; Epsztejn S.; Cabantchik Z. I. *J. Biol. Chem.* **1995**, *270*, 24209.

[30] Breuer W.; Epsztejn S.; Millgram P.; Cabantchik I. Z. *Am. J. Physiol.* **1995**, *268*, C1354.

[31] Yuan C.; Li J.; Xi H.; Li Y. *Materials Letters* **2019**, *236*, 9.

[32] Aysha T. S.; El-Sadik M. S.; Mohamed M. B. I.; Gaballah S. T.; Kamel M. M. *Dyes and Pigments* **2019**, *170*, 107549.

[33] Ros-Lis J. V.; Garcia B.; Jimenez D.; Martınez-Manez R.; Sancenon F.; Soto J.; Gonzalvo F.; Valldecabres M. C. *J. Am. Chem. Soc*. **2004**, *126*, 4064.

[34] Mishra R. K.; Vijayakumar S.; Mal A.; Karunakaran V.; Janardhanan J. C.; Maiti K. K.; Praveen V. K.; Ajayaghosh A. *Chem. Commun.* **2019**, *55*, 6046.

[35] Cao, X. W.; Lin, W.; He, L. *Org. Lett.* **2011**, *13*, 4716.

[36] Tang, B.; Yu, F.; Li, P.; Tong, L.; Duan, X.; Xie, T.; Wang, X. *J. Am. Chem. Soc.* **2009**, *131*, 3016.

[37] Urano, Y.; Asanuma, D.; Hama, Y.; Koyama, Y.; Barrett, T.; Kamiya, M.; Nagano, T.; Watanabe, T.; Hasegawa, A.; Choyke, P. L.; Kobayashi, H. *Nat. Medicine* **2009**, *15*, 104.

[38] Kwon, H.; Lee, K.; Kim, H. J. *Chem. Commun.* **2011**, *47*, 1773.

[39] Yu, F.; Li, P.; Li, G.; Zhao, G.; Chu, T.; Han, K. *J. Am. Chem. Soc.* **2011**, *133*, 11030.

[40] Demchenko, A. P. *J Fluoresc.* **2010**, *20*, 1099.

[41] Lee, M. H.; Han, J. H.; Lee, J. H.; Park, N.; Kumar, R.; Kang, C.; Kim, J. S. *Angew. Chem. Int. Ed.* **2013**, *52*, 6206.

[42] Divya, K. P.; Sreejith, S.; Ashokkumar, P.; Yuzhan, K.; Peng, Q.; Maji, S. K.; Tong, Y.; Yu, H.; Zhao, Y.; Ramamurthy, P.; Ajayaghosh, A. *Chem. Sci.* **2014**, *5*, 3469.

[43] Kurishita, Y.; Kohira, T.; Ojida, A.; Hamachi, I. *J. Am. Chem. Soc.* **2010**, *132*, 13290.

[44] Zhu, B. C.; Zhang, X. L.; Li, Y. M.; Wang, P. F.; Zhang, H. Y.; Zhuang, X. Q. *Chem. Commun.* **2010**, *46*, 5710.

[45] Lim, C. S.; Masanta, G.; Kim, H. J.; Han, J. H.; Kim, H. M.; Cho, B. R. *J. Am. Chem. Soc.* **2011**, *133*, 11132.

[46] Cialla-May, D.; Zheng, X.-S.; Weber, K.; Popp, J. *Chem. Soc. Rev.* **2017**, *46*, 3945.

[47] Joseph, M. M.; Narayanan, N.; Nair, J. B.; Karunakaran, V.; Ramya, A. N.; Sujai, P. T.; Saranya, G.; Arya, J. S.; Vijayan, V. M.; Maiti, K. K. *Biomaterials,* **2018**, *181*, 140.

[48] Robson, A. F.; Hupp, T. R.; Lickiss, F.; Ball, K. L.; Faulds, K.; Graham, D. *Proc. Natl. Acad. Sci. U. S. A* **2012**, *109*, 8073.

[49] Wang, G.; Lipert, R. J.; Jain, M.; Kaur, S.; Chakraboty, S.; Torres, M. P.; Batra, S. K.; Brand, R. E.; Porter, M. D. *Anal. Chem.***2011**, *83*, 2554.

[50] Xu, L.; Zhao, S.; Ma, W.; Wu, X.; Li, S.; Kuang, H.; Wang, L.; Xu, C. *Adv. Funct. Mater.* **2016**, *26*, 1602.

[51] Ramya, A. N.; Joseph, M. M.; Nair, J. B.; Karunakaran, V.; Narayanan, N.; Maiti, K. K. *ACS Appl. Mater. Interfaces* **2016**, *8*, 10220.

[52] Cao, Y.; Li, D. W.; Zhao, L. J.; Liu, X. Y.; Cao, X. M.; Long, Y. T. *Anal. Chem.* **2015**, *87*, 9696.

[53] Song, J.; Zhou, J.; Duan, H. *J. Am. Chem. Soc.* **2012**, *134*, 13458.

[54] Seo, S. H.; Kim, B. M.; Joe, A.; Han, H. W.; Chen, X.; Cheng, Z.; Jang, E. S. *Biomaterials*, **2014**, *35*, 3309.

[55] Narayanan, N.; Nair, L. V.; Karunakaran, V.; Joseph, M. M.; Nair, J. B.; Ramya, A. N.; Jayasree, R. S.; Maiti, K. K. *Nanoscale*, **2016**, *8*, 11392.

[56] Castano, A. P.; Demidova, T. N.; Hamblin, M. R. *Photodiagnosis Photodyn Ther.* **2004**, *1*, 279.

[57] Calixto, G.; Bernegossi, J.; de Freitas, L. M.; Fontana, C. R.; Chorilli, M. *Molecules*, **2016**, *21*, 342.

[58] Dougherty, T. J.; Grindey, G. B.; Fiel, R.; Weishaupt, K. R.; Boyle, D. G. *J. Natl. Cancer Inst.* **1975**, *55*, 115.

[59] Garland, M. J.; Cassidy, C.M.; Woolfson, D.; Donnelly, R. F. *Future Med. Chem.,* **2009**, *1*, 667.

[60] Wainwright, M. *Chem. Soc. Rev.*, **1996**, *25*, 351.

[61] Li, X.; Lee, S.; Yoon, J. *Chem. Soc. Rev.*, **2018**, *47*, 1174.

[62] Zhao, J.; Wu, W.; Sun, J.; Guo, S. *Chem. Soc. Rev.* **2013**, *42*, 5323.

[63] Celli, J. P.; Spring, B. Q.; Rizvi, I.; Evans, C. L.; Samkoe, K. S.; Verma, S.; Pogue, B. W.; Hasan, T. *Chem Rev*. **2010**, *110*, 2795.

[64] Lovel, J. F.; Liu, T. W. B.; Chen, J.; Zheng, G. *Chem Rev.* **2010**, *110*, 2839.

[65] Xue, F.; Lu, Y.; Zhou, Z.; Shi, M.; Yan, Y.; Yang, H.; Yang, S. *Organometallics* **2015**, *34*, 73.

[66] Wang, J.; Lu, Y.; McGoldrick, N.; Zhang, C.; Yang, W.; Zhaob, J.; Draper, S. M. *J. Mater. Chem. C* **2016**, *4*, 6131.

[67] Palao, E.; Sola-Llano, R.; Tabero, A.; Manzano, H.; Agarrabeitia, A. R.; Villanueva, A.; Ljpez-Arbeloa, C.; Martinez-Martinez, V.; Ortiz, M. J. *Chem. Eur. J.* **2017**, *23*, 10139.

[68] Wang, F. –X.; Chen, M. –H.; Lin, Y. –N.; Zhang, H.; Tan, C. –P.; Ji, L. –N.; Mao, Z. –W. *ACS Appl. Mater. Interfaces* **2017**, *9*, 42471.

[69] Qiu, K.; Huang, K.; Liu, B.; Liu, Y.; Huang, Z.; Chen, Y.; Ji, L.; Chao, H. *ACS Appl. Mater. Interfaces* **2016**, *8*, 12702.

[70] Li, C.; Yu, M.; Sun, Y.; Wu, Y.; Huang, C.; Li, F. *J. Am. Chem. Soc.* **2011**, *133*, 11231.

[71] Jayaram, D. T.; Romero, S. R.; Shankar, B. H.; Garrido, C.; Rubio, N.; Cid, L. S.; Gomez, S. B.; Blanco, J.; Ramaiah, D. *ACS Chem. Biol.* **2016**, 11, 104.

[72] Lv, W.; Zhang, Z.; Zhang, K. Y.; Yang, H.; Liu, S.; Xu, A.; Guo, S.; Zhao, Q.; Huang, W. *Angew. Chem. Int. Ed.* **2016**, *55*, 9947.

[73] Gao, Y.; Wang, X.; He, X.; He, Z.; Yang, X.; Tian, S.; Meng, F.; Ding, D.; Luo, L.; Tang, B. Z. *Adv. Func. Mater.* **2019**, *29*, 1902673.

Chapter 2

A Ratiometric Near-Infrared Fluorogenic Probe for the Real Time Monitoring of Intracellular Redox Status during Apoptosis

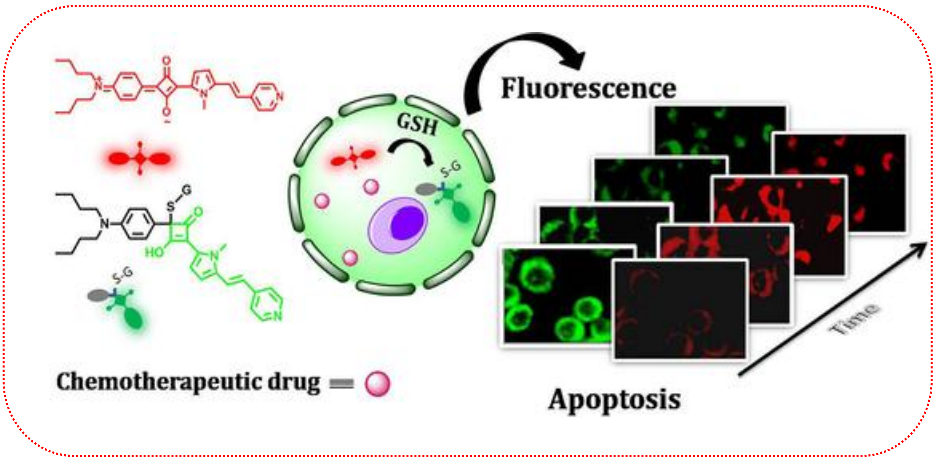

2.1. Abstract

Direct monitoring of apoptotic progression is a major step forward to the early detection of therapeutic efficacy and evaluation of disease condition. Herein, the regulatory role of glutathione (GSH) has been explored as a potential biomarker for tracking apoptosis. For this purpose, a near-infrared (NIR) squaraine dye was synthesized that is capable of sensing GSH in a ratiometric manner by switching its emission from NIR (690 nm) to visible region (560 nm). The favorable biocompatible attributes of the probe facilitated the real time monitoring of apoptotic process in line with the conventional apoptotic assay. Furthermore, the robust nature of the probe was utilized for the quantitative estimation of GSH during different stages of apoptosis. Through this study, an easy and reliable method of assaying apoptosis was developed, which can provide valuable insights in translational clinical research.

2.2. Introduction

Apoptosis, a highly organized phenomenon of programmed cell death, plays an important role in embryonic development and tissue homeostasis in all organisms.[1] Abnormalities in cell death regulation can inhibit homeostasis and can lead to several deadly diseases such as cancer, neurodegenerative and autoimmune disorders.[2-5] Therefore, tracking the advancement of apoptotic events is essential for the sensitive monitoring of therapeutic responses and evaluation of disease progression. A variety of strategies has been developed for screening the progress of treatment based on certain apoptotic phenotypes such as caspase activation,[6-10] phosphatidylserine externalization[11,12] and DNA fragmentation.[13-15] More recently, the role of antioxidant defenses, particularly the intracellular glutathione (GSH), which is a thiol containing peptide, have been found to play a central role in apoptosis.[16-18] Although apoptosis is a versatile cellular process which can be triggered by a variety of pathways, in a general sense, upon apoptotic induction, GSH, the primary contributor to intracellular redox state,[19] shows a depletion, and promotes the generation of reactive oxygen species (ROS), which in turn account to the cell death machinery. This implies that stimulation of apoptosis occurs as a direct consequence of GSH depletion and not directly from ROS induced cell damages.[20-22] Although the actual mechanism in the modulation of apoptosis by GSH still remains unclear, it has been well established that GSH is an early hallmark in the apoptotic cascade.[23,24] In contrast to other signaling events which occur during the execution phases or even later stages, exhaustion of GSH marks the beginning of the cell death phenomena [17,21,25] and can therefore serve as a promising means for assaying apoptosis right from the initiation step. Therefore, detection of thiol containing peptides, particularly GSH, is important in the study of intracellular redox state.

Among numerous detection techniques available for thiol sensing, fluorescence assay forms one of the most powerful and convenient tools to visualize the complex biological processes due to its desirable features in terms of simplicity, low cost and high sensitivity.[26-30] Since the report of a thiol probe by Sippel came as one of the first examples of thiol sensing,[31] there have been significant progress in this area of research. Taking advantage of the Michael

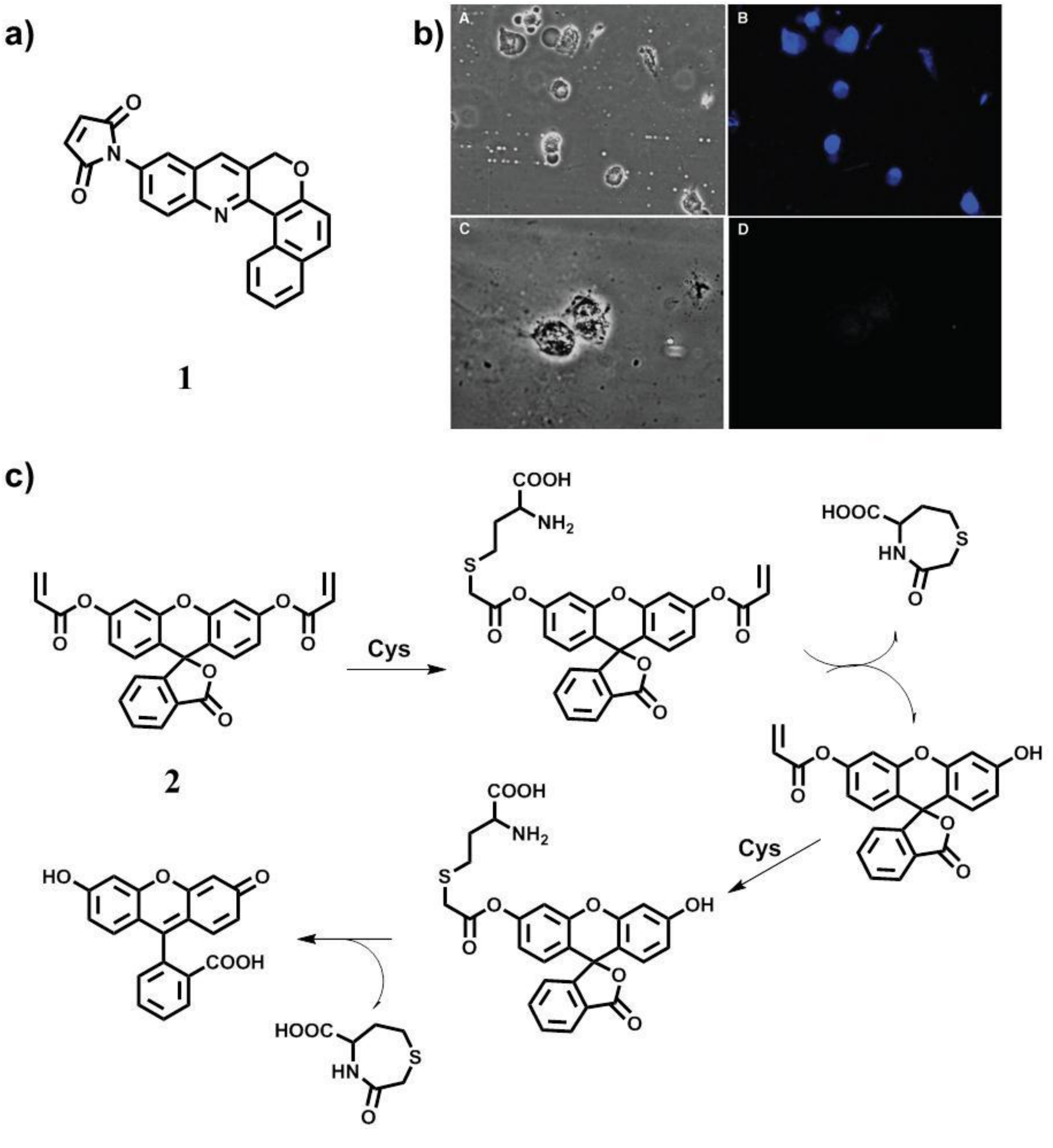

Figure 2.1. a) Structure of chromenoquinoline fluorescent probe, **1**. b) Transmission (A and C) and fluorescence (B and D) images of cells administered with **1** (25 μM) with (C, D) or without (A, B) pretreatment with *N*-phenylmaleimide (5 mM). c) Plausible mechanistic pathway of the reaction between **2** and Cys.

addition reactions of thiols, Kand *et al.*, demonstrated the design of a chromenoquinoline based fluorescent sensor (**1**) for the detection of thiols in biological systems.[32] The molecule, which was initially non-fluorescent underwent a ~223 fold enhancement in emission intensity upon addition of thiols. The probe exhibited a linear turn-on fluorescence response to biological thiols with a detection limit as low as 1.46 x 10^{-8} M. The authors have further utilized the probe

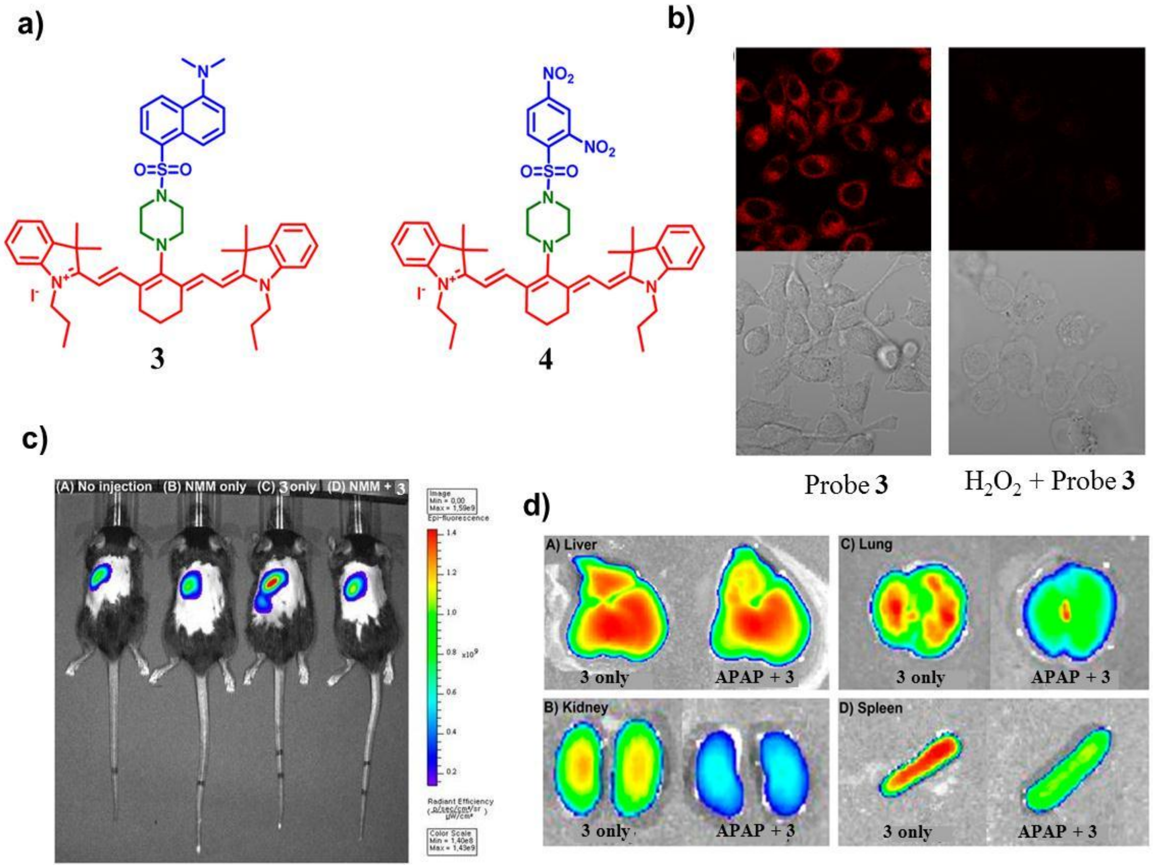

Figure 2.2. a) Structure of probes **3** and **4**. b) Fluorescence microscopic images of probe **3** in HeLa cells before and after treatment with H_2O_2. Cell images were acquired using an excitation wavelength of 635 nm and a band-path (655−755 nm) emission filter. c) *In vivo* fluorescence images of a mouse injected with probe **3** (50 μM) or *N*-methylmaleimide (NMM; 20 mM) via intravenous injection for 20 min. d) *Ex vivo* fluorescence images of tissues from a mouse intravenously injected with probe **3** (50 μM) or acetaminophen (APAP; 300 mg/kg in 200 μL of HEPES buffer solution).

for detecting endogenous thiol concentrations in MDA-MB 231 cells (**Figure 2.1a**). A fluorescein based chemodosimeter probe (**2**) was developed for the selective detection of cysteine (Cys). The probe displayed a turn-on colorimetric as well as fluorimetric response upon addition of Cys which was attributed to the adduct formation between acrolyl moiety present in the probe with the Cys molecules.[33] The presence of two acrolyl groups in the probe enabled dual addition cleavage processes between **2** and Cys which accounted for the selective discrimination of Cys over homocysteine (Hcy) (**Figure 2.1b**).

In 2014, Yin *et al.,* reported cyanine based fluorescent probes **3** and **4** for the selective detection of GSH (**Figure 2.2a**). In the presence of GSH, the probe **3** underwent an activation of its fluorescence signal at 736 nm which was found to be reversed upon addition of *N*-methylmaleimide. Furthermore, the probe was utilized for the visualization of intracellular thiol concentrations in the absence and presence of H_2O_2 (**Figure 2.2b**). Moreover, the authors demonstrated the reversible emission response of **3** *in vivo,* which offers opportunities for real time tracking of thiol fluctuations in living systems (**Figure 2.2c**). Finally, the probe was used to evaluate GSH levels in mouse tissues such as liver, spleen, kidney, lungs etc. (**Figure 2.2d**) which suggest the potential of **3** as an effective candidate for probing cellular functions related to GSH.[34] In another study, He and colleagues designed a coumarin based ratiometric probe (**5**) for specific detection of Cys.[35] The probe was built on a coumarin-sulfonyl benzoxadiazole based FRET platform which undergoes a selective aromatic substitution–rearrangement in the presence of Cys that helped in distinguishing Cys from GSH and Hcy (**Figure 2.3a** and **2.3b**). After successful demonstration in solution state conditions, the authors utilized the probe for ratiometric fluorescence imaging in live HeLa cells (**Figure 2.3c**) and zebrafish upon the addition of varying Cys doses. Moreover, the probe enabled the visualization of Cys fluctuations *in vivo,* which served as a potential tool for elucidation of the role of cysteine in real time investigation of oxidative stress responses.

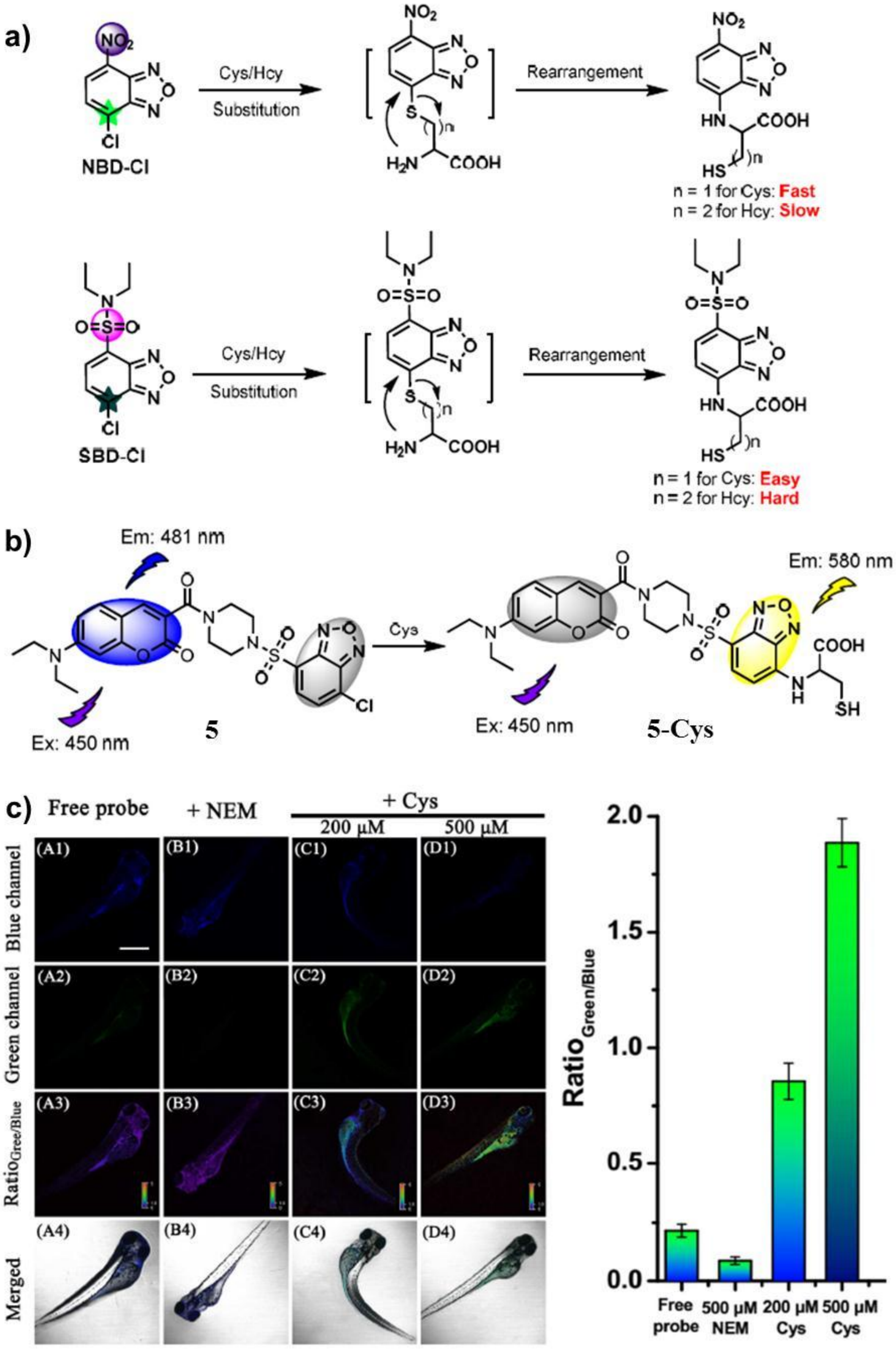

Figure 2.3. a) Reaction mechanism and b) sensing strategy involved in the selective detection of Cys. c) Confocal fluorescence images of probe **5** in zebrafish subjected to various treatments, (A) **5** alone, (B) NEM + **5**, (C and D) NEM + Cys+ **5**.

Recently, the research group of Munoz reported a xanthene based fluorescent probe, **6** for sensing of biothiols under oxidative stress conditions (**Figure 2.4a**).[36] The sensing mechanism involves the thiolysis of the sulfonyl

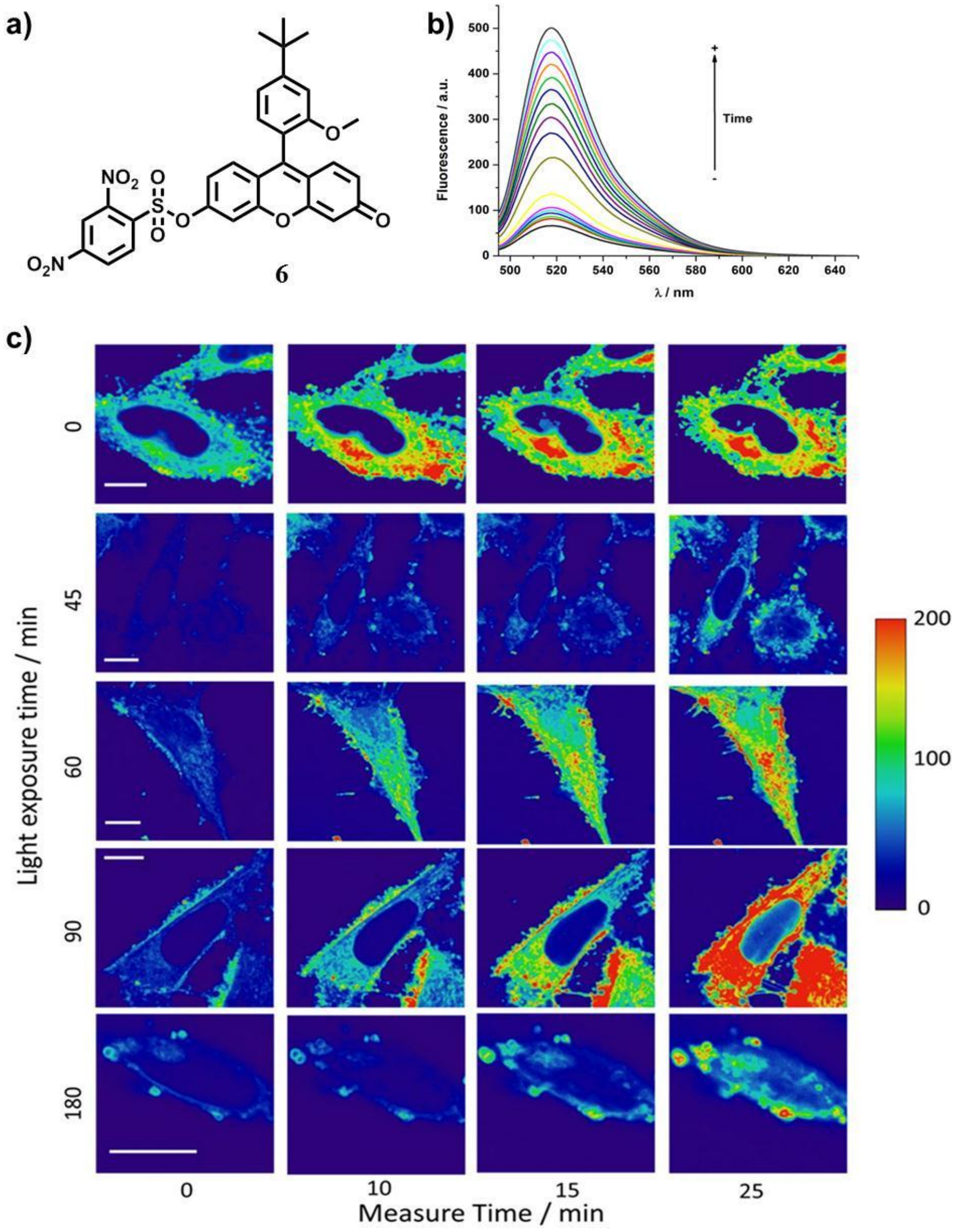

Figure 2.4. a) Chemical structure of **6**. b) Time dependent fluorescence changes of **6** towards GSH. c) Fluorescence microscopic images of photoreceptor-derived cell line (661 W), administered with probe and subjected to light mediated stress at different exposure times (0 min, 45 min, 60 min, 90 min and 180 min).

group which causes an enhancement in the emission intensity at 520 nm (**Figure 2.4b**). The dye enabled a rapid detection of intracellular thiol variations resulting from ROS and light mediated oxidative stress via single cell imaging (**Figure 2.4c**). In another report, Yuan and co-workers designed and synthesized a thiol specific fluorescent probe (**7**) for endogenous imaging of biothiols in living mice. The probe containing a 2,4-dinitrobenzenesulfonate unit as the sensor moiety displayed a 50 fold enhancement in the emission intensity at 716 nm in the presence of Cys (**Figure 2.5a**) at a physiological pH of 7.4 (PBS–CH_3CN, 7:3). The ability of the sensor for NIR imaging of thiols was performed *in vitro* in Bel 7702 cells (**Figure 2.5b**). Further, the authors have evaluated the suitability of the probe for *in vivo* imaging of endogenous thiol levels wherein the mice injected with different concentrations (0, 20, 40, or 160 nanomoles) of **7** presented an

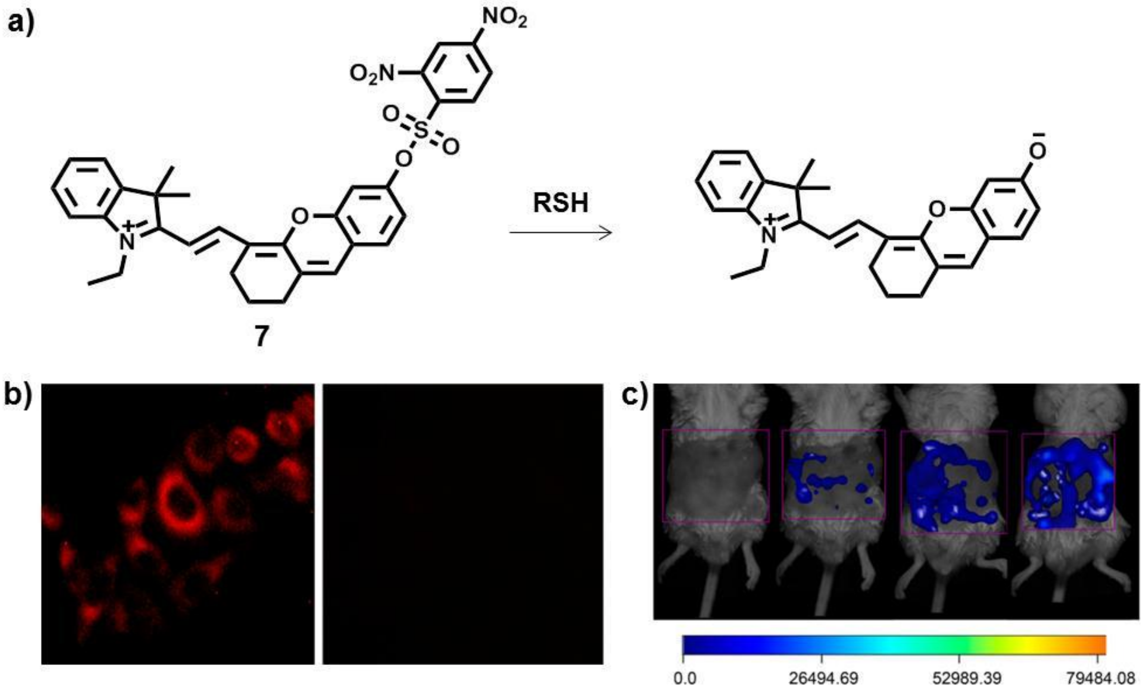

Figure 2.5. a) Sensing strategy of probe **7** for sensing thiols. b) Fluorescence images of Bel 7702 cells treated with probe **7** (5 μM) alone (first image) and probe **7** (5 μM) after treating with *N*-ethylmaleimide (1 mM) (second image). c) *In vivo* fluorescence images (pseudo-color) of mice injected (*ip*) with different concentrations (0, 20, 40, or 160 nanomoles) of probe **7**.

increase in the NIR fluorescence signal in a dose-dependent manner (**Figure 2.5c**).[37]

Squaraine dyes are a well-established class of molecular probes with favorable optical properties of intense absorption and emission in the visible and near-infrared (NIR) regions.[38-43] The reactivity of thiols to squaraines has been investigated extensively for various applications. These dyes possess an electron deficient center which is susceptible to attack by nucleophilic thiols that often results in the bleaching of the absorption as well as the fluorescence properties of the dye. On the basis of this design principle, Manez and co-workers synthesized two squaraine dyes **8** and **9** for the detection of thiols (**Figure 2.6a**).[44] In acetonitrile–water (2:8 v/v) system, both the molecules displayed an emission band centered at about 640 nm with a quantum yield of 0.1. However, in acetonitrile/pH

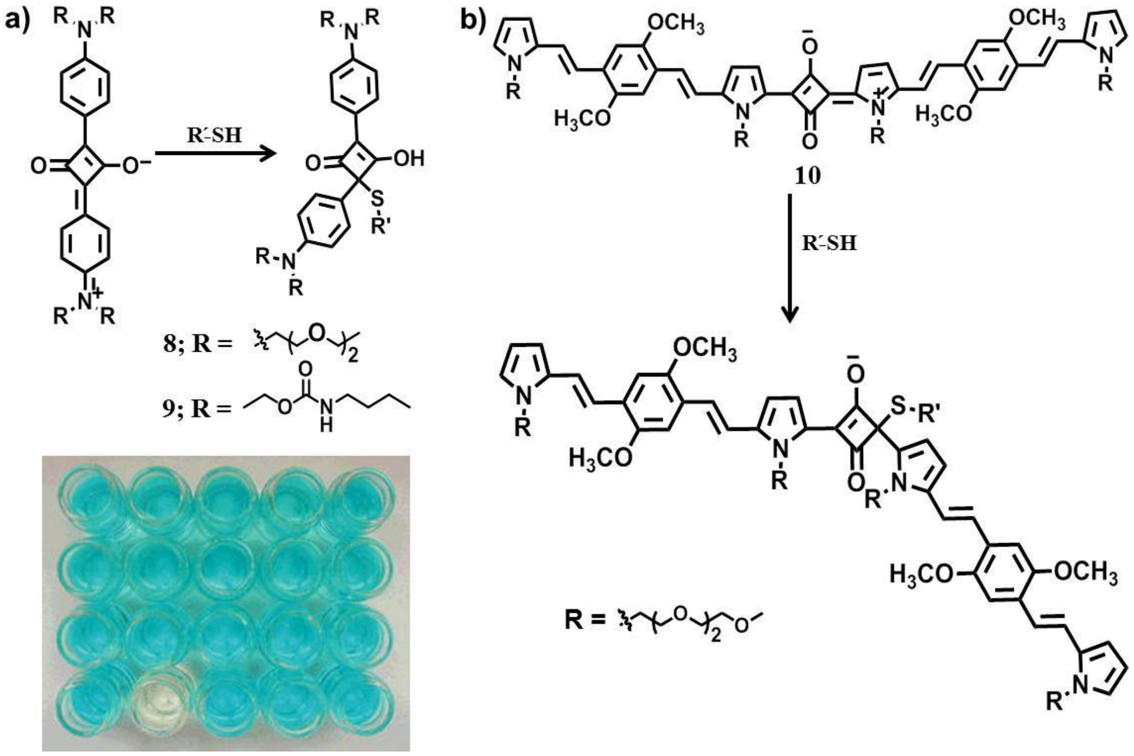

Figure 2.6. a) Chemical structure of the squaraine derivatives **8** and **9**. b) Schematic illustration of the chemical activation of the weak NIR fluorophore **10** to an active fluorophore via addition of thiols.

6 buffer (2:8 v/v, MES, 0.01 M), both the dyes underwent a remarkable bleaching of their absorption together with a complete quenching of their emission signals in the presence of Cys among other amino acids.

In 2009, Ajayaghosh *et al.*, reported a bispyrrole based π-extended NIR squaraine dye **10** for the fluorescent detection of biological thiols (**Figure 2.6b**).[45] In the presence of GSH and Cys, the π-conjugation of the probe **10** was broken that resulted in a quenching of its NIR emission (λ_{ex} = 730 nm, λ_{em} = 802 nm) while displaying a strong emission in the 595 nm region (λ_{ex} = 410 nm),

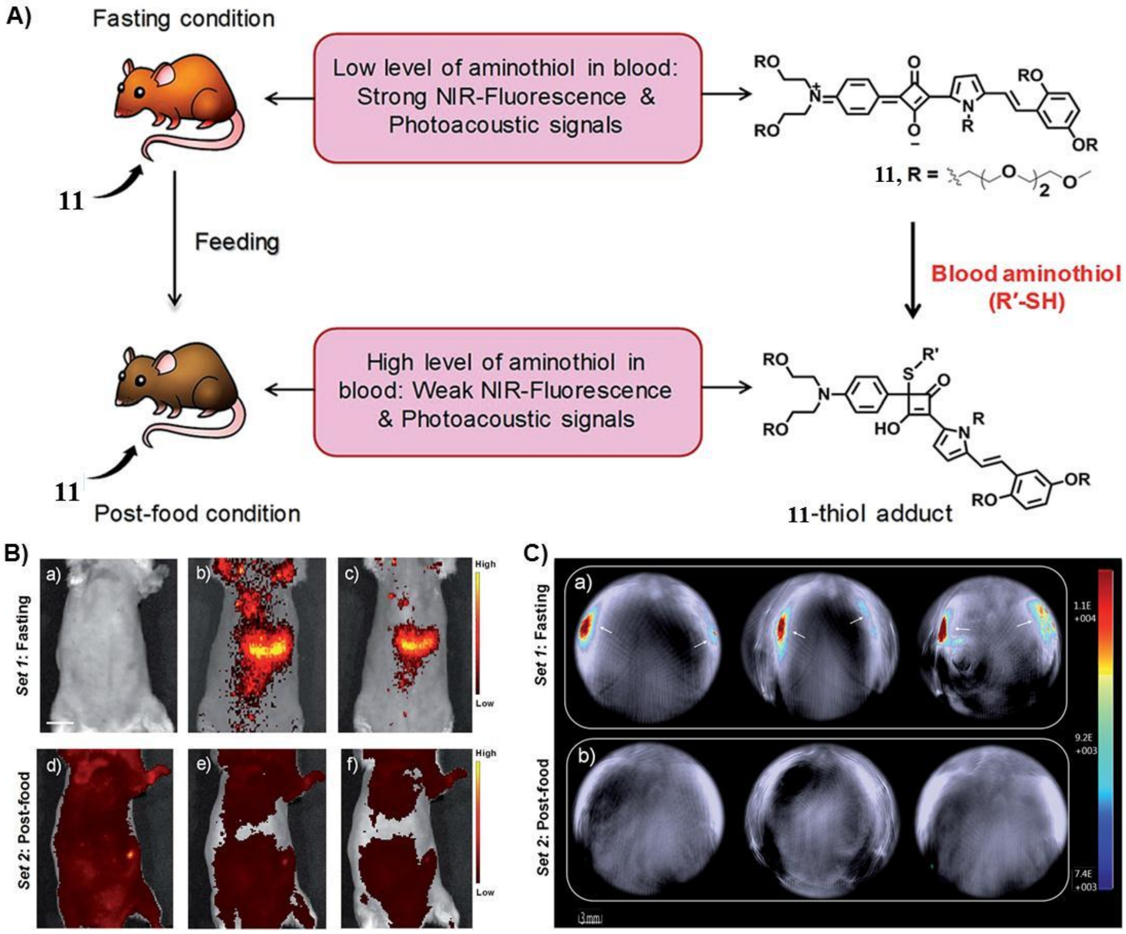

Figure 2.7. A) Schematic representation of the bimodal (fluorescence/photoacoustic) sensing strategy of aminothiols using **11**. *In vivo* fluorescence (B) and photoacoustic (C) images of probe treated mouse under fasting (Set 1) and post-food (Set 2) conditions.

characteristic of the bispyrrole moiety. These emission changes enabled the detection of thiols in a ratiometric manner, which is more advantageous than the usually employed color bleaching or fluorescence quenching approaches. More recently, in 2016, the same group reported the design and synthesis of an unsymmetrical NIR squaraine dye (**11**) for fluorescence and photoacoustic bimodal imaging of biothiol variations *in vitro* and *in vivo* (**Figure 2.7A**).[46] The strong NIR emission profile of **11** enabled it for deep tissue optical imaging which displayed a turn-off response in the presence of thiols. The authors further explored the *in vitro* and *in vivo* imaging potential of **11** and utilized it for investigating the effect of food uptake on aminothiol variations in mice models (**Figure 2.7B** and **2.7C**).

Though there are several reports on the use of squaraine dyes for thiol sensing applications, none of them is applicable for real time tracking of thiol variations in biological specimens. To address this issue, a ratiometric squaraine based fluorescent probe (**Sq**) has been designed for biothiols which has a great potential for quantification of thiol levels *in vitro*. The promising potential of **Sq** was further utilized for quantifying the GSH imbalance during various stages of apoptosis in *in vitro* models (**Scheme 2.1**). The application of **Sq** for real time monitoring of apoptosis via the quantification of intracellular GSH status as described in the present work is the first example of such kinds.

2.3. Results and Discussion

2.3.1. Synthesis Strategy

Towards the synthesis of **Sq**, a multistep synthetic strategy was adopted which is shown in **Schemes 2.2 to 2.4**. *N*-methylpyrrole-2-carbaldehyde (**12**) on reaction with 4-methylpyridine (**13**) gave the corresponding pyrrole styryl derivative (**14**) in 70% yield. The intermediate *N*, *N*-dibutylaniline (**16**) was prepared by the reaction of aniline (**15**) with butyl bromide in the presence of Na_2CO_3 under reflux conditions in 90% yield. The subsequent treatment of **16** with squaryl chloride in dry benzene followed by hydrolysis in acetic acid/HCl gave the semisquaraine derivative (**17**) in 80% yield. The so-formed semi-squaraine upon reaction with the styryl derivative (**14**) in 1:1 *n*-butanol/benzene mixture under azeotropic conditions afforded the desired compound **Sq** in quantitative yield. All the intermediates and final compounds after purification were subjected to characterization by nuclear magnetic resonance spectroscopy (NMR) and high resolution mass spectrometry (HRMS).

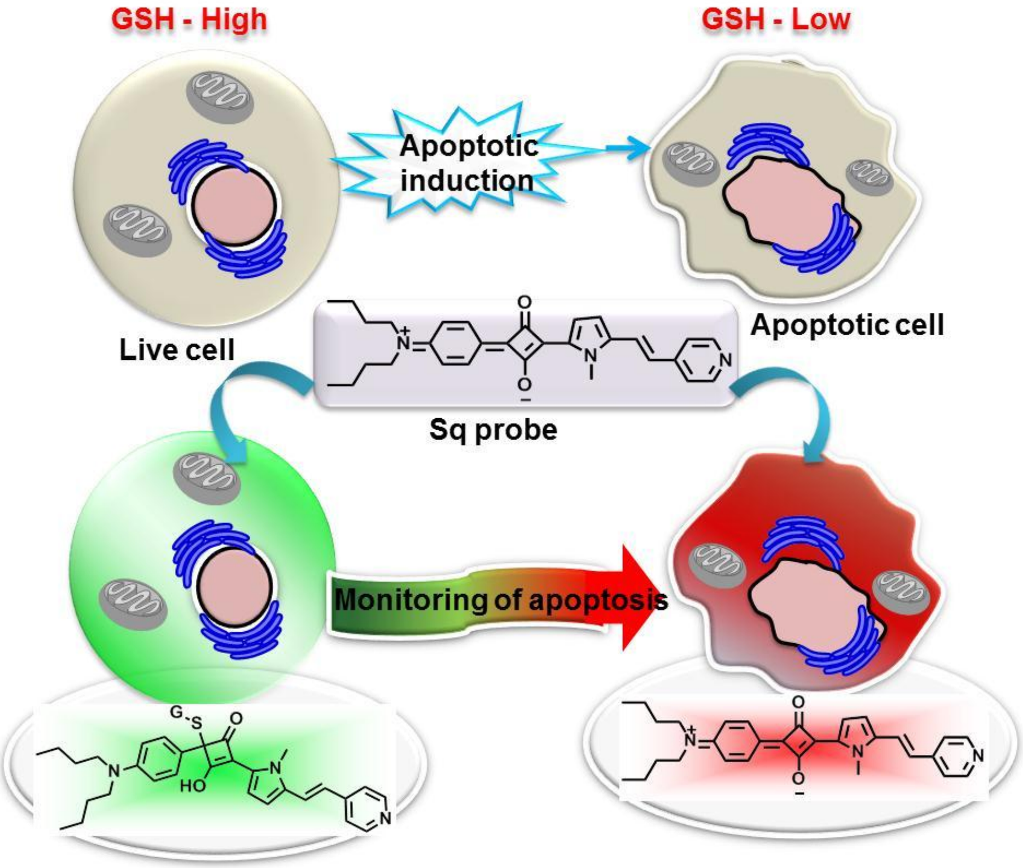

Scheme 2.1. Schematic illustration of ratiometric sensing of GSH during apoptosis using **Sq** dye.

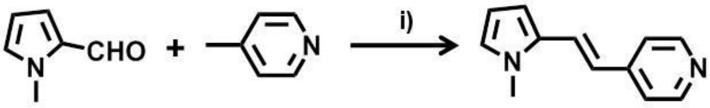

12 **13** **14**

Scheme 2.2. Reagents and conditions: [i] NaH, dry DMF, 70 °C, 12 h.

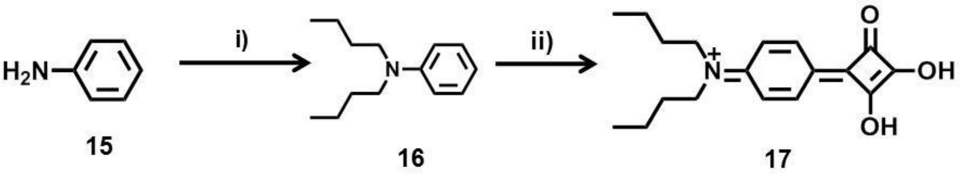

Scheme 2.3. Reagents and conditions: [i] 1-bromobutane, Na_2CO_3, I_2, *n*-butanol, 100 °C, 24 h; [ii] Squarylchloride, benzene, 80 °C , 6 h and CH_3COOH, HCl, 100 °C, 3 h.

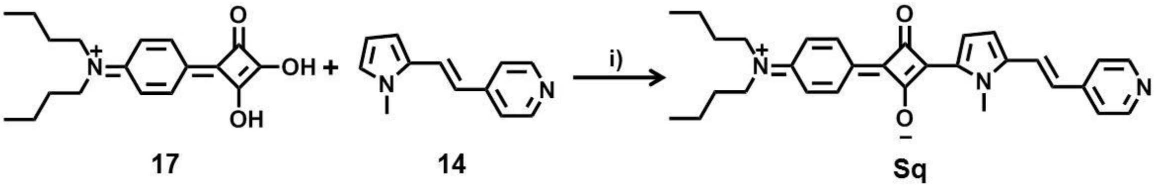

Scheme 2.4. Reagents and conditions: [i] 1:1 *n*-butanol/benzene azeotropic mixture, 90 °C, 10 h.

2.3.2. Photophysical Studies

The photophysical properties of **Sq** were first examined in 20% acetonitrile/phosphate buffer (25 mM, pH 7.4). **Sq** exhibited an absorption maximum at 670 nm and an emission at 690 nm (Φ_F = 0.07 with Nile blue in ethanol as reference, Φ_R = 0.27). Upon interaction with biothiols, **Sq** displayed ratiometric changes in its absorption and emission characteristics. On addition of GSH, the absorption maximum at 670 nm decreased with the simultaneous formation of a new absorption band at 400 nm (**Figure 2.8a**). Similarly, titration of **Sq** with GSH resulted in the formation of a new emission band at 560 nm (Φ_F = 0.12 with Rhodamine 6G in ethanol as reference, Φ_R = 0.95) with the concomitant quenching of the NIR emission at 690 nm (**Figure 2.8b**). The ratiometric sensing mechanism underlying the above changes in absorption and emission spectra is based on the chemical activation of the initially dormant fluorophore through a conjugation break via Michael addition reaction of thiol to the cyclobutene ring of the squaraine moiety. The chemical reaction of thiol towards **Sq** was confirmed by ESI mass spectrometry. The mass spectrum of **Sq** in presence of hexanethiol showed a peak at m/z 584.3312 corresponding to the mass of **Sq**-hexanethiol adduct (**Figure 2.8c**).

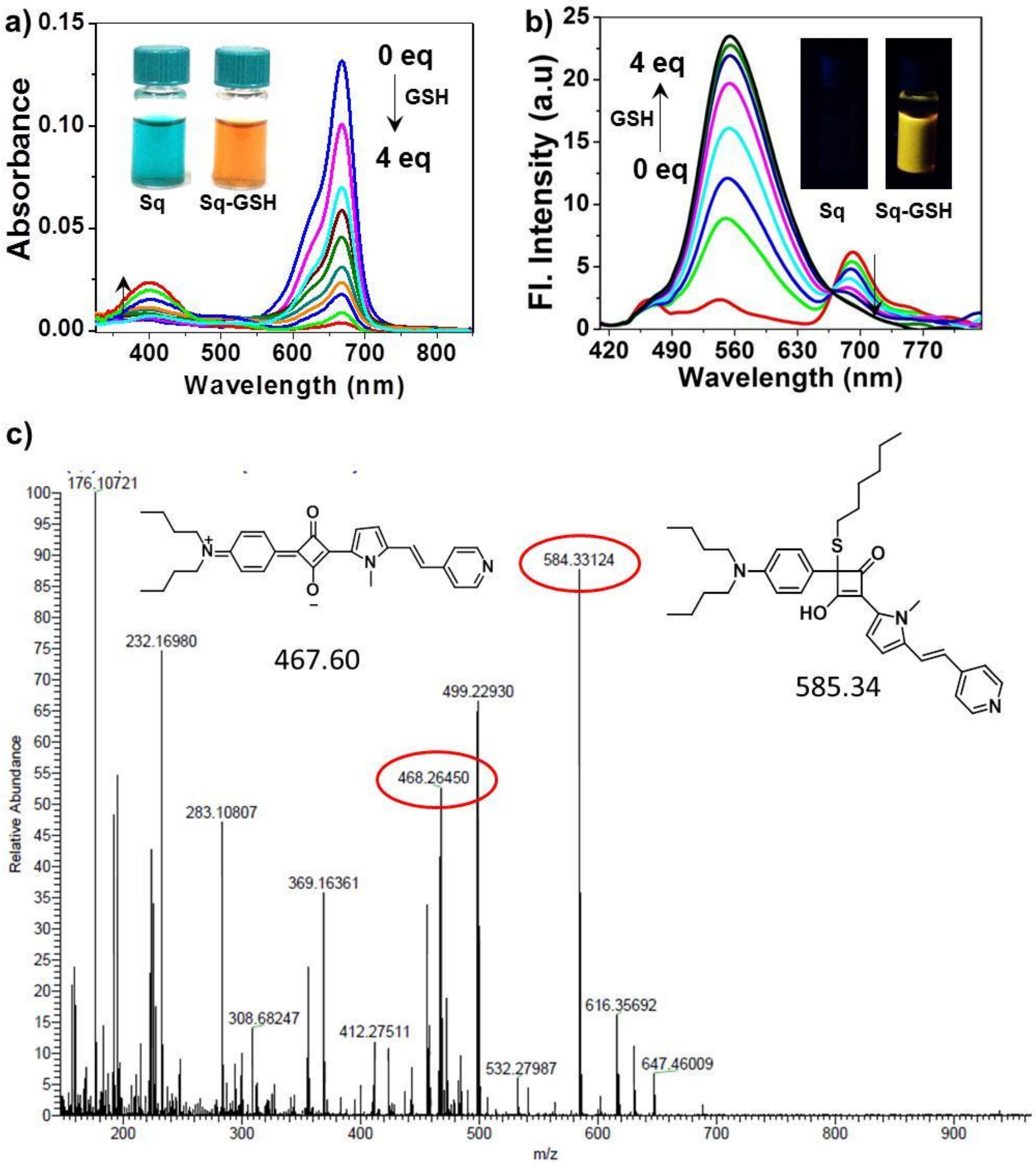

Figure 2.8. a) UV-Vis absorption and b) emission spectral changes of **Sq** with increasing concentrations of GSH (0-4 eq.). Inset: photographs showing the visual color (a) and fluorescence (b) changes of **Sq** in the absence (left) and in the presence (right) of GSH. Fluorescence changes were detected under UV illumination at 365 nm. c) High Resolution Mass Spectrum corresponding to **Sq**-hexanethiol adduct (m/z 584.3312) in 80% phosphate buffer, pH 7.4-CH_3CN buffered solvent mixture.

2.3.3. Sensitivity and Selectivity Studies

The detection response of the probe towards GSH has been studied over a wide range of concentration varying from 5.0 × 10^{-7} – 5.0 × 10^{-4} M as indicated in

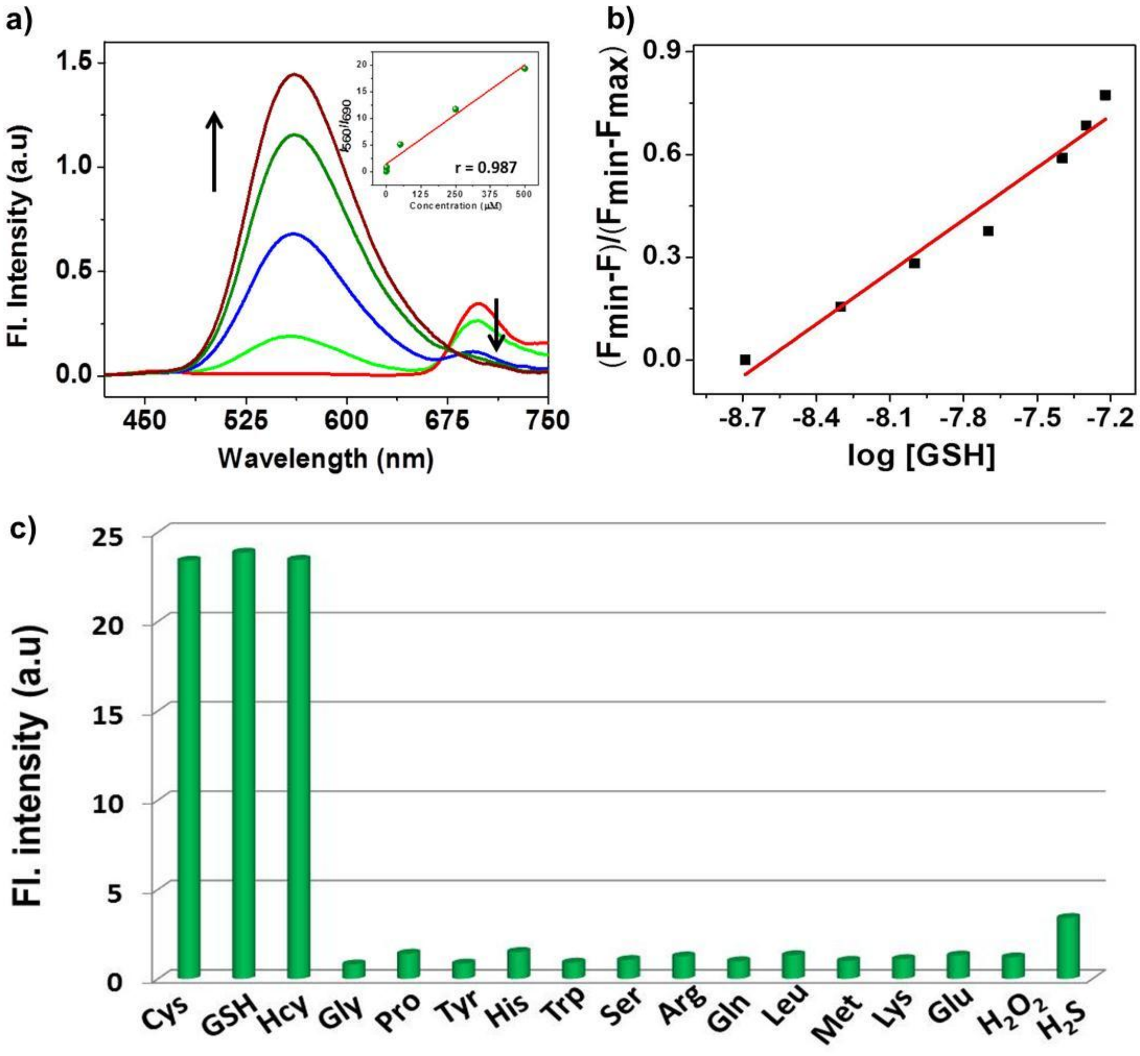

Figure 2.9. a) Fluorescence responses of **Sq** (6 µM, 80% phosphate buffer, pH 7.4-CH_3CN, λ_{ex} @ 400 nm) towards increasing GSH concentrations. Inset shows the linear relation of **Sq** towards incremental amounts of GSH. b) Linear plot showing the fluorescence intensity of **Sq** at 560 nm as a function of incremental concentrations of GSH, normalized between the minimum fluorescence intensity, recorded at zero eq. of GSH, and the maximum fluorescence intensity, recorded at [GSH] = 6 x 10^{-8} M. c) Fluorescence responses of **Sq** (2 µM, 80% phosphate buffer, pH 7.4-CH_3CN, λ_{ex} @ 400 nm) toward various amino acids (AA), H_2O_2 and H_2S. [AA] = 20 µM, [H_2O_2] = 20 µM, [H_2S] = 20 µM, [Cys] = 2 µM, [Hcy] = 2 µM, [GSH] = 2 µM.

Figure 2.9a. The sensitivity of the probe was then investigated by the fluorescence response of **Sq** with increasing concentrations of GSH. A typical calibration plot showed a linear increase in the fluorescence intensity of **Sq** with GSH concentration with a correlation coefficient of 0.984, achieving a detection limit as low as 2 nM (**Figure 2.9b**). The selectivity of the probe was evaluated towards other biologically relevant amino acids, H_2O_2 and H_2S (**Figure 2.9c**). It can be seen that only GSH, cysteine and homocysteine induced a fluorescence response while no such detectable signal was observed even with excess quantities (10 eq.) of other analytes. These results reveal the potential of **Sq** for measurement of intracellular redox state without interference from other biologically relevant analytes.

2.3.4. Reversibility and Kinetic Studies

The probe exhibited a reversible interaction with thiols as evident from the response of **Sq** with GSH and H_2O_2 (**Figure 2.10a**). Addition of H_2O_2 to **Sq** restored the NIR emission of the dye with simultaneous quenching of the 560 nm emission which could be repeated for several cycles (**Figure 2.10b**). This observation implies that addition of H_2O_2 to **Sq**-GSH adduct causes the oxidation of GSH to its oxidized form, glutathione disulphide (GSSG) which thereby releases the molecule free for further sensing of GSH. We then examined the response velocity of **Sq** towards GSH by monitoring the emission intensity at 560 nm as a function of time under the pseudo first order conditions. The time course of fluorescence response of **Sq** in presence of GSH is shown in **Figure 2.10c**. It is noteworthy that the reaction was completed within 50 seconds ($k_{obs} = 7.0 \times 10^{-2}\ s^{-1}$) implying the fast response of the probe towards GSH and thereby demonstrating its capability for real time detection of thiols in biological specimens (**Figure 2.10d**).

2.3.5. Photostability and Cytocompatibility Studies

Photostability of the probe is an important criterion for imaging application. Exposure of the molecule at 385 nm over a period of 15 minutes revealed that **Sq** is photostable (**Figure 2.11a**). Encouraged by the outstanding features of the probe, its suitability for evaluation of redox imbalance in biological systems was

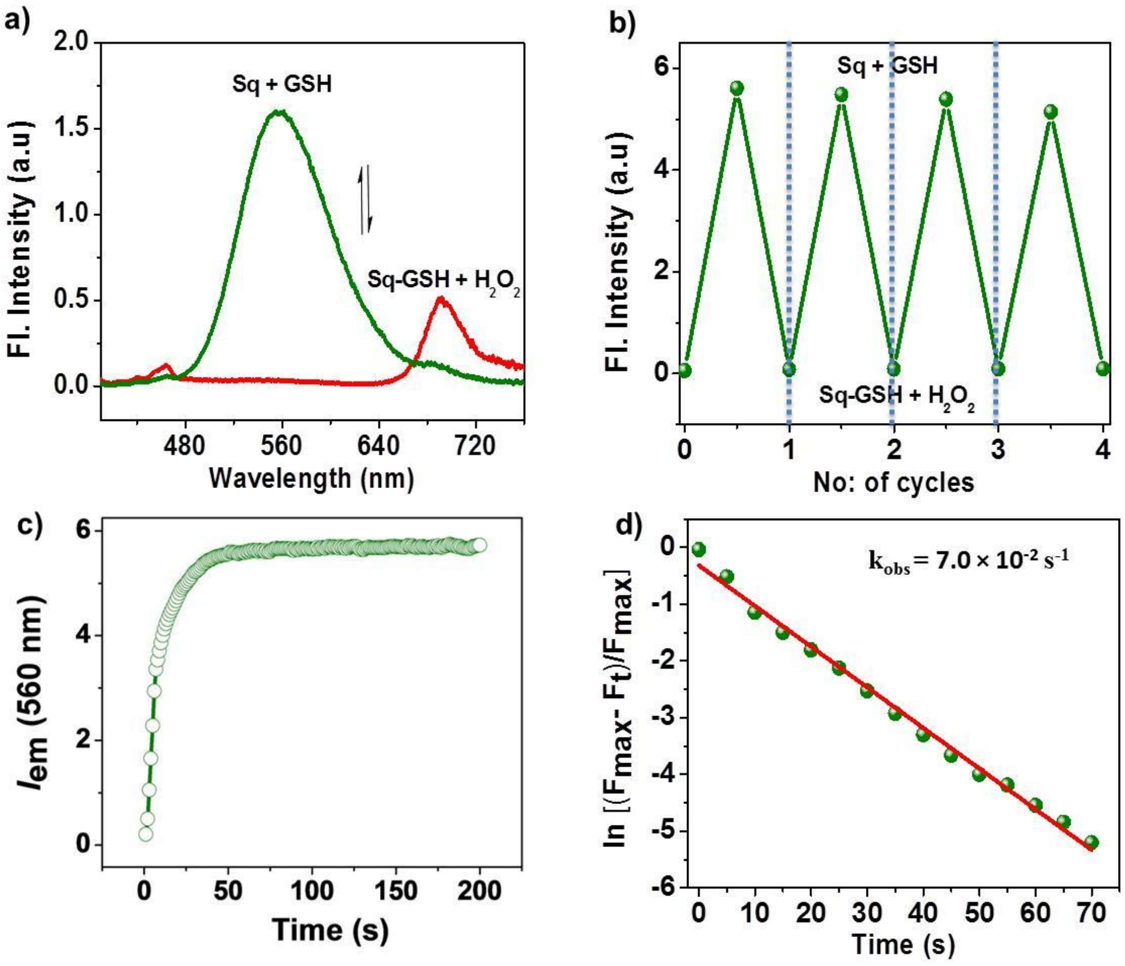

Figure 2.10. a) Fluorescence responses of **Sq**-GSH adduct in the presence and absence of H_2O_2. b) Fluorescence response of **Sq** at 560 nm with alternative addition of GSH and H_2O_2. c) Time dependent fluorescence enhancement profile of **Sq** (λ_{em}@ 560 nm) in presence of 100 eq. of GSH. d) Pseudo-first order kinetic plot of the reaction of **Sq** (2 μM, 80% phosphate buffer, pH 7.4-CH_3CN) towards GSH (100 eq.) at 560 nm (λ_{ex} @ 400 nm). The best fitting gives the observed first-order rate constant (k_{obs}) to be 7.00 × 10^{-2} s^{-1}. All experiments were performed using 2 μM **Sq** in 20% acetonitrile/phosphate buffer (25 mM, pH 7.4). The emission spectra were obtained by excitation at 400 nm.

then investigated. Prior to cell tests, 3-(4,5-dimethylthiazol-2-yl)-2,5-diphenyltetrazolium bromide (MTT) assay was performed to quantify the cytotoxicity of the probe (**Figure 2.11b**). In the MTT assay, HepG2 and 3T3L1 cells were treated with varying concentrations of the probe (1 µM to 50 µM) for 24 h. The results reveal that the probe possessed high cell viabilities among all the tested concentrations suggesting that the probe can be safely applied to culture cells under standard experimental conditions. Owing to the favourable biocompatible characteristics of **Sq**, the intracellular uptake and distribution of **Sq** in cancer cells was evaluated using fluorescence microscopy. Incubation of HepG2

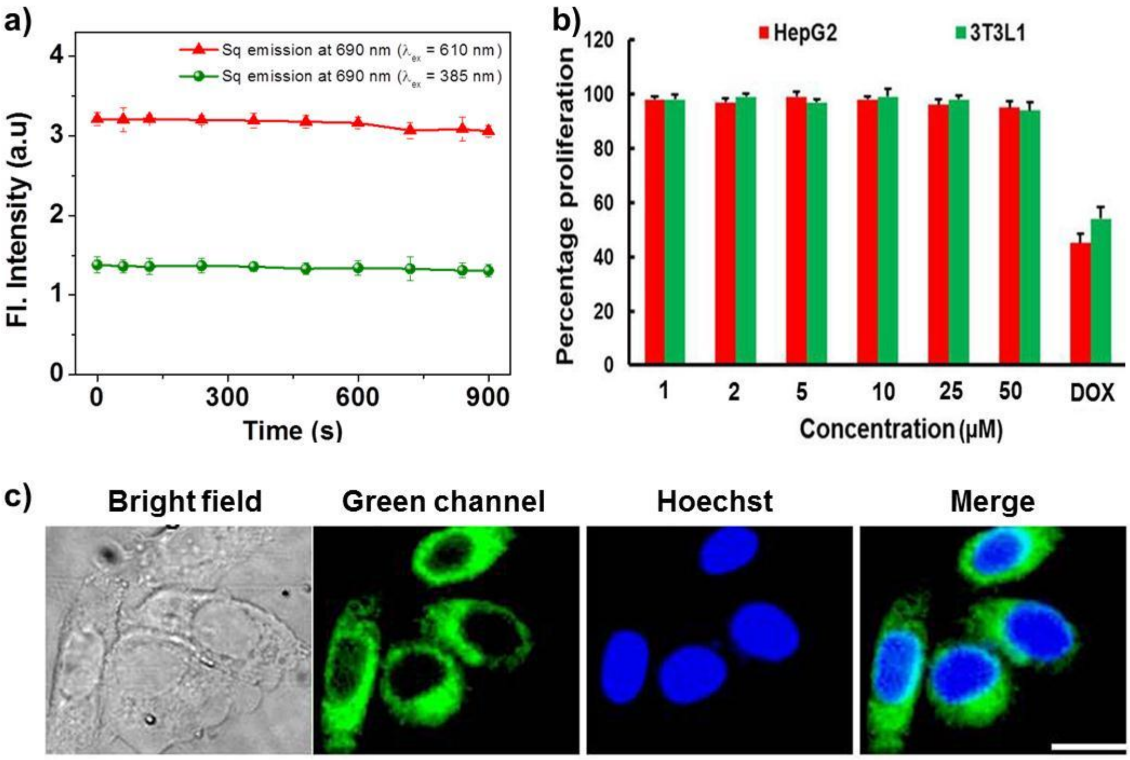

Figure 2.11. a) Time dependent fluorescence intensity of **Sq** at 690 nm in 80% phosphate buffer, pH 7.4-CH_3CN upon excitation at 385 nm and 610 nm. b) Cytotoxicity evaluation using MTT assay with cancer (HepG2) and normal (3T3L1) cells treated with **Sq** dye (1 µM to 50 µM) for 24 h where doxorubicin (1 µM) was used as positive control. Data are the mean standard deviation (SD) of three independent experiments. c) Fluorescence microscopic images for intracellular localization of **Sq** in HepG2 cells treated with 10 µM **Sq** and imaged after counterstaining with Hoechst 33342.

cells with **Sq** produced significant green fluorescence in the extranuclear environment suggestive of the excellent membrane permeability and intracellular localization of the probe. Co-staining studies with Hoechst 33342 revealed that fluorescence signals from **Sq** is mainly localized in the cytosolic regions with much little or no fluorescence from the nuclei (**Figure 2.11c**). These results make **Sq** a suitable candidate for the estimation of cytoplasmic GSH concentrations inside the cells.

2.3.6. *In Vitro* Response of Sq towards Biological Thiols

The thiol specificity of the probe in cellular environment was demonstrated with HepG2 cells in the presence and absence of a GSH blocking agent, *N*-ethylmaleimide (NEM) and GSH inducing agent α-lipoic acid (LPA). As shown in **Figure 2.12a**, the cells displayed strong green fluorescence and weak red fluorescence on incubation with **Sq.** When the cells were pretreated with LPA for 24 h, a significant enhancement in the green fluorescence was observed with much less emission from the red channel (**Figure 2.12b**). Contrarily, cells pretreated with LPA followed by treatment with NEM generated weak green fluorescence and strong red emission (**Figure 2.12c**). Finally, cells pretreated with NEM alone produced a remarkable fluorescence in the red channel with much weaker signals from the green region (**Figure 2.12d**). The corresponding ratiometric pixel intensity ratios (G/R) obtained from the ratio images is shown in **Figure 2.12B**.

The practical applicability of the probe was illustrated by evaluating its potential for visualizing endogenous thiols in live cells. Since there is a marked increase in the GSH levels in cancer cells when compared to normal cells,[15,19] the first intention was to detect the thiol levels in a cancer and a normal cell which were chosen to be the HepG2 and 3T3L1 cells respectively. HepG2 cells incubated with **Sq** for 4 h exhibited a strong green emission and a weak red emission indicative of high levels of GSH in cancer cells (**Figure 2.13A**). Contrarily, 3T3L1 cells showed a dramatic decrease in the fluorescence intensity in the green channel with a substantial amplification in the red channel well correlating with the reduced levels of GSH in normal cells (**Figure 2.13B**). As shown in **Figure 2.13b**, the ratio of fluorescence pixel intensities at 560 and 690 nm (G/R) of **Sq** incubated with HepG2 and 3T3L1 cells were found to be 1.95 and 0.15 respectively, accounting for a 13 fold increase in the thiol level in HepG2 cells which demonstrates the successful discrimination of cancer cells from normal cells. Although cysteine and homocysteine have similar reactivities, their presence at relatively low concentrations inside the cells when compared to GSH levels, will not introduce much error in our measurements. Furthermore, **Sq** was exploited for

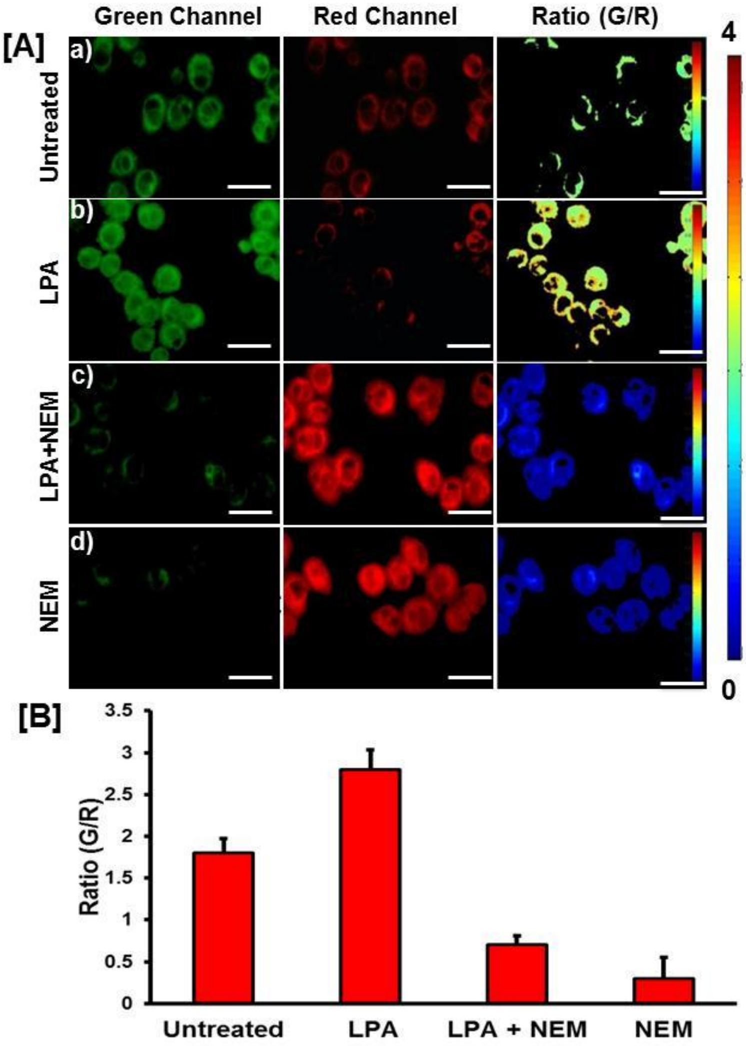

Figure 2.12. A) Fluorescence images of **Sq** labeled HepG2 cells either untreated (a) or pre-treated with (b) LPA (500 μM for 24h), (c) LPA (500 μM for 24h) + NEM (200 μM for 30 min) and (d) NEM (200 μM for 30 min) before labeling with **Sq**. Scale bar corresponds to 30 μm. Green channel at 540-580 nm and red channel at 640-700 nm. B) Average intensity ratios from ratio images of A.

the quantitative assessment of GSH in various living cells and compared those with a commercial GSH assay kit. Lysates from eight different cells with varying amounts of GSH were subjected to quantitative evaluation by monitoring the **Sq** emission at 560 nm and 690 nm. The GSH contents were then estimated from the value of I_{560}/I_{690} using a calibration graph (**Figure 2.13c**). **Figure 2.13d** shows a comparative plot of the GSH concentrations in different cell extracts using the probe and those obtained by the standard kit which reveals a substantially good agreement between the two results.

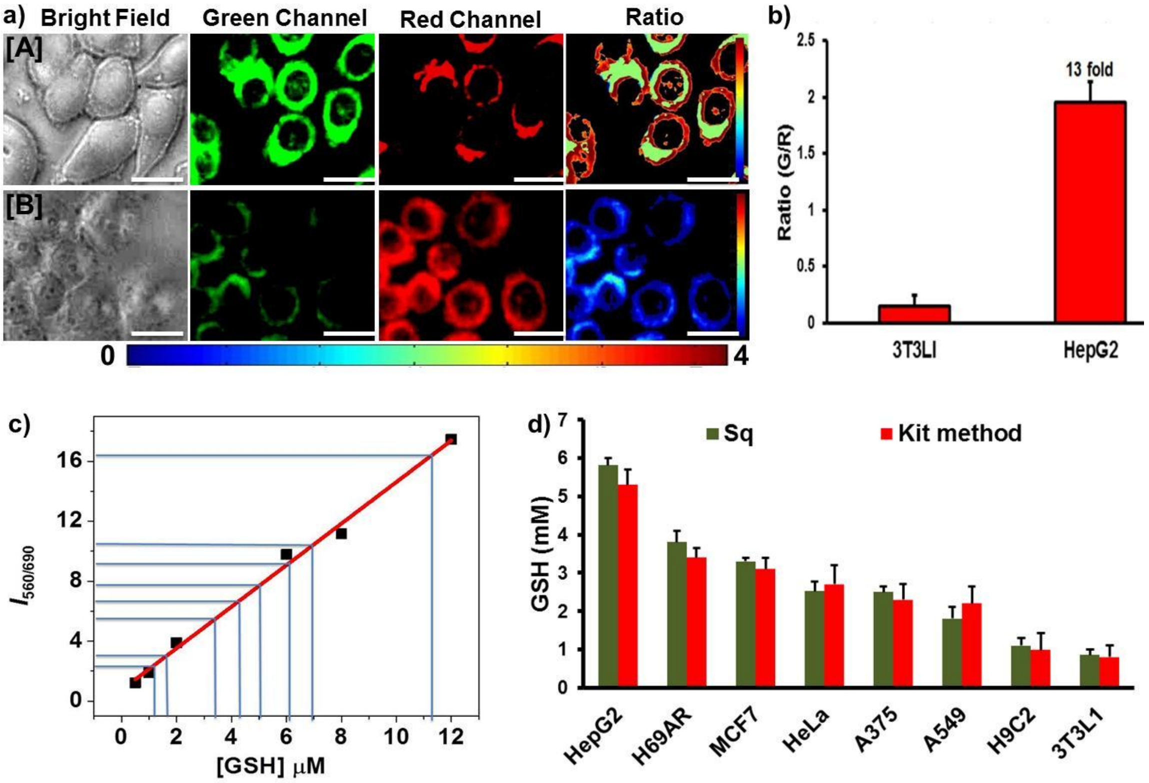

Figure 2.13. a) Fluorescence imaging of (A) HepG2 and (B) 3T3L1 cells with **Sq** dye (10 μM). Green channel at 540−580 nm; red channel at 640−700 nm. Ratio images generated from green/red channel using Matlab software. Scale bar corresponds to 30 μm. b) Average intensity ratios from ratio images of A and B. c) Plot of intensity of **Sq** emission at 560 nm against known concentrations of GSH. Concentration of unknown GSH in a specific volume of the lysate sample was calculated from the standard plot. d) Quantification of intracellular thiol from cell lysates using **Sq** dye and commercial GSH assay kit. Data are the mean SD of three independent experiments.

2.3.7. Apoptosis Monitoring via the Estimation of Intracellular GSH Status

Depletion of GSH level is a common feature of the apoptotic signaling cascade and the degree of GSH reduction is directly related to the progression of apoptosis.[18,47] Thus it was reasonable to anticipate that the intracellular redox state, primarily controlled by GSH, could be used to assay apoptosis. To explore this possibility,

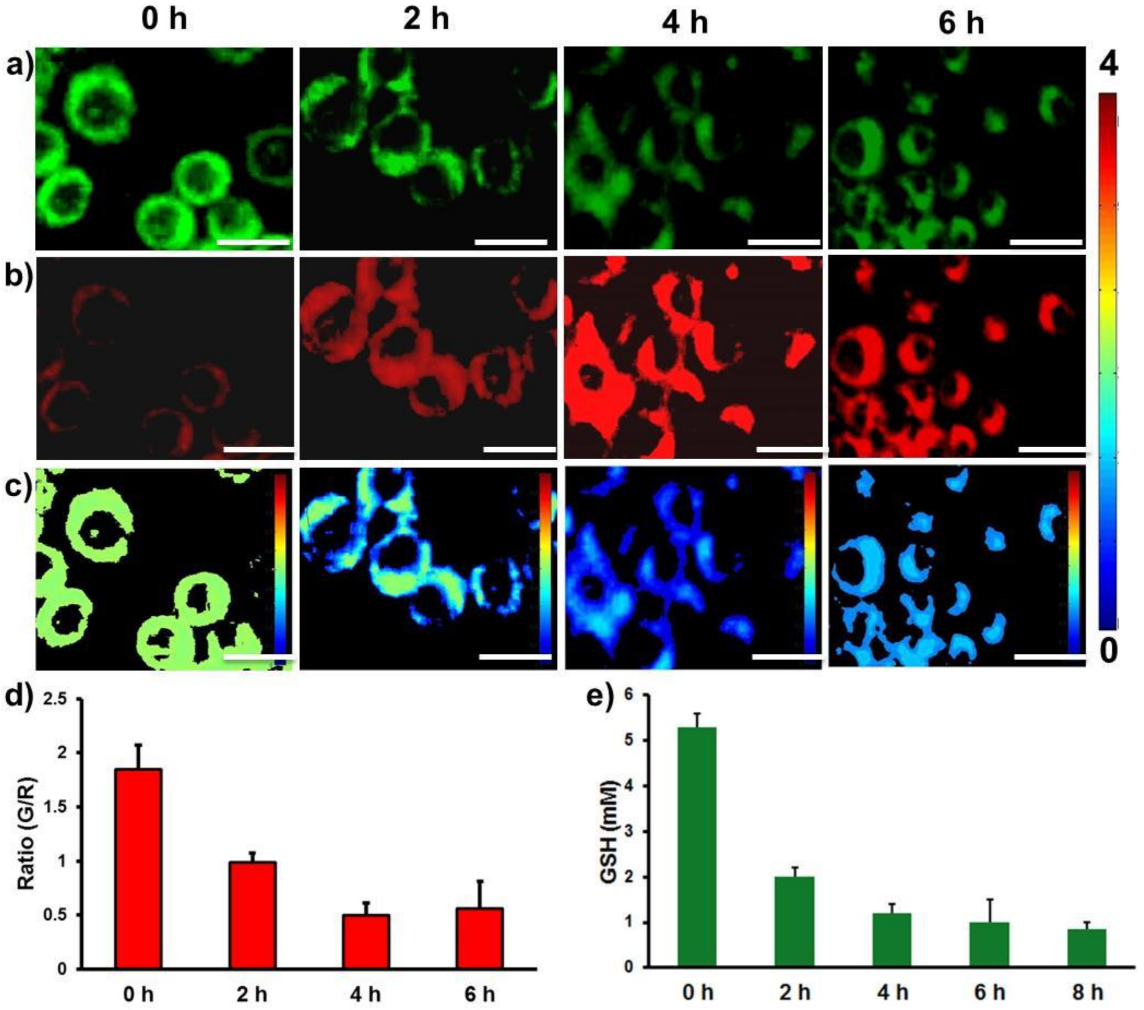

Figure 2.14. Real time fluorescence imaging of HepG2 cells with **Sq** dye (10 µM) after apoptotic induction with paclitaxel (10 µM) from 0 to 6 h. a) Green channel at 540−580 nm, b) red channel at 640−700 nm and c) ratio images generated from green/red channel using Matlab software. Scale bar corresponds to 30 µm. d) Average intensity ratios obtained from ratio images of c. e) Quantification of intracellular GSH from apoptotic cell lysates using **Sq** dye. Data are the mean SD of three independent experiments.

we aimed to investigate the cellular redox changes during the different stages of apoptosis. HepG2 cells were induced to undergo apoptosis by a well-known anticancer drug, paclitaxel and ratiometric changes in the GSH levels of **Sq** labeled cells were recorded at 0, 2, 4 and 6 h respectively (**Figure 2.14a-d**). The high levels of GSH indicated by an intense green emission and a weak red emission during the 0th h showed a noticeable drop in the green channel and a dramatic enhancement in the red channel at the 2nd h, resulting in approximately 1.9 fold decline in the emission ratio. The emission ratio further exhibited a drop by 1.98 fold during the 4th h resulting in a significant enhancement in the red channel and a noticeable decrease in the green channel. At the 6th h, no significant changes in the red or green emission was observed and the ratio of emission intensities reached

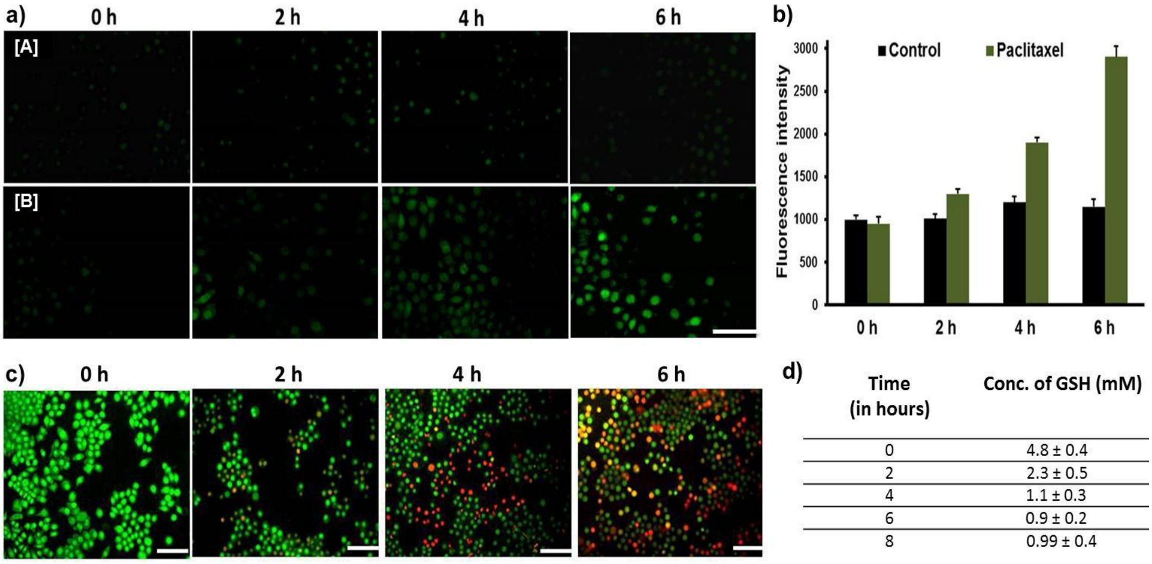

Time (in hours)	Conc. of GSH (mM)
0	4.8 ± 0.4
2	2.3 ± 0.5
4	1.1 ± 0.3
6	0.9 ± 0.2
8	0.99 ± 0.4

Figure 2.15. a) Fluorescence micrographs showing ROS generation in HepG2 cells untreated (A) and after administration with Paclitaxel (10 µM) (B) from 0 to 6 h. Scale bar corresponds to 50 µm. b) Average fluorescence intensity of dichlorofluorescein from untreated and paclitaxel administered HepG2 cells from 0-6 h measured using a fluorescence plate reader. Data represent mean standard deviation of three independent experiments. c) Fluorescence micrographs of apoptotic progression in HepG2 cells after administration with Paclitaxel (10 µM) from 0 to 6 h using acridine orange–ethidium bromide dual staining assay. Scale bar corresponds to 30 µm. d) Quantification of intracellular thiol from cell lysates during apoptosis using commercially available GSH assay kit. Data are the mean SD of three independent experiments.

more or less the same value as that observed in the 4th h. These results underpin the fact that GSH extrusion occurs at the onset of apoptosis, declines at a faster rate during the initial stages and attains a stable level, causing an increase in the level of reactive oxygen species and thereby facilitating efficient cell death. To reaffirm this point, the ROS generation in cells was investigated using 2’, 7’-dichlorofluorescein diacetate (DCFDA) assay for the same time intervals and found that GSH depletion causes an obvious increase in the level of ROS as shown in **Figure 2.15a** and **2.15b**. These changes in the GSH levels were found to be well correlating with the apoptotic progression as evidenced by the conventional apoptotic assay using acridine orange-ethidium bromide staining (**Figure 2.15c**). In order to gain a quantitative picture of the apoptotic process, we further monitored the emission responses of **Sq** towards apoptosis induced HepG2cell lysates during different intervals between 0-8 h (**Figure 2.14e**). At the onset, HepG2 cells possessed high levels of GSH amounting to about 5.30 ± 0.1 mM which decreased to 2.26 ± 0.2 mM after two hours. In another two hour, it dropped down to 1.26 ± 0.2 mM and the GSH level during the 6th and 8th h turned out to be 1.02 ± 0.3 mM and 0.96 ± 0.15 mM respectively. These results were also validated by the commercial GSH assay kit, reaffirming the reliability of the probe in estimating the intracellular GSH changes during apoptosis (**Figure 2.15d**). Collectively, these results imply the immense potential of **Sq** for the ratiometric detection of apoptosis on both qualitative and quantitative grounds.

2.4. Conclusion

In conclusion, a squaraine based fluorescent sensor has been successfully developed for the quantitative ratiometric fluorescence imaging of GSH, leading to the visualization of the redox process during apoptosis. The favourable attributes of high biocompatibility, excellent membrane permeability and fast response inspired us to utilize the **Sq** dye for detecting the intracellular GSH concentrations in live cells and cell extracts. The probe afforded a promising strategy for discriminating cancer cells from normal cells via the investigation of cellular redox status. Further applicability of the probe was elucidated by developing an easy and reliable method for the on-demand apoptotic progression assay in real-time by probing the role of GSH during various time spans of apoptosis on both semi-quantitative and quantitative grounds. These results open up a new non-invasive pathway for diagnosing apoptosis which is of prime importance in drug discovery and the effective follow-up of treatment responses.

2.5. Experimental Section

2.5.1. Materials and Methods

All chemical reagents, unless otherwise specified, were purchased from Sigma-Aldrich Co. All solvents were of reagent grade and were purchased from local companies. All solvents were dried and distilled prior to use by following standard procedures. ^{1}H NMR spectra were recorded on a Bruker 500 MHz FT-NMR (model: Advance-DPX 300) spectrometer at 25 °C. The chemical shift (δ) data and coupling constant (J) values were given in parts per million (ppm) and Hertz (Hz), respectively, unless otherwise mentioned. High-resolution mass spectra (HRMS) were recorded on a Thermo Scientific Exactive ESI-MS spectrophotometer.

2.5.2. Description of Experimental Techniques

2.5.2.1. UV/Vis Absorption and Emission Spectral Measurements

Electronic UV/Vis absorption spectra were recorded on a Shimadzu UV–2600 spectrophotometer and emission spectra were recorded on a SPEX–Fluorolog FL–1039 spectrofluorimeter with a 1 cm quartz cuvette. All experiments were carried out at 298 K.

2.5.2.2. Cell Culture

The human cancer cell lines HepG2 (hepatocellular carcinoma), H69AR (multidrug resistant lung cancer), HeLa (cervical cancer), MCF-7 (breast cancer), and A549 (lung adenocarcinoma) were obtained from American Type Culture Collection (ATCC, Manassas, VA, USA). A375 (malignant melanoma) and H9C2 (murine myoblast) cells were obtained from National Centre for Cell Science (NCCS, Pune, India). The fibroblast-like murine pre-adipocyte cell line 3T3L1 was gifted from Regional Cancer Centre (Thiruvananthapuram, India). Cells were maintained in DMEM with 10% FBS and under an atmosphere of 5% CO_2 at 37 ºC. Cells were cultured in glass bottom, 96-well black plates for imaging experiment 2 days prior to conduction of experiments.

2.5.2.3. Evaluation of Cytotoxicity using MTT Assay

The cell growth inhibition potential of **Sq** was measured against HepG2 and 3T3LI cells with the MTT (3-[4, 5-dimethylthiazol-2-yl]-2, 5-diphenyltetrazolium) assay as described previously.[48] Cytotoxicity was evaluated with cancer and normal cells treated with **Sq** dye (1 μM to 50 μM) for 24 h where doxorubicin (1 μM) was used as positive control. MTT assay is based on the cleavage of a tetrazolium salt by mitochondrial dehydrogenases in viable cells. Quantities of 100 μL of the cell suspension of 5×10^3 cells/well were seeded in a 96-well plate and 100 μL of **Sq** at various concentrations and a positive control (doxorubicin) was similarly added to the appropriate wells. The plates were then incubated for 24 h in a CO_2 incubator at 37 °C. After incubation, 20 μL MTT (5 mg/mL) was added to each well and incubation was continued for an additional 2 h. The insoluble formazan crystals formed were solubilised by the addition of 100 μL MTT lysis buffer (SDS and dimethyl formamide) followed by an incubation of 4 h and the absorbance was measured at 570 nm using a microplate spectrophotometer (BioTek, Power Wave XS). The proliferation rate was calculated as:

Proliferation [%] = $A_{sample} / A_{control} \times 100$

Inhibition [%] = 100 - % Proliferation

2.5.2.4. Fluorescence Imaging of Cells using Sq

GSH detection in HepG2 and 3T3L1 cells was performed by fluorescence microscopic technique. For fluorescence imaging, the culture medium was removed and the cells were washed with phosphate buffered saline (PBS pH 7.4) twice. 10 µM **Sq** was added and the adherent cells were washed with PBS three times to remove the excess probe from the medium. In order to reduce GSH concentration in HepG2 cells, the cells were pretreated with *N*-ethylmaleimide (200 µM) for 30 min, followed by incubation with **Sq** (10 µM) for 30 min and finally washed twice with PBS prior to imaging. To increase the concentration of GSH, the cells were pretreated with α-lipoic acid (500 µM) for a period of 24 h followed by treating with **Sq** (10 µM) which were then washed twice with PBS before imaging. Fluorescence imaging experiments were performed under an inverted fluorescence microscope using a green and red filter (Olympus 1X51, Singapore). The fluorescence was collected in the ranges of 540-580 nm (green) (λ_{ex}@480 nm) and 640−700 nm (red) (λ_{ex}@620 nm) respectively. Image processing was performed with Progress software and analysis was performed with Image J and Matlab 14 software, and the ratio of intensities was calculated. All data were expressed as mean ± standard deviation.

2.5.2.5. Subcellular Co-localization Imaging

For nuclear staining, HepG2 cells were treated with Hoechst 33342 in PBS (pH 7.4), 15 min prior to imaging. The cells were also co-stained with 10 µM **Sq** in 80% PBS (pH 7.4)/CH_3CN for 30 min and fluorescent images were acquired as described above. Images were collected in the ranges of 440-480 nm (blue) for Hoechst 33342 and 540-580 nm (green) for **Sq**.

2.5.2.6. Quantification of GSH from Cell Lysates

Estimation of the intracellular GSH was performed with the cell lysates of cancer and normal cells. Cell lysates were prepared as described elsewhere,[48] with modifications. Briefly, cells were plated onto 12-well plates (1 x 10^5 cells/well) on a 5% CO_2 incubator at 37 ºC. When the cells became confluent, they were trypsinized and washed with ice cold PBS (pH 7.4) thrice and lysed with PBS containing 1% Triton-X with rigorous vortexing. The supernatant was collected by centrifugation at 10,000 rpm for 5 min and the concentration of GSH in the cell lysates was measured with a fluorimeter at an excitation wavelength of 400 nm and an emission wavelength of 560 nm after adding **Sq**. The same has been performed by a commercial GSH assay kit (ApoGSH Glutathione detection kit, Biovision, USA) which utilizes a non-fluorescent dye, monochlorobimane, which upon interaction with thiols form a fluorescent adduct (λ_{em} = 461 nm) and is capable of detecting GSH ranging from micromolar to millimolar level. Cell lysates were prepared following the same procedure for the estimation of GSH during time lapsed stages of apoptosis also.

2.5.2.7. Detection of Intracellular ROS by DCFDA Assay

DCFDA assay is a fluorometric microplate assay used for the detection of oxidative stress by detecting oxidation of 2',7'-dichlorofluorescin diacetate (DCFDA) into the highly fluorescent compound 2',7'-dichlorofluorescein (DCF) due to the presence of reactive oxygen species. HepG2 cells (1 x 10^5) were seeded onto 96-well plate and cultured overnight. Cells were then washed and treated with 10 µM paclitaxel. After giving a cell wash, cells were incubated with 10 µM DCFDA reagent. Subsequently, cells were washed twice and fluorescence imaging experiments were carried out under an inverted fluorescence microscope. Images were collected in the range of 500-540 nm region under an excitation wavelength of 485 nm.

2.5.2.8. Acridine Orange-Ethidium Bromide Staining for Apoptosis

Evaluation of apoptosis after administration of Paclitaxel (10 µM) from 0 to 6 h using acridine orange–ethidium bromide staining was performed as described previously.[49] Cells were observed under an inverted fluorescence microscope using a FITC filter (Olympus 1X51, Singapore) to view apoptotic or non-apoptotic cells. Apoptotic cells will change the color from green to yellow/red, which is associated with other apoptotic features such as the presence of apoptotic bodies, damaged cell membrane, and nuclear condensation.

2.5.2.9. Fluorescence Imaging of HepG2 Cells during Apoptosis using Sq

The culture medium was removed and the cells were washed with PBS (pH 7.4) twice prior to fluorescence imaging. Apoptosis was induced in HepG2 cells by administration of 10 µM paclitaxel followed by incubation with 10 µM **Sq**. The adherent cells were washed three times with PBS (pH 7.4) to remove excess probes from the medium and fluorescence microscopic images were acquired during different time intervals in a similar manner as described above.

2.5.3. Synthesis and Characterization

Synthesis of (E)-4-2-(1-methyl-1H-pyrrol-2-yl)vinyl)pyridine (14)

To a solution of sodium hydride (1.08 g, 45 mmol) in dry DMF (20 mL), 4-methylpyridine (2.79 g, 30 mmol) was added dropwise followed by stirring at 60 °C under argon atmosphere. After 2 h, a solution of *N*-methylpyrrole-2-carbaldehyde (3.27 g, 30 mmol) in 10 mL DMF was added dropwise and the reaction mixture was refluxed for 8 h. The reaction mixture was then cooled and poured into crushed ice. The yellow precipitate formed was then filtered and finally dried. Yield: 70%; mp. 132 °C; ^{1}H NMR (500 MHz, $CDCl_3$, TMS) δ (ppm): 8.51 (d, 2H, Ar-*H*), 7.26 (d, 2H, Ar-*H*), 7.16 (d, J = 16 Hz, 1H, vinylic-*H*), 6.74 (d, J = 16 Hz, 1H, vinylic-*H*), 6.67 (d, 1H, Ar-*H*), 6.56 (d, 1H, Ar-*H*), 6.16 (d, 1H, Ar-*H*), 3.71 (s, 3H); ^{13}C NMR (125 MHz, $CDCl_3$) δ (ppm): 149.78, 145.48, 130.90, 125.06, 123.30, 122.24, 121.31, 120.28, 108.84, 34.23. HRMS calculated for $C_{12}H_{12}N_2$ (M^+): 184.10, found: 185.10.

Preparation of *N, N*-dibutylaniline (16)

To a solution of aniline (5.58 g, 60 mmol) and sodium carbonate (19.08 g, 180 mmol) in dry butanol (80 mL) under argon atmosphere, butylbromide (20.55 g, 150 mmol) and iodine (200 mg) were added. After refluxing for 24 h, the reaction mixture was cooled and the solvent was removed by reduced pressure. The residue obtained was suspended in water and extracted with dichloromethane. The organic layer was separated, washed with brine, dried over anhydrous Na_2SO_4 and concentrated to give a crude product which was further purified by column chromatography over silica gel (100-200 mesh) using 5% ethyl acetate/hexane to give the desired product as a light yellow colored liquid. Yield: 90%; ^1H NMR (500 MHz, $CDCl_3$, TMS) δ (ppm): 7.22 (t, 2H, Ar-*H*), 6.65 (d, 2H, Ar-*H*), 6.59 (d, 1H, Ar-*H*), 3.36 (t, 4H), 1.57 (m, 4H), 1.36 (m, 4H), 0.95 (t, 6H); ^{13}C NMR (125 MHz, $CDCl_3$) δ (ppm): 149.80, 129.61, 121.94, 114.32, 53.46, 30.12, 20.39, 13.82; HRMS calculated for $C_{14}H_{23}N$ (M^+): 205.34, found: 205.45.

Preparation of 3-*N,N*-(dibutylamino)phenyl,4-hydroxy-3-cyclobutene-1,2-dione (17)

Squaryl chloride (2 g, 13.2 mmol) and *N*, *N*-dibutyl aniline derivative (4.2 g, 13.24 mmol) were dissolved in 50 mL dry benzene and refluxed for 6 h. The reaction mixture was cooled and poured into ice water (500 mL). The two layers were separated. The organic layer was washed with water (250 mL), dried and evaporated under vacuum. The residue was dissolved in a mixture of acetic acid (20 mL), hydrochloric acid (1 mL) and water (20 mL). This mixture was refluxed for 2 h, and cooled to room temperature. After cooling to room temperature, the solid product (**17**) was isolated by filtration, washed with ether and dried. Yield: 80%; mp. 225-228 °C; ^1H NMR (500 MHz, $CDCl_3$, TMS) δ (ppm): 7.83-7.86 (d, 2H, Ar-*H*), 6.73-6.75 (d, 2H, Ar-*H*), 3.38 (t, 4H), 1.28-1.49 (m, 8 H), 0.91 (t, 6 H); ^{13}C NMR (125 MHz, $CDCl_3$) δ (ppm): 194.10, 173.55, 128.42, 113.01, 40.11, 29.01, 20.02, 14.20; HRMS calculated for $C_{18}H_{23}NO_3$ (M^+): 301.38, found: 301.72.

Synthesis of Squaraine Dye, Sq

Squaraine dye, **Sq** was synthesized by the condensation reaction of (*E*)-4-2-(1-methyl-1*H*-pyrrol-2-yl)vinyl)pyridine (**14**) (184 mg, 1 mmol) with the semi-squaraine derivative of *N,N*-dibutyl aniline, **17** (301 mg, 1 mmol) in 1:1 *n*-butanol/benzene mixture (80 mL) under azeotropic conditions (**Scheme 2.4**). After refluxing for 10 h, the reaction mixture obtained was cooled followed by the removal of the solvents. The crude product was thus precipitated from petroleum ether, filtered and redissolved in $CHCl_3$. The crude product obtained was purified by column chromatography over silica gel (100-200 mesh) using 3% methanol/dichloromethane**.** Yield 40%; ^{1}H NMR (500 MHz, $CDCl_{3,}$ TMS) δ (ppm): 8.60 (d, 2H, Ar-*H*), 8.33 (d, 2H, Ar-*H*), 7.82 (d, 1H, Ar- *H*), 7.36 (d, 2*H*, Ar-*H*), 7.25 (d, *J* = 15.5 Hz, 1H, vinylic-*H*), 7.12 (d, 1H, *J* = 16 Hz, vinylic-*H*), 6.91 (d, 1H, Ar-*H*), 6.72 (d, 2H, Ar-*H*), 4.34 (s, 3H), 3.45 (t, 4H), 1.65 (t, 8H), 0.99 (t, 6H); ^{13}C NMR (125 MHz, $CDCl_3$) δ (ppm): 184.29, 174.27, 164.89, 153.78, 150.32, 144.58, 143.47, 133.35, 131.25, 123.70, 120.86, 119.73, 119.19, 114.24, 113.65, 112.72, 112.64, 51.32, 34.23, 29.69, 29.63, 20.22, 13.85; HRMS calculated for $C_{30}H_{33}N_3O_2$ (M^+): 467.26, found: 468.26.

2.6. References

[1] Hotchkiss, R. S.; Strasser, A.; McDunn, J. E.; Swanson, P. E. *New Engl. J. Med.* **2009**, *361*, 1570.

[2] Carson, D. A.; Ribeiro, J. M. *Lancet* **1993**, *341*, 1251.

[3] Herzenberg, L. A.; De Rosa, S. C.; Dubs, J. G. ; Roederer, M.; Anderson, M. T.; Ela, S. W.; Deresinski, S. C. *Proc. Natl. Acad. Sci. U.S.A.* **1997**, *94*, 1967.

[4] Refsum, H.; Ueland, P. M.; Nygard, O.; Vollset, S. E. *Annu. Rev. Med.* **1998**, *49*, 31. (d) Haunstetter, A.; Izumo, S. *Circ. Res.* **1998**, *82*, 1111.

[5] Seshadri, S.; Beiser, A.; Selhub, J.; Jacques, P. F.; Rosenberg, I. H.; Agostino, R. B. D'.; Wilson, P. W. F. *New Engl. J. Med.* **2002**, *346*, 476.

[6] Wu, Y.; Xing, D.; Luo, S.; Tang, Y.; Chen, Q. *Cancer Lett.* **2006**, *235*, 239.

[7] Edgington, L. E.; Berger, A. B.; Blum, G.; Albrow, V. E.; Paulick, M. G.; Lineberry, N.; Bogyo, M. *Nat. Med.* **2009**, *15*, 967.

[8] Boeneman, K.; Mei, B. C.; Dennis, A. M.; Bao, G.; Deschamps, J. R.; Mattouss, H.; Medintz, I. L. *J. Am. Chem. Soc.* **2009**, *131*, 3828.

[9] Dai, N.; Guo, J.; Teo, Y. N.; Kool, E. T. *Angew. Chem. Int. Ed.* **2011**, *50*, 5105.

[10] Nguyen, Q. D.; Lavdas, I.; Gubbins, J.; Smith, G.; Fortt, R.; Carroll, L. S.; Graham, M. A.; Aboagye, E. O. *Clin. Cancer Res.* **2013**, *19*, 3914.

[11] Petrovsky, A.; Schellenberger, E.; Josephson, L.; Weissleder, R.; Bogdanov, A. *Cancer Res.* **2003**, *63*, 1936.

[12] van Tilborg, G. A. F.; Mulder, W. J. M.; Chin, P. T. K.; Storm, G.; Reutelingsperger, C. P.; Nicolay, K.; Strijkers, G. J. *Bioconjugate Chem.* **2006**, *17*, 865.

[13] Loannou, Y. A.; Chen, F. W. *Nucl. Acids Res.* **1996**, *24*, 992.

[14] Walker, P. R.; Leblanc, J.; Smith, B.; Pandey, S.; Sikorska, M. *Methods* **1999**, *17*, 329.

[15] Matassov, D.; Kagan, T.; Leblanc, J.; Sikorska, M.; Zakeri, Z. *Mol Biol.* **2004**, *282*, 1.

[16] Marchetti, P.; Decaudin, D.; Macho, A.; Zamzami, N.; Hirsch, T.; Susin, S. A.; Kroemer, G. *Eur. J. Immunol.* **1997**, *27*, 289.

[17] Coffey, R. N. T.; Watson, R. W. G.; Hegarty, N. J.; Neill, A. O'; Gibbons, N.; Brady, H. R.; Fitzpatrick, J. M. *Cancer* **2000**, *88*, 2092.

[18] Circu, M. L.; Aw, T. Y. *Free Radic Res.* **2008**, *42*, 689.

[19] Hwang, C.; Sinskey, A. J.; Lodish, H. F. *Science* **1992**, *257*, 1496.

[20] Franco, R.; Panayiotidis, M. I.; Cidlowski, J. A. *J Biol Chem.* **2007**, *282*, 30452.

[21] Ortega, A. L.; Mena, S.; Estrela, J. M. *Cancers* **2011**, *3*, 1285.

[22] Armstrong, J. S.; Steinauer, K. K.; Hornung, B.; Irish, J. M.; Lecane, P.; Birrell, G. W.; Peehl, D. M.; Knox, S. J. *Cell Death Differ.* **2002**, *9*, 252.

[23] Fernandez, A.; Kiefer, J.; Fosdick, L.; McConkey, J. *J. Immunol.* **1995**, *155*, 5133.

[24] Franco, R.; Schoneveld, O. J.; Pappa, A.; Panayiotidis, M. I.; *Arch. Physiol. Biochem.* **2007**, *113*, 234.

[25] Tormos, C.; Chaves, F. J.; Garcia, M. J.; Garrido, F.; Jover, R.; O'Connor, J. E.; Iradi, A.; Oltra, A.; Oliva, M. R.; Saez, G. T. *Cancer Lett.* **2004**, *208*, 103.

[26] (a) Zhang, M.; Yu, M.; Li, F.; Zhu, M.; Li, M.; Gao, Y.; Li, L.; Liu, Z.; Zhang, J.; Zhang, D.; Yi, T.; Huang, C. *J. Am. Chem. Soc.* **2007**, *129*,10322. (b) Cho, D. G.; Sessler, J. L. *Chem. Soc. Rev.* **2009**, *38*, 1647. (c) Lee, M. H.; Yang, Z.; Lim, C.W.; Lee, Y. H.; Dongbang, S.; Kang, C.; Kim, J. S. *Chem. Rev.* **2013**, *113*, 5071.

[27] (a) Jung, H. S.; Chen, X.; Kim, J. S.; Yoon, J. *Chem Soc. Rev.* **2013**, *42*, 6019. (b) Yin, C.; Huo, F.; Zhang, J.; Martinez-Manez, R.; Yang, Y.; Lv, H; Li, S. *Chem. Soc. Rev.* **2013**, *42*, 6032. (c) Barbieri, A.; Bandini, E.; Monti, F.; Praveen, V. K.; Armaroli, N. *Top. Curr. Chem.* **2016**, *374*, 47.

[28] (a) de Silva, A. P.; Gunaratne, H. Q. N.; Gunnlaugsson, T. A.; Huxley, T. M.; McCoy, C. P.; Rademacher, J. T.; Rice, T. E. *Chem. Rev.* **1997**, *97,* 1515. (b) Hong, V.; Alexander, A. K.; Finn, M. G. *J. Am. Chem. Soc.* **2009**, *131*, 9986.

[29] (a) Wu J.; Liu, W.; Ge, J.; Zhang, H.; Wang, P. F. *Chem. Soc. Rev.* **2011**, *40*, 3483. (b) Zhai, D.; Lee, S. C.; Yun, S. W.; Chang, Y. T. *Chem. Commun.* **2013**, *49*, 7207. (c) Such, G. K.; Yan, Y.; Johnston, A. P. R.; Gunawan, S. T.; Caruso, F. *Adv. Mater.* **2015**, *27*, 2278.

[30] (a) Liu, Y.; Tian, Y.; Tian, Y.; Wang, Y.; Yang, W. *Adv. Mater.* **2015**, *27*, 7156. (b) Fernandez, A.; Vendrell, M. *Chem. Soc. Rev.* **2016**, *45*, 1182.

[31] Sippel T. O. *J. Histochem. Cytochem.*, **1981**, *29*, 314.

[32] Kand, D.; Kalle, A. M.; Varma S. J.; Talukdar P. *Chem. Commun.* **2016**, *48*, 2722.

[33] Wang, H.; Zhou, G.; Gai H.; Chen X. *Chem. Commun.* **2016**, *48*, 8341.

[34] Yin, J.; Kwon, Y.; Kim, D.; Lee, D.; Kim, G.; Hu, Y.; Ryu, J. H.; Yoon, J. *J. Am. Chem. Soc.* **2014**, *136*, 5351.

[35] He, L.; Yang, X.; Xu, K.; Lin, W. *Anal. Chem.* **2017**, *89*, 9567.

[36] Puente-Munoz, V.; Paredes, J. M.; Resa, S.; Vilchez, J. D.; Zitnan, M.; Miguel, D.; Giron, M. D.; Cuerva, J. M.; Salto, R.; Crovetto, L. *Sci. Rep.* **2019**, *9*, 1659.

[37] Yuan, L.; Lin, W.; Zhao, S.; Gao, W.; Chen, B.; He, L.; Zhu, S. *J. Am. Chem. Soc.* **2012**, *134*, 13510.

[38] (a) Ajayaghosh, A. *Acc. Chem. Res.* **2005**, *38*, 449. (b) Hewage, H. S.; Anslyn, E. V. *J. Am. Chem. Soc.* **2009**, *131*, 13099.

[39] (a) Sreejith, S.; Ma, X.; Zhao, Y. *J. Am. Chem. Soc.* **2012**, *134*, 17346. (b) Zhang, Y.; Yue, X.; Kim, B.; Yao, S.; Bondar, M. V.; Belfield, K. D. *ACS Appl. Mater. Interface* **2013**, *5*, 8710.

[40] (a) Gao, F.-P; Lin, Y.-X.; Li, L.-L.; Mayerhöffer, U.; Spenst, P.; J.-G. Su, J.-G.; Li, J.-Y.; Würthner, F.; Wang, H. *Biomaterials* **2014**, *35*, 1004. (b) Anees, P.; Sreejith, S.; Ajayaghosh, A. *J. Am. Chem. Soc.* **2014**, *136*, 13233. (c) Karpenko, I. A.; Collot, M.; Richert, L.; Valencia, C.; Villa, P.; Mely, Y.; Hibert, M.; Bonnet, D.; Klymchenko, A. S. *J. Am. Chem. Soc.* **2015**, *137*, 405–412.

[41] (a) Xu, Y.; Li, B.; Xiao, L.; Li, W.; Zhang, C.; Sun, S.; Pang, Y. *Chem. Comm.* **2013**, *49*, 7732. (b) Anees, P.; Sudheesh, K. V.; Jayamurthy, P.; Chandrika, A. R.; Omkumar, R. V.; Ajayaghosh, A. *Chem. Sci.* **2016**, *7*, 6808.

[42] (a) Johnson, J. R.; Fu, N.; Arunkumar, E.; Leevy, W. M.; Gammon, S. T.; Piwnica-Worms, D.; Smith, B. D. *Angew. Chem. Int. Ed.* **2007**, *46*, 5528. (b) Sun, W.; Guo, S.; Hu, C.; Fan, J.; Peng, X. *Chem. Rev.* **2016**, *116*, 7768.

[43] Zhang, D.; Zhao, Y.-X.; Qiao, Z.-Y.; Mayerhoffer, U.; Spenst, P.; Li, X.-J.; Wurthner, F.; Wang, H. *Bioconjugate Chem.*, **2014**, *25*, 2021–2029.

[44] Ros-Lis, J. V.; Garcia, B.; Jimenez, D.; Martinez-Manez, R.; Sanceno, F.; Soto, J.; Gonzalvo, F.; Valldecabres, M. C. *J. Am. Chem. Soc.* **2004**, *126*, 4064.

[45] Sreejith, S.; Divya, K. P.; Ajayaghosh, A. *Angew. Chem., Int. Ed.* **2008**, *47*, 7883.

[46] Anees, P.; Joseph, J.; Sreejith, S.; Menon, N. V.; Kang, Y.; Yu, S. W.-K.; Ajayaghosh, A.; Zhao, Y. *Chem. Sci.* **2016**, *7*, 4110.

[47] Franco, R.; Cidlowski, J. A. *Cell Death Differ.* **2009**, *16*, 1303.

[48] Wong, H. L.; Rauth, A. M.; Bendayan, R.; Manias, J. L.; Ramaswamy, M.; Liu, Z.; Erhan, S. Z.; Wu, X. Y. *Pharm. Res.* **2006**, *23*, 1574.

[49] Joseph, M. M.; Aravind, S. R.; George, S. K.; Pillai, R. K.; Mini, S.; Sreelekha, T. T. *J. Biomed. Nanotechnol.* **2014**, *10*, 3253.

Chapter 3

Enzyme Responsive Fluorescence-SERS Bimodal Probes for Multiplex Detection of Lung Cancer Biomarkers

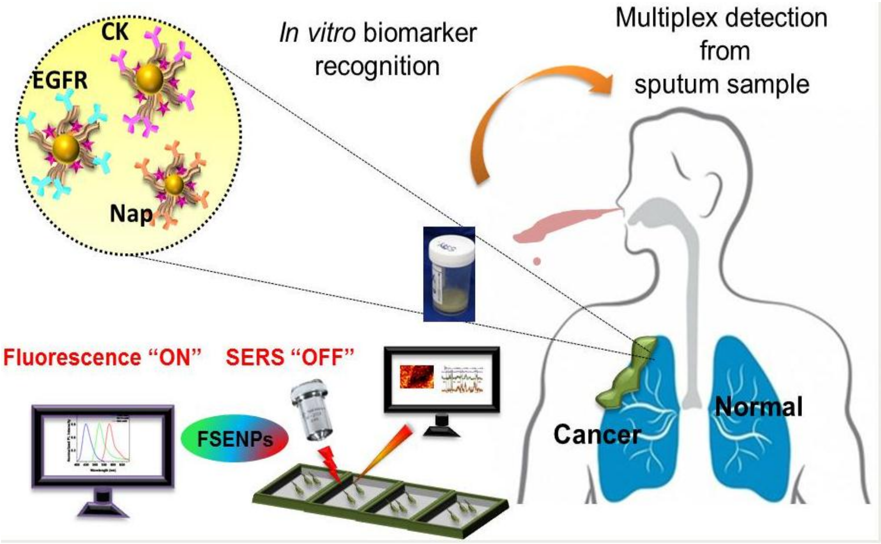

3.1. Abstract

Comprehensive profiling of multiple protein targets plays a critical role in the deeper understanding of specific disease conditions associated with high heterogeneity and complexity. Herein, the design and fabrication of smart programmable nanoarchitectures, which could integrate clinically relevant diagnostic modalities for the multiplexed detection of most prevalent panel of disease biomarkers present in lung cancer is presented. The multiplex nanoprobes were prepared by attaching dual-functional Raman active fluorogens onto spherical gold nanoparticles through a peptide linker, Phe-Lys-Cys (FKC) which is engineered with a cathepsin B (cathB) enzyme cleavage site. Presence of the cathB induces the scission of FKC upon homing into the cancer cells, resulting in the release of the initially latent fluorophores with a concomitant quenching of the surface enhanced Raman signal intensity, thereby realizing an 'on-off' switching *between the fluorescence and Raman modalities. The enzyme triggered switchable nanoprobes were utilized for the simultaneous detection of pathologically relevant lung cancer targets by tethering with specific antibody units. The multiplex-targeted multi-color coded detection capability of the antitags was successfully developed as a valid protein screening methodology which can address the unmet challenges in the conventional clinical scenario for the precise and early diagnosis of lung cancer.*

3.2. Introduction

The emergence of nanotechnology and nanoarchitectonics has paved way for the creation of smart functional materials that possess wide ranging applications in biology and medicine.[1] In this scenario, development of intelligent nanomaterials that serve as stimuli-responsive molecular devices to achieve specific biological functions remains as a long standing goal in biomedicine.[2,3] The ability to probe multiple protein targets in cell and tissue environment plays a decisive role in the accurate understanding of the function and regulation of many cellular events and in the profiling of heterogeneous disease states such as cancer. Recent research has shown that no single targeting motif is sufficient to provide adequate information required to fully characterize or identify a specific disease condition.[4,5] Thus, the development of highly sensitive techniques that can simultaneously recognize multiple biomarkers is of great relevance for the early diagnosis and management of diseases.[6-9] Lung cancer, one of the most leading causes of death worldwide is characterized by the upregulation of many proteins which makes its prognosis and diagnosis a challenging task. The currently available clinical methods which mainly rely on morphological changes, often fail to screen the early progress of the disease thereby leading to false positive and false negative results. In the present work, a highly sensitive screening method has been demonstrated for the mutiplex detection of lung cancer biomarkers which can address the limitations associated with the currently employed clinical techniques with great accuracy, which may help early detection and treatment.

In recent years, considerable efforts have been put forward towards the development of multiplexing diagnostic platforms in view of their unique advantages in terms of high-throughput screening capacity, improved working efficacy and overall cost effectiveness.[10-12] Although a number of techniques such as mass spectrometry and microarray based assays have been adopted for facilitating multiplexed analysis, most of them fail to provide a rapid, highly sensitive and accurate detection response.[13,14] In an effort to address these limitations, fluorescence and SERS techniques have transpired as frontline biosensing approaches, offering broad range analyte detection with high sensitivity and specificity.[15-23] Fluorescence based assays have gained significant attention due to its ability to analyze complex biological events with high spatial and temporal resolution.[24-28]

SERS platforms have recently appeared as a promising diagnostic tool for bioimaging applications with the advantages of high spectral specificity, excellent contrast and unique multiplexing potential.[29,30] The multiplexing ability of SERS encoded probes relies greatly on the narrow peakwidths and utilization of a single laser excitation line which confer distinct fingerprint spectral signatures and allows the identification of closely related targets in a complex biochemical environment.[31-33] Although SERS tags offer superior multiplexing capacity with single-cell sensitivity, it poses relatively low temporal resolution due to the slow imaging speed, thereby hindering the fast recognition of a large number of target biomarkers within a limited time frame.[34] Combination of these two techniques can integrate the advantages of both fluorescence and SERS, which can fill the gaps that may be created by the independent use of any one of these methodologies. Although conceptually impressive, these bimodal probes are still at a stage of infancy. The probes reported so far made use of silica nanoparticles to accommodate the fluorescent dyes and the Raman reporters, where the silica coating acts as a spacer to prevent the interference from each other. For instance, Yu *et al.*, reported the design of multifunctional fluorescent SERS probes comprising of silver nanoparticle modified silica spheres embedded with a fluorescent dye and Raman reporter for multiplexed detection applications (**Figure 3.1**).[35] The nanoparticles after modification with specific antibodies were utilized

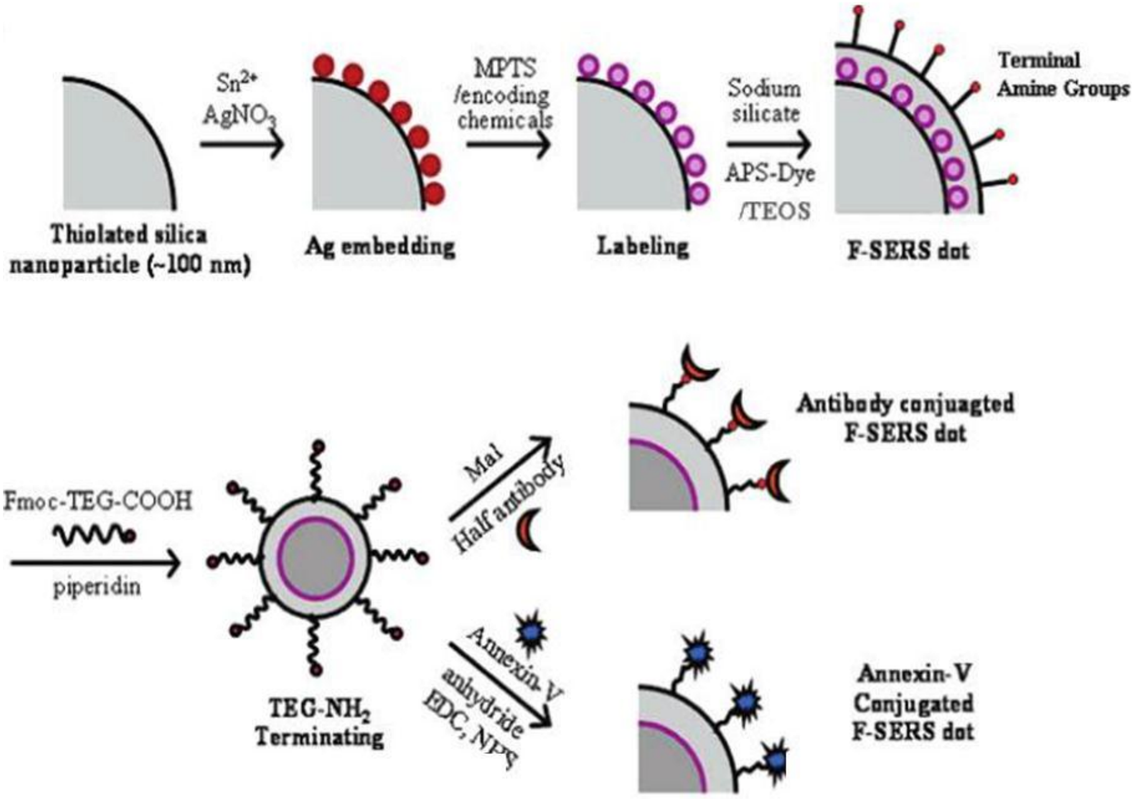

Figure 3.1. Schematic representation of the synthesis of silver nanoparticle modified silica spheres for bimodal imaging guided multiplexed detection applications.

for the detection of apoptosis through bimodal imaging channels which offered a simple, effective and reliable approach for the investigation of cellular events. Later, in 2009, the same group employed the same system for the simultaneous detection of CD34, Sca-1, and SP-C, the three proteins expressed in the bronchialveolar stem cells of murine lungs.[36]

In 2012, Wang and co-workers demonstrated the design and fabrication of a core-shell nanoarchitecture composed of silver nanoparticle/silica/titania ($Ag@SiO_2@mTiO_2$) hybrid for fluorescence/SERS bimodal imaging guided drug delivery (**Figure 3.2a** and **3.2b**).[37] The dye label, 4-mercaptopyridine present inside the nanoparticle served the role of Raman reporter which was separated from the fluorescent label, flavin mononucleotide through a silica shell. The mesoporous titania layer over the nanoparticle offered excellent loading of a chemotherapeutic agent (doxorubicin), thereby providing it with imaging and therapeutic properties. The *in vitro* cytotoxicity studies on cancer cells revealed a comparable or even better therapeutic performance by the nanoconstruct when compared against the free drug, attributed to the increased cellular accumulation of the probe (**Figure 3.2c**). This study presented the utility of a multifunctional nanosystem for rapid and multiplexed sensing assisted cancer therapy. Another study by Lee and colleagues utilized silica encapsulated gold nanoparticles for multiplexed imaging of cancer cells (**Figure 3.3a** and **3.3b**).[34]

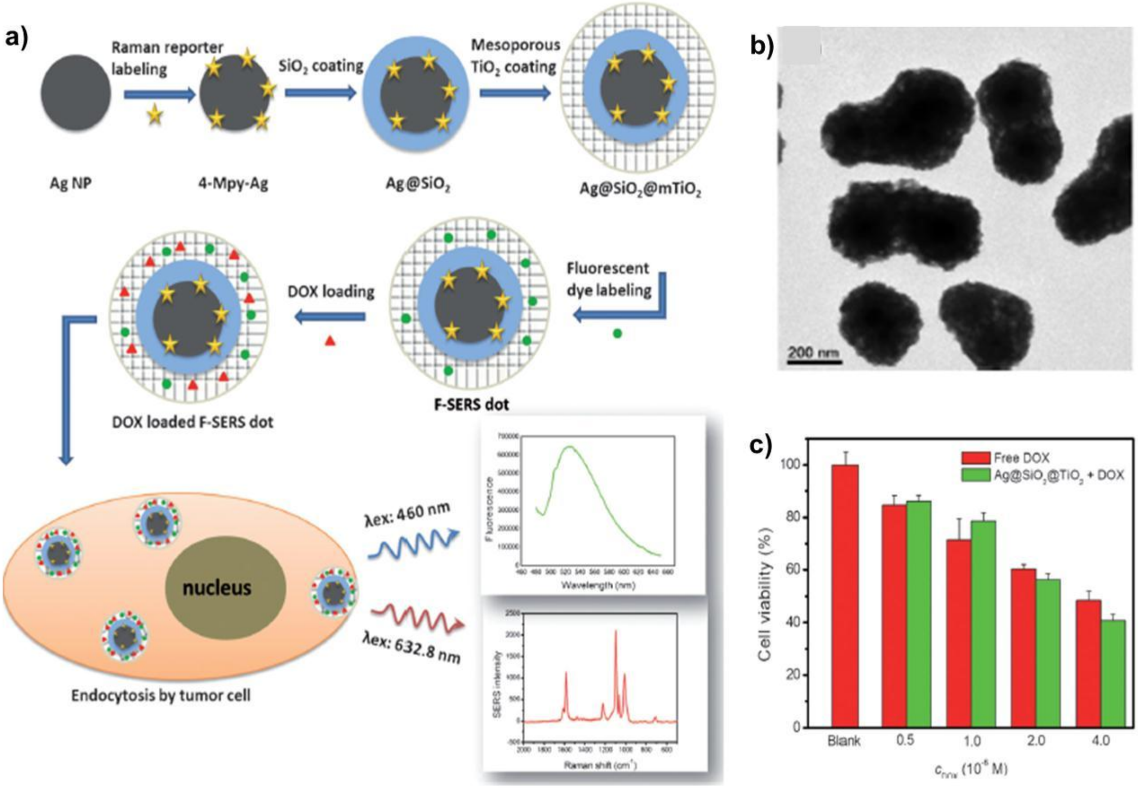

Figure 3.2. a) Schematic illustration of the preparation of drug loaded $Ag@SiO_2@mTiO_2$ core-shell nanoprobe. b) TEM image of $Ag@SiO_2@mTiO_2$ nanoparticles. c) Cytotoxic evaluation of DOX loaded $Ag@SiO_2@mTiO_2$ and free DOX on MCF7 cells.

The gold nanoparticles were labeled with Raman reporters and organic fluorophores separated by a 20 nm silica shell to account for interference free SERS and fluorescence imaging. The nanoprobes were subsequently labeled with anti-CD24 and anti-CD44 antibodies to afford target specific imaging of cancer biomarkers in breast cancer cells (**Figure 3.3c**). Similarly, there have been a few other reports demonstrating the potential of fluorescence and SERS bimodal detection for disease screening applications.[38,39] However, a major challenge in multiplexed detection based on these dual modal probes stems from the complexity of fabrication especially in controlling the distance between the fluorophore and metal substrates and also in tuning the thickness of the silica spacer without compromising the efficacy of any one of them. There is a preferential need to develop smart and intelligent nanoplatforms which could conveniently integrate

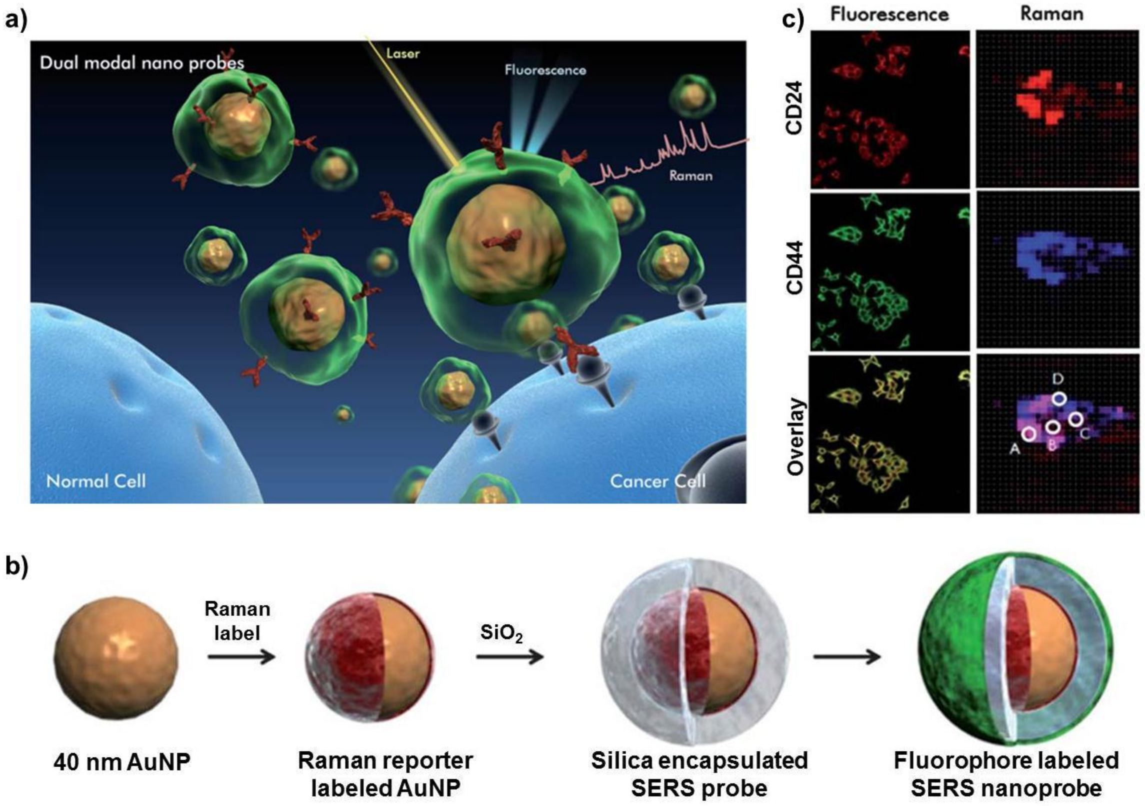

Figure 3.3. a) Schematic representation of cancer biomarker detection using silica encapsulated gold nanoprobes. b) Scheme showing the synthesis of the nanoprobe. c) Duplex imaging of CD24 and CD44 antigens in MDA-MB 231 cells using fluorescence and SERS modalities.

these complementary imaging modalities in an orthogonal fashion. To explore the complete potential of fluorescence-SERS guided multiplexing probe development, a design strategy has been adopted for fabricating programmable nanoparticles that feature an “on-off” switching transition between fluorescence and SERS. The framework of the nanosystem comprises of dual responsive Raman active fluorophores attached to the surface of gold nanospheres through a strategically positioned peptide (Phe-Lys-Cys; FKC) sequence which is recognized as a specific substrate for cathepsin B (cathB), a key protease involved in cancer invasion and progression.[40] The tripeptide linker is engineered to be cleaved by the enzymatic action of cathB, at the acidic pH in the tumor microenvironment. This pH-sensitive enzymatic cleavage at the tumor site facilitates the activation of the initially dormant fluorophores through a break in the conjugation which increases the distance of the dyes from the gold nanoparticle (AuNP) surface thereby causing the arresting of SERS activity via the suppression of strong chemical enhancement induced by the nanoroughened metal substrate. The anticipated mode of action of fluorescence-SERS encoded nanoparticle probes (**FSENP**s) was utilized for the detection of defined protein targets after decorating with specific monoclonal antibody recognition units. The unique fingerprinting SERS peaks at 837, 354 and 617 cm^{-1} and the emission peaks at 450, 520 and 580 nm of the three probes were employed for the simultaneous detection of multiple biomarkers with high sensitivity and specificity. Moreover, as a major step towards the clinical applicability of the probe, a precise profiling of the disease biomarkers in clinical patient specimens has been demonstrated. To the best of our knowledge, no study has been reported thus far to demonstrate the enzyme triggered “on-off” biosensing approach for the detection of multiple protein targets using SERS and fluorescence based bimodal strategies. Schematic illustration of the fabrication and mechanism of action of **FSENP**s for the multiplexed detection guided multicolor imaging of protein biomarkers is shown in **Figure 3.4**.

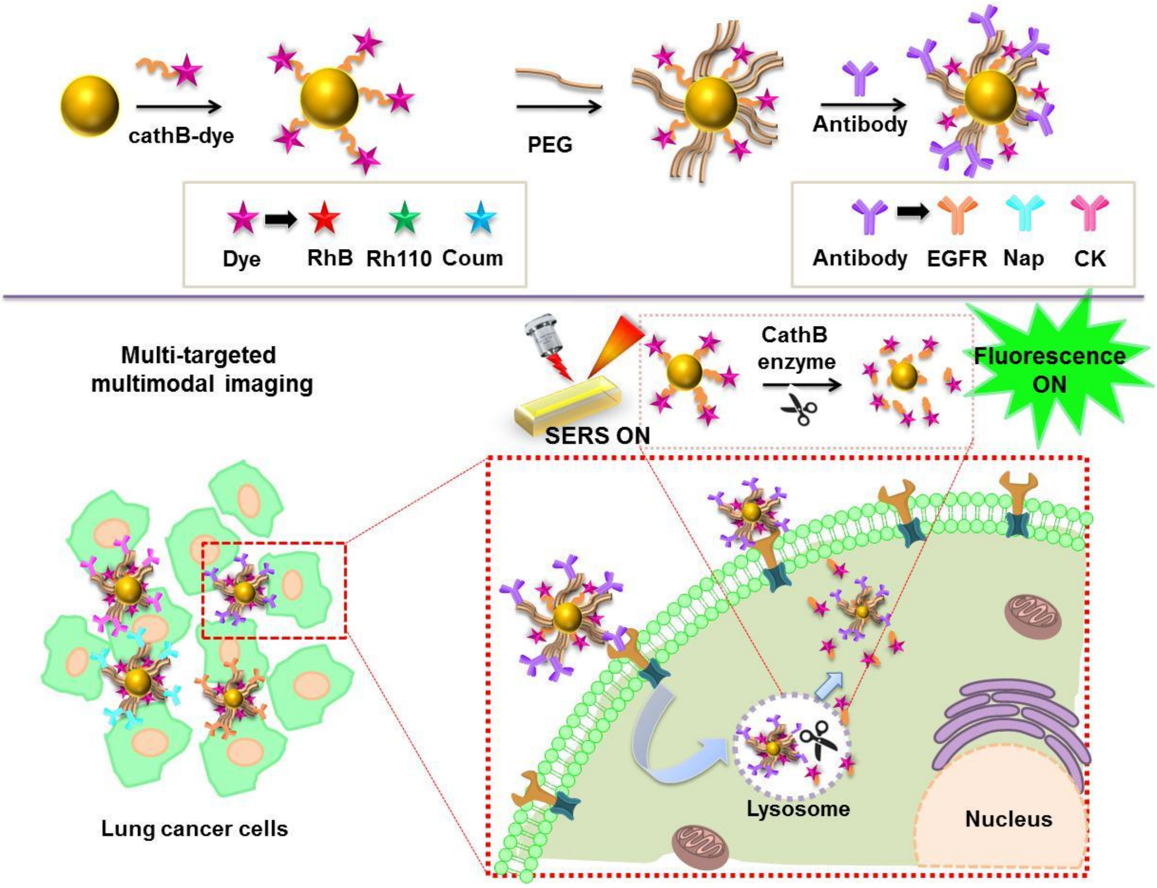

Figure 3.4. Schematic illustration of enzyme triggered switching of antibody functionalized **FSENPs** for the multiplexed detection of lung cancer biomarkers.

3.3. Results and Discussion

3.3.1. Design and Fabrication of FSENPs

Multimodal nanodimensional **FSENPs** were fabricated by the labeling of fluorogenic Raman reporter dyes onto the surface of gold nanospheres through a tripeptide sequence. The dyes were chosen to be 7-hydroxy-3-carboxycoumarin, rhodamine 110 and rhodamine B which possessed unique multiplexing spectral signatures in both fluorescence and SERS modalities. A cathB peptide substrate with the representative amino acid sequence Phe-Lys-Cys (FKC) was synthesized by means of the solid phase peptide synthesis (**Scheme 3.1**), which was conjugated to the carboxy terminal of the respective dyes using carbodiimide chemistry to afford dye tagged peptide substrates; Coum-cathB, Rh110-cathB and

RhB-cathB (**Scheme 3.2**). The compounds were cleaved from the resin bed under acidic conditions which were subjected to characterization by NMR and HRMS spectral analyses. UV-Vis absorption spectra of Coum-cathB, Rh110-cathB and RhB-cathB showed absorption bands centered at about 360, 495 and 550 nm with the corresponding emission peaks positioned at 450, 520 and 580 nm respectively (**Figure 3.5a** and **3.5b**). The presence of non-overlapping emission bands clearly revealed the potential of the probes for multiplexing applications. The capability of the molecules for multiplexed Raman fingerprinting was then evaluated through SERS analysis which was performed by functionalization with AuNPs of size around 40 nm (**Figure 3.5c**). A shift in the plasmonic absorption band from 530 to 532 nm (**Figure 3.6a-c**) indicates the formation of the dye conjugated nanotags which were also validated by TEM and DLS analysis showing a clear retention of the spherical morphology of the nanoparticles with high monodispersity (**Figure 3.6d-f**). On an average, the number of Coum-cathB,

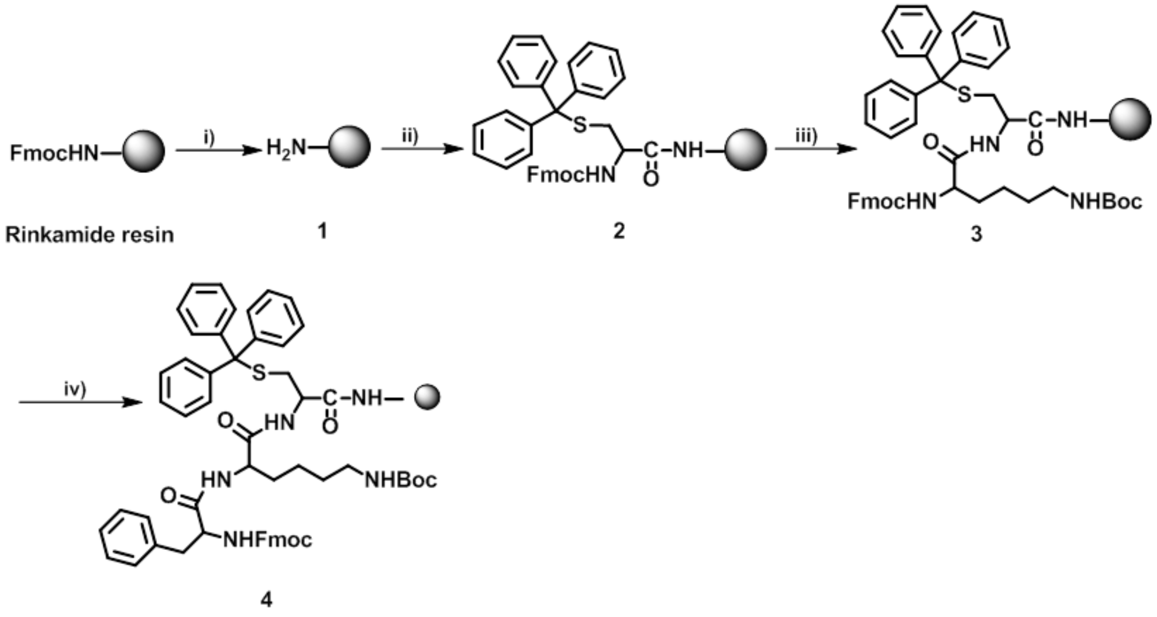

Scheme 3.1. Reagents and conditions: i) 20% piperidine in DMF, ii) Fmoc-Cys(STr)-OH, HBTU, DIPEA, iii) 20% piperidine in DMF, Fmoc-Lys(Boc)-OH, HBTU, DIPEA, iv) Fmoc-Phe-OH, HBTU, DIPEA.

Rh110-cathB and RhB-cathB molecules attached per AuNP was estimated to be 1.46 x 10^3, 1.57 x 10^3 and 1.52 x 10^3 respectively, as quantified by absorption

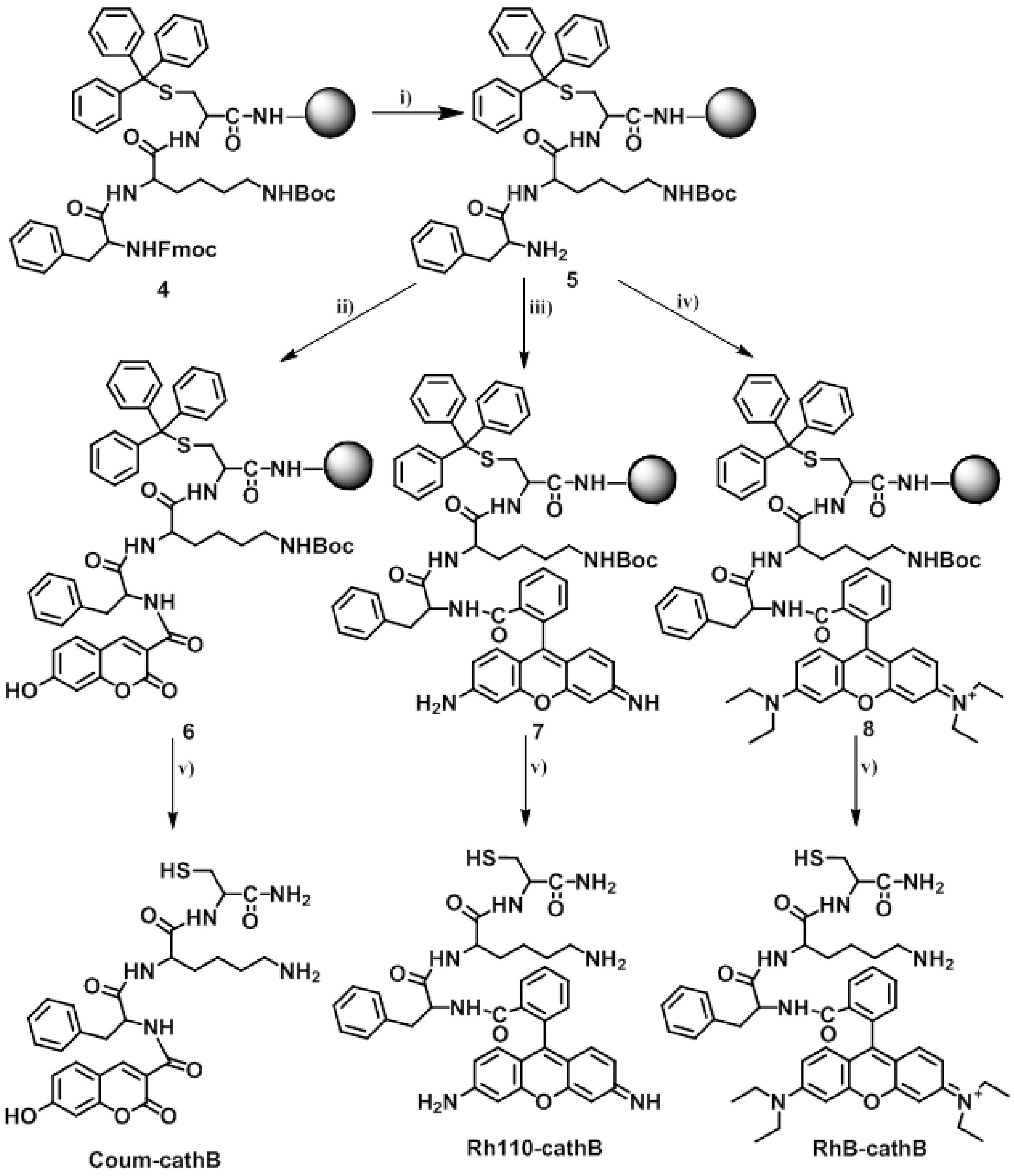

Scheme 3.2. Reagents and conditions: i) 20% piperidine in DMF, ii) DIC, HOBt, 7-hydroxycoumarin-3-carboxylic acid, iii) DIC, HOBt, rhodamine 110, iv) DIC, HOBt, rhodamine B, v) 95% TFA, 2.5% TIS, 2.5% H_2O.

spectral measurements. As shown in **Figure 3.5d**, the strong chemisorption offered by Au-S bond between the gold particle and Cys terminus produced intense SERS signals with distinct multiplexing peaks at 837, 354 and 617 cm^{-1} which accounts to the C-H str. C-C str. and C-C-C bending vibrations of Coum-cathB, Rh110-cathB and RhB-cathB respectively. Moreover, the Raman peaks located at 1130, 1410 and 1275 cm^{-1} corresponding to C-O-C sym. str., C-C aliphatic str. and

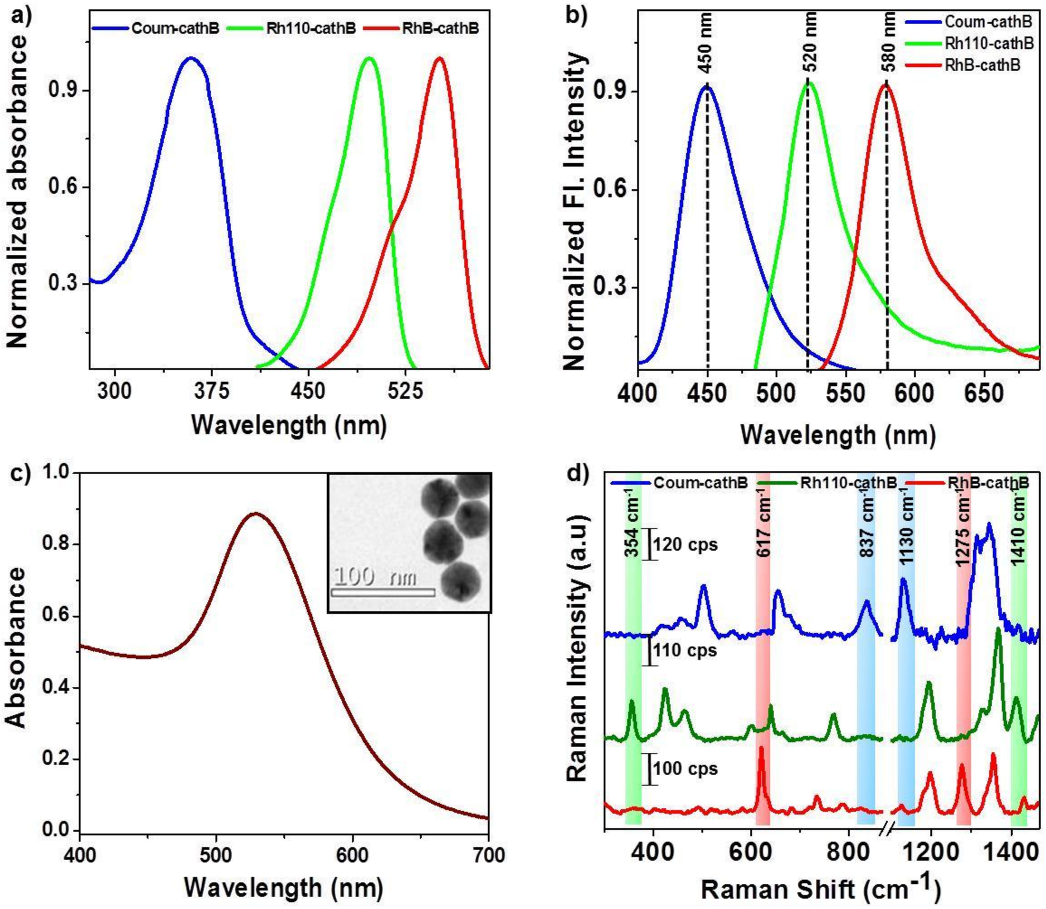

Figure 3.5. a) UV-Vis absorption spectrum of 10 μM solutions of Coum-cathB, Rh110-cathB and RhB-cathB in PBS buffer (25 mM, pH 7.4). b) Fluorescence spectra of 10 μM solutions of Coum-cathB, Rh110-cathB and RhB-cathB in PBS (25 mM, pH 7.4). The emission spectra were obtained by exciting Coum-cathB, Rh110-cathB and RhB-cathB at 360, 475 and 520 nm respectively. c) UV-Vis absorption spectrum of spherical gold nanoparticles. Inset shows the TEM image of the gold nanospheres. d) SERS spectral analysis of 10 μM solutions of Coum-cathB, Rh110-cathB and RhB-cathB in PBS (25 mM, pH 7.4) SERS spectra were obtained by excitation using a 633 nm laser.

aromatic C-H bending vibrations respectively for the three nanotags served as spatially distinct fingerprints, making them promising candidates for an ideal multiplexing analysis.

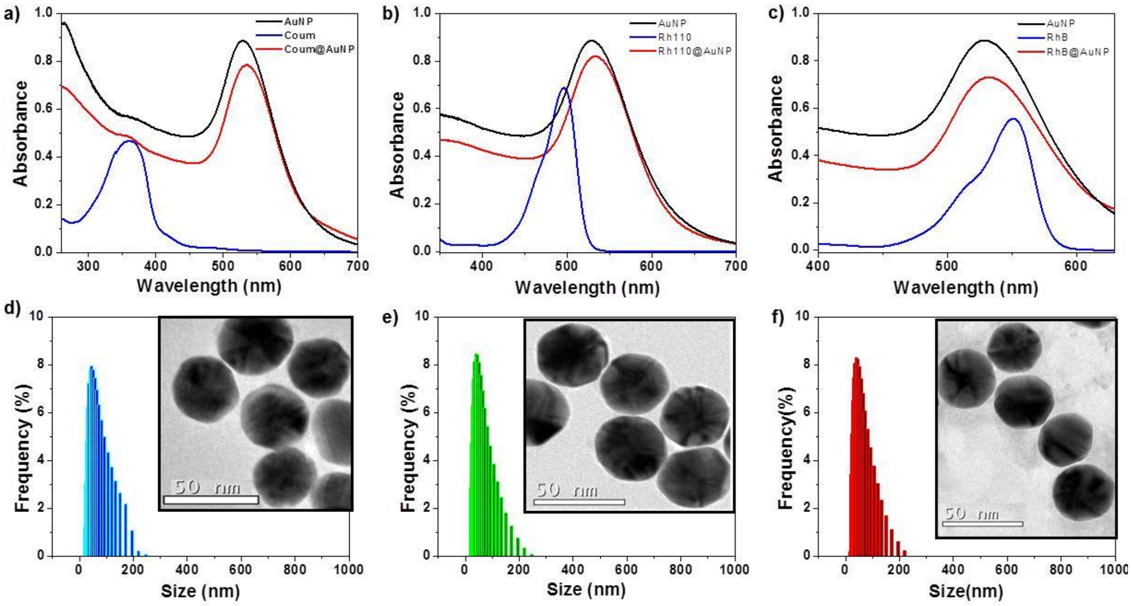

Figure 3.6. UV-Vis absorption spectra and DLS analysis of Coum-cathB@AuNP (a,d), Rh110-cathB@AuNP (b,e) and RhB-cathB@AuNP (c,f). Insets in (d-f) represent the TEM images of Coum-cathB@AuNP, Rh110-cathB@AuNP and RhB-cathB@AuNP respectively.

3.3.2. Photophysical Evaluation of FSENPs

To demonstrate the utility of enzyme triggered ‘on-off’ signaling property of the probes, time dependent fluorescence and SERS experiments were performed in the presence of cathB enzyme (60 ng/mL) by mimicking the intracellular enzymatic conditions. CathB is a lysosomal protease, which has been upregulated in many cancers and has great implications in the early stage invasion and progression of glioma, melanoma, colon cancer, lung cancer and lot more.[40-46] Thus, an optimal pH of 5.5, which is close to the pH of the lysosomal regions,[47] was chosen as the key parameter for this study. The enzymatic cleavage studies were examined in acetate buffer (25 mM sodium acetate, 1 mM EDTA; pH 5.5) at 37 ºC to mimic the physiological conditions. In the absence of the enzyme, the probes represent a state of SERS signal "on" and fluorescence signal "off" as a result of the closer proximity between AuNP and dye molecules, which render them with high signal amplification in the Raman channel and negligible activity in the fluorescence

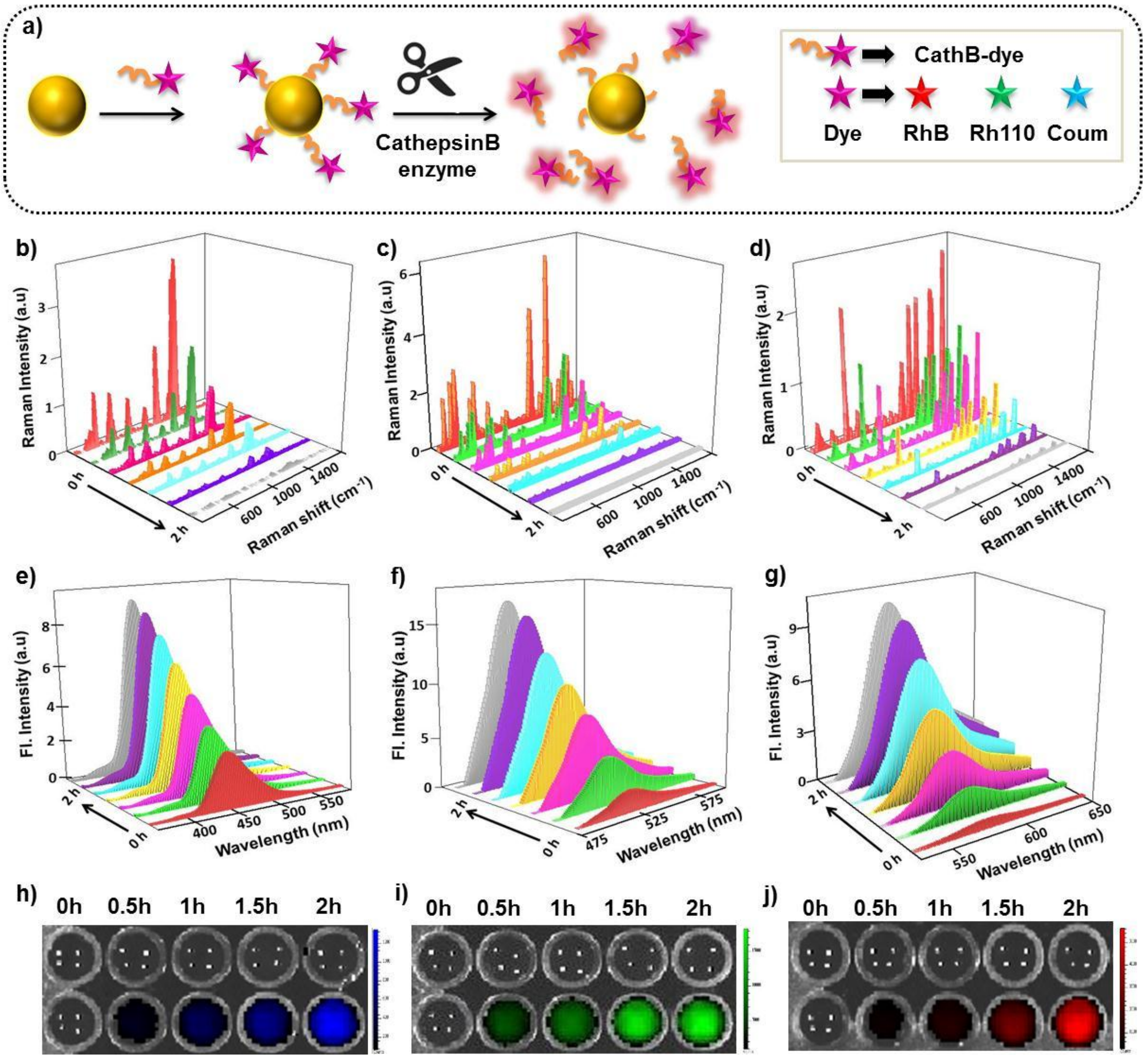

Figure 3.7. a) Schematic illustration showing the switching of SERS and fluorescence properties of **FSENP**s upon administration with cathB enzyme. SERS quenching and fluorescence activation studies of AuNP functionalized Coum-cathB (b, e), Rh110-cathB (c, f) and RhB-cathB (d, g) upon addition of cathB enzyme (60 ng/mL) in acetate buffer (pH 5.5, 37 ºC). Fluorescence images of Coum-cathB@AuNP (h), Rh110-cathB@AuNP (i) and RhB-cathB@AuNP (j) in the absence (upper panel) and in the presence (lower panel) of the enzyme recorded using IVIS animal imaging system. Fluorescence spectra and images were recorded by excitation at 360, 475 and 530 nm for Coum-cathB@AuNP, Rh110-cathB@AuNP and RhB-cathB@AuNP respectively. SERS spectra were acquired by excitation at 633 nm.

channel. However, incubation of the nanoparticles (Coum-cathB@AuNP, Rh110-cathB@AuNP and RhB-cathB@AuNP) with cathB enzyme triggered the switching of the optical signals; the probes got switched to the state of SERS signal “off” and fluorescence signal “on” (**Figure 3.7a**). From **Figure 3.7**, it is clear that the SERS signals showed a gradual reduction in their intensity (**Figure 3.7b-d**) with a subsequent amplification of the emission signals (**Figure 3.7e-j**) upon increasing time for all the three probes. These observations can be clearly correlated with the aforementioned design concept where the enzyme trigger will cause the cleavage of cathB peptide substrate present in the probes resulting in an increased separation of the dye molecules from the AuNP surface which facilitates the quenching of the Raman signals with the simultaneous activation of the initially dormant fluorophores. The limit of detection (LOD) of cathB enzyme was determined through both SERS as well as fluorescence modalities (**Figure 3.8**) wherein SERS showed a better sensitivity for cathB with values

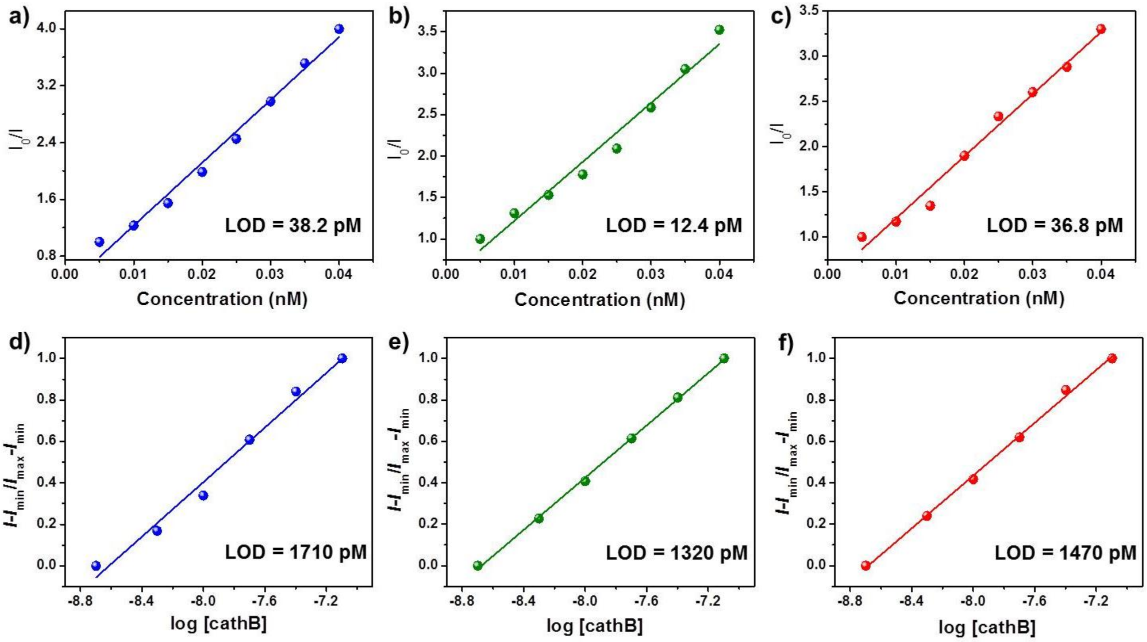

Figure 3.8. a) SERS and fluorescence based analysis of limit of detection of cathB enzyme by Coum-cathB@AuNP (a,d), Rh110-cathB@AuNP (b,e), and RhB-cathB@AuNP (c,f).

reaching up to 38.2, 12.4 and 36.8 pM for Coum-cathB@AuNP, Rh110-cathB@AuNP and RhB-cathB@AuNP respectively while fluorescence experiments revealed LOD values in the range of 1710, 1320 and 1470 pM for the enzyme by the probe molecules, Coum-cathB@AuNP, Rh110-cathB@AuNP and RhB-cathB@ AuNP respectively. In a control experiment, the Raman active dye molecules (without the peptide linker) were mixed directly with AuNPs and found that the SERS intensity as well as the fluorescence quenching intensity is less in comparison to those obtained from the probes containing the peptide substrate, which can be attributed to the strong chemisorption offered by the cysteine unit of the peptide moiety. Furthermore, treatment of the physically mixed nanoparticles with cathB enzyme could neither activate the fluorescence nor quench the Raman signals, i.e. fluorescence was always switched “off” and SERS was always switched “on” in contrast to the on-off switching property exhibited by our probes (**Figure 3.9**). In order to establish the role of pH in this cleavage mechanism, the experiments have been carried out under normal physiological (pH 7.4) conditions. Expectantly, neither the SERS nor the fluorescence properties showed any

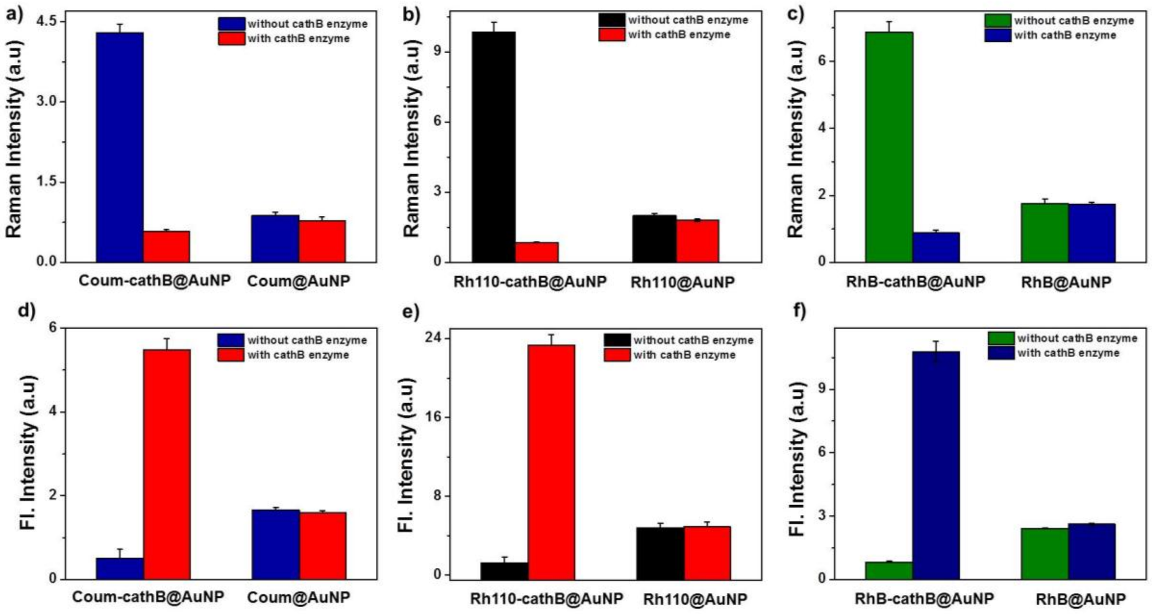

Figure 3.9. SERS and fluorescence analysis of Coum-cathB@AuNP and Coum@AuNP (a,d), Rh110-cathB@AuNP and Rh110@AuNP (b,e) and RhB-cathB@AuNP and RhB@AuNP (c,f) in the absence and presence of cathB enzyme (60 ng/mL) in PBS (pH 7.4, 37 ºC). Data constitute the mean ± SD of three independent experiments.

significant change in their intensity profiles as evident from **Figure 3.10**. These studies apparently suggest that the pH sensitive peptide linker serves as a superior substrate for the simultaneous dual-signal switching of fluorescence and SERS activities.

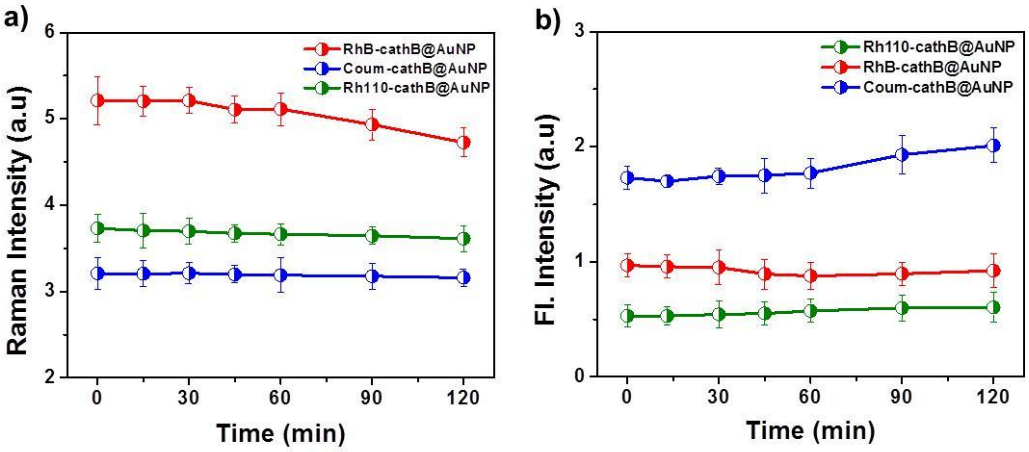

Figure 3.10. a) SERS and b) emission spectra of Coum-cathB@AuNP (λ_{ex} @ 360 nm and λ_{em} @ 450 nm), Rh110-cathB@AuNP (λ_{ex} @ 475 nm and λ_{em} @ 520 nm) and RhB-cathB@AuNP (λ_{ex} @ 520 nm and λ_{em} @ 580 nm) in the presence of cathB enzyme (60 ng/mL) in PBS (pH 7.4, 37 ^{o}C). SERS spectral analysis was performed by excitation using a 633 nm laser. Data constitute the mean ± SD of three independent experiments.

Considering the structural similarity of proteins, the effects of other proteins and enzymes on the optical responses of the probes were investigated to assess their selective nature. The results from SERS spectral evaluation indicated that only cathB could induce a quenching of their signals while no such noticeable signal intensity change was observed with other competing species (**Figure 3.11a-c**). Similar trends were observed with fluorescence experiments (**Figure 3.11d-f**) where the probes exhibited an enhancement in the emission intensities only upon treatment with cathB while remaining silent towards all other tested analytes. These features warrant that the probes can be programmed to get activated upon their autonomous homing to the tumor environment where cathB enzymes are mostly located, without posing any interference from other biologically relevant species.

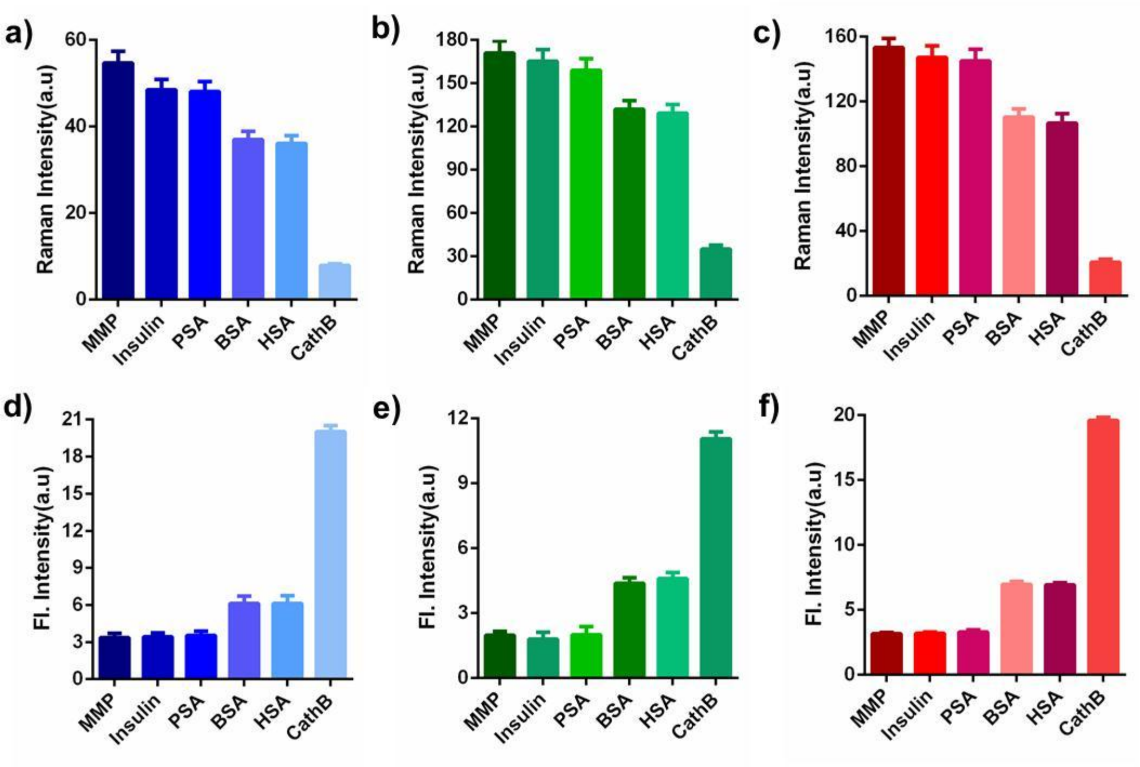

Figure 3.11. SERS and fluorescence responses of Coum-cathB@AuNP (λ_{ex} @ 360nm and λ_{em} @ 450 nm) (a, d), Rh110-cathB@AuNP (λ_{ex} @ 475 nm and λ_{em} @ 520 nm) (b, e) and RhB-cathB@AuNP (λ_{ex} @ 520nm and λ_{em} @ 580 nm) (c, f) towards various proteins and enzymes. SERS spectra were recorded by excitation at 633 nm. Data indicate the mean ± SD of four independent experiments.

After gaining a clear picture of the enzyme driven switching of the probes in aqueous solution, the same was validated in living cancer cells by complementary Raman and fluorescence imaging modalities. Human lung adenocarcinoma (A549) cells were incubated with each of the probes and single-cell SERS imaging was performed in a time dependent manner. At the initial time point of 15 min, all the three probes showed intense Raman signals indicative of their effective internalization which was visualized by false color SERS imaging and spectral signaling from the cells. Upon increasing time, the SERS signals witnessed a gradual decline in their intensities which finally got turned off after 120 min as evident from the real-time SERS imaging experiments (**Figure 3.12a**

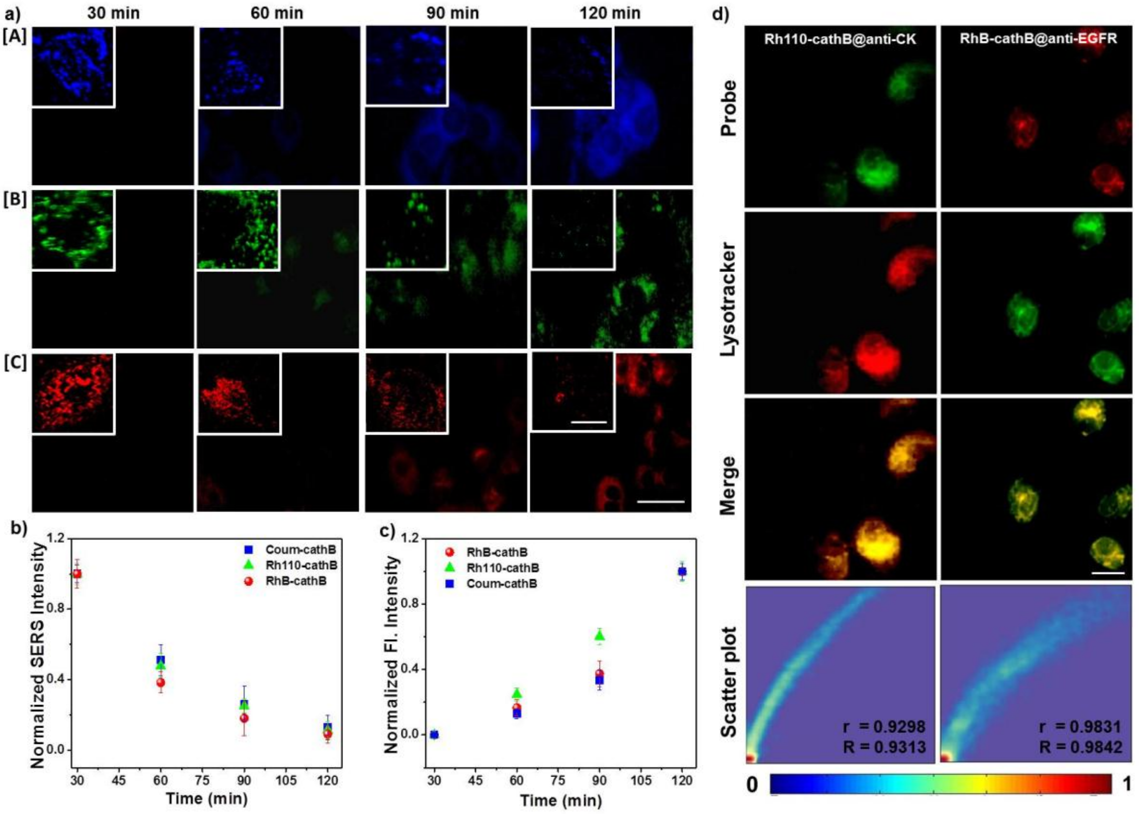

Figure 3.12. a) Fluorescence microscopic images of Coum-cathB@AuNP (A), Rh110-cathB@AuNP (B) and RhB-cathB@AuNP (C) in A549 cells from 30 to 120 min. Scale bar 20 μm. Insets in A, B and C represent the confocal SERS images of A549 cells treated with Coum-cathB@AuNP, Rh110-cathB@AuNP and RhB-cathB@AuNP respectively for the same time interval. Scale bar 10 μm. Time-dependent b) SERS and c) fluorescence intensity profiling from the cells at different time points. d) Fluorescence micrographs for the intracellular localization of Rh110-cathB@AuNP and RhB-cathB@AuNP with lysotracker green/red. Green channel at 510-550 nm and red channel at 580-620 nm. In the scatter plot, r and R represent Pearson's correlation coefficient and Mander's overlap coefficient respectively. Scale bar 20 μm. Data represent the mean ± SD of three independent experiments.

inset and **3.12b**). Fluorescence imaging experiments performed in line with the SERS studies under the same conditions initially conceived the dyes in passive state as apparent from the absence of any significant fluorescence signals from the blue, green or red channels. Upon increased accumulation in the cancer cells, these activatable nanoprobes presented amplification in their emission signals which got saturated after 120 min (**Figure 3.12a** and **3.12c**). To facilitate this 'on-off' switching mechanism, it is necessary that the probes be present at the site where cathB enzymes are located. To this end, the intracellular localization of the probes was investigated by costaining with lysotracker which specifically stains the lysosome. As shown in **Figure 3.12d**, the green and red fluorescence coming respectively from Rh110-cathB and RhB-cathB overlapped mainly with that of Lysotracker, indicating the localization of the probes in the lysosomal compartment of the cells where cathB enzymes are preferentially recruited. These observations underpin the fact that the enzymatic recognition-driven cleavage of the peptide sequence occurs in the lysosomes and this scission process is responsible for the quenching of the signals in the Raman channel and activation of the signals in the fluorescence channel.

3.3.3. Formulation of Antitag Nanoprobes of FSENPs for Multiplexed Recognition of Lung Cancer Biomarkers

Owing to the favorable switching property and excellent multiplexing characteristics of the as-designed probes, it was envisaged that the present strategy may facilitate the development of switchable bimodal nanoprobes for the point-of-care diagnosis of clinically relevant disease biomarkers. Towards achieving this goal, the three different types of **FSENP**s were conjugated with three monoclonal antibody units to afford antitag nanoprobes: Coum-cathB@anti-Nap, Rh110-cathB@anti-CK and RhB-cathB@anti-EGFR that are specific towards epidermal growth factor receptor (EGFR), cytokeratin-19 (CK) and napsin-A (Nap). EGFR is a transmembrane glycoprotein involved in the pathogenesis of tumor malignancies while CK and Nap serve as differentiating markers for the various subtypes of lung cancer such as adenocarcinoma and non-small cell lung carcinoma.[48-50] UV-Vis spectral analysis of the as-formed constructs showed the appearance of an additional protein absorption peak at 260 nm with a slight shift in the plasmonic absorption of nanoparticles which confirmed the successful conjugation of the antibody elements (**Figure 3.13 a-c**). Subsequently, an MTT assay was performed to examine the cytotoxicity of the dye-peptide conjugates as shown in **Figure 3.13**

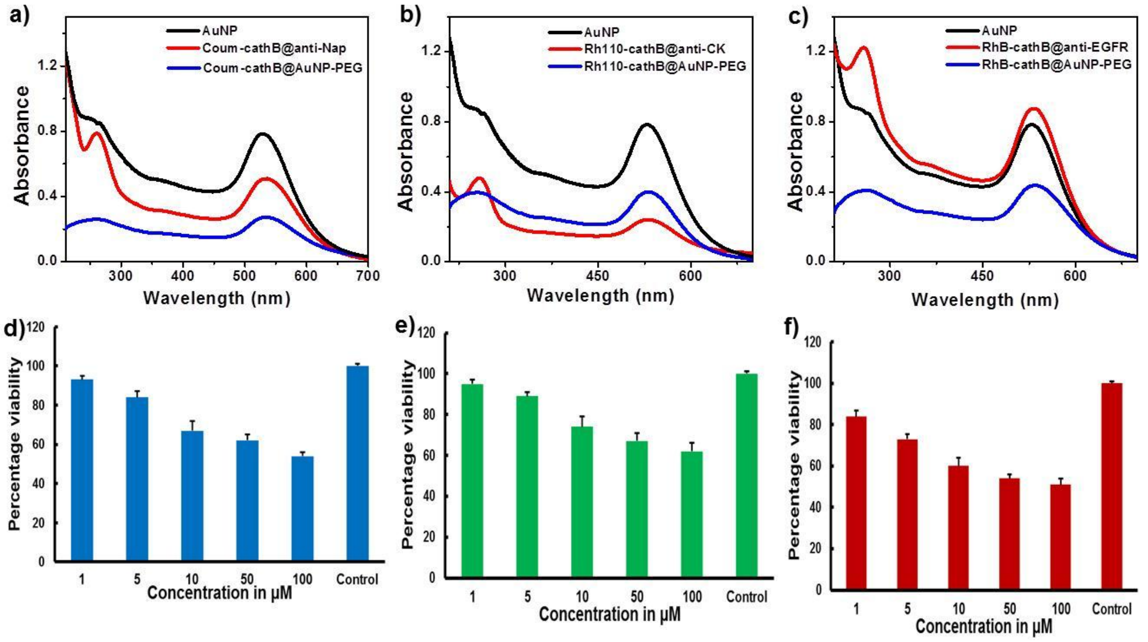

Figure 3.13. UV-Vis absorption spectra of Coum-cathB@anti-Nap (a), Rh110-cathB@anti-CK (b) and RhB-cathB@anti-EGFR (c) in PBS (25 mM, pH 7.4). Cytotoxicity evaluation using MTT assay with A549 cells treated with d) Coum-cathB, e) Rh110-cathB and f) RhB-cathB for 24 h. Data represent the mean ± SD of three independent experiments.

d-f. Although the molecules alone exhibited a dose dependent toxicity, the nanotags containing 10 µM of the dye molecules were found to be safe for application in cultured cells under standard conditions (**Figure 3.14**). Next, the sensitivity of the probes for specific detection of single proteins was investigated

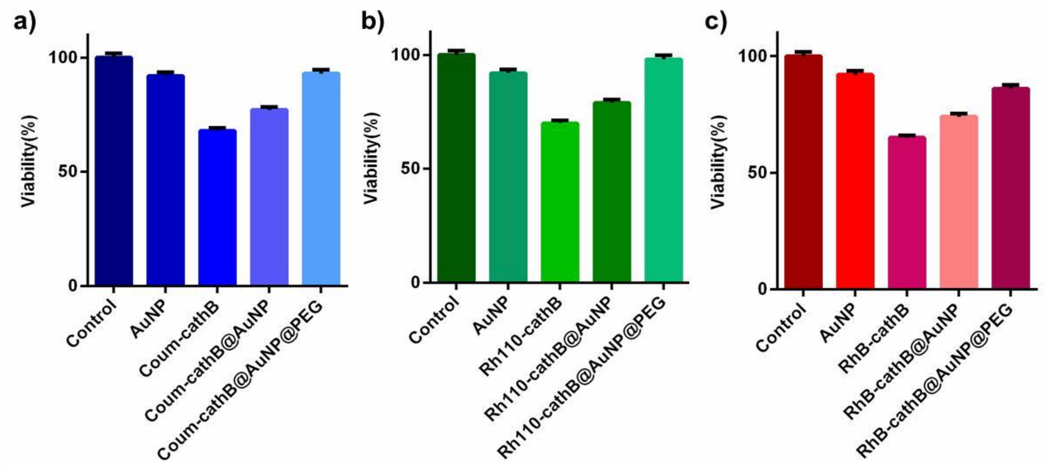

Figure 3.14. Cytotoxicity evaluation using MTT assay with A549 cells treated with the constructs for 24 h. Data represent the mean ± SD of three independent experiments.

by the separate administration of each antitag under *in vitro* conditions. SERS measurements from A549 cells incubated with RhB-cathB@anti-EGFR showed

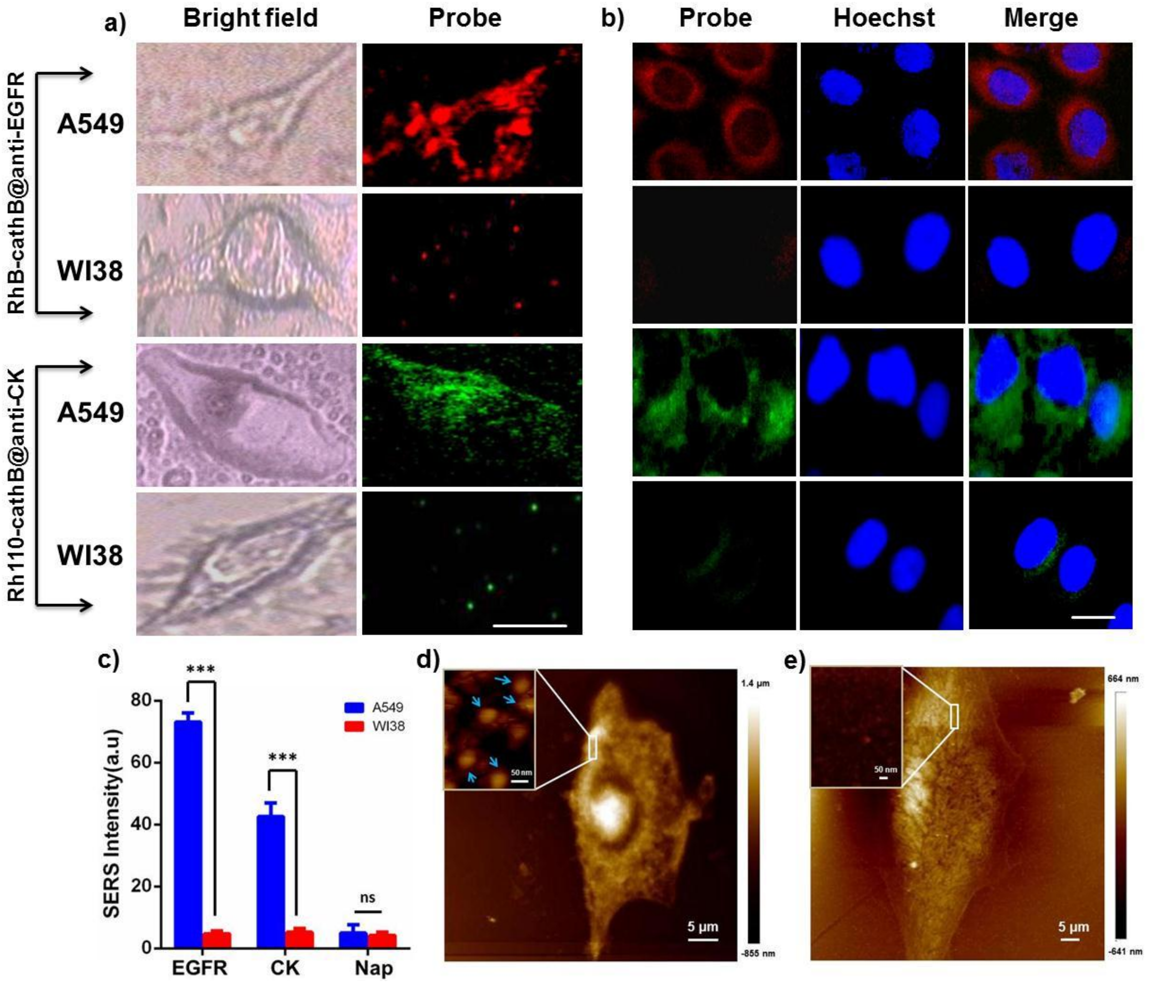

Figure 3.15. a) Confocal SERS and b) fluorescence microscopic images of RhB-cathB@anti-EGFR and Rh110-cathB@anti-CK in A549 and WI38 cells. SERS images of RhB-cathB@anti-EGFR and Rh110-cathB@anti-CK were obtained by imaging at 617 and 354 cm^{-1} respectively. Scale bar 10 µm. Fluorescence images were collected from the blue channel at 440-480 nm, green channel at 510-550 nm and red channel at 580-620 nm. Scale bar 10 µm. c) Semi-quantitative evaluation of EGFR, CK and Nap in A549 and WI-38 cells as obtained by SERS analysis. Statistically significant differences at *** $p < 0.001$; ns, not significant in comparison with the control. AFM images of A549 (d) and WI-38 (e) cells after treatment with RhB-cathB@anti-EGFR. Insets represent the magnified image of the labeled portion of the cell surface. Data are the mean ± SD of three independent experiments.

prominent Raman fingerprints indicating the abundance of EGFR proteins while the WI-38 cells incubated with the same, revealed very low expression of EGFR as evident from the lack of any noticeable Raman signals (**Figure 3.15a**). Similarly, incubation of A549 and WI-38 cells with Rh110-cathB@anti-CK witnessed high expressions of CK protein in the cancer cells with very minimal expression coming

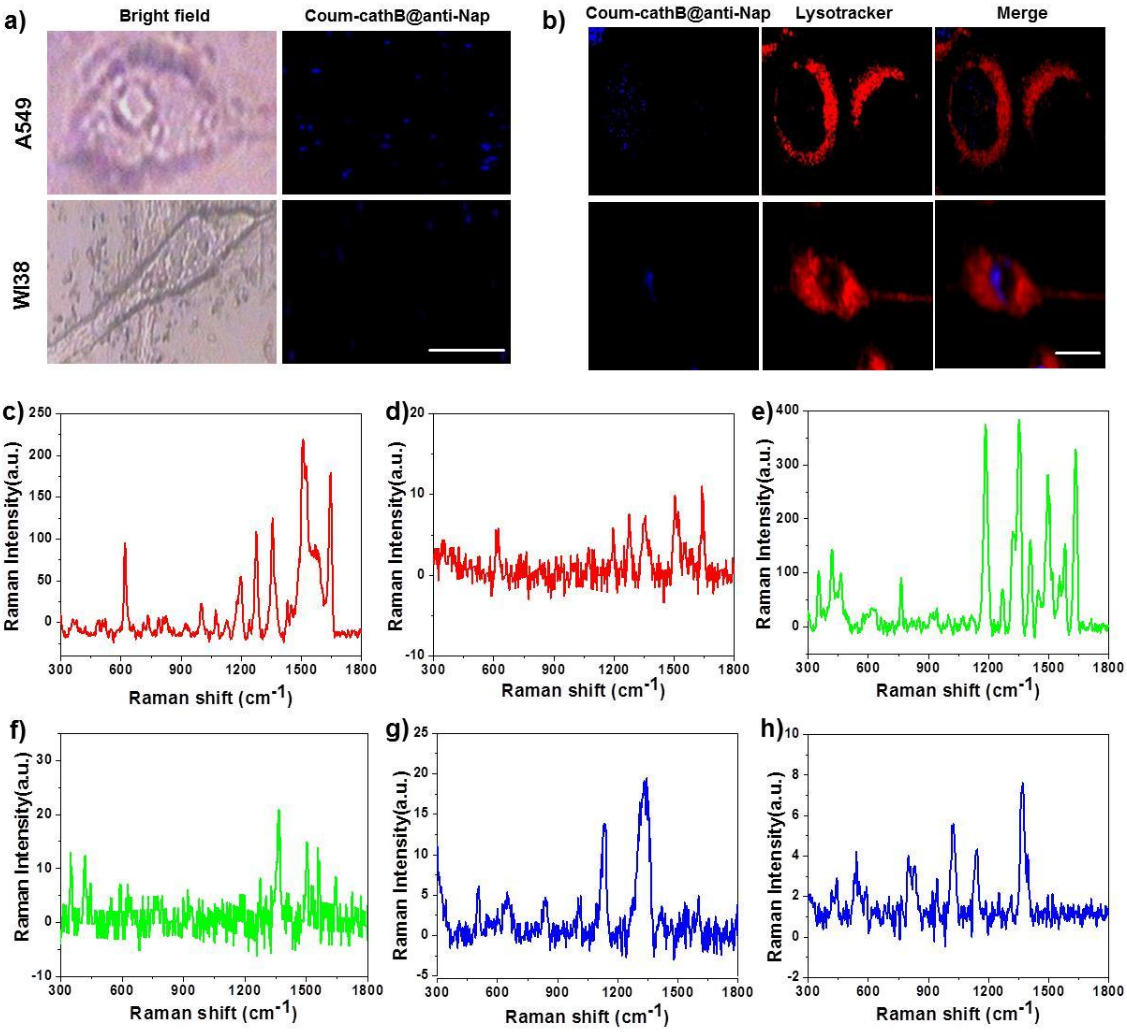

Figure 3.16. a) Confocal SERS and b) fluorescence microscopic images of Coum-cathB@anti-Nap in A549 and WI38 cells. SERS images of Coum-cathB@anti-Nap obtained by imaging at 837 cm^{-1}. Scale bar 10 μm. Fluorescence images were collected from the probe at 440-480 nm. Scale bar 10 μm. c), e) and g) represent the respective SERS signals of RhB-cathB@anti-EGFR, Rh110-cathB@anti-CK and Coum-cathB@anti-Nap obtained from A549 cells. The SERS signals acquired from WI-38 cells treated with RhB-cathB@anti-EGFR, Rh110-cathB@anti-CK and Coum-cathB@anti-Nap are shown in d), f) and h) respectively.

from the normal ones (**Figure 3.15a**). However, Coum-cathB@anti-Nap displayed weak signal intensity in both cancer and normal cells suggestive of the low expression of Nap in these cell lines (**Figure 3.16a**). The Raman spectral signals obtained from the cells in each case is shown in **Figure 3.16c-h**. Furthermore, fluorescence recovery facilitated by the enzyme mediated scission process enabled the precise visualization of disease biomarkers in the emission channel as well. From the fluorescence microscopic images shown in **Figure 3.15b** and **3.16b**, it is clear that A549 cells displayed strong emission in the red and green channels with much less fluorescence from the blue channel, which accounts for the high levels of EGFR and CK proteins and low levels of Nap. However, WI-38 cells treated with the probes did not produce any noticeable emission in the blue, green or red channels, confirming the low expression of these biomarkers in normal cells. The expression levels of these biomarkers in A549 and WI-38 cells were also validated

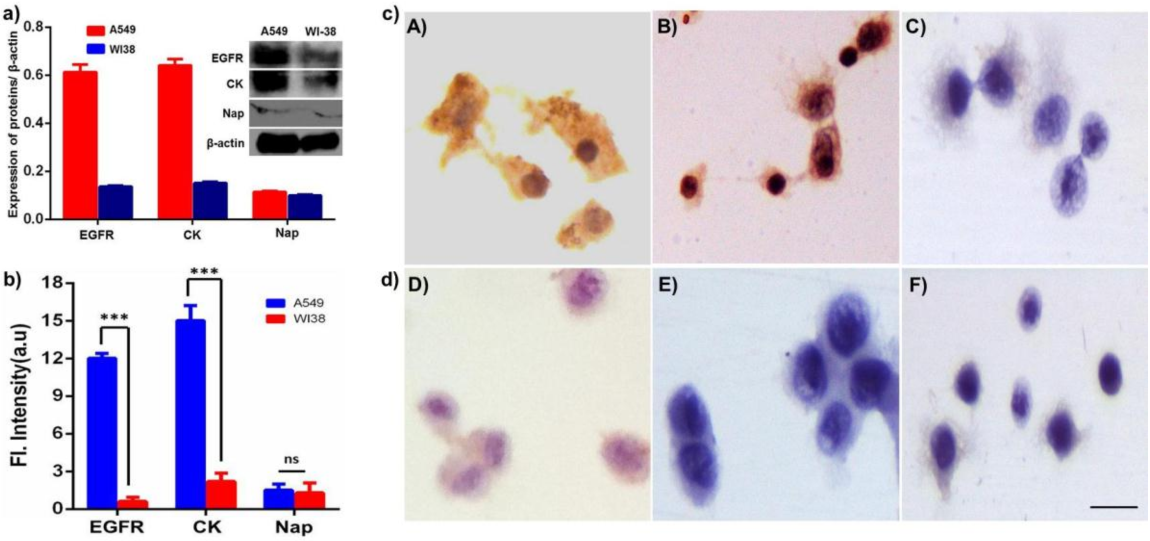

Figure 3.17. a) Western blot analysis showing the expression status of EGFR, CK and Nap in A549 and WI-38 cells and quantitation of protein bands normalized with β-actin as estimated using ImageJ software. b) Estimation of EGFR, CK-19 and Nap levels in A549 and WI38 cells as measured by fluorescence analysis. Data are the mean ± SD of three independent experiments. Immunocytochemical staining of A549 (c) and WI-38 (d) cells for the recognition of EGFR (A and D), CK (B and E) and Nap (C and F). Counterstaining was performed with haematoxylin. Scale bar 20 μm.

through Western blot analysis by using antibodies directed against EGFR, CK and Nap (**Figure 3.17a**). The results were in agreement with our experimental analysis which showed high expressions of EGFR and CK and low levels of Nap in the cancer cells against the normal ones. The expression status of the three biomarkers were further confirmed by immunocytochemistry technique where positive brown staining was observed with EGFR (**Figure 3.17A**) and CK (**Figure 3.17B**) but not with Nap (**Figure 3.17C**), in the case of A549 cells while none of them were stained positive in WI-38 cells (**Figure 3.17D-F**). Semi-quantitative evaluation of the biomarkers through SERS and fluorescence measurements revealed ≈ 15, 8 and 1.2 fold increase in the respective EGFR, CK and Nap levels in the A549 cells when compared to the normal WI-38 cells (**Figure 3.15c** and **3.17b**). Furthermore, the target specificity of RhB-cathB@anti-EGFR in cancer cells was evaluated through atomic force microscopy (AFM) experiments (**Figure 3.15d** and **3.15e**). Inset in **Figure 3.15d** clearly shows the presence of nanoparticles on the surface of A549 cells which affords the specific binding of nanotags to the EGFR protein overexpressed on the cell surface. In contrast, there was hardly any particle in the WI38 cells treated with the probe, suggesting the selectivity and specificity of the nanotags towards lung cancer cells (**Figure 3.15e**).

On account of the excellent specificity offered by the antitags for the detection of the target biomarkers, the next focus was directed towards evaluating the efficacy of mixed nanotags for the specific detection of their respective protein entities. In this experiment, SERS spectral evaluation and fluorescence imaging were performed after treating A549 and WI-38 cells with a combination of two antitags each. Following incubation and washing process, the measured SERS spectra acquired from the A549 cells treated with a mixture of RhB-cathB@anti-EGFR and Rh110-cathB@anti-CK revealed distinct fingerprint signatures corresponding to each Raman tag (**Figure 3.18a**). While treatment of the cells with a combination of RhB-cathB@anti-EGFR and Coum-cathB@anti-Nap produced

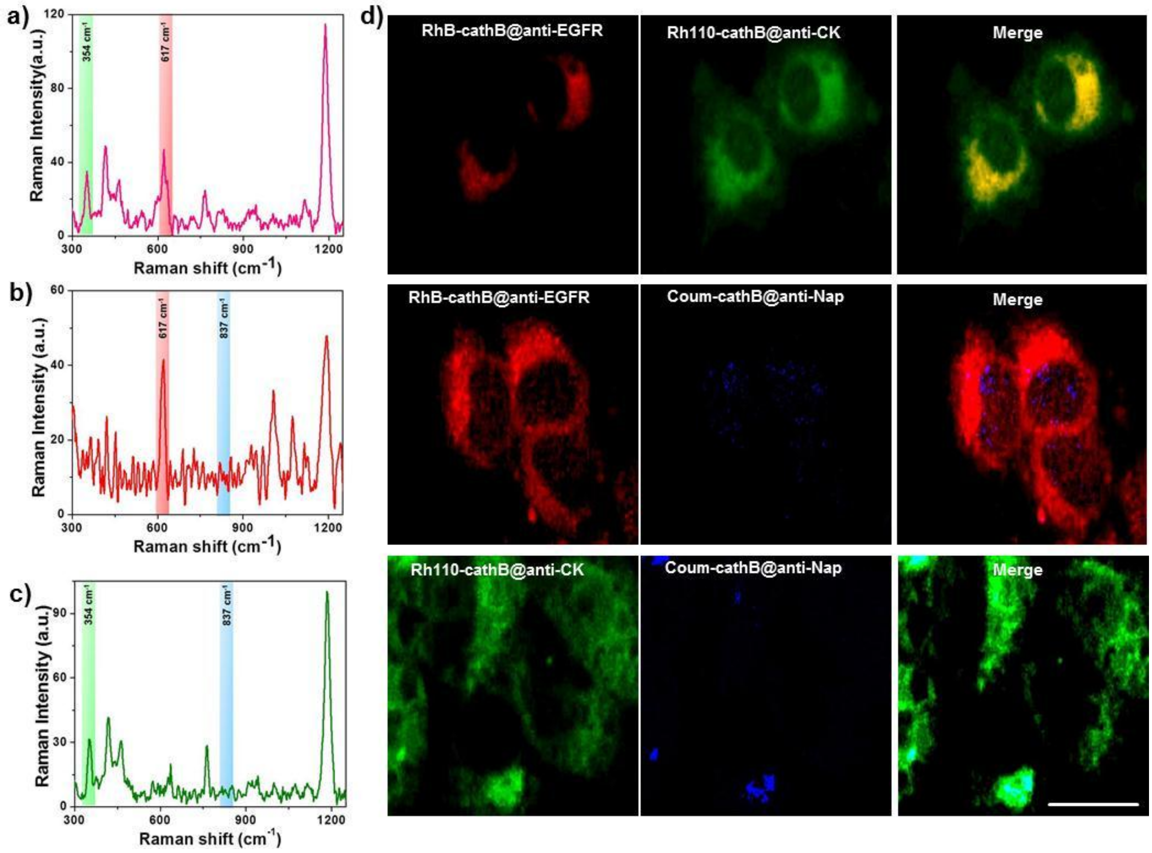

Figure 3.18. SERS spectral analysis of A549 cells incubated with a mixture of RhB-cathB@anti-EGFR and Rh110-cathB@anti-CK (a), RhB-cathB@anti-EGFR and Coum-cathB@anti-Nap (b) and Rh110-cathB@anti-CK and Coum-cathB@anti-Nap (c) respectively. d) Fluorescence microscopic imaging of A549 cells treated with a combination of two antitags each. Fluorescence images acquired from the blue channel at 440-480 nm, green channel at 510-550 nm and red channel at 580-620 nm. Scale bar 20 μm.

signals characteristic of the Raman label tagged with anti-EGFR antibody together with weak signals arising from the latter (**Figure 3.18b**). Similarly, administration of the cells with a mixture of Rh110-cathB@anti-CK and Coum-cathB@anti-Nap accounted mainly for the prevalence of cytokeratin-19 in the cells (**Figure 3.18c**). These results were further visualized by fluorescence imaging experiments, confirming the potential of the probes for interference-free multiplexing applications (**Figure 3.18d** and **3.19**).

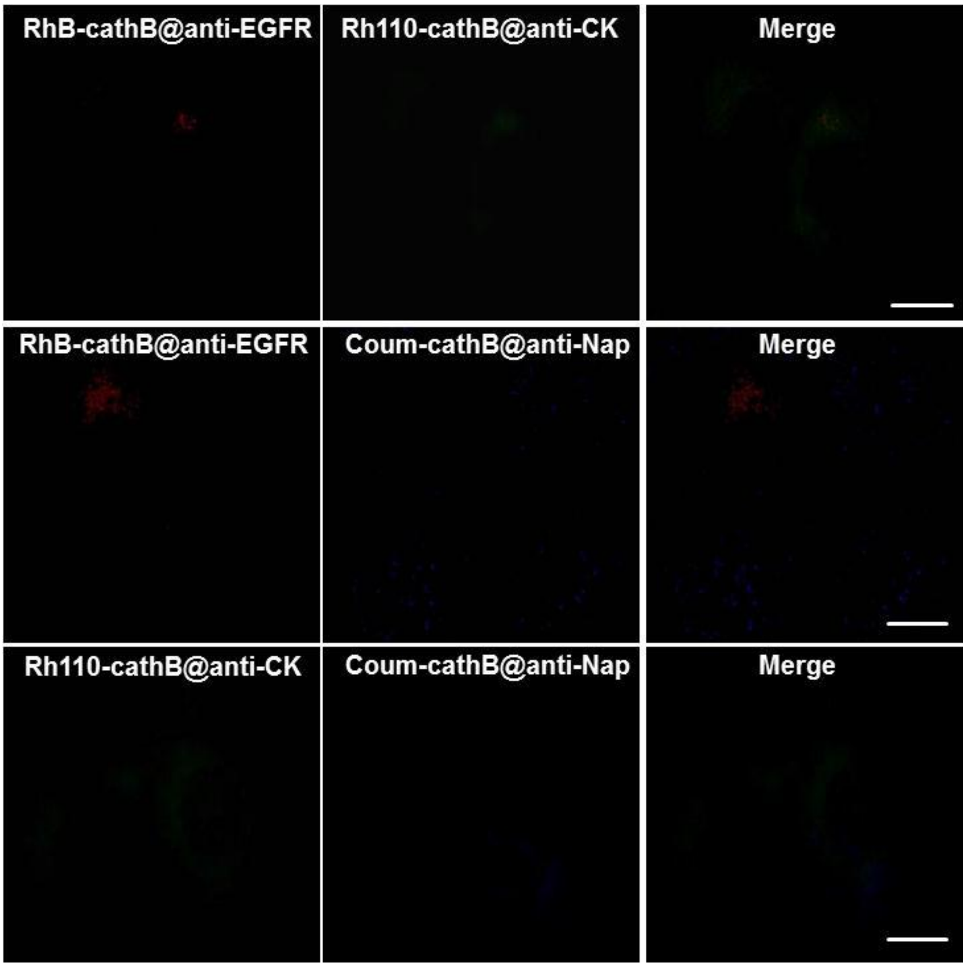

Figure 3.19. Fluorescence microscopic analysis of WI38 cells treated with a mixture of two antitags each. Blue channel at 440-480 nm, green channel at 510-550 nm and red channel at 580-620 nm. Scale bar 10 µm.

In a final evaluation, a cocktail of all the three nanotags were administered to the cancer cells (**Figure 3.20a**). It is interesting to note that SERS (**Figure 3.20A** and **3.22a**) and fluorescence imaging studies (**Figure 3.20B**) showed the specific recognition of the tags to their respective protein codes without any cross-talk between cocktail antitags, emphasizing the suitability of the assay for profiling the right protein from a pool of other structurally and functionally similar biomolecules in a complex biological setting. The same experiment has been repeated with the normal WI-38 cells which produced weak signals as indicated in **Figure 3.21** and **3.22b**. These results demonstrate the utility of the probes for differential diagnosis of biomarker status in cancer and normal

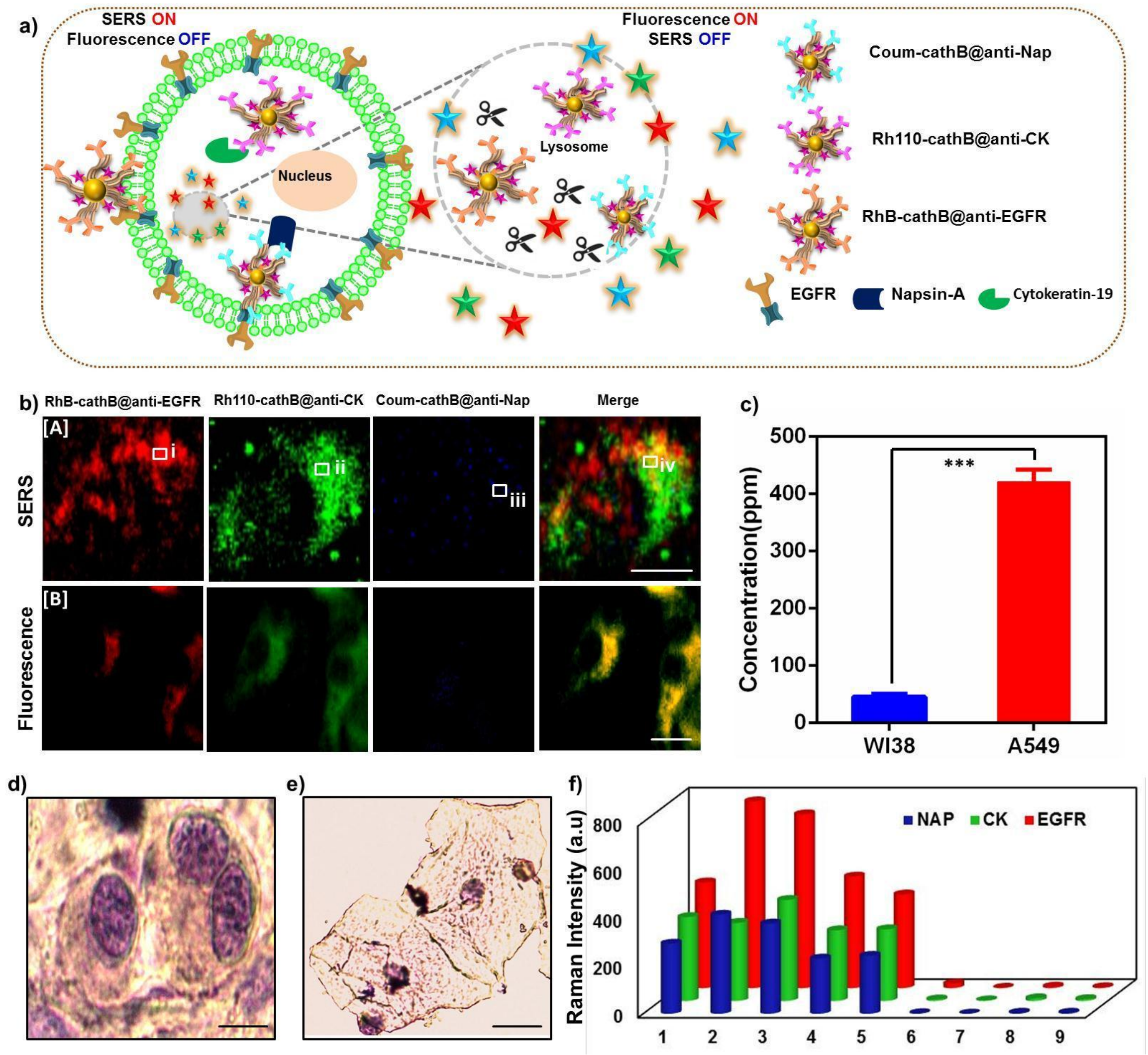

Figure 3.20. a) Schematic illustration of the multiplexing detection of the biomarkers in lung cancer cells by the cocktail probe. b) Confocal SERS (A) and fluorescence (B) microscopic analysis of EGFR, CK and Nap in A549 cells after treatment with the cocktail probe. Scale bar 10 µm. SERS images acquired by imaging RhB-cathB@anti-EGFR, Rh110-cathB@anti-CK and Coum-cathB@anti-Nap at 617, 354 and 837 cm^{-1} respectively. c) ICPMS analysis of gold content in A549 and WI38 cells incubated with the cocktail probe (*** $p < 0.001$). Representative bright field microscopic images of sputum specimens collected from a cancer patient (d) and a normal healthy person (e). Scale bar 10 µm. f) Evaluation of EGFR, CK and Nap levels in sputum specimens treated with the probe by SERS analysis. Data represent the mean ± SD of three independent experiments.

cells. These observations were further supported by inductively coupled plasma mass spectrometry (ICP-MS) analysis, wherein the A549 cells administered with the cocktail showed significantly ($p < 0.001$) higher gold content of 421.13 ± 21 ppm against the very low concentration of 45.70 ± 5 ppm in the normal cell line, indicating the target specific accumulation of our probe in cancer cells (**Figure 3.20c**).

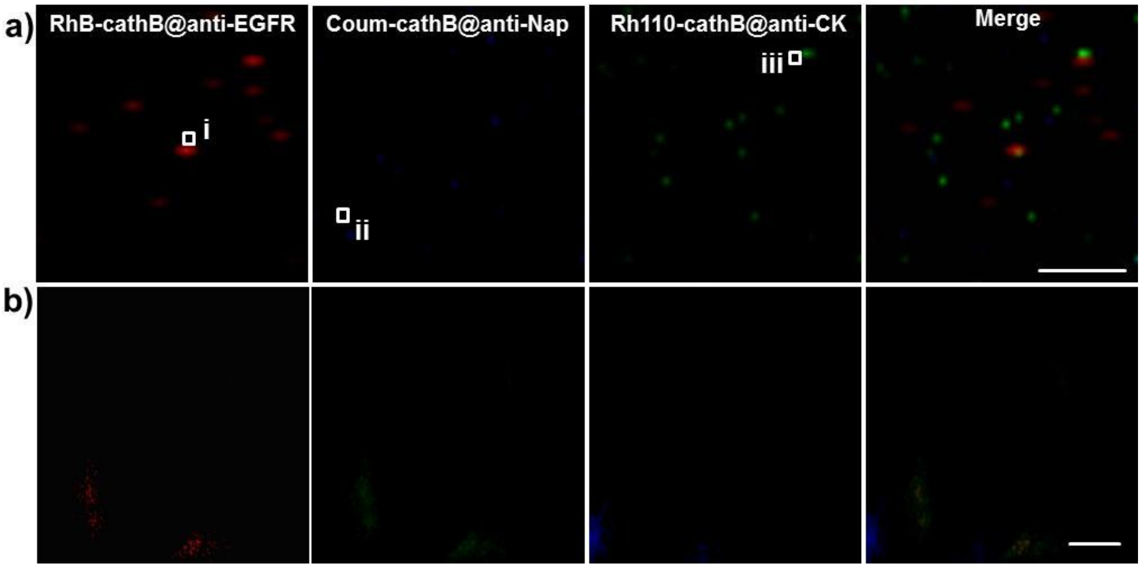

Figure 3.21. a) SERS and b) fluorescence microscopic analysis of WI38 cells treated with the cocktail probe. SERS images collected at 617, 354 and 837 cm^{-1} for RhB-cathB@anti-EGFR, Rh110-cathB@anti-CK and Coum-cathB@anti-Nap respectively. Blue channel at 440-480 nm, green channel at 510-550 nm and red channel at 580-620 nm. Scale bar 10 μm.

3.3.4. Validation of Antitag Cocktail Nanoprobe as a Clinical Screening Tag towards Point-of-care Diagnosis of Lung Cancer Biomarkers

As a major step forward, the real potential of the multiplex antitag cocktail probe was investigated in the clinical scenario via the detection of target proteins from the sputum samples of lung cancer patients. Most of the currently available methods such as virtual bronchoscopy, chest X-rays, spiral computed tomography are not promising candidates for the early detection of lung cancer. The role of sputum cytology for early diagnosis is being evaluated as it is a noninvasive and easy procedure to screen but the conventional method often rely on morphological changes alone which may sometimes lead to false positive results.[51-54] Towards developing a validated screening method for lung cancer, the present strategy was explored to assess the biomarker levels by administration of the antitag cocktail to the sputum samples. Prior to the experiment, the samples were made free of mucus by continuous rounds of washing with alcoholic solution of dithiothreitol (DTT). The microscopic cytological evaluation of sputum specimen obtained from a cancer patient and a healthy person is represented in **Figure 3.20d** and **3.20e** respectively. SERS analysis of the samples from patients diagnosed with lung adenocarcinoma showed noticeably higher expressions of EGFR, CK and Nap as evident from the unique spectral fingerprints of the cocktail probe (**Figure 3.20f**). On the other hand, the cocktail probe presented negligible signals in the samples collected from normal healthy persons, thereby validating the specificity of the probes as promising tools for cancer detection and diagnosis. However, the treatment of the samples with the cocktail probe didn't elicit any significant fluorescence response. The loss of fluorescence property can be attributed to the loss of cathB enzyme activity which might have happened during the fixation of

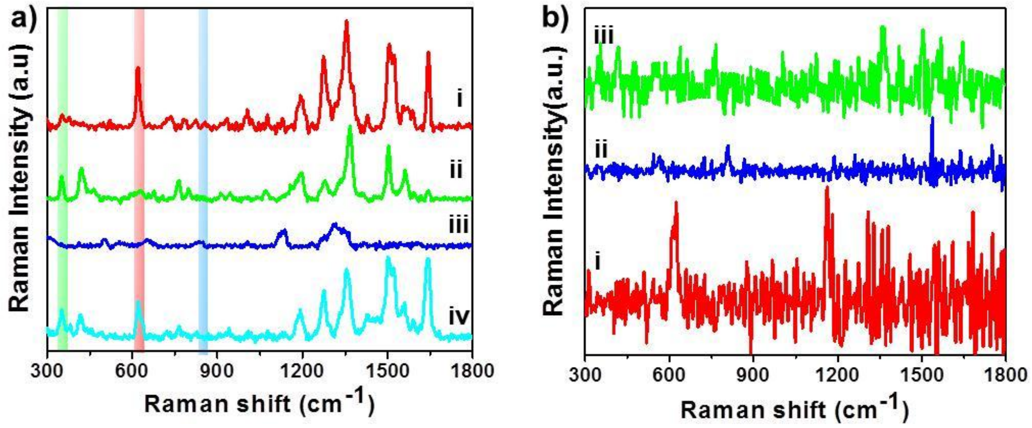

Figure 3.22. a) SERS spectra obtained from A549 cells treated with the cocktail probe. i), ii), iii) and iv) represent the spectra extracted from the respective points shown in Figure 3.20A. b) Representative SERS spectra obtained from the labeled points of the WI-38 cells shown in Figure 3.21a.

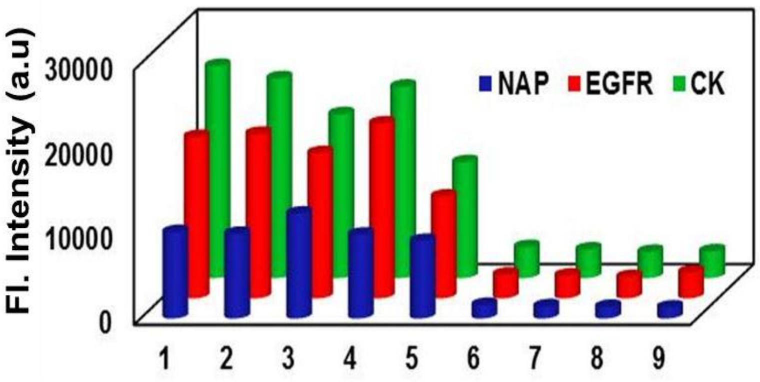

Figure 3.23. Evaluation of EGFR, CK and Nap in sputum specimens treated with cathepsin B enzyme after incubation with the cocktail probe as measured by fluorescence analysis (λ_{ex} : 360 nm and λ_{em} : 450 nm for Coum-cathB@anti-Nap; λ_{ex} : 475 nm and λ_{em} : 520 nm for Rh110-cathB@anti-CK; λ_{ex} : 520 nm and λ_{em} : 580 nm for RhB-cathB@anti-EGFR.

the sputum specimens with alcohol, which in turn prevented the cleavage of the dye from gold surface, thereby arresting the fluorescence recovery of the latent fluorophores. In an effort to restore the fluorescence property, the sputum samples treated with the probe were administered with external cathB enzyme. As expected, the fluorescence of the bound tags got switched on via the enzyme cleavage process which also allowed the clear discrimination of cancer patients from normal ones (**Figure 3.23**). This proof-of-concept strategy is believed to provide a blueprint for the diagnosis and differential staging of lung cancer into various histological subtypes based on the differential expression of the antigens, which may provide huge impacts in future clinical practices.

3.4. Conclusion

In conclusion, enzyme driven fluorescence-SERS encoded nanoparticle probes capable of sensitive and specific profiling of disease targets through multimodal approach were developed as an efficient biomarker detection protocol. The interplay of cathB enzyme with the newly developed nanoprobe facilitated the accurate and simultaneous detection of multiple targets through fluorescence and SERS modalities via an ‘on-off’ switching mechanism. The highly efficient bimodal approach achieved specific recognition of single as well as multiple biomarkers in a complex biological setting through multi-color image guided spectral tracking. Semi-quantitative evaluation of biomarkers through both the modalities revealed ≈ 15, 8 and 1.2 fold increase in the respective EGFR, CK and Nap levels in the cancer cells against the normal ones. Furthermore, the as-described platform provides accurate multiplexing of target antigens in the pathologically tested patient specimens which offer new avenues for the development of a clinical screening tag for point-of-care diagnosis and personalized treatment applications. In view of the huge impact made by nanotechnology in cancer detection and management, these smartly engineered nanostructures are expected to serve as a promising platform for high throughput screening assisted early diagnosis of diseases.

3.5. Experimental Section

3.5.1. Materials and Methods

All chemicals, unless otherwise mentioned, were purchased from Sigma-Aldrich Co. All antibodies were purchased from Santa Cruz Biotechnology, Inc. The solvents used were of reagent grade and were purchased from local companies. ^{1}H NMR spectra were recorded on a Bruker 500 MHz FT-NMR (model: Advance-DPX 300) spectrometer at 25 ºC. The chemical shift (δ) data and coupling constant (J) values were represented in parts per million (ppm) and Hertz (Hz), respectively. High-resolution mass spectra (HRMS) were recorded on a Thermo Scientific Exactive ESI-MS spectrophotometer. TEM imaging was performed on a FEI (TECNAI G^2 30 S–TWIN) microscope with an accelerating voltage of 100 kV and without staining. The samples were prepared by drop casting over a carbon coated copper grid. Experimental procedures for the absorption and fluorescence spectral measurements and *in vitro* cytotoxicity assay are described in the previous chapter.

3.5.2. Description of Experimental Techniques

3.5.2.1. SERS Spectral Measurements

SERS experiments were carried out using a WI-Tec Raman microscope (WI-Tec, Inc., Germany) containing 600 g/mm grating and Peltier cooled CCD detector unit. The samples were excited using a 633 nm laser with 7 mW power and the Stoke shifted Raman spectra were collected in the region of 300-1800 cm^{-1} with a resolution of 1 cm^{-1} and an integration time of 1 sec and 10 accumulations. Prior to each measurement, calibration was done with a silicon standard (Raman peak at 520 cm^{-1}). Data processing was carried out using WI-Tec Project Plus (v2.1) software package.

3.5.2.2. Preparation of Antibody Tagged FSENPs for the Multiplexed Recognition of Lung Cancer Biomarkers

Three Raman active fluorophores (7-hydroxy-coumarin-3-carboxylic acid, rhodamine 110 and rhodamine B) were covalently conjugated to the amine terminal of the tripeptide, Phe-Lys-Cys which were then incubated with gold nanoparticles of size 40 nm to obtain multifunctional **FSENP**s in 1:9 (v/v) ratio. The as-obtained nanoprobes were PEGylated and functionalized with three antibodies (anti-EGFR, anti-CK and anti-Nap) to furnish Coum-cathB@anti-Nap, Rh110-cathB@anti-CK and RhB-cathB@anti-EGFR.

3.5.2.3. SERS Imaging of Cells

SERS detection of A549 and WI-38 cells were performed using confocal Raman microscopy. For SERS imaging, cells were cultured in 4-well chamber slides which were incubated with the constructs containing 10 µM concentrations of the dye molecules for 90 minutes and washed with PBS (pH 7.4) twice to remove the excess probes from the medium. SERS imaging experiments were performed using WI-Tec Raman microscope (WI-Tec, Inc., Germany). The images were acquired on a 50 x 50 μm mapping area along the X and Y directions with 150 x 150 points per line and an integration time of 0.05 s.

3.5.2.4. Fluorescence Imaging of Cells

Fluorescence detection of the probes in A549 and WI-38 cells were performed using fluorescence microscopic technique as detailed in **Chapter 2**. The fluorescence was collected in the ranges of 440-480 nm (blue), 510-550 nm (green) (λ_{ex}@ 480 nm) and 580−620 nm (red) (λ_{ex}@ 560 nm) respectively. Image processing was performed with Progress software and analysis was carried out using Image J software (version 1.48, NIH, USA).

3.5.2.5. Subcellular Co-localization Imaging

For labeling of lysosomes, A549 and WI-38 cells were treated with Lysotracker Red/Lysotracker Green in PBS (pH 7.4), 30 min prior to imaging. The cells were also co-stained with the probes in PBS (pH 7.4) for 60 min and fluorescence images were acquired as described in **Chapter 2**. Images were collected in the ranges of 510-550 nm (green) for Lysotracker Green and 580-620 nm (red) for Lysotracker Red. Image processing and analyses were performed with the softwares, Progress, Image J (version 1.48, NIH, USA) and MATLAB 8.3 (MATLAB R2014a, MA, USA). The extent of co-localization was calculated using Pearson´s correlation coefficient (r) and Manders overlap coefficients (R). The Pearson´s correlation and Manders overlap coefficients (r and R, respectively) are defined as follows:

$$r = \frac{\sum (S1i - S1mean) \times (S2i - S2mean)}{\sqrt{\sum (S1i - S1mean)^2 \times (S2i - S2mean)^2}}$$

and

$$R = \frac{\sum S1i \times S2i}{\sqrt{\sum (S1i)^2 \times \sum (S2i)^2}}$$

where S1*i* and S2*i* represent signal intensity of pixels in channel 1 and channel 2 respectively; $S1_{mean}$ and $S2_{mean}$ denote the average intensities of their respective channels. r is invariant to background and intensity scales, and thus serves as a robust estimator for co-localization. All data were expressed as mean ± standard deviation.

3.5.2.6. Statistical Analysis

The data were expressed as the mean ± standard deviation (SD) of the three replicates and analyzed using Graph Pad PRISM software version 5.0 (San Diego, USA). One-way analysis of variance was used for the repeated measurements and the differences were considered to be statistically significant if $p < 0.05$. Images were analyzed using Image J and MATLAB R 2014a software using custom made algorithms.

3.5.2.7. Western Blot Analysis

Proteins were extracted from A549 and WI-38 cells (2 x10^6) using RIPA buffer (Thermo Scientific, Rockford, IL, USA). The concentration of proteins was then estimated using Coomassie Plus Protein Assay reagent and bovine serum albumin (BSA) standards. Proteins were separated by 10% SDS-PAGE and subsequently transferred to polyvinylidene difluoride membranes (Millipore, Billerica, MA, USA). The transferred membranes were blocked with 5% skim milk and incubated with the specific primary antibodies. Horseradish peroxidase (HRP) conjugated secondary antibody was used for all primary antibodies which were detected by the chemiluminescent ECL substrate (Bio-Rad, USA). The resulting bands were then quantified using Image J software and normalized with beta-actin.

3.5.2.8. Immunocytochemical Staining of A549 and WI-38 Cells using anti-EGFR, anti-CK and anti-Nap Antibodies

Cells were fixed in absolute alcohol, which were then kept in methanol and subsequently in 70% ethanol. Then the cells were dipped in distilled water for 5 min and finally in sodium deoxycholate. After 15 min, cells were washed with distilled water which were then subjected to treatment with antigen retrieval solution made of trisodium citrate. After blocking the peroxidase activity, cells were incubated with primary antibodies overnight. Next day, primary block has been added which was then incubated with novolink polymer after the washing process. Staining was done by the addition of 3,3´–diaminobenzidine chromogen followed by washing with distilled water. Counterstaining was performed with haematoxylin and the slides were then dehydrated with 50%, 95% and 100% ethanol and finally with xylene. In the final step, permanent mounting of the slides were performed using DPX.

3.5.2.9. Atomic Force Microscopy Imaging Experiments

Adherent cancer cells (A549) and normal cells (WI-38) were grown overnight on 12 mm circular glass coverslips with 10% DMEM on 24-well culture plates for a period of 24 h. Cells were then incubated with RhB-cathB@anti-EGFR for 2 h. The cells in the cover slips were washed well with ice cold PBS thrice and fixed with 4% paraformaldehyde and were carefully taken out for imaging. Gold nanoparticles were subjected to AFM experiments by drop casting the solution on freshly cut mica surface after thorough drying under vacuum. AFM images were recorded under ambient conditions using a NTEGRA (NT-MDT) microscope operating with a tapping mode regime. Micro-fabricated TiN cantilever tips (NSG10) with a resonance frequency of 299 kHz and a spring constant of 20-80 Nm^{-1} was used. AFM section analysis was done offline.

3.5.2.10. ICP-MS Measurements for Nanoparticle Internalization in Cells

For ICP-MS analysis in A549 and WI-38 cells, the cells were first seeded in 12-well plates (1×10^5 cells/well), which were then incubated with the probe for a period of 24 h. Prior to analysis, cells were washed with PBS thrice to wash off the unbound probe molecules. Cells were then trypsinized and lysed with PBS containing 1% Triton-X with vigorous vortexing. The cell lysate was then subjected to digestion in a microwave reactor (Anton Paar, Multiwave 3000) by mixing the sample with aquaregia in 1:2 v/v ratio. The samples were held at zero ramp time at a power of 400 W for 25 min, which was then retained at 5 ramp and 500 W power for 30 min. After cooling, the sample vials were opened and the samples were diluted to 100 mL with Type 1 water (Thermo Scientific, Barnstead, Smart 2 pure). The vials were closed and shaken vigorously to complete the dissolution which was finally subjected to ICP-MS analysis using Thermo Scientific iCAP Qc spectrometer.

3.5.2.11. Processing of sputum specimens

Fresh sputum samples were treated with 0.2% DTT in 60% ethanol. After vortexing for 30 min at room temperature, the samples were subjected to centrifugation (600g, 5 min). Cell pellet was re-suspended with equal volume of alcoholic solution of DTT and the same process was repeated until the samples were free of mucus. The samples were treated with the cocktail probe for 60 min and then washed with PBS four times to remove the unbound tags. Following the washing process, the samples were subjected to analysis.

3.5.3. Synthesis and Characterization

Synthesis of Phe-Lys-Cys (FKC) cathB Peptide Sequence (4)

The synthesis of the cathB sequence, FKC was performed using solid phase peptide synthesis with rink amide resin as the solid support. Firstly, the resin was swelled in dry dichloromethane (DCM) which was then washed with *N,N*-dimethyl formamide (DMF) (3 × 3 mL) and the Fmoc protection group was removed by treating with piperidine in DMF (20%, 2 × 5 mL, 2 × 25 min). After washing with DMF (3 × 3 mL), Fmoc-Cys(STr)-COOH (165 mg, 0.426 mmol) was charged to the resin bed after activating with 2-(1*H*-benzotriazo-1-yl)-1,1,3,3-tetramethyluronium hexafluorophosphate (HBTU, 161 mg, 0.426 mmol) and diisopropyl ethylamine (DIPEA) (2 or 3 drops). The reaction was continued for 12 h under mechanical shaker and the progress of the reaction was monitored by Kaiser test. After completion of the coupling reaction, the resin was washed with

DMF (3 × 3 mL) and Fmoc group was deprotected by treatment with 20% piperidine in DMF as in the same manner. The reaction cycle was continued in a similar manner with Fmoc-Lys-(Boc)-OH (260 mg, 0.426 mmol) and Fmoc-Phe-OH (195 mg, 0.426 mmol) amino acids were charged to the resin to yield resin bound peptide.

General Procedure for the Syntheses of Coum-cathB, Rh110-cathB and RhB-cathB

After subjecting the peptide bound resin (**4**) (0.01 mmol) to Fmoc deprotection using 20% piperidine in DMF (2 × 5 mL, 2 × 25 min), a solution of *N, N'*-diisopropylcarbodiimide (DIC, 0.03 mmol) was added and stirred for 20 minutes. Then a solution of hydroxybenzotriazole (HOBt, 0.03 mmol) in dry DCM was added together with 0.03 mmol of dye (7-hydroxycoumarin-3-carboxylic acid/ rhodamine 110/ rhodamine B) and the mixture was stirred for about 16-20 h at room temperature. After completion of the reaction, the resin containing the dye conjugated peptides were washed with DMF followed by DCM (3 × 5 mL) to remove the unbound dyes. Finally the dye labeled peptides were cleaved from the resin bed by treatment with 95% trifluoroacetic acid (TFA), 2.5% triisopropyl silane (TIS) and 2.5% water (cleavage cocktail for rinkamide resin) to afford Coum-cathB, Rh110-cathB and RhB-cathB. The resulting residues were concentrated and finally precipitated in diethylether to obtain the products in pure form.

Coum-cathB: ^{1}H NMR (500 MHz, CD_3COCD_3, TMS): δ 8.792 (s, 1H), 7.890 (s, 1H), 7.544 (d, 1H), 7.23-7.01 (m, 6H), 6.83 (s, 1H), 6.7 (s, 1H), 4.76-4.37 (m, 3H), 3.63-3.54 (m, 4H), 3.27 (dd, J_1=15 Hz, J_2 = 10 Hz, 3H), 1.84-1.79 (m, 1H), 1.66-1.57 (m, 3H), 1.31 (bs, 1H) ppm. HRMS calculated for $C_{28}H_{33}N_5O_7S$ (M + Na): 606.21, found: 606.20.

Rh110-cathB: ^{1}H NMR (500 MHz, CD_3COCD_3, TMS): 7.85 (s, 2H), 7.50-7.36 (m, 2H), 7.27-7.08 (m, 3H), 6.90 (s, 1H), 6.86-6.81 (m, 4H), 6.34-6.24 (m, 2H), 6.15 (s, 1H), 4.56-4.39 (m, 2H), 4.06-3.81 (m, 3H), 3.63 (s, 2H), 3.31-3.26 (m, 3H), 2.98-2.97 (m, 2H), 2.76 (bs, 1H), 2.08-2.02 (m, 1H), 1.43 (bs, 2H), 1.23-1.07 (m, 4H), 0.98 (t, 1H), ppm. HRMS calculated for $C_{38}H_{41}N_7O_5S$ (M^+): 707.29, found: 708.29.

RhB-cathB: ^{1}H NMR (500 MHz, CD_3COCD_3, TMS): 7.86 (s, 2H), 7.45-7.37 (m, 2H), 7.26-7.11 (m, 7H), 6.96-6.78 (m, 3H), 6.40-6.24 (d, 3H), 5.94-5.74 (m, 1H), 5.19 (s, 1H), 4.57-4.48 (m, 2H), 4.11-3.90 (m, 3H), 3.64 (t, 2H), 3.27 (dd, J_1=15 Hz, J_2 = 10 Hz 3H), 3.17-2.69 (m, 6H), 2.07-2.04 (m, 1H), 1.82-1.57 (m, 6H), 1.16 (s, 2H), 1.07-1.01 (m, 1H), 0.98 (t, 6H) ppm. HRMS calculated for $C_{46}H_{58}N_7O_5S$ (M+Na): 843.42, found: 842.40.

Synthesis of Gold Nanoparticles

Synthesis of gold nanoparticles of size 40 nm was achieved by citrate reduction method described by Turkevich and his co-workers.[55] In a typical synthesis, water was heated to boiling to which 100 µL of chloroauric acid solution (250 mM) was added. After stirring for 10 minutes, an aqueous solution of sodium citrate (100 mM) was added resulting in the color change from yellow to dark purple to red within 5 min. The solution was then cooled to room temperature under stirring at 600 rpm. The as-formed gold nanoparticles were characterized by UV-Vis spectrophotometry and TEM analysis.

PEGylation and Antibody Conjugation of Dye Labeled Gold Nanoparticles

The dye tagged peptides were incubated with gold nanoparticles for a period of 15 minutes which was then treated with HS-PEG-COOH. After shaking for 15 min, the as-obtained dye nanoparticle conjugate was incubated with PEG-SH to provide high surface coverage and stability for the nanoparticle. After 3 h, free PEG molecules were removed by continuous rounds of washing and centrifugation (8000 rpm, 20 min) and the pellet was dispersed in PBS for antibody conjugation.

The carboxyl groups of the PEGylated nanoparticles were activated by addition of *N*-(3-(dimethylamino)-propyl)-*N'*-ethylcarbodiimide (EDC, 25 mM) and *N*-hydroxysuccinimide (NHS, 25 mM). After 30 min, excess reagents were removed by centrifugation (8000 rpm, 20 min) and the nanotags were re-suspended in PBS which were subsequently reacted with antibodies for 2 h. After keeping the tags overnight at 4 °C, the unbound antibodies were removed by 4 rounds of centrifugation (10,000 rpm, 5 min) to afford the antibody conjugated tags.

3.6. References

[1] Kosaki, Y.; Izawa, H.; Ishihara, S.; Kawakami, K.; Sumita, M.; Tateyama, Y.; Ji, Q.; Krishnan, V.; Hishita, S.; Yamauchi, Y.; Hill, J. P.; Vinu, A.; Shiratori, S.; Ariga, K. *ACS Appl. Mater. Interfaces* **2013**, *5*, 2930.

[2] Komiyama, M.; Yoshimoto, K.; Sisido, M.; Ariga, K. *Bull. Chem. Soc. Jpn.* **2017**, *90*, 967.

[3] Kim, H. J.; Kim, A.; Miyata, K.; Kataoka, K. *Adv. Drug Deliv. Rev.* **2016**, *104*, 61.

[4] Zheng, G.; Patolsky, F.; Cui, Y.; Wang, W. U.; Lieber, C. M. *Nat. Biotechnol.* **2005**, *23*, 1294.

[5] Zhang, Y.; Guo, Y.; Xianyu, Y.; Chen, W.; Zhao, Y.; Jiang, X. *Adv. Mater.* **2013**, *25*, 3802.

[6] Giljohann, D. A.; Seferos, D. S.; Daniel, W. L.; Massich, M. D.; Patel, P. C.; Mirkin, C. A. *Angew. Chem. Int. Ed.* **2010**, *49*, 3280.

[7] Chen, S.; Svedendahl, M.; van Duyne, R. P.; Kall, M. *Nano Lett.* **2011**, *11*, 1826.

[8] Saha, K.; Agasti, S. S.; Kim, C.; Li, X.; Rotello, V. M. *Chem. Rev.* **2012**, *112*, 2739.

[9] Panikkanvalappil, S. R.; Mackey, M. A.; El-Sayed, M. A. *J. Am. Chem. Soc.* **2013**, *135*, 4815.

[10] Kricka, L. J. *Clin. Chem.* **1992**, *38*, 327.

[11] Ho, S.-L.; Xu, D. Wong, M. S.; Li, H. W. *Chem. Sci.* **2016,** *7*, 2695.

[12] Hu, J.; Zhang, C. *Chem. Commun.* **2014**, *50*, 13581.

[13] Altelaar, A. F.; Munoz, J.; Heck, A. J. R. *Nat. Rev. Genet.* **2012**, *14*, 35.

[14] Gaster, R. S.; Hall, D. A.; Nielsen, C. H.; Osterfeld, S. J.; Yu, H.; Mach, K. E.; Wilson, R. J.; Murmann, B.; Liao, J. C.; Gambhir, S. S.; Wang, S. X. *Nat. Med.* **2009**, *15*, 1327.

[15] Perfetto, S.P.; Chattopadhyay, P.K.; Roederer, M. *Nat. Rev. Immunol.* **2004**, 4, 648.

[16] Smith, A. M.; Nie, S. *J. Am. Chem. Soc.* **2011**, *133*, 24.

[17] Lim, D.-K.; Jeon, K.-S.; Hwang, J.-H.; Kim, H.; Kwon, S.; Suh, Y. D.; Nam, J-M. *Nat. Nanotech.* **2011**, *6*, 452.

[18] Bruchez, M.; Moronne, M.; Gin, P.; Weiss, S.; Alivisatos, A. P. *Science* **1998**, *281*, 2013.

[19] Rao, J.; Dragulescu-Andrasi, A.; Yao, H. *Curr Opin Biotechnol.* **2007**, *18*, 17.

[20] Lane, L. A.; Qian, X.; Nie, S. *Chem. Rev.* **2015**, *115*, 10489.

[21] Wang, Z.; Zong, S.; Wu, L.; Zhu, D.; Cui, Y. *Chem. Rev.* **2017**, *117*, 7910.

[22] Narayanan, N.; Nair, L. V.; Karunakaran, V.; Joseph, M. M.; Nair, J. B.; Ramya A. N., Jayasree, R. S.; Maiti, K. K. *Nanoscale* **2016**, *8,* 11392.

[23] Niu, X.; Chen, H.; Wang, Y.; Wang, W.; Sun, X.; Chen, L. *ACS Appl. Mater. Interfaces* **2014**, *6*, 5152.

[24] Liu, J.; Lau, S. K.; Varma, V. A.; Moffitt, R. A.; Caldwell, M.; Liu, T.; Young, A. N.; Petros, J. A.; Osunkoya, A. O.; Krogstad, T.; Leyland-Jones, B.; Wang, M. D.; Nie, S. *ACS Nano* **2010**, *4*, 2755.

[25] Wang, F.; Banerjee, D.; Liu, Y.; Chen, X.; Liu, X. *Analyst* **2010**, *135*, 1839.

[26] Rauf, S.; Glidle, A.; Cooper, J. M. *Chem. Commun*. **2010**, *46*, 2814.

[27] Saranya, G.; Anees, P.; Joseph, M. M.; Maiti, K. K.; Ajayaghosh, A. *Chem. Eur. J.* **2017**, *23*, 7191.

[28] Medintz,I. L.;Uyeda, H. T.;Goldman,E. R.;Mattoussi, H. *Nat. Mater.* **2005**, *4*, 435.

[29] Wang, Y.; Yan, B.; Chen, L.; *Chem. Rev.* **2012**, *113*, 1391.

[30] Cheng, Z.; Choi, N.; Wang, R.; Lee, S.; Moon, K. C.; Yoon, S.-Y.; Chen, L.; Choo, J. *ACS Nano* **2017**, *11*, 4926.

[31] Maiti, K. K.; Samanta, A.; Vendrell, M.; Soh, K.-S.; Olivo, M.; Chang, Y.-T. *Chem. Commun.* **2011**, *47*, 3514.

[32] Zavaleta, C. L.; Smith, B. R.; Walton, I.; Doering, W.; Davis, G.; Shojaei, B.; Natan, M. J.; Gambhir, S. S. *Proc. Natl. Acad. Sci. U. S. A.* **2009**, *106*, 13511.

[33] Xu, L.; Yan, W.; Ma, W.; Kuang, H.; Wu, X.; Liu, L.; Zhao, Y.; Wang, L.; Xu, C. *Adv. Mater.* **2015**, *27*, 1706.

[34] Lee, S.; Chon, H.; Yoon, S.-Y.; Lee, E. K.; Chang, S.-I.; Lim, D. W.; Choo, J. *Nanoscale* **2012**, *4*, 124.

[35] Yu, K. N.; Lee, S.-M.; Han, J. Y.; Park, H.; Woo, M.-A.; Noh, M. S.; Hwang, S.-K. Kwon, J.-T.; Jin, H.; Kim,Y.-K.; Hergenrother, P. J.; Jeong, D. H.; Lee, Y. S.; Cho, M.-H. *Bioconjugate Chem.* **2007**, *18*, 1155.

[36] Woo, M.-A.; Lee, S. M.; Kim, G.; Baek, J. H.; Noh, M. S.; Kim, J. E.; Park, S. J.; Tehrani, A.; Park, S,-C.; Seo, Y. T.; Kim, Y.-K.; Lee, Y.-S.; Jeong, D. H.; Cho, M.-H. *Anal. Chem.* **2009**, *81*, 1008.

[37] Wang, Y.; Chen, L.; Liu, P. *Chem. Eur. J.* **2012**, *18*, 5935.

[38] Jeong, S.; Kim, Y.; Kang, H.; Kim, G.; Cha, M. G.; Chang, H.; Jung, K. O.; Kim, Y.-H.; Jun, B.-H.; Hwang, D. W.; Lee, Y.-S.; Youn, H.; Lee, Y.-S.; Kang, K. W.; Lee, D. S.; Jeong, D. H. *Sci. Rep.* **2015**, *5*, 1.

[39] Zhang, Y.; Wang, Z.; Wu, L.; Zong, S.; Yuna, B; Cui, Y. *RSC Adv.* **2016**, *6*, 81046.

[40] Zhong, Y.-J.; Shao, L.-H.; Li, Y. *Int. J. Oncol.* **2013**, *42*, 373.

[41] Roshy, S.; Sloane, B. F.; Moin, K. *Cancer Metastasis Rev.* **2003**, *22*, 271.

[42] Cavallo-Medved, D.; Mai, J.; Dosescu, J.; Sameni, M.; Sloane, B. F. *J Cell Sci.* **2005**, *118*, 1493.

[43] Thomssen, C.; Schmitt, M.; Goretzki, L.; Oppelt, P.; Pache, L.; Dettmar, P.; Janicke, F.; Graeff, H. *Clin. Cancer Res.* **1995**, *1*, 741.

[44] Strojnik, T.; Kos, J.; Zidanik, B.; Golouh, R.; Lah, T.; *Clin. Cancer Res.* **1999**, *5*, 559.

[45] Zhang, H.; Fu, T.; Mcgettigan, S.;Kumar, S.; Liu, S.; Speicher, D.; Schuchter, L.; Xu, X. *Int J Mol Sci.* **2011**, *12*, 1505.

[46] Choi, K. Y.; Swierczewska, M.; Lee, S.; Chen, X., *Theranostics* **2012**, *2*, 156.

[47] Nilsson, C., Kagedal, K., Johansson, U., Ollinger, K. *Methods Cell Sci.* **2004**, *25*, 185.

[48] Bethune, G.; Bethune, D.; Ridgway, N.; Xu, Z.; *J Thorac Dis.* **2010**, *2*, 48.

[49] Stieber, P.; Bodenmuller, H.; Banauch, D.; Hasholzner, U.; Dessauer, A., Ofenloch-Hahnle, B.; Jaworek, D.; Fateh-Moghadam, A. *Clin. Biochem.* **1993**, *26*, 301.

[50] Turner, B.M.; Cagle, P.T.; Sainz, I.M.; Fukuoka, J.; Shen, S.S.; Jagirdar, J. *Arch Pathol Lab Med.* **2012**, *136*, 163.

[51] Mao, L.; Hruban, R. H.; Boyle, J. O.; Tockman, M.; Sidransky, D. *Cancer Res.* **1994**, *54*, 1634.

[52] Mulshine, J. L.; *Nat. Rev. Cancer*, **2003**, *3*, 65.

[53] McWilliams, A.; MacAulay, C.; Gazdar, A. F.; Lam, S. *Oncogene* **2002**, *21*, 6949.

[54] Schmiemann, V.; Bocking, A.; Kazimirek, M.; Onofre, A. S. C.; Gabbert, H. E.; Kappes, R.; Gerharz, C. D.; Grote, H. J. *Clin. Cancer Res.* **2005**, *11*, 7728.

[55] Enustun, B.V. ; Turkevich, J. *J. Am. Chem. Soc.* **1963**, 85, 3317.

Chapter 4

A Singlet Oxygen Photogenerator for Tumor Specific Luminescence Imaging and Intracellular Oxygen Independent Multiphase Photodynamic Therapy

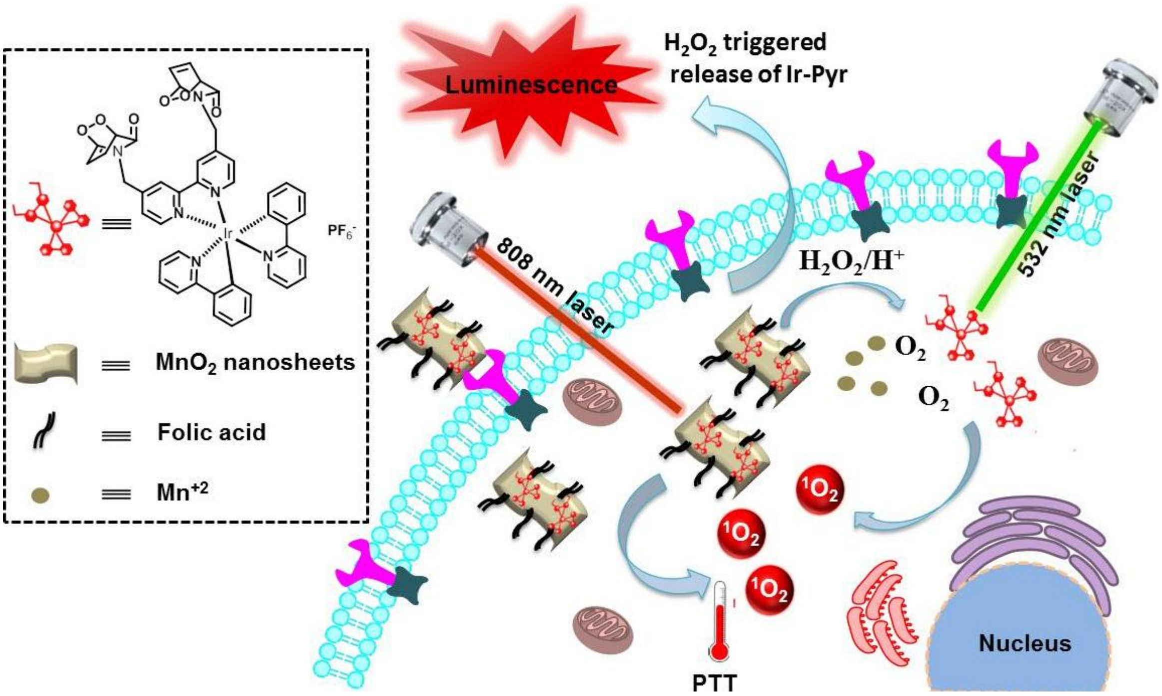

4.1. Abstract

*Hypoxia, as featured by low oxygen concentrations severely attenuates the treatment outcome of photodynamic therapy (PDT), which puts it beyond the reach of a successful therapeutic procedure in clinical scenario. More troublesome, the photosensitization process further worsens the situation by diminishing the available intracellular oxygen reserves, which makes PDT a self-limiting strategy. To address this issue, a new strategy for cutting off the intracellular oxygen consumption has been reported by developing a redox activatable singlet oxygen ($^1O_2$) self-enriched photogenerator (**Ir-Pyr-EPO@MnO$_2$-FA**) for sequential $^1O_2$ generation to overcome hypoxia induced resistance to PDT. Upon target specific accumulation into the cancer cells followed by near infrared light irradiation, the*

photothermal effect generated by MnO_2 nanosheets will facilitate the rapid thermal cycloreversion of the attached ***Ir-Pyr-EPO*** *which in turn release cytotoxic $^1O_2$ to pave way for the first phase of photodynamic therapy. Additionally, the redox responsive features (high H_2O_2 and low pH) of tumor environment causes an activation of the luminescence properties of* ***Ir-Pyr*** *by the reduction of MnO_2, thereby enabling it for self-guided therapeutic applications. Taking advantage of the reduction properties of MnO_2, the so-produced molecular oxygen gets slowly released into the tumor area which provides room for the second stage of PDT by photosensitization using a 532 nm laser. Benefiting from the intracellular oxygen independent multi-phase $^1O_2$ generation properties, the probe displayed excellent therapeutic efficacy in vitro and in vivo by conquering the Achilles Heel of photodynamic therapy, offering opportunities for the development of next generation cancer phototherapeutics.*

4.2. Introduction

Photodynamic therapy (PDT), a minimally invasive treatment protocol has gained tremendous attention in precision medicine owing to its excellent therapeutic potential which in some cases has shown to be effective over the conventional treatment options such as chemotherapy, radiotherapy and surgery.[1-4] However, PDT has not yet been realized as a frontline therapeutic approach besides a few peripheral clinical applications. The limited applicability is not related to the availability of efficient photosensitizers or delivery vehicles instead the problem has been identified at the core of the photodynamic process. Most tumors including the metastatic ones develop a region of low oxygen concentrations (hypoxia) which hampers the production of reactive oxygen species and thereby restrains the PDT process.[5-8] Moreover, PDT itself, by utilizing the intracellular oxygen reserves, leads to severe hypoxia, thereby making the situation more complex. These inevitable hurdles severely affects the therapeutic outcome of the PDT agents in many solid tumors characterized by poor oxygen availability.[9-11] Therefore, attention has been paid more towards this direction to afford a sustainable photodynamic therapy. The direct delivery of molecular oxygen (O_2) by various oxygen carriers such as hemoglobin, perfluorocarbons etc. has been viewed as an effective strategy towards conquering the limits imposed by hypoxia. For instance, Luo *et al.*, reported the fabrication of artificial red blood cells which consisted of a photosensitizer molecule, indocyanine green and an oxygen carrier, hemoglobin held in a biomimetic polymer system. The close proximity between the photosensitizer and the oxygen carrier, held in the nanosystem via hydrophobic and electrostatic interactions enabled self-generation of oxygen for effective production of ROS during the PDT process. Additionally, the as-generated ROS caused the oxidation of hemoglobin in the ferrous state to the cytotoxic ferric

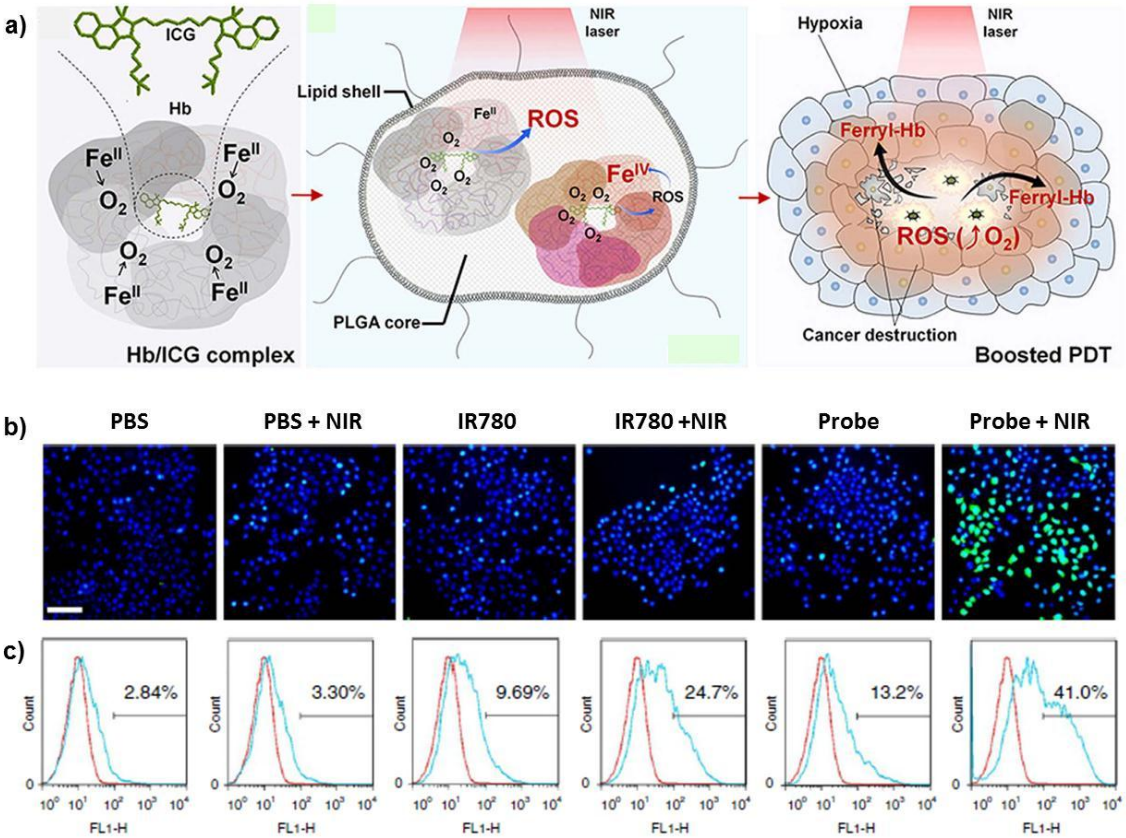

Figure 4.1. a) Schematic representation of artificial blood cells encased photosensitizer system for tumor-boosted PDT. b) Evaluation of ROS generation efficacy of O_2 loaded perfluorocarbon nanodroplets through DCFDA assay. c) Flow cytometry analysis of ROS generation in cells subjected to various treatments detected using DCFDA assay.

ferric form, which accounted for a synergistic effect on the destruction of tumor cells. Furthermore, the nanoprobe enabled the precise monitoring of therapeutic responses via its inherent fluorescence and photoacoustic properties, thereby forming an effective theranostic nanoformulation for cancer management (**Figure 4.1**).[12]

In an alternate strategy, Cheng and coworkers demonstrated the use of O_2 loaded perfluorocarbon (PFC) nanodroplets for self-powered PDT wherein the high loading capacity of perfluorocarbons enabled a more improved and enhanced therapeutic outcome.[13] The NIR photosensitizer held inside the nanoprobe caused the sensitization of the molecular oxygen released from the nanodroplet upon excitation using 808 nm laser, thereby offering a targeted therapeutic application. Recently, Song and colleagues demonstrated the fabrication of a human serum albumin stabilized PFC nanodroplet for ultrasound (US) treatment modulated photodynamic therapy.[14] After intravenous injection of the nanodroplet into 4T1 tumor-bearing mice, the mice were exposed to pure O_2 followed by ultrasound treatment for 30 min. During this procedure, the nanodroplet adsorbs the O_2 into the lungs, takes it to the tumor through the blood stream, and subsequently releases it within the tumor region for an enhanced PDT and radiotherapy (RT) (**Figure 4.2**). Indeed, these strategies have shown success in overcoming hypoxia, however, the re-oxygenation process can serve the cancer cells with an oxygen-rich environment, thereby boosting their proliferative capacity, which can counterbalance the positive treatment response facilitated by the therapeutic process.[15] To resolve this issue, efforts were directed towards conceptualizing the direct transportation of singlet oxygen ($^1O_2$) itself, instead of molecular oxygen, which will directly perform its action on the cancer cells without any intracellular oxygen consumption. Although the approach seems to be impressive, there are severe concerns associated with the very short lifetime of singlet oxygen, making its delivery a challenging task.[16] To this end, aromatic endoperoxides, which act as chemical sources of singlet oxygen, constitute a perfect fit, owing to their potential to *in situ* generate the payload when demanded.[17-20] Endoperoxides of polycyclic aromatic hydrocarbons like naphthalene, anthracene and a few other organic molecules like 2-hydroxypyridine (2-pyridone) have shown to be successful in generating singlet oxygen upon induction with a thermal trigger.[18] In 2016, Kolemen *et al.*, reported the synthesis of a thiol terminated water-soluble 9,10-disubstituted anthracene (**1**) for realizing remote controlled release of singlet oxygen for hypoxic cancer therapy (**Figure 4.3**).[21] The molecule **1** was further functionalized with NIR absorbing gold

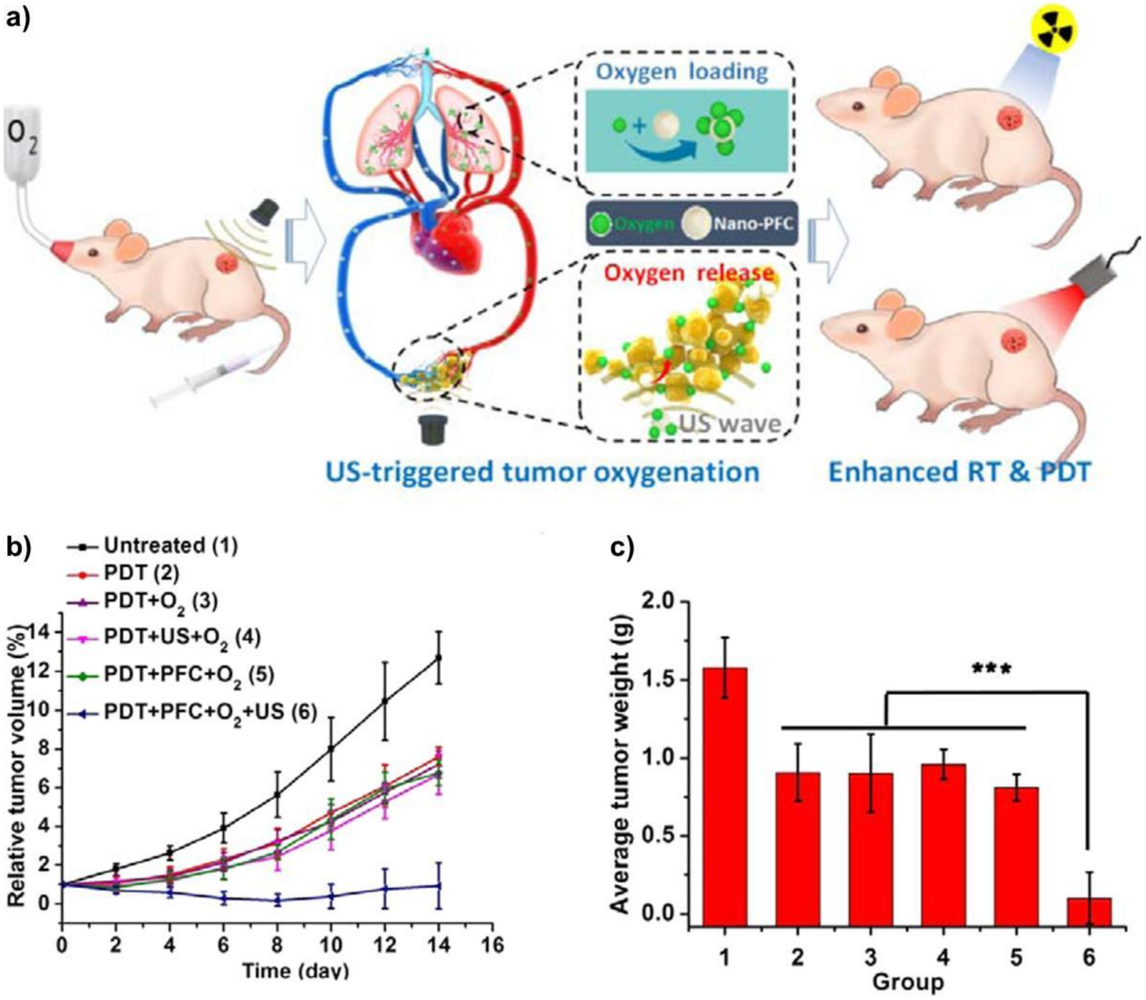

Figure 4.2. a) Schematic illustration of the working action of perfluorocarbon nanoemulsion for ultrasound modulated tumor-specific delivery of oxygen for enhanced PDT and RT. b) Tumor reduction studies of mice after various treatments. c) Average tumor weights of different mice groups subjected to various treatments as shown in (b).

nanorods (AuNR) through a poly ethylene glycol linkage to afford the nanoprobe (**EPT1**). Upon light irradiation of a solution containing the probe molecule, methylene blue and molecular oxygen, singlet oxygen generation took place via the photosensitization of O_2 by methylene blue which in turn got trapped in the anthracene units to form the endoperoxide. The endoperoxide-AuNR hybrid was then administrated to HeLa cells which after internalization underwent a thermal cycloreversion to release $^1O_2$ upon irradiation with an 830 nm laser. The therapeutic performance of the probe was investigated *in vitro* which showed effective killing of cancer cells by the chemical generation of singlet oxygen from the probe molecule.

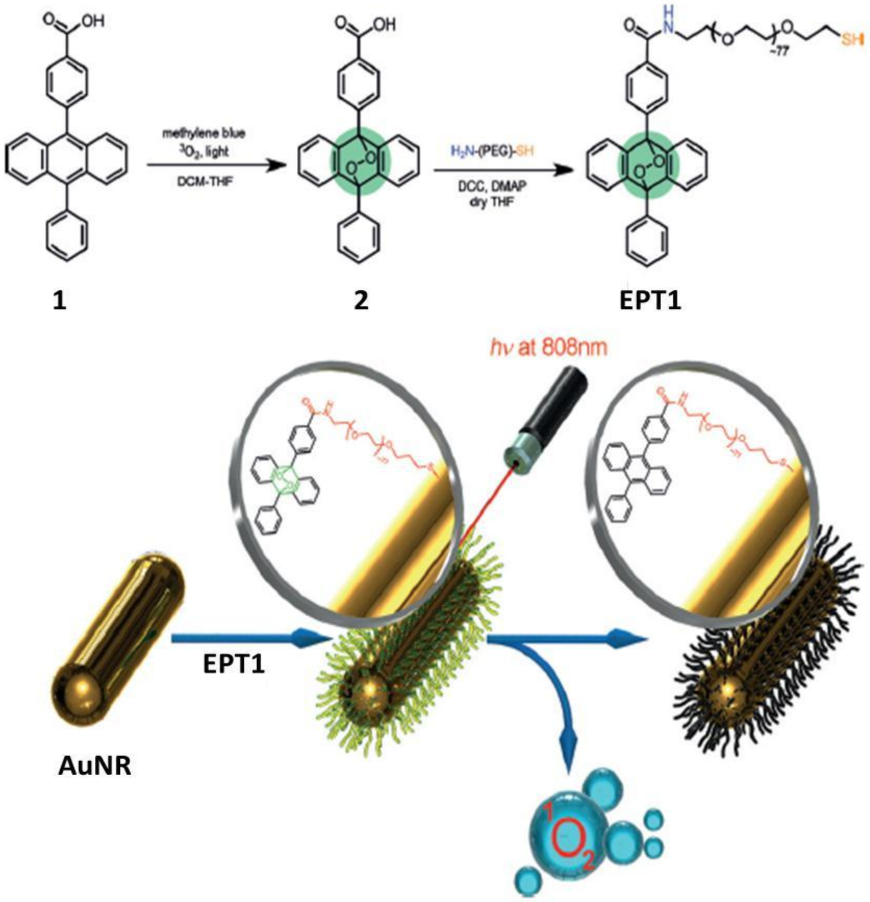

Figure 4.3. Schematic representation of the synthesis of gold nanorod functionalized **EPT1** for the remote controlled release of singlet oxygen in cancer cells.

Turan and coworkers attempted a fractional PDT treatment by employing a BODIPY based photosensitizer (**3**).[22] The dye molecule was tethered with 2-pyridone such that upon light irradiation, it traps the $^1O_2$ that is generated by the photosensitization of molecular oxygen to form the corresponding endoperoxide (**4**). In the *in vitro* conditions, the molecule, **3** generates $^1O_2$ in the presence of laser while in its absence, the endoperoxide (**4**) releases the trapped $^1O_2$, as a result of the thermal cycloreversion to regenerate **3**. Thus, the proposed strategy could perform PDT both in the light and dark phases of the cycle, which greatly improved the therapeutic efficacy over the traditional PDT process (**Figure 4.4**).

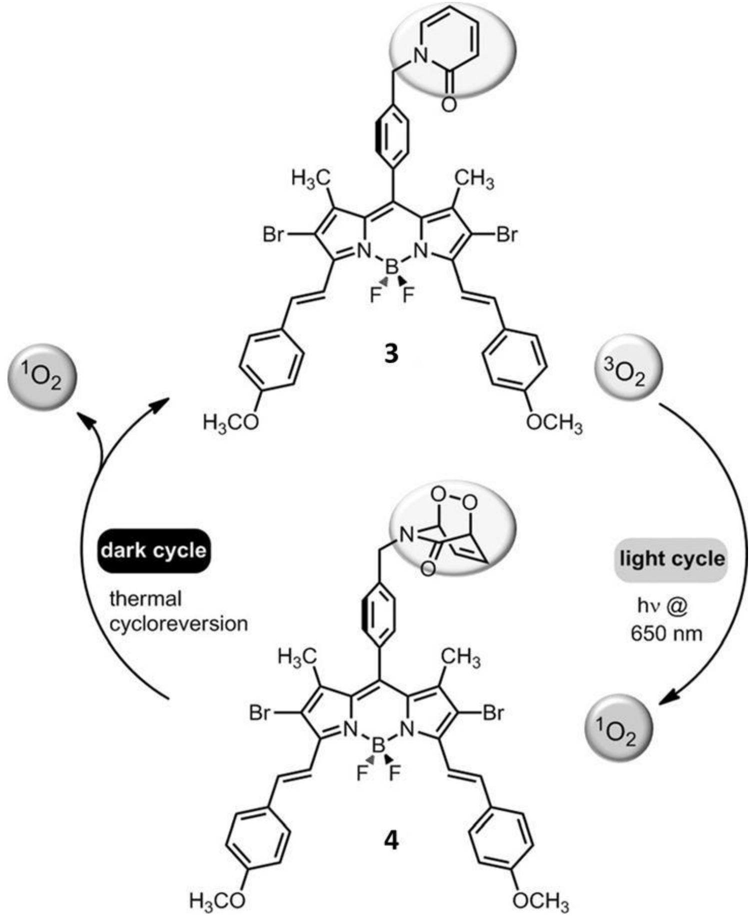

Figure 4.4. Scheme showing the generation of singlet oxygen upon irradiation of **3** with a 650 nm light source, and subsequent thermal cycloreversion of **4** in the dark to regenerate **3**.

Recently, Lv *et al.*, demonstrated the design and fabrication of a multifunctional polymeric carrier containing a photosensitizer (Iridium (III) complex) and a $^1O_2$ scavenging moiety (naphthalene) for intracellular oxygen independent photodynamic therapy (**Figure 4.5**).[23] The release of $^1O_2$ was facilitated by the photothermal heating ability of NIR absorbing AuNRs which offered a localized therapy combining both photothermal and oxidative damages.

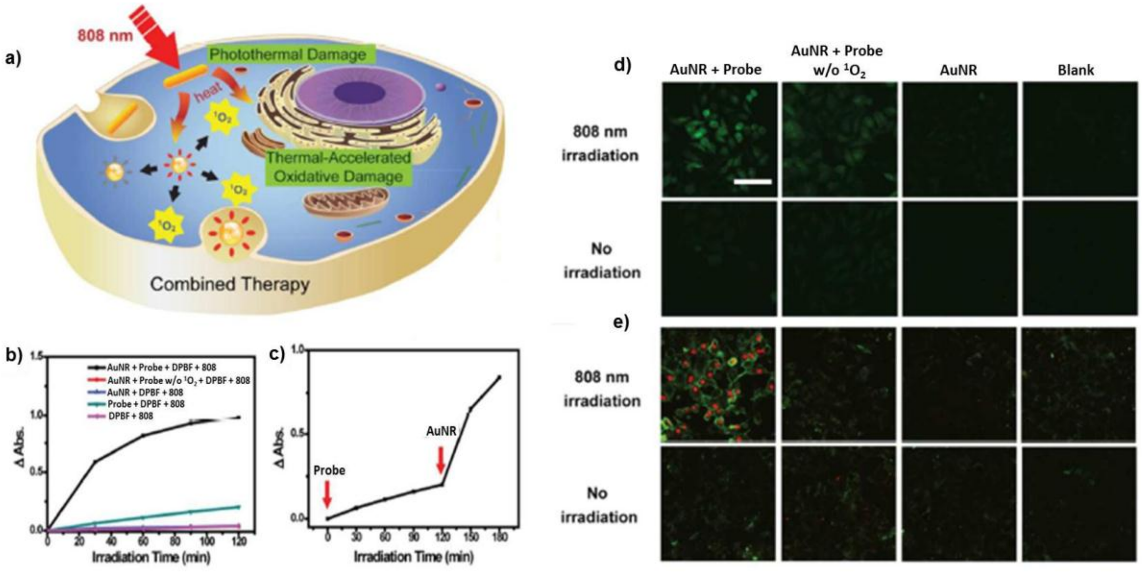

Figure 4.5. a) Schematic representation of the dual therapeutic effects combining both thermal-triggered oxidative damage and photothermal damage. b) Time dependent absorbance changes of different constructs upon exposure to 808 nm light irradiation (0.88 W/cm^2). (c) Time dependent absorbance changes of the mixture of probe and DPBF in DMSO under 808 nm laser irradiation (0.88 W/cm^2). After that, AuNR was added and the change in absorbance recorded as a function of time under the same laser condition. Fluorescence microscopic images of HeLa cells subjected to (d) DCFDA and (e) Annexin V flow cytometry assay under different conditions.

Considering the high singlet oxygen generation capability of iridium based cyclometalated complexes[24-26] and the reliability of 2-pyridone derivatives in regenerating trapped singlet oxygen in good yields,[18,27-29] a rational design has been adopted to synthesize an iridium based photosensitizer complex (**Ir-Pyr**) containing 2-pyridone tethered ligand to meet the requirements of intracellular oxygen independent photodynamic therapy. The working principle of the probe is displayed in **Scheme 4.1**. Upon light excitation of **Ir-Pyr** in cuvette condition, the molecule generates singlet oxygen which will be trapped in its pyridone units to afford the endoperoxide (**Ir-Pyr-EPO**) which can undergo thermal cycloreversion to yield $^1O_2$ with the regeneration of **Ir-Pyr**. In order to realize a remote controlled heating application, MnO_2 nanosheets was chosen as the photothermal agent which will facilitate PDT via the release of $^1O_2$ from the endoperoxide upon irradiation with NIR light at the target site. Furthermore, the tumor microenvironment (TME) responsiveness of MnO_2 can be utilized in a favorable manner to increase the local oxygen concentration via its degradation by H_2O_2, which in turn provides room for the second phase of photodynamic therapy. To the best of our knowledge,

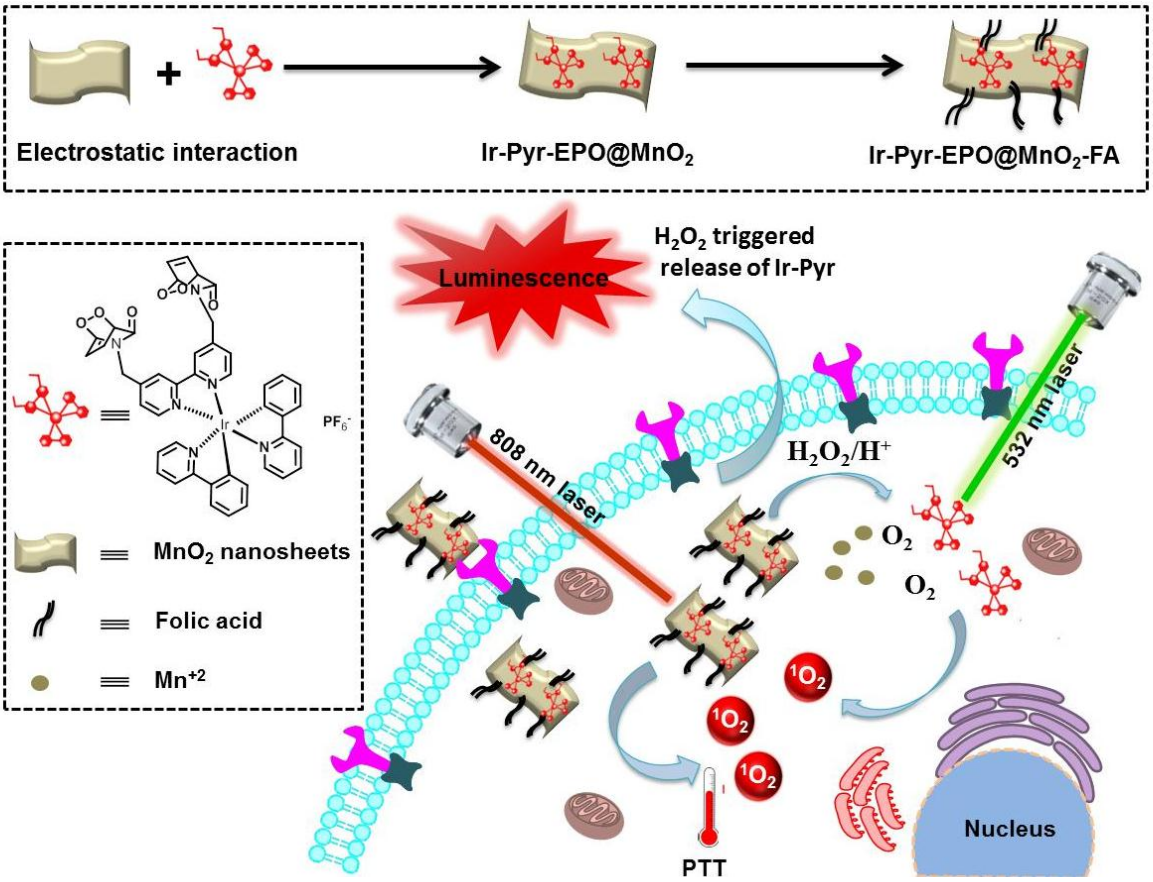

Scheme 4.1. Schematic illustration of working action of the probe for intracellular oxygen independent PDT applications.

this could be the first report ever to demonstrate a full-fledged multi-stage PDT process without any intracellular oxygen demand to offer a meaningful therapeutic procedure in hypoxic tumors.

4.3. Results and Discussion

4.3.1. Synthesis of Ir-Pyr

The synthesis of the target compound **Ir-Pyr** was initiated with the preparation of the bipyridine ligand **7**, which was proceeded through a two-step synthetic strategy as shown in **Scheme 4.2**. The cyclometalated intermediate (Ir (III) dimer), **9** was prepared as shown in **Scheme 4.3**. The reaction of the dimer with the ligand molecule **7** in a mixture of dichloromethane/ethanol (1:3 v/v) under reflux conditions under Argon atmosphere followed by anion exchange using NH_4PF_6 afforded the product (**Scheme 4.4**). The purification of **Ir-Pyr** was carried out using silica gel column chromatography which was finally subjected to precipitation in dichloromethane/hexane mixture to obtain the product in 39% yield.

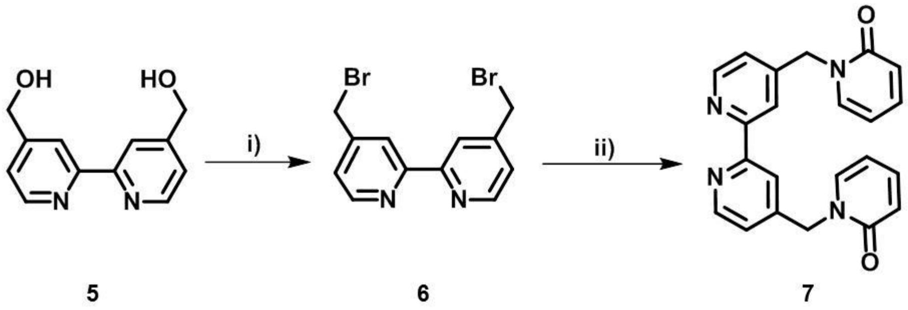

Scheme 4.2. Reagents and conditions: [i] 48% HBr, H_2SO_4; [ii] 2-hydroxypyridine, K_2CO_3, 18-crown-6, KI, CH_3CN, 50 °C.

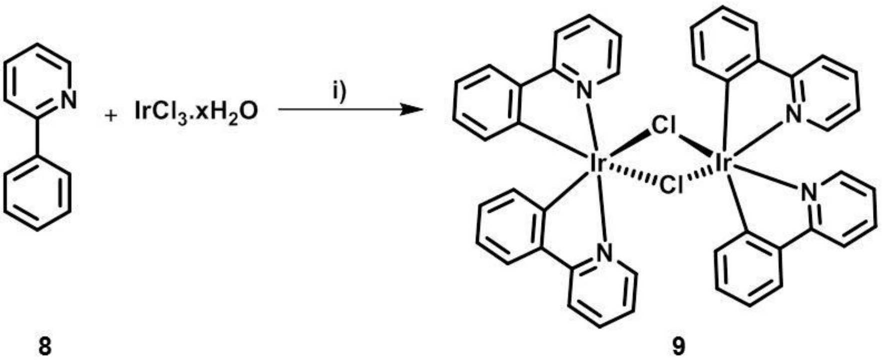

Scheme 4.3. Reagents and conditions: [i] 2-ethoxyethanol/water (8:2), reflux, 24 h.

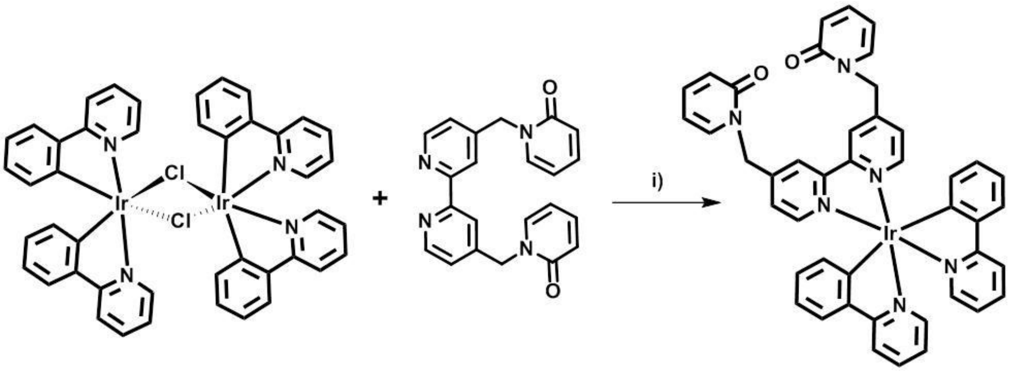

Scheme 4.4. Reagents and conditions: [i] Na_2CO_3, DCM/ethanol (1:3), Argon, 60 °C, 12 h and NH_4PF_6.

4.3.2. Photophysical Studies

The photophysical characteristics of **Ir-Pyr** were first examined through UV-Vis absorption and emission spectral analyses which showed a metal to ligand charge transfer (MLCT) band in the 460-515 nm region with a corresponding emission centered at 630 nm (**Figure 4.6**). The singlet oxygen generation capability of the molecule was then investigated using a singlet oxygen scavenging dye, 1, 3-diphenylisobenzofuran. As expected, **Ir-Pyr** caused the photo-sensitization of ground state molecular oxygen to form singlet oxygen, which in turn gets scavenged by DPBF resulting in a decline in its absorption as well as emission profiles (**Figure 4.7b** and **4.7c**). Having seen an excellent $^1O_2$ generation by the

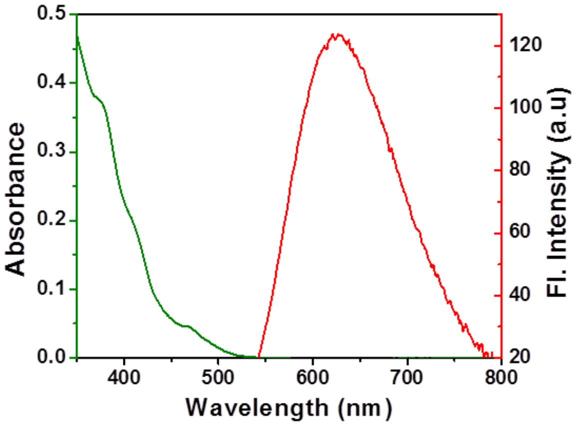

Figure 4.6. UV-Vis absorption spectrum and luminescence spectrum of **Ir-Pyr** (10 μM, acetonitrile).

probe molecule, it was equally important to demonstrate that the generated singlet oxygen gets trapped in the pyridone units of the complex to act as a reservoir for the on-demand release of $^1O_2$. For this study, the solution containing **Ir-Pyr** was irradiated for a period of 15 minutes (to ensure maximum $^1O_2$ generation and trapping) towards which DPBF was added and monitored its temperature dependent absorbance changes while heating the solution from 30 to 60 °C. The results revealed the release of trapped singlet oxygen via the thermal decomposition of endoperoxide which was indicated by a decrease in the absorbance of the DPBF peak as shown in **Figure 4.7d** and **4.7e**. It is important to note that the absorbance measurements carried out with DPBF alone (in the absence of **Ir-Pyr**) under similar experimental condition did not show any significant change which rules out the probability of any experimental error arising from the photoirradiation of DPBF (**Figure 4.7e**). The singlet oxygen quantum yield (Φ) of **Ir-Pyr** was found to be 0.71 when compared against the reference ($Ru(bpy)_3Cl_2$) which has a Φ value of 0.57.[30] However, owing to the $^1O_2$ trapping nature of **Ir-Pyr**, it is necessary to block the pyridone sites with $^1O_2$ by preparing the endoperoxide (**Ir-Pyr-EPO**) prior to the experiment to account for the accurate amount of singlet oxygen generation by the complex. Thus, the Φ value determined with the endoperoxide turned out to be 0.79 which highlights the superior photosensitizing ability of the probe (**Figure 4.8a**). Moreover, the direct

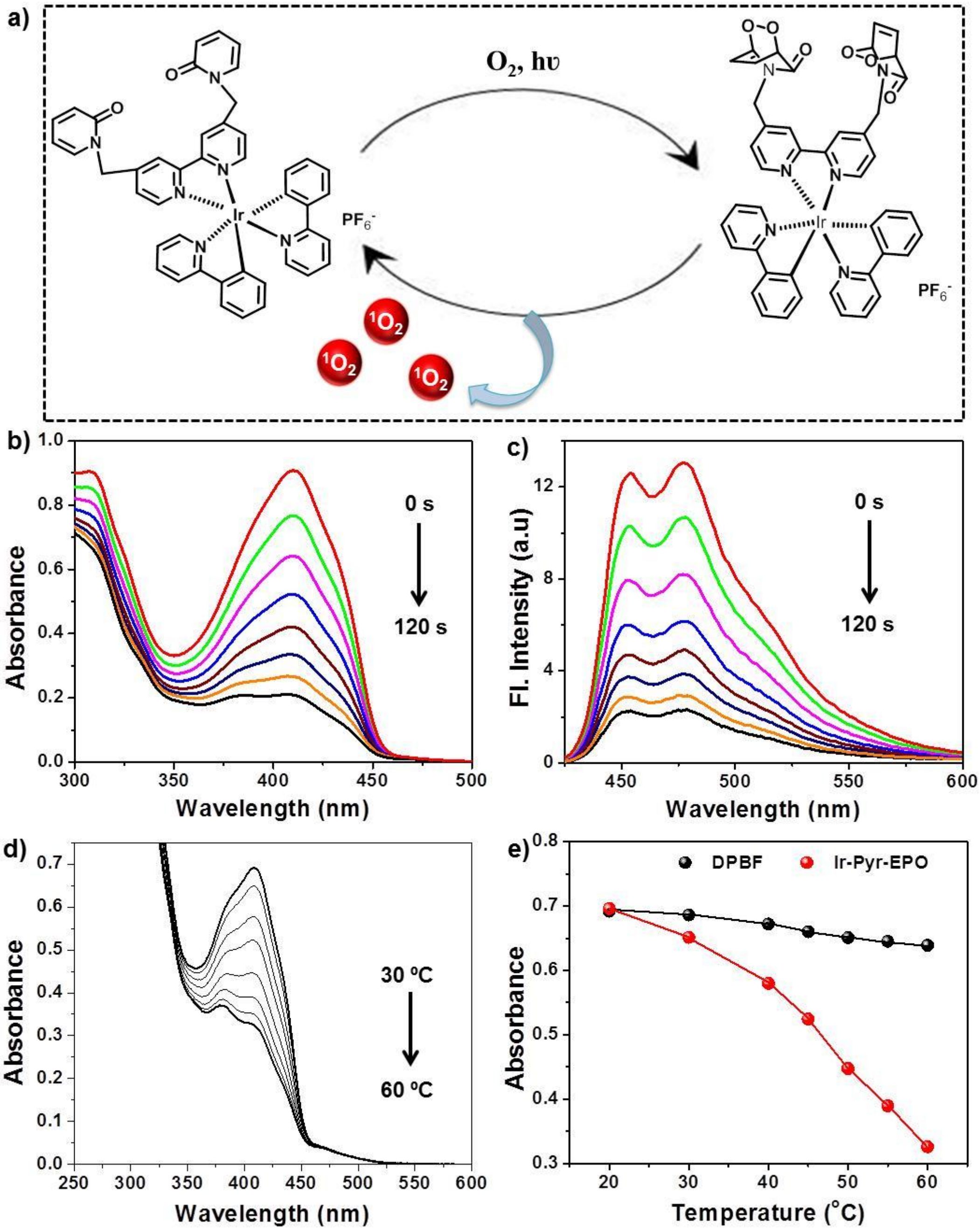

Figure 4.7. a) Schematic representation showing the photo-generation and heat triggered release of $^1O_2$ by **Ir-Pyr**. b) UV-Vis absorption and c) fluorescence spectral changes of DPBF in the presence of **Ir-Pyr** upon irradiation with light from 0 to 120 s. d) Absorption changes of DPBF in the presence of pre-photo irradiated **Ir-Pyr** upon heating from 30 to 60 ºC. e) Decrease in absorbance of DPBF at 414 nm recorded as a function of temperature.

monitoring of $^1O_2$ was also carried out by recording its emission at 1275 nm (**Figure 4.8b**) wherein a dramatic increase in the luminescence signal was

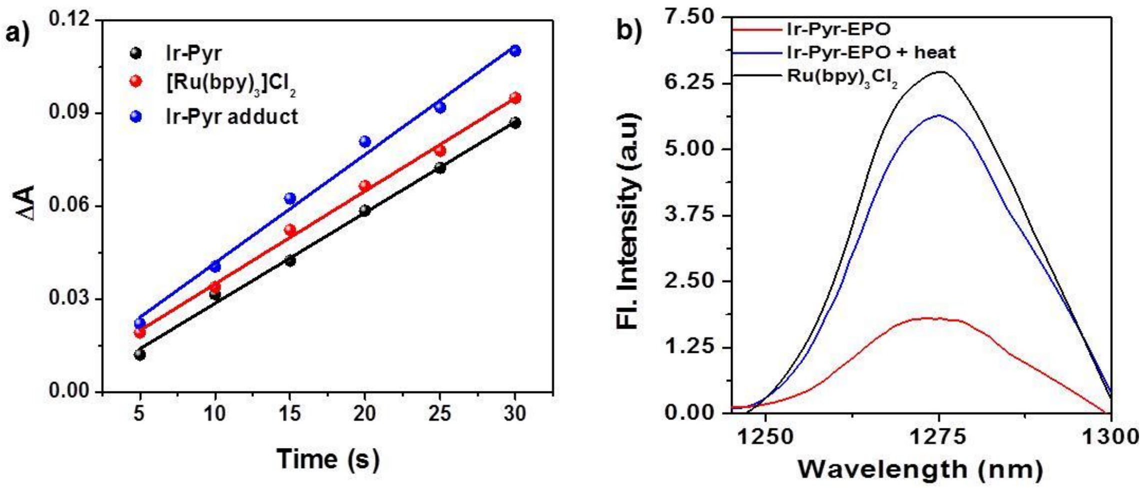

Figure 4.8. a) Determination of singlet oxygen generation efficiency of **Ir-Pyr** and **Ir-Pyr-EPO** using $[Ru(bpy)_3]Cl_2$ as the standard. b) Direct monitoring of $^1O_2$ generation potential of **Ir-Pyr** and **Ir-Pyr-EPO**, detected by recording the emission at 1275 nm.

observed upon heating the endoperoxide, **Ir-Pyr-EPO** which further supports the $^1O_2$ trapping and thermal triggered releasing properties of **Ir-Pyr** (**Figure 4.7a**). Meanwhile, the photo (**Figure 4.9a** and **4.9b**) and thermal (**Figure 4.9c** and **4.9d**) stabilities of the complex were also evaluated which showed that the complex is stable over the detected time and temperature range, thereby ensuring its eligibility for bioimaging applications also.

The next aim was to design and synthesize a suitable photothermal agent that can induce a thermal trigger to activate the decomposition of **Ir-Pyr-EPO** to produce singlet oxygen at the target site. Towards this, MnO_2 nanosheets with a size range of 150-200 nm was synthesized via a redox reaction between potassium permanganate ($KMnO_4$) and sodium dodecyl sulphate (SDS) following a facile nanochemical protocol. The TEM analysis revealed a two-dimensional sheet like morphology with an average lateral dimension below 200 nm (**Figure 4.10a**). UV-Vis absorption spectral analysis of MnO_2 showed a broad absorption

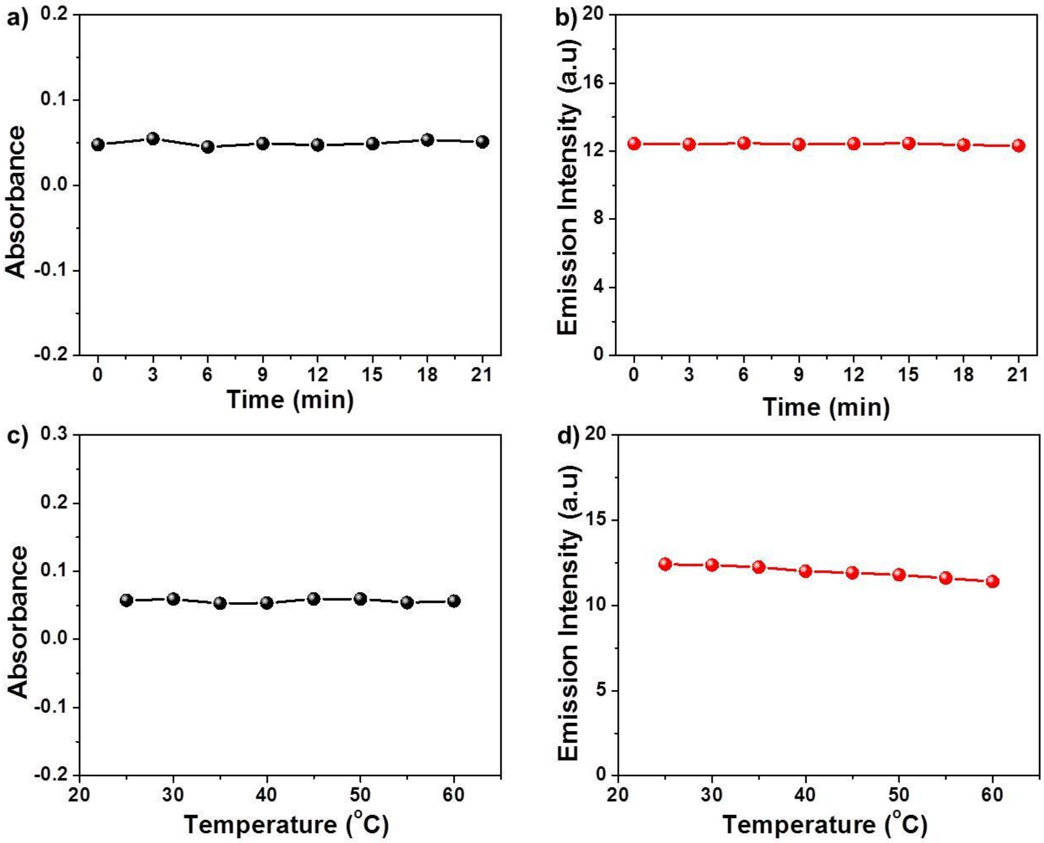

Figure 4.9. a) UV-Vis absorption and b) emission spectral analysis of **Ir-Pyr** upon irradiation with 532 nm laser source (0.5 W/cm^2). c) UV-Vis absorption and d) emission spectral analysis of **Ir-Pyr** upon heating from 30 to 60 °C.

spanning from the UV to NIR regions (**Figure 4.10b**) which endows it with NIR laser activatable photothermal property (**Figure 4.10c**). Furthermore, detailed investigation was performed using Raman spectral analysis which showed the presence of two peaks at 570 and 650 cm^{-1} attributable to the Mn-O stretching vibrations (**Figure 4.10d**). The as-prepared MnO_2 nanosheets was then electrostatically attached to the positively charged **Ir-Pyr** to afford **Ir-Pyr@MnO$_2$** (**Figure 4.11a**). Due to large overlap between the absorption spectrum of MnO_2 and emission spectrum of **Ir-Pyr**, the luminescence intensity of **Ir-Pyr** was quenched considerably leading to a 'turn-off' of the emission signal as indicated in **Figure 4.11b**. These observations further support the formation of the photosensitizer-MnO_2 hybrid complex, which can perform the therapeutic

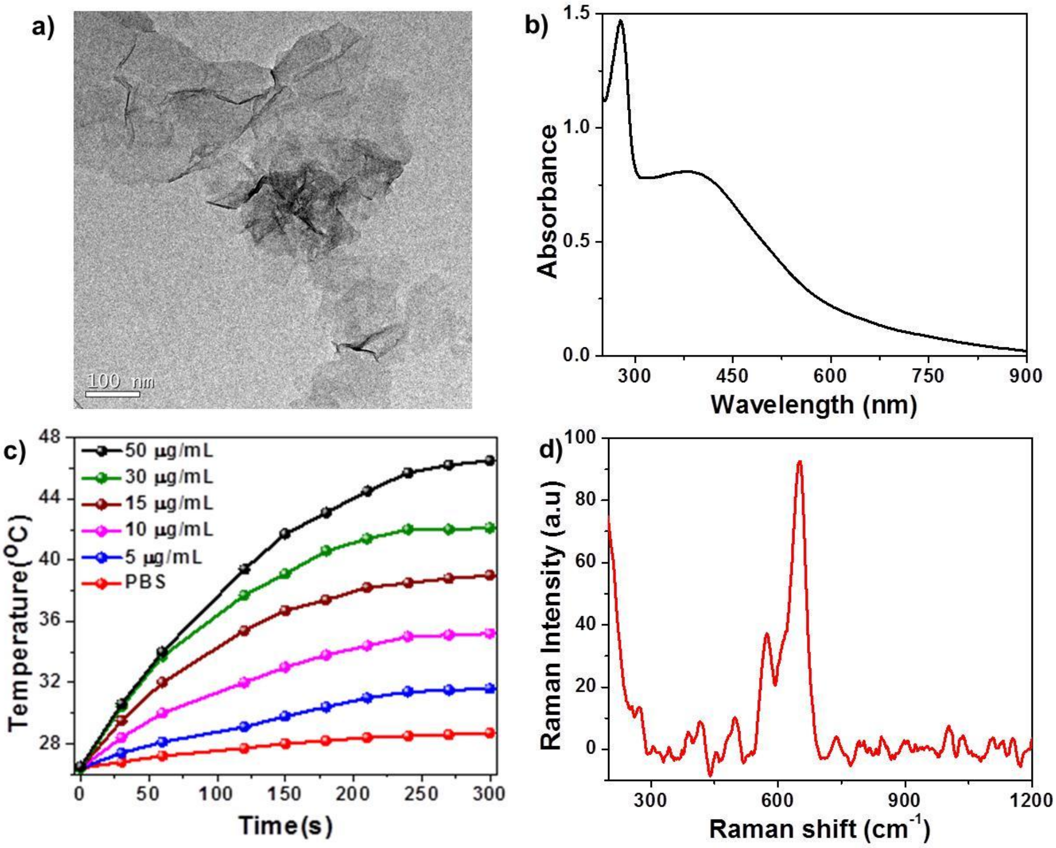

Figure 4.10. a) TEM image and b) UV-Vis absorption spectrum of MnO_2 nanosheets. c) Temperature changes of different concentrations of MnO_2 nanosheets upon irradiation with 808 nm laser (0.5 W/cm^2). d) Raman spectral analysis of MnO_2 nanosheets.

processes accurately in an oxygen independent mode to produce enhanced treatment outcome with minimal side effects.

Besides the photothermal properties, MnO_2 nanosheets endows with a TME responsive degradation property that facilitates the reduction of MnO_2 to Mn^{+2} by H_2O_2[31,32] at acidic pH with the production of molecular oxygen, which paves way for the second phase of intracellular oxygen independent PDT. To test this, the absorbance changes of MnO_2 nanosheets were recorded with increasing concentrations of H_2O_2 at pH 7.4 and pH 5.5. The results indicated that under the acidic pH condition, MnO_2 undergoes a much faster reduction when compared to

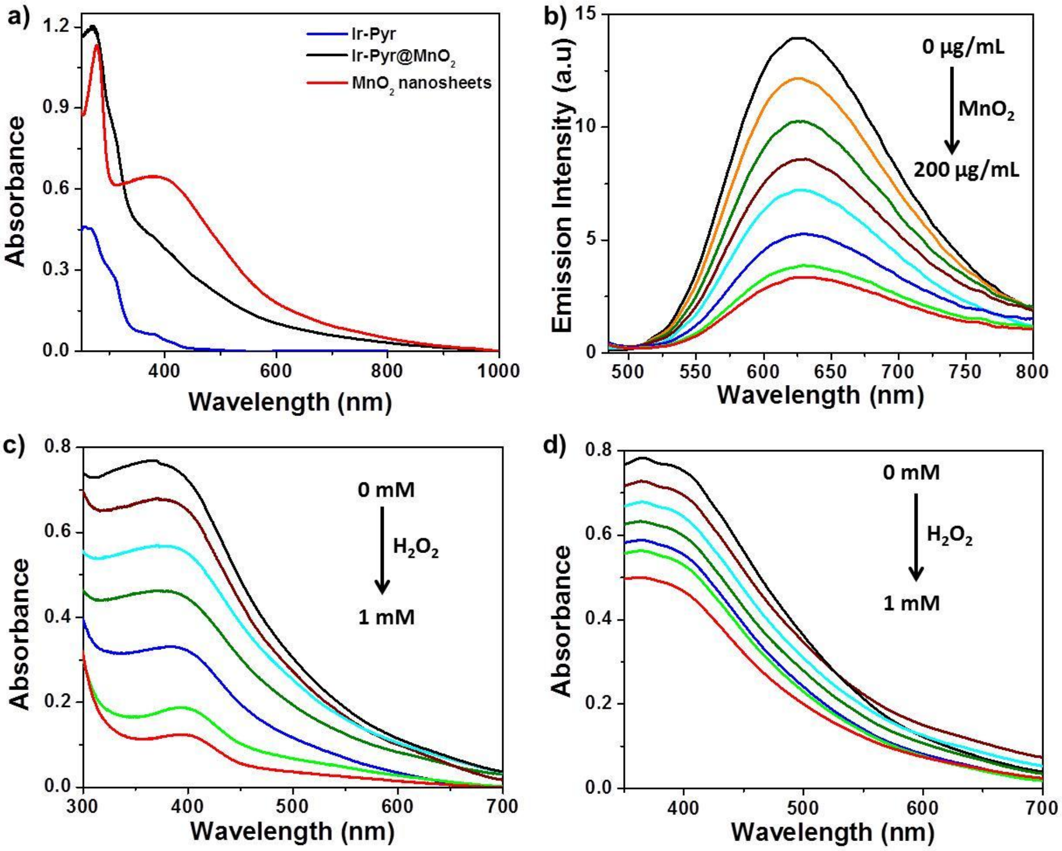

Figure 4.11. a) UV-Vis absorption spectra of various constructs. b) Emission spectral changes of **Ir-Pyr** in presence of increasing concentrations of MnO_2 nanosheets. Absorbance changes of MnO_2 nanosheets in the presence of increasing concentrations of H_2O_2 (0-1 mM) at pH 5.5 (c) and pH 7.4 (d).

the normal physiological pH as evident from **Figure 4.11c** and **4.11d**. The degradation property of MnO_2 nanosheets was further confirmed through Raman spectral analysis which showed a sharp decline in the Mn-O stretching peaks with increasing concentrations of H_2O_2 (**Figure 4.12a**). Furthermore, this tumor specific degradation caused the restoration of luminescence activity of **Ir-Pyr** which can be realized for probing the localization of the nanomaterial both *in vitro* and *in vivo* (**Figure 4.12b**).

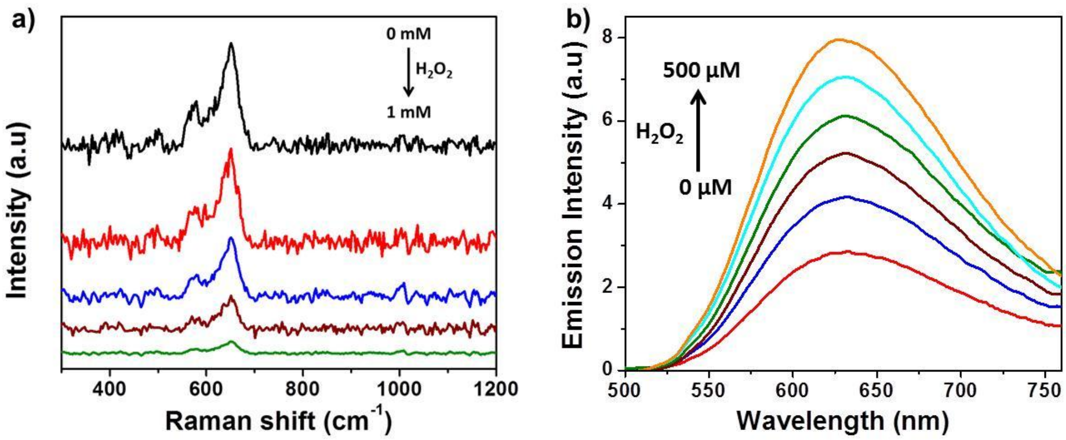

Figure 4.12. a) Raman spectra of MnO_2 nanosheets and b) luminescence recovery of **Ir-Pyr** in the presence of increasing concentrations of H_2O_2 at pH 5.5.

In order to establish the multi-phase $^1O_2$ generation capability of the probe, a crucial experiment was carried out wherein an aqueous solution of the hybrid material, **Ir-Pyr@MnO$_2$** was irradiated with 532 nm light to form the endoperoxide prior to the addition of DPBF. The solution was then subjected to irradiation with 808 nm laser which caused a huge decrease in the emission intensity of DPBF resulting from the heat triggered cycloreversion process to produce singlet oxygen (**Figure 4.13a**). At this point, H_2O_2 was added to the above solution to induce reduction of MnO_2 nanosheets which was subsequently followed by light irradiation. The results showed a drastic decline in the DPBF fluorescence, accounting for the second phase of PDT resulting from the photosensitizing activity of the hybrid complex on the molecular oxygen produced via the reduction of MnO_2 nanosheets. Thereafter, irradiation with 808 nm laser triggered a further reduction in the DPBF signal which can be attributed to the thermal release of trapped $^1O_2$ from **Ir-Pyr-EPO** (**Figure 4.13a**). It is interesting to note that the whole process can be repeated again following a similar procedure (**Figure 4.13b**), thereby highlighting the potential of the probe for high performance sequential PDT in hypoxic tumors.

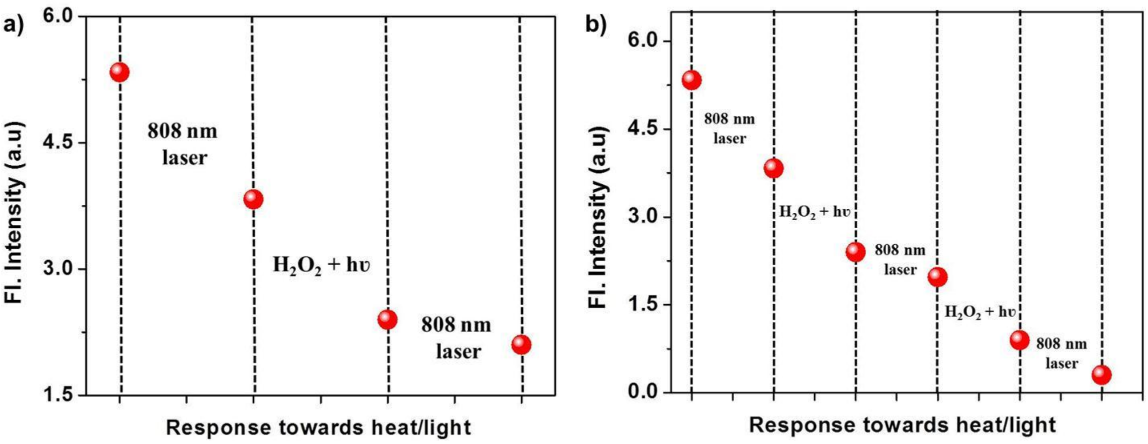

Figure 4.13. Emission spectral changes of DPBF in the presence of **Ir-Pyr@MnO$_2$** subjected to various treatments for one cycle (a) and two cycles (b).

4.3.3. *In vitro* Imaging Studies

Next, the suitability of the nanomaterial as a remote controlled source of $^1O_2$ was investigated under *in vitro* conditions. Prior to the cell experiments, the surface of MnO_2 nanosheets was modified with folic acid functionalized BSA to facilitate

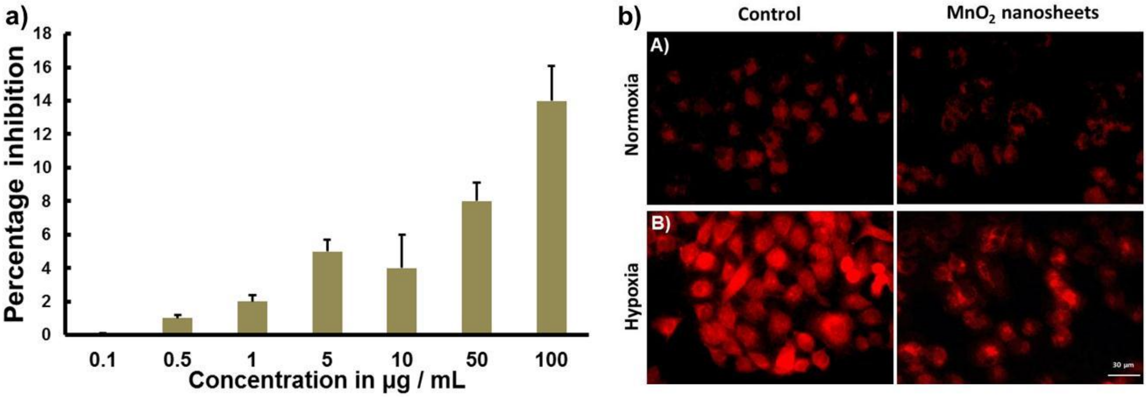

Figure 4.14. a) Cytotoxic evaluation on HeLa cells treated with various concentrations of **Ir-Pyr-EPO@MnO$_2$-FA** (0.1 to 100 µg/mL) determined using MTT assay. b) Microscopic images of the intracellular oxygen probe, $[Ru(dpp)_3]Cl_2$ stained HeLa cells after treatment with MnO_2 nanosheets for 12 h under A) normoxic and B) hypoxic conditions. Scale bar corresponds to 30 µm.

target specificity that has been further attached to the photosensitizer **Ir-Pyr** to afford **Ir-Pyr@MnO$_2$-FA**. The cell viability experiments performed with **Ir-Pyr-EPO@MnO$_2$-FA** on folate receptor overexpressing HeLa cells indicated that the nanomaterial is safe to be administered in a range of concentrations from 0.1 to 50 µg/mL (**Figure 4.14a**). It has been reported that hypoxic cancer cells produce high concentrations of endogenous acidic H_2O_2[33,34] which may aid in an enhanced reduction of MnO_2 present in the probe to generate molecular oxygen for efficient ROS generation. To test this hypothesis, a hypoxic variant of HeLa cells was prepared which was subsequently incubated with MnO_2 nanosheets. After the administration of MnO_2 for 12 h, the intracellular oxygen levels were monitored by staining with a commercial luminescent oxygen probe, $[Ru(dpp)_3]Cl_2$ (dpp, 4,7-diphenyl-1,10-phenanthroline) which shows a quenching of its emission with

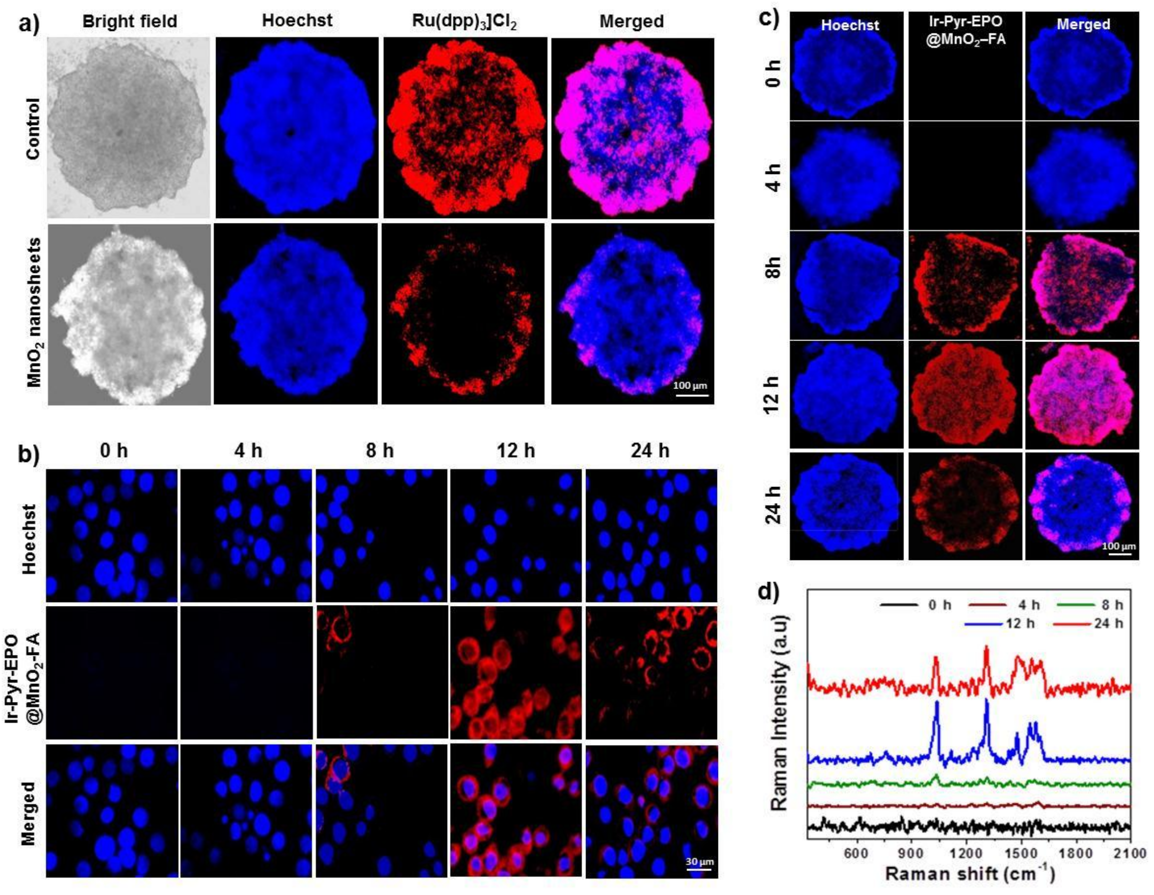

Figure 4.15. a) Microscopic images of the intracellular oxygen probe, $[Ru(dpp)_3]Cl_2$ stained HeLa cells after treatment with MnO_2 nanosheets for 12 h. Scale bar corresponds to 100 µm. b) and c) represent the cellular uptake studies of **Ir-Pyr@MnO$_2$-FA** at different time points in monolayer cells (scale bar 30 µm) and spheroids (scale bar 100 µm) respectively. d) SERS spectral evaluation of material administrated HeLa cells at different time points.

increase in oxygen concentrations. The microscopic images shown in **Figure 4.14b** revealed a remarkable reduction in the red emission of $[Ru(dpp)_3]Cl_2$ in the cells maintained under hypoxic conditions (**Figure 4.14B**) when compared against the normoxic ones (**Figure 4.14A**), thereby establishing the presence of overexpressed H_2O_2 in hypoxic tumors and the massive oxygen production from the probe for improved therapeutic efficacy. Excitingly, a similar trend was observed with the multicellular tumor spheroids of HeLa cells which also supports the tumor specific oxygenation process by intracellular H_2O_2 (**Figure 4.15a**). Furthermore, the oxygenation process happened as a result of the reduction of MnO_2 to Mn^{+2} was accompanied by a gradual light up of the luminescent signals of **Ir-Pyr** present in **Ir-Pyr@MnO$_2$-FA** which allowed for a precise tracking of the intracellular location of the probe. It is quite evident from **Figure 4.15b** that the cells which are initially non-luminescent gradually underwent a time dependent increase in the red emission signals which finally got saturated at about 12 h. These observations were clearly followed in the luminescent microscopic imaging performed with HeLa spheroids as well (**Figure 4.15c**), suggesting the tumor specific activatable imaging potential of the nanomaterial. Moreover, the internalization event was monitored through surface enhanced Raman scattering technique which was performed by the addition of spherical gold nanoparticles (~40 nm size) to the nanomaterial treated cells by probing the signals at 1037 cm^{-1}

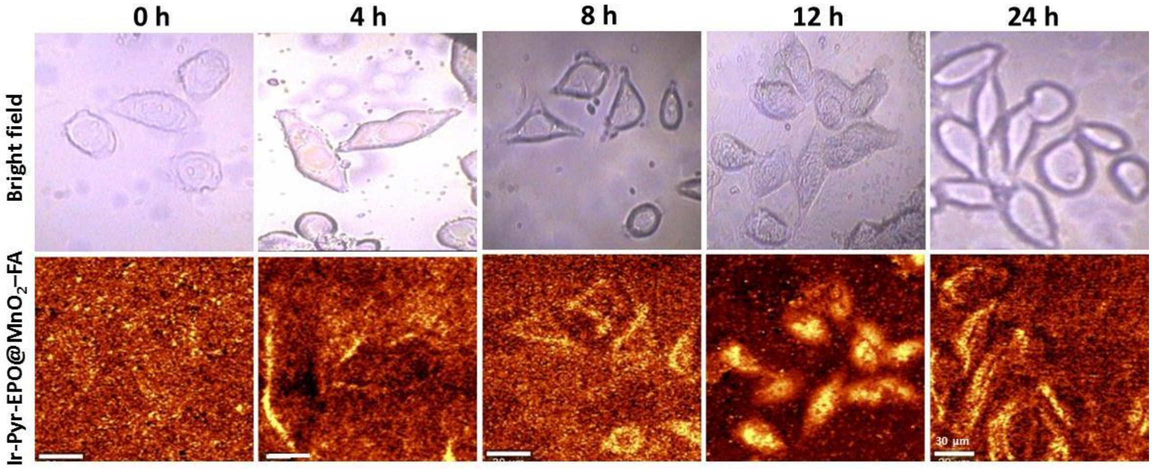

Figure 4.16. *In vitro* SERS imaging of nanomaterial incubated HeLa cells at different time points.

(C-H bending) and 1308 cm^{-1} (C-N stretching), which are the peaks characteristic of **Ir-Pyr**. A careful examination of the spectra revealed a time dependent enhancement in the signal intensity with a corresponding increase in the brightness of the images that further supported the detachment of **Ir-Pyr** from the MnO$_2$ nanosheet surface, thereby enabling it for self-guided therapeutic applications (**Figure 4.15d** and **4.16**).

4.3.4. *In vitro* Therapeutic Studies

The evaluation of the *in vitro* therapeutic performance of the probe was initiated with singlet oxygen sensor green (SOSG) assay that accounts for the singlet oxygen generation potential of a molecule by producing a green emission. The endoperoxide of **Ir-Pyr@MnO$_2$-FA** was prepared in the laboratory settings by

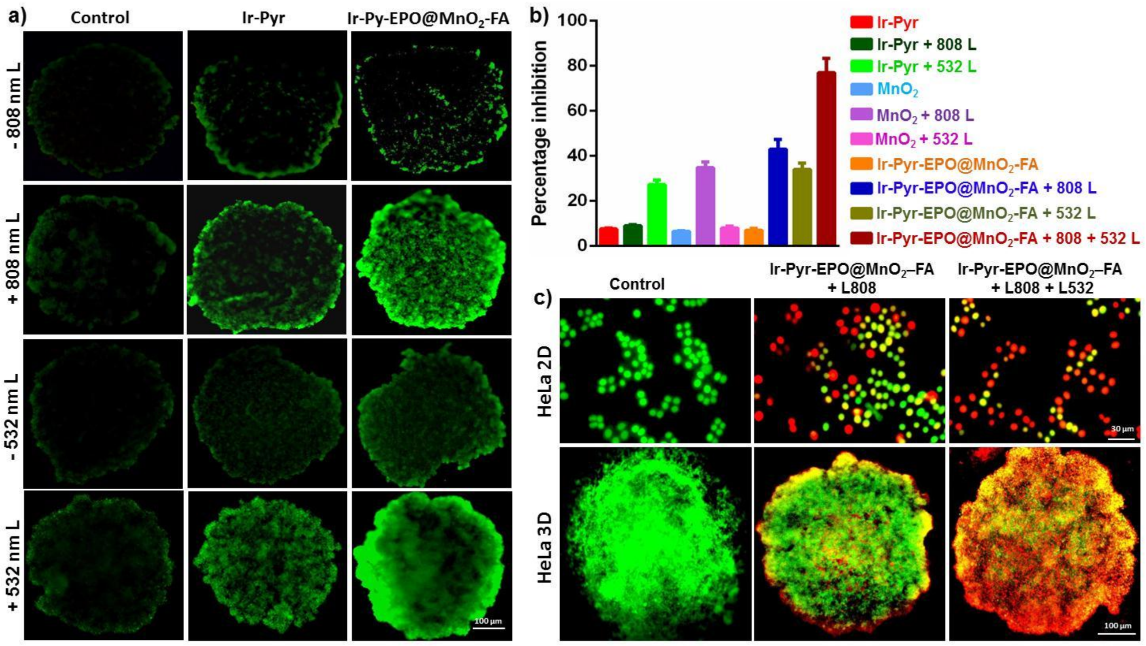

Figure 4.17. a) Evaluation of $^1O_2$ generation efficacy of **Ir-Pyr-EPO@MnO$_2$-FA** on HeLa spheroids using SOSG assay. Scale bar represents 100 µm. b) *In vitro* cytotoxicity assay of various constructs with and without laser irradiation on HeLa cells. c) Apoptotic evaluation of **Ir-Pyr-EPO@MnO$_2$-FA** on HeLa cells (scale bar 30 µm) and spheroids (scale bar 100 µm) using acridine orange-ethidium bromide dual staining.

irradiation with 532 nm laser (0.2 W/cm^2) for a period of 15 minutes. The as-formed endoperoxide complex (**Ir-Pyr-EPO@MnO$_2$-FA**) was then incubated with HeLa spheroids for 4 h followed by irradiation using an 808 nm laser (0.5 W/cm^2). These spheroids were then imaged for visualizing the $^1O_2$ generation capability of the probe by staining with SOSG. The fluorescence microscopic images revealed a strong green fluorescence in the 808 nm laser treated spheroids against the untreated as well as the **Ir-Pyr** treated ones (**Figure 4.17a**). These observations clearly suggest the execution of the first phase of intracellular oxygen independent PDT by photothermally triggered cycloreversion of the endoperoxide to regenerate **Ir-Pyr@MnO$_2$-FA** with the production of $^1O_2$. In order to account for the second phase of PDT, the spheroids were incubated with the material for 12 h which was then subjected to irradiation with 532 nm laser. The results indicated that the spheroids incubated with **Ir-Pyr-EPO@MnO$_2$-FA** followed by 532 nm laser irradiation produced a significantly enhanced green emission against the **Ir-Pyr** and laser free conditions (**Figure 4.17a**). Taken together, these results unveil the nanomaterial to be a self-replenished source of $^1O_2$ for facilitating multi-stage photodynamic therapy without any intracellular oxygen demand. The cytotoxic potential of various constructs was then evaluated using MTT assay in a series of cell lines wherein **Ir-Pyr-EPO@MnO$_2$-FA** after irradiation with both 808 and 532 nm lasers imparted much higher toxicity in monolayer HeLa cells and multicellular HeLa spheroids when compared with the other counterparts (**Figure 4.17b and 4.18a**), owing to the combined therapeutic effects facilitated by the multi-stage

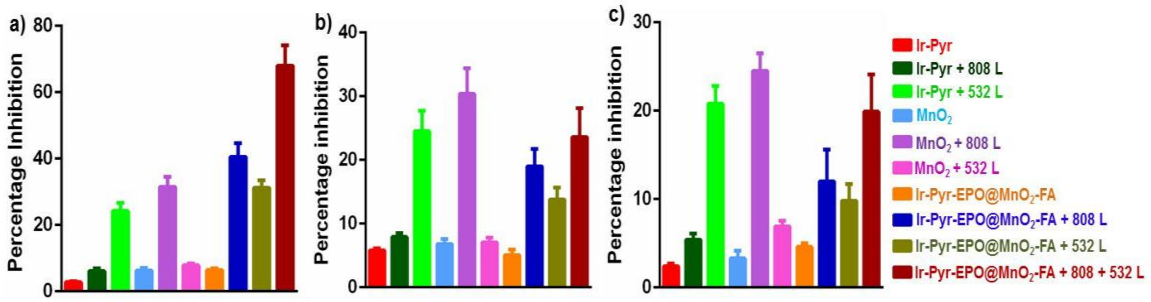

Figure 4.18. *In vitro* cell viability assay of various constructs with and without laser irradiation on a) HeLa spheroids, b) A549 and c) WI38 cells.

PDT process along with the photothermal effects. On the contrary, the material was found to be relatively non-toxic to the folate receptor (FR) negative A549 (**Figure 4.18b**) and WI-38 (**Figure 4.18c**) cell lines which can be attributed to the folate specific recognition of the probe. The therapeutic action of the nanoconstruct was further validated through various apoptotic assays. In

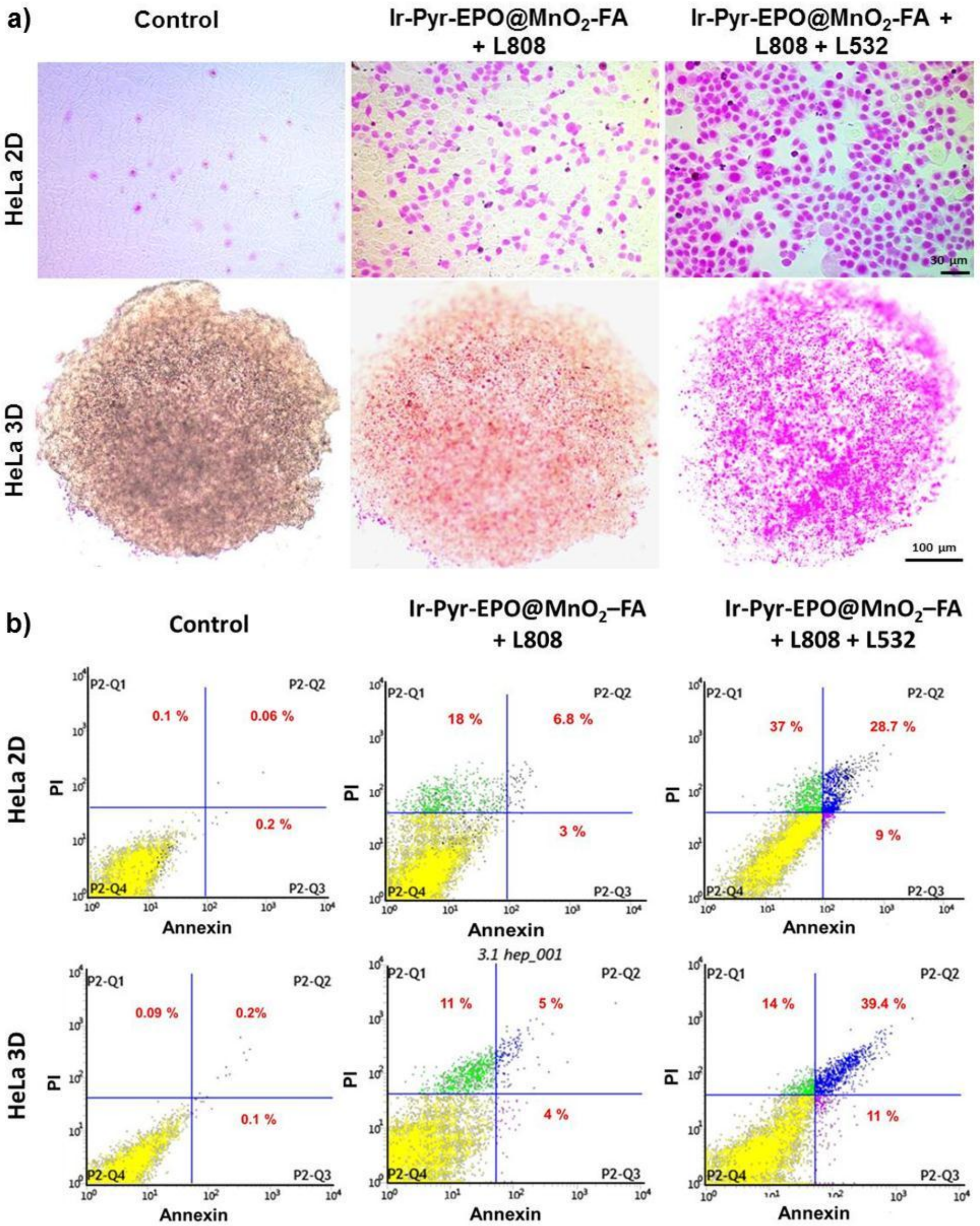

Figure 4.19. *In vitro* evaluation of apoptosis on HeLa cells and spheroids using APOP assay (a) and Annexin V FITC flow cytometric assay (b). Scale bar for HeLa cells and spheroids in Figure (a) corresponds to 30 µm and 100 µm respectively.

comparison with the control cells, cells incubated with **Ir-Pyr-EPO@MnO$_2$-FA** followed by dual laser irradiation showed pronounced indications of apoptosis as apparent from the very large population of orange/red stained cells when estimated using live/dead assay (**Figure 4.17c**). To further visualize the apoptotic induction in a non-fluorescent platform, APOPercentage assay was performed which also shed light into the superior therapeutic performance of the probe, as clear from the much higher population of apoptotic cells stained by pink color (**Figure 4.19a**). Furthermore, the cell death mechanism imparted by the nanoprobe was subjected to detailed investigation using Annexin V-FITC assay wherein HeLa cells as well as spheroids were administered with **Ir-Pyr-EPO@MnO$_2$-FA** under different laser conditions and subsequently labeled with propidium iodide and Annexin V. The results showed that **Ir-Pyr-EPO@MnO$_2$-FA** with dual laser administration caused remarkably higher apoptosis in both cell and spheroid models when compared against the respective controls (**Figure 4.19b**).

4.3.5. *In vivo* Imaging and Therapy

Encouraged by the promising imaging and therapeutic attributes of **Ir-Pyr-EPO@MnO$_2$-FA** under *in vitro* conditions, the *in vivo* targeted theranostic potential of the probe was evaluated by intra-peritoneal (*ip*) injection into FR positive DLA solid tumor bearing syngeneic mice. The *in vivo* imaging ability of the nanomaterial was first investigated through luminescence imaging at different time points. The intrinsic tumor niche responsive nature of the probe enabled a turn-on optical imaging response via a gradual amplification in the red emission at the target site. From **Figure 4.20a**, it is quite evident that the probe displayed very weak signal intensity in the initial time periods which underwent a noticeable light-up at 8th h that got further increased at 12 h finally attaining a saturation at about 16 h. Moreover, various organs were subjected to *ex vivo* imaging analysis wherein more accumulation was observed in the tumor site along with some signals in the liver and kidney regions while other organs such as brain, heart and lungs excluded the presence of **Ir-Pyr-EPO@MnO$_2$-FA** (**Figure 4.21a**). The tumor homing potential of the nanoconstruct was further visualized in the SERS platform on tumor bearing nude mice model by using a hand held Raman spectrometer (λ_{ex}:785 nm), wherein we could observe the marked presence of the peaks at 1037 and 1308 cm^{-1} while no detectable signal was obtained from other anatomical locations (**Figure 4.20b**). Having seen an excellent tumor specific localization of the material, the next intention was to investigate its efficacy in treating solid tumors. In this study, DLA tumor bearing mice were randomly

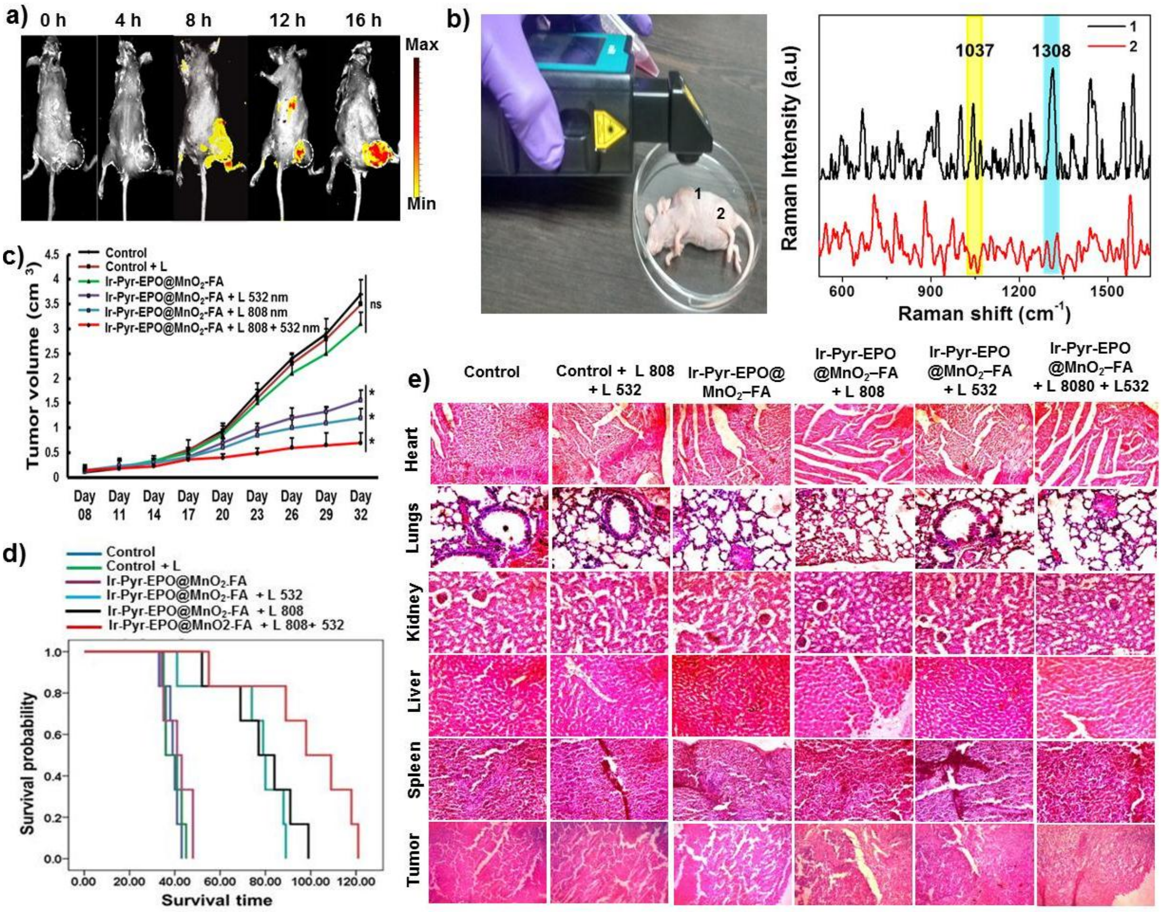

Figure 4.20. a) *In vivo* luminescence images of DLA tumor bearing mice at various time periods. Inset circles represent the tumor area. b) *In vivo* SERS detection of material administered tumor bearing mice (Legends 1 and 2 in the figure represent the tumor region and ventral area respectively). c) Tumor volume reduction studies after various treatments. d) Kaplan Meier survival analysis of mice groups administered with different agents. e) H&E examination of different organs subjected to various treatments.

divided into six groups (n = 12) *viz.* saline as control, saline + laser, **Ir-Pyr-EPO@MnO$_2$-FA** alone, **Ir-Pyr-EPO@MnO$_2$-FA** with 808 nm laser, **Ir-Pyr-EPO@MnO$_2$-FA** with 532 nm laser and **Ir-Pyr-EPO@MnO$_2$-FA** with combined 808 and 532 nm lasers. Following the material administration, 808 and 532 nm laser irradiation were performed at the 4th and 12th h respectively and the treatment responses were subsequently subjected to monitoring using various experiments. After various therapeutic strategies, tumor reduction studies revealed a significant decline in the tumor volumes of mice injected with the nanoconstruct after dual laser (808 + 532 nm) and single laser (808/532 nm) administration (**Figure 4.20c**) accompanied with increased survival benefits when compared against the ones injected with saline and **Ir-Pyr-EPO@MnO$_2$-FA** alone (**Figure 4.20d**). Detailed examination of body weight changes, hematological parameters, biochemical factors, and major pathological changes with various organs revealed a relatively safer therapeutic procedure without eliciting any significant damage to other major organs (**Tables 4.1-4.8**). After 32 days, all the animals were sacrificed and the tumors were snipped out wherein a clear reduction in the size of the tumor was observed with the mice subjected to **Ir-Pyr-EPO@MnO$_2$-FA** with dual laser treatments (**Figure 4.21b**). Finally, the hematoxylin & eosin (H&E)

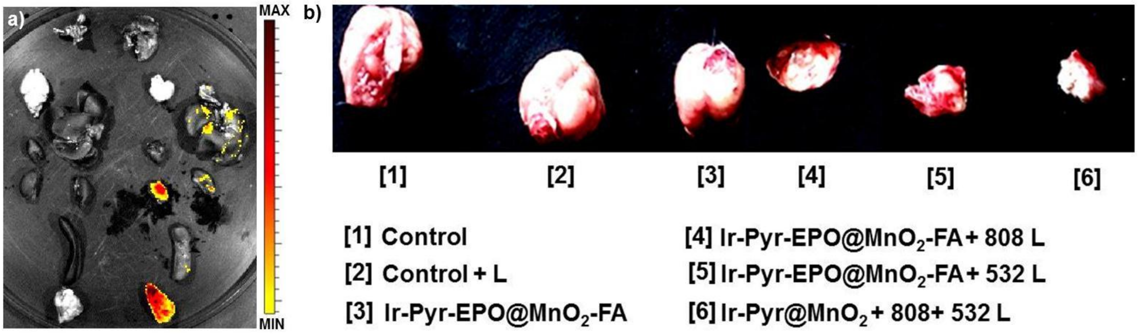

Figure 4.21. a) *Ex vivo* luminescence images of DLA tumor bearing mice before (left) and after administration with **Ir-Pyr-EPO@MnO$_2$-FA** (right). b) Photographs depicting the reduction in tumor size of mice after various therapeutic strategies.

staining performed on various organs of the euthanized animals showed severe signs of damage to the tumor tissues extracted from the material + laser (808 + 532 nm) treated animals while offering a safer side to all other major organs, indicating the suitability of **Ir-Pyr-EPO@MnO$_2$-FA** as an effective therapeutic tool for cancer theranostics (**Figure 4.20e** and **Tables 4.4-4.8**).

Treatment groups	Average weight at day 0 (mg)	Average weight at day 10 (mg)	Average weight at day 20 (mg)	Average weight at day 30 (mg)
Vehicle control	**25.0 ± 1.6**	**25.2 ± 0.9**	**25.4 ± 0.6**	**25.9 ± 0.4**
Control + laser	**25.2 ± 0.1**	**25.3 ± 0.8**	**25.2 ± 0.6**	**25.4 ± 1.2**
Ir-Pyr-EPO@MnO$_2$-FA	**24.9 ± 0.3**	**25.2 ± 0.5**	**25.0 ± 1.0**	**25.2 ± 0.5**
Ir-Pyr-EPO@MnO$_2$-FA + 808 nm laser	**25.5 ± 0.9**	**24.9 ± 0.4**	**25.1 ± 0.4**	**24.6 ±0.4**
Ir-Pyr-EPO@MnO$_2$-FA + 532 nm laser	**25.6 ± 0.6**	**24.7 ± 0.4**	**24.5 ± 0.4**	**24.7 ±0.9**
Ir-Pyr-EPO@MnO$_2$-FA + 808 + 532 nm laser	**25.0 ± 1.0**	**24.8 ± 0.4**	**24.7 ± 0.8**	**24.3 ±0.9**

Table 4.1. Change in body weight after various treatments in BALB/c mice. The data is presented as the mean ± SD value of three replicates.

	Control	Control + laser	Ir-Pyr-EPO@ MnO_2-FA	Ir-Pyr-EPO@MnO_2 -FA + 808 nm laser	Ir-Pyr-EPO@MnO_2 -FA + 532 nm laser	Ir-Pyr-EPO@MnO_2 -FA + 808 + 532 nm laser
Haematology						
Hb (gm %)	12.2	12.5	11	11.2	10	11.9
TC (/cmm)	4800	5200	4800	4850	5100	4690
DC(%) Poly	40	41	47	44	45	57
Lymph	59	58	50	55	44	40
Eosin	1	1	3	1	1	3
Mono	Nil	Nil	Nil	Nil	Nil	Nil
Baso	Nil	Nil	Nil	Nil	Nil	Nil
ESR (mm/hr)	5	4	6	4	5	6
Platelets (/cmm)	950000	930000	870000	840000	900000	880000

Table 4.2. Estimation of various haematological parameters of mice after treatment with **Ir-Pyr-EPO@MnO_2-FA**. Data represent the mean ± SD value of three replicates.

	Control	Control + laser	Ir-Pyr-EPO@ MnO_2-FA	Ir-Pyr-EPO@MnO_2 -FA + 808 nm laser	Ir-Pyr-EPO@MnO_2 -FA + 532 nm laser	Ir-Pyr-EPO@MnO_2 -FA + 808 + 532 nm laser
Biochemistry						
RBS (mg %)	110	111	109	103	112	108
B. Urea (mg%)	34	36	41	39	43	45
S. Creatinine (mg%)	1.1	0.9	1.4	0.8	1.5	2
SGOT (IU/L)	31	30	41	40	44	45
SGPT (IU/L)	28	32	42	33	40	39
S. Cholesterol (mg/dl)	166	180	164	155	185	177
Triglyceride (mg/dl)	152	149	140	141	132	130
Bilirubin Total (mg%)	0.8	0.8	1.3	0.9	0.9	1
Bilirubin Direct (mg%)	0.01	0.01	0.01	0.01	0.02	0.01
Total Protein (g/dl)	7.9	7.2	7.8	7	6.8	6.7
Albumin (g/dl)	3.4	3.5	3.2	3.6	3.1	3
Globulin (g/dl)	4	3.1	3	3.4	2.9	2.8

Table 4.3. Estimation of various biochemical parameters of mice after treatment with **Ir-Pyr-EPO@MnO_2-FA**. Data represent the mean ± SD value of three replicates.

HEART	Control	Control + laser	Ir-Pyr-EPO@ MnO_2-FA	Ir-Pyr-EPO@ MnO_2-FA + 808 nm laser	Ir-Pyr-EPO@ MnO_2-FA + 532 nm laser	Ir-Pyr-EPO@ MnO_2-FA + 808 + 532 nm laser
Interfibrillar haemorrhage	-	-	-	-	+	-
Disruption of cardiac muscle	-	-	-	+	+	+
Infiltration of lymphocytes	-	-	-	+	+	++
Hydropic degeneration	-	-	-	-	-	-
Disruption of cardiac muscle banding pattern	-	-	-	-	-	-
Focal myolysis	-	-	+	-	-	+
Endothelial cell hyperplasia of cardiac blood vessels	-	+	-	-	-	+
Edema of arterial blood vessels	-	-	-	-	+	-

Table 4.4. Evaluation of major pathological changes of heart of mice after various treatments with **Ir-Pyr-EPO@MnO_2-FA** through H&E staining analysis. The legends, [-] represents absence, [+] represents mild changes, [++] represents moderate changes and [+++] represents severe changes. Data represent the mean ± SD value of three replicates.

LIVER	Control	Control + laser	Ir-Pyr-EPO@ MnO_2-FA	Ir-Pyr-EPO@ MnO_2-FA + 808 nm laser	Ir-Pyr-EPO@ MnO_2-FA + 532 nm laser	Ir-Pyr-EPO@ MnO_2-FA + 808 + 532 nm laser
Dilation of sinusoidal spaces	-	-	-	+	+	+
Infiltration of lymphocytes	-	-	+	+	+	+
Infiltration of histocytes	-	-	+	+	-	-
Bi-nucleation	-	-	-	-	+	+
Condensation of nuclei	-	-	-	+	-	+
Nuclear enlargement	-	-	-	-	+	+
Cellular edema	-	-	-	+	++	++
Kupffer cell proliferation	-	-	-	-	+	+
Bile duct proliferation	-	-	-	-	-	-
Multi-nucleation	-	-	-	-	++	+

Table 4.5. Evaluation of major pathological changes of liver of mice after various treatments with **Ir-Pyr-EPO@MnO_2-FA** through H&E staining analysis. The legends, [-] represents absence, [+] represents mild changes, [++] represents moderate changes and [+++] represents severe changes. Data represent the mean ± SD value of three replicates.

KIDNEY	**Control**	**Control + laser**	**Ir-Pyr-EPO@ MnO_2-FA**	**Ir-Pyr-EPO@ MnO_2-FA + 808 nm laser**	**Ir-Pyr-EPO@ MnO_2-FA + 532 nm laser**	**Ir-Pyr-EPO@ MnO_2-FA + 808 + 532 nm laser**
Degenerative changes in tubules	-	-	-	-	+	+
Enlargement of glomerulus	-	-	-	+	+	++
Shortening of capsular space	-	-	-	-	-	-
Enlarged nuclei in tubules	-	-	+	+	+	+
Chromatin condensation of glomerulus	-	-	+	+	+	+
Hydrophic degeneration	-	-	++	+	+	+
Focal infiltration of inflammatory cells	-	-	-	++	++	++
Tubular necrosis	-	-	-	-	+	+

Table 4.6. Evaluation of major pathological changes of kidney of mice after various treatments with **Ir-Pyr-EPO@MnO_2-FA** through H&E staining analysis. The legends, [-] represents absence, [+] represents mild changes, [++] represents moderate changes and [+++] represents severe changes. Data represent the mean ± SD value of three replicates.

LUNGS	Control	Control + laser	Ir-Pyr-EPO@ MnO_2-FA	Ir-Pyr-EPO@MnO_2-FA + 808 nm laser	Ir-Pyr-EPO@MnO_2-FA + 532 nm laser	Ir-Pyr-EPO@MnO_2-FA + 808 + 532 nm laser
Necrosis	-	-	-	-	-	-
Alveolar fibrosis	-	-	+	+	-	-
Edema	-	-	+	+	+	+
Peribranchial lymphocyte infiltration	-	-	+	-	-	-
Metaplasia	-	-	-	+	+	+
Emphysema	-	-	-	-	+	-
Bronchial cell hyperplasia	-	-	-	+	+	++

Table 4.7. Evaluation of major pathological changes of lungs of mice after various treatments with **Ir-Pyr-EPO@MnO_2-FA** through H&E staining analysis. The legends, [-] represents absence, [+] represents mild changes, [++] represents moderate changes and [+++] represents severe changes. Data represent the mean ± SD value of three replicates.

SPLEEN	Control	Control + laser	Ir-Pyr-EPO@MnO$_2$-FA	Ir-Pyr-EPO@MnO$_2$-FA + 808 nm laser	Ir-Pyr-EPO@MnO$_2$-FA + 532 nm laser	Ir-Pyr-EPO@MnO$_2$-FA + 808 + 532 nm laser
Congestion of spleen	-	-	+	+	-	+
Degenerative changes	-	-	-	-	+	-
Presence of macrophages	-	-	+	+	++	++
Lymphoid necrosis	-	-	-	-	+	-
Apoptotic bodies	-	-	-	-	-	-
Lymphocyte hyperplasia	-	-	-	+	+	++
Tingible body macrophages	-	-	-	-	-	-
Eosinophil infiltration	-	-	+	+	+	++
Fatty infiltration	-	-	-	-	-	-
Pigmentosis	-	-	-	-	-	-

Table 4.8. Evaluation of major pathological changes of spleen of mice after various treatments with **Ir-Pyr-EPO@MnO$_2$-FA** through H&E staining analysis. The legends, [-] represents absence, [+] represents mild changes, [++] represents moderate changes and [+++] represents severe changes. Data represent the mean ± SD value of three replicates.

4.4. Conclusion

In conclusion, we have successfully demonstrated that the limitation of PDT with hypoxic tumors could be surmounted by sequential singlet oxygen photogeneration using **Ir-Pyr-EPO@MnO$_2$-FA**. Due to the $^1O_2$ self-enriching characteristics together with tumor microenvironment responsive oxygen generation features, the probe afforded a multi-stage photodynamic therapy to generate intracellular oxygen independent cytotoxic singlet oxygen species. Meanwhile, the luminescence recovery of the photosensitizer facilitated by the stimuli responsive reduction of MnO$_2$ allowed the probe to be a theranostic platform for the accurate diagnosis and positioned treatment of hypoxic tumors via oxygen irrelevant PDT/PTT under the guidance of luminescence imaging. The *in vitro* and *in vivo* results demonstrated the execution of the first phase of PDT via the thermal cycloreversion process while getting prepared for the next round of singlet oxygen generation by the photosensitization of the molecular oxygen produced by the TME mediated reduction of MnO$_2$. Considering the fact that hypoxia and PDT mediated hypoxia are the major issues hampering the wider applicability of PDT, the work presented here lead to a paradigm change in cancer treatment and might offer great benefits for future clinical translations.

4.5. Experimental Section

4.5.1. Materials and Methods

All chemical reagents, unless otherwise specified, were purchased from Sigma-Aldrich Co. All solvents used were of reagent grade and were purchased from local companies. The solvents were dried and distilled prior to use by following standard procedures. NMR spectra were recorded on a Bruker 500 MHz FT-NMR (model: Advance-DPX 300) spectrometer at 25 °C. The chemical shift (δ) data and coupling constant (J) values were given in parts per million (ppm) and Hertz (Hz), respectively, unless otherwise mentioned. High-resolution mass spectra (HRMS) were recorded on a Thermo Scientific Exactive ESI-MS spectrophotometer. Experimental procedures for the absorption, emission and SERS spectral measurements are described in **Chapters 2** and **3**.

4.5.2. Description of Experimental Techniques

4.5.2.1. Determination of Singlet Oxygen Generation using DPBF Assay

Singlet oxygen generated from the probe was evaluated by monitoring the quenching of absorbance of DPBF, a widely used $^1O_2$ scavenging agent. A 10 µM solution of the probe was dissolved in acetonitrile and subsequently mixed with DPBF and subjected to light irradiation using a 532 nm laser (0.2 W/cm^2). The decrease in absorbance of DPBF at 410 nm was monitored at predetermined time intervals. Singlet oxygen generation efficiency was determined from a plot of change in absorbance (ΔA) versus irradiation time.

4.5.2.2. Investigation of Photothermal Efficacy of MnO_2 Nanosheets

The photothermal efficacy of MnO_2 nanosheets was evaluated by taking various concentrations of the material (6.25, 12.5, 25, 50, 100 µg/mL) and subjected to irradiation with an 808 nm laser at a power density of 0.5 W/cm^2 for 10 minutes.

4.5.2.3. Cell Culture

Human cancer cell lines HeLa (cervical cancer) and A549 (lung adenocarcinoma) were obtained from American Type Culture Collection (Manassas, USA). Human lung fibroblast cell line, WI-38 was kindly gifted form Indian Institute of Chemical Biology (IICB) Kolkata, India. Spheroids of HeLa cells were developed with the transfer of cells into ultra-low attachment cell culture flasks. Cells were maintained in Dulbecco's modified Eagle medium (DMEM) with 10% fetal bovine serum (FBS) and 5% CO_2 at 37 °C, while the resistant cell lines were maintained in the media with the desired drug concentration. Hypoxic variant of HeLa cells were produced by incubation with cobalt chloride ($CoCl_2$), which has the advantage to be inexpensive and fast. HeLa cells were seeded into 96 well plate and after 6 h, media was removed and replaced with fresh medium containing $CoCl_2$ (100 µM) for 24 h.

4.5.2.4. Cytotoxicity Evaluation using MTT Assay

The cytotoxicity was evaluated for a period of 24 h using various constructs viz **Ir-Pyr**, MnO_2 nanosheets and **Ir-Pyr-EPO@**$\mathbf{MnO_2}$**-FA**. The cell growth inhibitory potential of HeLa, A54 and WI38 cells was measured using the MTT assay as described in **Chapter 2**. MTT assay for the spheroids was carried out with slight modification to the standard protocol. Spheroids (6-8 days) were maintained in the 96 well plates and subjected to different treatments for 24 - 48 h. Later, 20 µL of MTT solution was added into each well and incubated for 4 h. The content of each well containing the spheroids was transferred to a new, flat-bottom 96-well plate before the plate was centrifuged at 1,000 × g for 5 min. Then, 150 µL of media was aspirated from each well, followed by the addition of 100 µL of DMSO. Finally, absorbance was recorded at 570 nm (BioTek, PowerWave XS, USA).

4.5.2.5. *In Vitro* Oxygen Generation Studies

To check whether the MnO_2 nanosheets alone, without laser trigger could alleviate hypoxia, normoxic and hypoxic HeLa monolayer and spheroids were treated with the nanosheets for a peroid of 12 h. Later, a commercial hypoxia detecion probe ($Ru(dpp)_3Cl_2$) (100 µM) was incubated with the cells for 10 minutes. Spheroids were counter stained with Hoechst and imaged under an inverted fluorescence microscope with a PI filter and Dapi filter (Olympus 1X51, Singapore).

4.5.2.6. Detection of Intracellular Singlet Oxygen Generation

The generation of singlet oxygen *in vitro* was determined with SOSG. Spheroids were incubated with the probe for 4 h and later subjected to laser (808 nm, 0.5

W/cm^2) irradiation. SOSG (10 μM) was added and observed under an FITC filter. The generation of singlet oxygen in the second phase was also determined in a similar manner after treating the spheroids with the material for a peroid of 12 h followed by irradiation with 532 nm laser (0.2 W/cm^2).

4.5.2.7. Apoptosis Evaluation

To gather information about the mechanistic action, various apoptosis assays were performed on cells and spheroids. Acridine orange-ethidium bromide dual staining effectively differentiates viable and non-viable cells which was carried out as per the procedure described in **Chapter 2**. Cells and spheroids were observed under a FITC filter. In order to access information about the early stages of the execution of apoptosis, FITC-Annexin V staining (BD Pharmingen no. 556547, BD Biosciences, San Jose, CA) was also performed by flow cytometry, using kit-specified instructions on a FACS Jazz flow cytometer (BD Biosciences, San Jose, CA), and the data were analyzed with the FACSDIVA software. Early-onset of programmed cell death was further confirmed using APOPercentage dye (Biocolor, Belfast, Northern Ireland) as per the manufacturer's instructions.

4.5.2.8. *In Vivo* Experiments

Animal experiments were performed according to the CPCSEA (Committee for the Purpose of Control and Supervision of Experiments on Animals) guidelines and were approved by the Institutional Animal Ethics Committee (IAEC). The murine transplantable lymphoma cell line DLA, was maintained in the peritoneal cavity of mice by *ip* transplantation of $1x10^6$ cells per mouse. Tumor reduction experiments were initially performed with DLA solid tumor-bearing BALB/c mice. The experiments were performed as described before.[35,36] When the tumor diameters reached 100-200 mm^3, the mice were randomly divided into six groups, and administerd with (1) saline, (2) saline + laser (808 nm + 532 nm laser), (3) **Ir-Pyr-EPO@MnO_2-FA** without laser, (4) **Ir-Pyr-EPO@MnO_2-FA** + 808 nm laser, (5) **Ir-Pyr-EPO@MnO_2-FA** + 532 nm laser, (6) **Ir-Pyr-EPO@MnO_2-FA** +808 nm + 532 nm laser. The injections were performed on days 8, 12, 16 and 20 (once per day). Initially animals were administered with the constructs (*ip*) and later the tumors were irradiated by NIR light for 5 min at the power dose of 0.5 W/cm^2 at 4th h with an 808 nm laser and subsequent irradiation with 532 nm laser (0.2 W/cm^2, 5 min) at the 12th h. The tumor volume was measured on every three days interval up to day 32. Changes in body weight were also recorded. On day 32, the mice were sacrificed, and the tumors as well as the major organs were harvested and sectioned for H&E staining. The mean survival time (MST) and the percentage of increase in life span (% ILS) were calculated as previously reported. Finally, the survival analysis was made using Kaplan−Meier survival analysis (IBM Inc., New York, USA). Whole-body luminescence imaging was performed using a Perkin Elmer (Waltham, MA, USA) IVIS instrument. In order to quantify the organ wise biodistribution, the animals were sacrificed, and the organs were examined for the luminescence intensity.

4.5.2.9. Synthesis of MnO_2 Nanosheets

MnO_2 nanosheets were synthesized as per previously reported procedure.[37] Briefly, 5 mL of sodium dodecyl sulfate (0.1 M) and 0.25 mL of H_2SO_4 were added to 44.25 mL of distilled water and heated at 95 °C for a period of 15 min. To this solution, 0.5 mL of $KMnO_4$ (0.05 M) was added dropwise and kept for another 60 min. The as-formed MnO_2 nanosheets were then purified by washing with Milli Q water by continuous rounds of centrifugation at 10,000 rpm (10 min). The surface of MnO_2 nanosheets was modified with bovine serum albumin (BSA) by incubation with 5 mg/mL BSA solution for 24 h and purified by centrifugation (10,000 rpm, 10 min). The BSA stabilized MnO_2 nanosheets were subjected to characterization by UV-Vis spectrophotometry, Raman spectroscopy and TEM analysis.

4.5.2.10. Synthesis of MnO_2-FA Nanosheets

Towards the preparation of FA functionalized MnO_2, we have covalently conjugated FA to BSA using EDC-NHS chemistry as reported elsewhere.[38] The as formed BSA-FA conjugates were purified by dialysis (molecular weight cut-off : 8000) for 2 days using PBS and 2 days with distilled water to remove the unreacted reactants and excess byproducts. The SDS stabilized MnO_2 nanosheets (2 mg/mL) synthesized using the above procedure were then incubated with BSA-FA (1.5 mg/mL) at room temperature for 24 h to afford MnO_2-FA which was purified by repeated washing with distilled water.

4.5.2.11. Preparation of Ir-Pyr@MnO_2 and Ir-Pyr@MnO_2-FA Hybrid

The preparation of **Ir-Pyr@MnO_2** was performed by mixing MnO_2 nanosheets with **Ir-Pyr** by sonication for 15 min at room temperature which will cause the electrostatic attachment of negatively charged MnO_2 with positively charged **Ir-Pyr**. For the preparation of **Ir-Pyr@MnO_2-FA**, FA functionalized MnO_2 (MnO_2-FA) nanosheets were added to the **Ir-Pyr** solution instead of bare MnO_2 sheets and followed the same procedure as described above.

4.5.2.12. Preparation of Ir-Pyr-EPO

The preparation of **Ir-Pyr-EPO** was done by dissolving **Ir-Pyr** in oxygenated acetonitrile solution and then subjected it to light irradiation under a 532 nm laser source (0.2 W/cm^2) for 15 minutes. The as-generated endoperoxide adduct was used as such or kept at -20 ºC until further use.

4.5.3. Synthesis and Characterization

Synthesis of 4,4'-bis(bromomethyl)-2, 2'-bipyridine (6)

900 mg (4.16 mmol) of **5** was dissolved in a mixture of 48% aqueous HBr (5 mL) and conc. H_2SO_4 (2 mL) and the reaction was kept at 90 ºC under Argon

atmosphere for 12 h. After cooling to room temerature, 10 mL of water was added to the above mixture and the pH was adjusted to 7-8 using NaOH. The as-formed precipitate was washed repeatedly with water and dried under vacuum to afford the product. Yield: 48%. ^{1}H NMR (500 MHz, $CDCl_3$, TMS) δ (ppm): 8.60 (d, 2H), 8.35 (s, 2H), 7.29 (d, 2H), 4.41 (s, 4H); ^{13}C NMR (125 MHz, $CDCl_3$) δ (ppm): 147.85, 146.29, 145.97, 133.97, 129.75, 60.42. HRMS calculated for $C_{12}H_{10}Br_2N_2$ (M^+): 341.9190, found: 342.9268.

Synthesis of 1,1'-(2,2'-bipyridine-4,4'-diylbis(methylene))dipyridin-2(1H)-one (7)

100 mg (1 equivalent) of **6** and 57.36 mg (2.05 equivalents) of 2-hydroxypyridine (2-pyridone) were taken in an oven-dried two-neck round bottom flask. K_2CO_3 (203.29 mg, 5 equivalents) was added to the above mixture dissolved in acetone. Then catalytic amounts of KI and 18-crown-6 were added and the reaction was done under stirring at 50 ºC for 72 h. After cooling the reaction mixture to room temperature, the solvent was evaporated and the residue was extracted using dichloromethane/water. The reaction crude was further subjected to purification using silica gel column chromatography using $CHCl_3$/methanol as the mobile phase to obtain **7** in pure form.

Yield: 48%. ^{1}H NMR (500 MHz, $CDCl_3$, TMS) δ (ppm): 8.55 (d, 2H), 8.25 (d, 2H), 7.74-7.72 (m, 2H), 7.33-7.22 (m, 4H), 6.57 (d, 2H), 6.18 (t, 2H), 5.14 (s, 4H); ^{13}C NMR (125 MHz, $CDCl_3$) δ (ppm): 162.04, 155.70, 149.82, 147.94, 140.31, 134.52, 125.53, 118.04, 106.36, 51.43. HRMS calculated for $C_{22}H_{18}N_4O_2$ (M^+): 370.1430, found: 371.1511.

Synthesis of Ir-Pyr

The synthesis of Ir dimer complex (**9**) was carried out by reacting $IrCl_3.xH_2O$ (299.15 mg, 1.0 mmol) with 2-phenylpyridine (320.25 mg, 2.1 mmol) in 20 mL 2-ethoxyethanol/water (8:2) mixture under reflux condition for 24 h. After cooling the solution to room temperature, 40 mL of water was added to afford the product as a yellow precipitate that was then filtered and washed with diethyl ether. The crude product thus obtained was used as such for the next reaction. For the synthesis of **Ir-Pyr**, 1 equivalent of dimer (**9**) was reacted with 2.5 equivalents of **7** in presence of sodium carbonate (10 equivalents) at 60 ºC in 40 mL of 1:3 dichloromethane (DCM)/ethanol under Ar atmosphere. The solvents were removed by evaporation under reduced pressure and the crude product was poured into an aqueous solution of NH_4PF_6. The reaction mixture was then extracted with DCM and the combined organic layers were dried *in vacuo* to afford the product which was subjected to purification by column chromatography over silica gel using DCM/methanol as the eluent. The desired complex was obtained as a yellow powder after re-precipitation in hexane/DCM. Yield: 39%. ^{1}H NMR (500 MHz, $CDCl_3$, TMS) δ (ppm): 8.47 (s, 2H), 7.82-7.75 (m, 4H), 7.67-7.62 (m, 4H), 7.57 (d, 2H), 7.41 (d, 2H), 7.32-7.29 (m, 4H), 6.95-6.92 (m, 4H), 6.80 (s, 2H), 6.48 (d, 2H), 6.24-6.16 (m, 4H), 5.24 (s, 4H); ^{13}C NMR (125 MHz, $CDCl_3$) δ (ppm): 167.69, 162.74, 155.70, 150.46, 149.92, 149.42, 148.74, 143.44, 140.83, 138.85, 138.11, 131.61, 130.80, 127.45, 124.75, 124.15, 123.46, 122.71, 120.71, 119.61, 107.41, 51.89. HRMS calculated for $C_{44}H_{34}IrN_6O_2$ (M^+): 871.2370, found: 871.2390.

4.6. References

[1] Dolmans, D. E. J. G. J.; Fukumura, D.; Jain, R. K. *Nat. Rev. Cancer* **2003**, *3*, 380.

[2] Narayanan, N.; Nair, L. V.; Karunakaran, V.; Joseph, M. M.; Nair, J. B.; Ramya, A. N.; Jayasree, R. S.; Maiti K. K. *Nanoscale,* **2016**, *8,* 11392.

[3] Lucky, S. S.; Soo, K. C.; Zhang, Y. *Chem. Rev.* **2015**, *115*, 1990.

[4] Sujai, P. T.; Joseph, M. M; Karunakaran, V.; Saranya, G.; Adukkadan, R. N; Shamjith, S.; Thomas, R.; Nair, J. B.; Swathi, R. S.; Maiti K. K. *ACS Appl. Bio Mater.* **2019**, *2*, 588.

[5] Guo, X.; Qu, J.; Zhu, C.; Li, W.; Luo, L.; Yang, J.; Yin, X.; Li, Q.; Du, Y.; Chen, D.; Qiu, Y.; Lou, Y.; You, J. *Drug Delivery* **2018**, *25*, 585.

[6] Höckel, M.; Vaupel, P. *Semin. Oncol.* **2001**, *28*, 36.

[7] Li, X.; Kwon, N.; Guo,; Liu, Z.; Yoon, J. *Angew. Chem., Int. Ed.* **2018**, *57*, 11522–11531.

[8] Zhu, W.; Dong, Z.; Fu, T.; Liu, J.; Chen, Q.; Li, Y.; Zhu, R.; Xu, L.; Liu, Z. *Adv. Funct. Mater.* **2016**, *26*, 5490.

[9] Sullivan, R.; Graham, C. H. *Cancer Metastasis Rev.* **2007**, *26*, 319.

[10] Brown, J. M.; Wilson, W. R. *Nat. Rev. Cancer* **2004**, *4*, 437.

[11] Vaupel, P.; Höckel, M.; Mayer, A. *Antioxid. Redox Signaling* **2007**, *9*, 1221.

[12] Luo, Z.; Zheng, M.; Zhao, P.; Chen, Z.; Siu, F.; Gong, P.; Gao, G.; Sheng, Z.; Zheng, C.; Ma, Y.; Cai, L. *Sci. Rep.* **2016**, *6*, 23393.

[13] Cheng, Y.; Cheng, H.; Jiang, C.; Qiu, X.; Wang, K.; Huan, W.; Yuan, A.; Wu, J.; Hu, Y. *Nat. Commun.* **2015**, *6*, 8785.

[14] Song, X.; Feng, L.; Liang, C.; Yang, K.; Liu, Z. *Nano Lett.* 2016, 1*6*, 6145.

[15] Xia, D.; Xu, P.; Luo, X.; Zhu, J.; Gu, H.; Huo, D.; Hu, Y. *Adv. Funct. Mater.* **2019**, *26*, 1807294.

[16] Lv, W.; Xia, H.; Zhang, K. Y.; Chen, Z.; Liu, S.; Huang, W.; Zhao, Q. *Mater. Horiz.* **2017**, *4*, 1185.

[17] Pierlot, C.; Rataj, V.; Aubry, J.-M. In *Singlet Oxygen: Applications in Biosciences and Nanosciences Vol. 1* (Eds.: S. Nonell, C. Flors), Royal Society of Chemistry, Cambridge, **2016**, pp. 49–73.

[18] Aubry, J.-M.; Pierlot, C.; Rigaudy, J.; Schmidt, R. *Acc. Chem. Res.* **2003**, *36*, 668.

[19] Fudickar, W.; Linker, T. *ChemPhotoChem* **2018**, *2*, 548.

[20] Wasserman, H. H.; Larsen, D. L. *J. Chem. Soc. Chem. Commun.* **1972**, 5.

[21] Kolemen, S.; Ozdemir, T.; Lee, D.; Kim, G. M.; Karatas, T.; Yoon, J.; Akkaya, E. U. *Angew. Chem., Int. Ed.* **2016**, *55*, 3606.

[22] Turan, I. S.; Yildiz, D.; Turksoy, A.; Gunaydin, G.; Akkaya, E. U. *Angew. Chem., Int. Ed.* **2016**, *55*, 2875.

[23] Lv, W.; Xia, H.; Zhang, K. Y.; Chen, Z.; Liu, S.; Huang, W.; Zhao, Q. *Mater. Horiz.,***2017**, *4*, 1185.

[24] Li, S. P.-Y.; Lau, C. T.-S.; Louie, M.-W.; Lam, Y.-W.; Cheng, S. H.; Lo, K. K.-W. *Biomaterials* **2013**, *34*, 7519–7532.

[25] Gao, R.; Ho, D. G.; Hernandez, B.; Selke, M.; Murphy, D.; Djurovich, P. I.; Thompson, M E. *J. Am. Chem. Soc.* **2002**, *124*, 14828.

[26] Sudheesh, K. V.; Jayaram, P. S.; Samanta, A.; Bejoymohandas, K. S.; Jayasree, R. S.; Ajayaghosh, A. *Chem. Eur. J.* **2018**, *24*, 10999.

[27] Matsumoto, M.; Yamada, M.; Watanabe, N. *Chem. Commun.* **2005**, *4*, 483.

[28] Wiegand, C.; Herdtweck, E.; Bach, T. *Chem. Commun.* **2012**, *48*, 10195.

[29] Benz, S.; Nçtzli, S.; Siegel, J. S.; Eberli, D.; Jessen, H. J. *J. Med. Chem.* **2013**, *56*, 10171.

[30] Eleftherios, K. P.; Christodouleas, D.; Giokas, D. L.; Papadopoulos, K.; Vougioukalakis, G. C. *Eur. J. Inorg. Chem.* **2013**, *26*, 4628.

[31] Spyratou, E.; Makropoulou, M.; Mourelatou, E. A.; Demetzos, C. *Cancer Lett.* **2012**, *327*, 111.

[32] Fan, W.; Bu, W.; Shen, B.; He, Q.; Cui, Z.; Liu, Y.; Zheng, X.; Zhao, K.; Shi, J. *Adv. Mater.* **2015**, *27*, 4155.

[33] López-Lázaro, M. *Cancer Lett.* **2007**, *252*, 1.

[34] Lopez-Lazaro, M. *FASEB J.* **2006**, *20*, 828.

[35] Ramya, A. N.; Joseph, M. M.; Maniganda, S.; Karunakaran, V.; Sreelekha T. T.; Maiti, K. K. *Small* **2017**, 13, 1700819.

[36] Joseph, M. M.; Nair, J. B.; Adukkadan, R. N.; Hari, N.; Pillai, R. K.; Nair, A. J.; Maiti, K. K.; Therakathinal, S. T. *ACS Appl. Mater. Interfaces* **2017**, 9, 19578.

[37] Wei, F.; Cui, X. W.; Chen, W. X.; Ivey, D. G. *Chem. Soc. Rev.* **2011**, 40, 1697.

[38] Ma, N.; Liu, J.; He, W.; Li, Z.; Luan, Y.; Song, Y.; Garg S. *J. Colloid Interface Sci.* **2017**, 490, 598−607.

Summary and Conclusion

The design and creation of smart functional bioanalytical tools for the detection and profiling of various biological targets and their associated functions poses wide ranging applications in clinical diagnostics and biomedicine. Among the various detection tools, optical assays allow an in-depth understanding of the molecular interactions in living systems which facilitate precise monitoring of biomarkers that can be used as targets for disease identification, therapy and follow-up of treatment responses. In this context, fluorescence imaging and SERS imaging are the two powerful techniques that allow real-time, non-invasive monitoring of biomolecules of interest in their native environments with high spatial and temporal resolution. In addition to effective diagnosis, development of multifunctional molecular theranostic platforms for the concordant visualization and precise treatment of diseases with high sensitivity and resolution has become a crucial strategy in the efficient management of diseases. In this scenario, development of new functional materials with improved sensing capabilities and high therapeutic potential is a hot topic of research among the scientific community. The present thesis deals with a systematic study on the design, synthesis and assessment of a few rationally designed small molecule based optical probes for diagnostic and therapeutic applications in cancer. We have demonstrated the synthesis of a few molecules and then investigated their optical properties that have been further utilized for various sensing, imaging and treatment applications. These functional materials have the potential to offer new avenues for the development of clinically relevant probes for point-of-care diagnosis and personalized treatment applications.

The introductory chapter of the thesis provides an overview of the recent developments in the construction of optical probes that work on fluorescence and SERS and their potential in the diagnostic and theranostic applications for efficient clinical outcome. A literature review on functional small molecule based optical probes and the biomedical applications of these materials are also discussed in this chapter. The second chapter of the thesis deals with the design and synthesis of a near infrared squaraine based fluorescent probe (**Sq**) for the real time imaging of biological thiols. The probe afforded a ratiometric detection of thiols by switching its emission from NIR (690 nm) to visible region (560 nm). Benefiting from the favorable attributes of high biocompatibility, excellent membrane permeability and fast response, the **Sq** dye was utilized for the quantification of endogenous GSH concentrations in live cells and cell extracts. The probe also offered a promising strategy for discriminating between cancerous and normal cells through the investigation of cellular redox status. Further applicability of the probe was elucidated by developing an easy and reliable method for the on-demand apoptotic progression assay in real-time by probing the role of GSH during various time spans of apoptosis on both semi-quantitative and quantitative grounds. Taken together, the results unveil a new non-invasive pathway for assaying apoptosis, which may offer a promising outcome in drug discovery and effective follow up of therapeutic responses in living systems.

The third part of the thesis describes the design and fabrication of smart programmable nanostructures for the multiplexed detection of most prevalent panel of disease biomarkers present in lung cancer. The multiplex nanoprobes comprised of dual responsive Raman active fluorophores attached to the surface of gold nanospheres through a strategically positioned peptide (Phe-Lys-Cys; FKC) sequence which is recognized as a specific substrate for cathepsin B (cathB), a key protease involved in cancer invasion and progression. The interplay of cathB enzyme with the nanoprobes induced the scission of FKC upon homing into the cancer cells, resulting in the release of the initially latent fluorophores with a concomitant decline in the surface-enhanced Raman signal intensity, thereby realizing an on−off switching between the fluorescence and Raman modalities. The anticipated mode of action of fluorescence-SERS encoded nanoparticle probes (**FSENP**s) was utilized for the detection of defined protein targets after decorating with specific monoclonal antibody recognition units. Taking advantage of the excellent dual functional multiplexing potential and the target specific recognition property, **FSENP**s served as perfect candidates for the accurate multiplexing of target antigens in the pathologically tested patient specimens, which offer new avenues for the development of a clinical screening tag for point-of-care diagnosis and personalized treatment applications.

In the last part of the study, the design and development of a multifunctional photosensitizer complex for theranostic applications is being discussed. This study demonstrated a new strategy for cutting off the intracellular oxygen consumption by developing a redox activatable singlet oxygen ($^1O_2$) self-enriched photoreactor (**Ir-Pyr-EPO@MnO$_2$-FA**) to meet the requirements of intracellular oxygen independent PDT. Upon target specific localization into the cancer cells followed by near infrared light irradiation, the photothermal effect generated by MnO_2 nanosheets facilitated the thermal cycloreversion of **Ir-Pyr-EPO** to release cytotoxic $^1O_2$, thereby paving way for the first phase of photodynamic therapy. Moreover, the tumor microenvironment responsiveness of MnO_2 was utilized in a favourable manner to increase the local oxygen concentration via the degradation of MnO_2 in presence of H_2O_2, which in turn provided room for the second phase of photodynamic therapy. Following the *in vitro* evaluation, the promising therapeutic performance of the probe was investigated *in vivo* in DLA tumor bearing mice which showed superior cytotoxic effects at the target site. Meanwhile, the luminescence recovery of the photosensitizer facilitated by the stimuli responsive reduction of MnO_2 allowed the probe to be a theranostic platform for the accurate diagnosis and positioned treatment of hypoxic tumors via oxygen irrelevant PDT/PTT under the guidance of luminescence imaging. Taken together, the results suggest that the as-developed hybrid complex serves as a potent candidate for addressing the current limitations of conventional photodynamic agents which demand high concentrations of intracellular oxygen to act upon.

Papers Presented at Conferences (Posters/Oral)

1. A Ratiometric Near-Infrared Fluorogen for the Real Time Visualization of Intracellular Redox Status during Apoptosis. **G. Saranya**, M. M. Joseph, V. Karunakaran, P. T. Sujai, K. K. Maiti & A. Ajayaghosh.

   A Poster Presented at the 8th East Asia Symposium on Functional Dyes and Advanced Materials (EAS8) held at CSIR-NIIST, Thiruvananthapuram, Kerala, September, **2017**.

2. A Ratiometric Near-Infrared Fluorogen for the Real Time Visualization of Intracellular Redox Status during Apoptosis. **G. Saranya**, M. M. Joseph, V. Karunakaran, P. T. Sujai, K. K. Maiti & A. Ajayaghosh.

   A Poster Presented at the 6th Asian Biomaterial Congress on Innovative Biomaterials: Technologies for Life and Society (ABMC6) held at SCTIMST, Thiruvananthapuram, Kerala, October, **2017**.

3. Bimodal Fluorescence-SERS Encoded Nanococktail for the Multiplex Detection of Lung Cancer Biomarkers. **G. Saranya**, M. M. Joseph, V. Karunakaran, K. Sujathan, A. Ajayaghosh & K. K. Maiti.

   A Poster Presented at 31st Kerala Science Congress (KSC 2019) held at Fatima Mata National College, Kollam, Kerala, February, **2019** (***Best poster award***).

4. Bimodal Fluorescence-SERS Encoded Nanococktail for the Multiplex Detection of Lung Cancer Biomarkers. **G. Saranya**, M. M. Joseph, V. Karunakaran, K. Sujathan, A. Ajayaghosh & K. K. Maiti.

   A Paper Presented at the 8th Annual Meeting of Indian Academy of Biomedical Sciences, (IABS 2019) held at CSIR-NIIST, Thiruvananthapuram, Kerala, February, **2019**.

List of Publications

Related to Thesis

1. A Ratiometric Near-Infrared Fluorogen for the Real Time Visualization of Intracellular Redox Status during Apoptosis. **G. Saranya**, P. Anees, M. M. Joseph, K. K. Maiti, A. Ajayaghosh *Chem. Eur. J.* **2017**, *23*, 7191−7195.

2. Enzyme-Driven Switchable Fluorescence-SERS Diagnostic Nanococktail for the Multiplex Detection of Lung Cancer Biomarkers. **G. Saranya**, M. M. Joseph, V. Karunakaran, J. B. Nair, V. N. Saritha, V. S. Veena, K. Sujathan, A. Ajayaghosh, K. K. Maiti, *ACS Appl. Mater. Interfaces* **2018**, *10*, 38807−38818.

3. A Rechargeable Singlet Oxygen Photogenerator with Tumor Niche Responsive Luminescence Imaging Capability for Intracellular Oxygen Independent Multiphase Photodynamic Therapy. **G. Saranya**, M. M. Joseph, P. T. Sujai, K. Jibin, R. S. Jayasree, A. Ajayaghosh, K. K. Maiti (Manuscript under preparation).

Not Related to Thesis

4. SERS-Active Multi-Channel Fluorescent Probe for NO: Guide to Discriminate Intracellular Biothiols; K. N. Bobba, **G. Saranya**, S. M. Alex, N. Velusamy, K. K. Maiti, S. Bhuniya, *Sensors and Actuators B* **2018,** *260*, 165 −173.
5. Biogenic Cluster-Encased Gold Nanorods as a Targeted Three-In-One Theranostic Nanoenvelope for SERS Guided Photo-Chemotherapy Against Metastatic Melanoma; P. T. Sujai, M. M. Joseph, V. Karunakaran, **G. Saranya**, A. N. Ramya, S. Shamjith, R. Thomas, J. B. Nair, R. S. Swathi, K. K. Maiti, *ACS Appl. Bio Mater.* **2018**, *2*, 588-600.

6. Exploring the Margins of SERS in Practical Domain: An Emerging Diagnostic Modality for Modern Biomedical Applications; M. M. Joseph, N. Narayanan, J. B.

Nair, V. Karunakaran, A. N. Ramya, P. T. Sujai, **G. Saranya**, J. S. Arya, V. M. Vijayan, K. K. Maiti, *Biomaterials* **2018,** *181*, 140–181.

7. Endogenous H_2S-Assisted Cancer-Cell-Specific Activation of Theranostics with Emission Readout. K. N. Bobba, **G. Saranya**, P. T. Sujai, M. M. Joseph, N. Velusamy, A. Podder, K. K. Maiti, S. Bhuniya, *ACS Appl. Bio Mater.* **2019**, *2*, 1322–1330.

8. Surface Charge Modulates the Internalization vs Penetration of Gold Nanoparticles: A comprehensive Scrutiny on Monolayer Cancer Cells, Multicellular Spheroids and Solid Tumor by SERS Modality. P. T. Sujai, M. M. Joseph, **G. Saranya**, J. B. Nair, V. P. Murali, K. K. Maiti, *Nanoscale* **2020**, *12*, 6971–6975.

9. Optically Controlled Hybrid Metamaterial of Plasmonic Spiky Gold Inbuilt Graphene Sheets for Bimodal Imaging Guided Multimodal Therapy. K. Jibin, J. S. Prasad, **G. Saranya**, S. J. Shenoy, K. K. Maiti and R. S. Jayasree, *Biomater. Sci.* **2020**, doi:10.1039/DOBM00312C.